Artificial Differentiation in 3D-Bioprinted Hydrogels

Julia Müller

Technische Universität München
Fakultät für Physik

Artificial Differentiation in 3D-Bioprinted Hydrogels

Julia Müller

Vollständiger Abdruck der von der Fakultät für Physik der Technischen Universität München zur Erlangung des akademischen Grades einer

Doktorin der Naturwissenschaften

genehmigten Dissertation.

Vorsitzende: Prof. Dr. Karen Alim

Prüfer der Dissertation:

1. Prof. Dr. Friedrich C. Simmel
2. Prof. Dr. Bernhard Wolfrum

Die Dissertation wurde am 02.11.2021 bei der Technischen Universität München eingereicht und durch die Fakultät der Physik am 20.12.2021 angenommen.

Contents

Abstract

Bioprinting is an emerging technology to produce spatially organized structures from soft biocompatible materials of desired shapes in a reproducible manner. In this work, a custom 3D bioprinting platform is constructed based on a commercially available 3D printing chassis. For the construction of the printer, hardware and software are developed to allow for the precise deposition of pico-liter hydrogel-voxels at dedicated locations. Suitable hydrogels are screened and two optimum mixtures for bioprintable inks are developed that can be extruded under mild printing conditions (low temperature, no photo- or chemical crosslinkers). The extruded amorphous samples are equipped with genetic circuits and a variety of sample patterns are generated to study reaction-diffusion within these samples. For the deposition of DNA-modified hydrogels, a bio-ink is developed that employs immobilized single stranded oligonucleotides. With this bio-ink, diffusion of DNA strands can be controlled and programmed. Immobilization of living *Escherichia coli* bacteria is successfully enabled with a second bacteria-ink. Further, bacterial growth and communication within a confined hydrogel environment is studied. The last project concerns the development of an independent electro-bio hybrid circuit to generate strong logic levels within hydrogel compartments containing genetic circuits. The channels between two adjacent hydrogel compartments contain photoresponsive hydrogels and can be switched open via irradiation by the electronic circuit if the circuit detects logic levels of neighboring compartments following a cellular automata approach. The goal of this work is to contribute to the growing field of artificial biological materials by extending the toolbox of available printers and printable inks to facilitate the generation of more complex printable structures and an easier access to bioprinting of bacteria or DNA hydrogels.

Zusammenfassung

Bioprinting - der Druck von Biomaterialien - ist eine neuartige Technologie, die es ermöglicht, genaue räumliche Strukturen biologischer Materialien präzise zu erstellen. In dieser Arbeit wird der Aufbau eines Biodrucker auf Basis eines kommerziellen 3D Druckers beschrieben. Hierzu werden sowohl Hardware - als auch Softwarekomponenten erstellt, sodass pikolitergroße Punkte präzise positioniert werden können. Für die Herstellung optimaler druckbarer Bio-Tinten werden verschiedene geeignete Hydrogele getestet, sodass zwei Mixturen gefunden werden, die unter milden Bedingungen druckbar sind (geringe Temperatur, keine photo- oder chemikalienbasierte Gelierung). Die Biodrucke können mit genetischen Schaltkreisen ausgestattet und in eine Vielzahl von Mustern gedruckt werden, sodass reaktions-diffusions Wechselwirkungen beobachtbar werden. Für die Integration von DNA-basierten Schaltkreisen wird eine Bio-Tinte entwickelt, an der kurze einzelsträngige DNA Moleküle immobilisiert sind. Hiermit kann die Diffusion von einzelsträngiger DNA im Gel kontrolliert und programmiert werden. Darüber hinaus können lebende *Escherichia coli* Bakterien mit dem Biodrucker und einer speziellen Bakterien-Tinte erfolgreich extrudiert werden. Bakterielles Wachstum und Zell-Zell Kommunikation innerhalb der begrenzten Hydrogelkompartimente werden ebenfalls untersucht. In einem weiteren Projekt wird an der Umsetzung einer Elektro-Bio Hybrid-Schaltung gearbeitet. Mit dieser können klar zu unterscheidende Logikpegel in Hydrogelkompartimenten erreicht werden, welche synthetische biologische Schaltungen beinhalten. Zwischen benachbarten Kompartimenten kann eine photo-schaltbare, hydrogelbasierte Verbindung platziert werden, welche von der Elektronikschaltung beleuchtet und damit geöffnet wird. Die Elektronikschaltung bedient sich hierbei der Theorie Zellulärer Automaten und nutzt als Eingangssignale die detektierten Logikpegel benachbarter Kompartimente. Diese Arbeit hat zum Ziel, einen Beitrag zum wachsenden Feld der künstlichen Biomaterialien zu leisten. Die vorhandenen Werkzeuge sollen so erweitert werden, dass in Zukunft für verschiedene Anwendungen, passende Druckerplattformen und Bio-Tinten verfügbar sind. Hiermit werden komplexere Strukturen druckbar und der Zugang zum Druck von Bakterien und DNA vereinfacht.

1. Introduction

In an ever changing world, rapid prototyping for the production of new and improved components and devices became of high importance to keep up with latest developments and find new solutions. While there is a variety of traditional crafts, which allow prototyping as well as manufacturing, no other production process can keep up with the speed of rapid additive prototyping. This new kind of manufacturing is one of the latest technologies and offers new opportunities to form various structures and shapes from Computer-Aided Design (CAD) files. Developed and patented already in 1969 by Johannes F. Gottwald [1] only a little more than 10 years later the first commercial stereolithograph was invented by Chuck Hull. [2] His device opened the path for laser - sinter 3D printers [3] and Fused Deposition Modelling (FDS), also known as Fused Filament Fabrication (FFF) [4] in the early 1990s. The latter evolved over the past decades and now a variety of commercial FFF 3D printers are available. Applications range from small desktop printers for the rapid design of small tools and components to industrial applications.

In recent years, additive manufacturing of biocompatible scaffold structures and 3D printing of gel-encapsulated mammalian cells have become popular approaches for the generation of spatially differentiated cell cultures, and models of living tissues, which promise to have a wide range of biomedical applications. Bioprinting of biological materials is also able to generate soft structures that are biocompatible and non-toxic to surrounding cells. Now, bioprinting is a promising new technology that is extremely interesting for medical applications such as the replacement of injured tissue or parts of dysfunctional organs. It can provide, however, also ideal test environments for research in synthetic biology. [5], [6]

With a 3D printing approach, the deposition of singular lines and voxels can be precisely planned and reproducible structuring of arbitrary shapes from nanometer and micrometer up to millimeter and centimeter scale is possible with a variety of different printing approaches. While droplets [7], [8] are a well established and extremely useful environment to screen new synthetic biological gene circuits on a controllable small environment with direct feedback at short time intervals, bioprinting allows the structuring of larger communities by patterning with singular voxels to observe more global processes.

"Biofabrication can be defined as a multidisciplinary research field with a combination of principles, protocols, and fabrication techniques from engineering, electronics, material science, cell biology, and biomedicine."(Silva et al. [9])

Within this research field, bioprinting allows the generation of complex structures in a reproducible manner. Applications vary from organ-mimicking scaffolds, [10] and artificial wound-healing bandages, [11] to spatially changing hydrogel structures - so called to 4D shapes. [12] Of the various bioprinting methods, extrusion-based bioprinting is versatile, low cost and applicable to a wide range of materials.

Over the past years, much progress was achieved in the field of cell bioprinting to generate artificial tissue and organoid shapes [13], [14], [15]. Researchers found a multitude of bioprintable pastes and mixtures that mimic the extra cellular matrix. With this, they were able to embed living cells on the extruded scaffolds, and to generate printing conditions mild enough to extrude the living cells along with the scaffold. [16]

In addition to these biomedical aspects of bioprinting, also a multitude of possibilities can be enabled, if this technique is extended to other research fields such as electronics or synthetic biology. Examples are printed photodetector arrays or printed aqueous compartments on solids or linked together as networks. [16]

The focus of this work was therefore the integration of synthetic circuits to bioprinted structures. These synthetic circuits include designed DNA - computing circuits and genetically engineered bacteria. With the integration of localized DNA, the diffusion and patterning of short oligonucleotides were shown to be controllable and self-differentiation processes lead to pattern formation. Embedding genetically modified living bacteria within artificial 3D structures allow for potential future studies on bacteria-based biomaterials or engineered biofilms. Within this work, known issues for the integration of viable bacteria into 3D structures were tackled in a facile manner. The setup consists solely of low-cost or widely available materials and machines. With this, the application of bioprinting for other groups in the field of synthetic biology should be facilitated to improve experimental precision and reproducibility.

Working with localized synthetic circuits in hydrogel scaffolds also gave the idea of gated communication channels between two adjacent hydrogel compartments. With signal - driven gate switching, stronger logic levels within the compartments could be achieved.

One of the major goals of this work included the development of an affordable and reliable bioprinting platform that offers the possibility to include a variety of available synthetic biological circuits. Further goals were the development of suitable bioprintable hydrogel - pastes, the integration of a DNA - computing circuit, and to embed living genetically modified *Escherichia coli* (*E. coli*) bacteria. Additionally, the implementation of an electro-bio hybrid circuit to control communication between adjacent hydrogel compartments containing synthetic circuits was approached. While the synthetic circuit is based on DNA - computing, the electronic circuit employs the principles of cellular automata. A focus was also set on the realization of a photoswitchable hydrogel channel.

In the following chapter, the current developments in bioprinting and the background of dynamic DNA nanotechnology are discussed. A consideration of bacterial gene expression, bacterial growth in confined environments, along with a coverage of bacterial response to stresses they encounter during extrusion is given. All protocols for experimental setups are described in Chapter 3 in detail. Chapter 4 covers the construction of a realiable 3D printing platform, the structure of the software tool and the composition of suitable hydrogel mixtures as printable bioinks. Afterwards, in Chapter 5, programming of DNA pathways with the immobilization of DNA circuits within printed gel structures and reaction-diffusion dynamics will be considered. Further, the integration of living *E. coli* bacteria in extruded 3D hydrogel scaffolds, the growth dynamics, and cell-cell communication observed are stated in Chapter 6. Design considerations and experiments for the generation of a setup for clear logic levels within hydrogel compartments is shown in Chapter 7. This setup includes an electro-biological hybrid attempt, where photoresponsive communication gates are controlled by a light matrix whose output is computed via cellular automata rules. An overview over the goals achieved and possibilities to apply the findings of this work are given in Chapter 8.

2. Theoretical Background

Synthetic biological materials gain their functionality mainly by small chemical compounds that can be triggered, switched, released, or otherwise stimulated. Rarely the material shape itself gives the material its functionality. Examples where the functionality of a biological material is given solely by its shape can mostly be found in living tissue, like structures of bone or cartilage cells. The generation of intelligent functional materials that exhibit the ability to react on variations in its surroundings require the modification of hydrogel structures with biological, chemical, or other stimulatable components. To control the shape of this functional material and generate arbitrary structures, a variety of well developed techniques can be applied: stereolithograpy, casting, 2D and 3D printing. For the generation of spatial patterned structures, 3D printing approaches are a promising approach.

The following sections give an overview over the procedures and materials used to generate functional biological materials at various shapes with a drop-on-demand 3D printer. Further, the included materials for the design of synthetic circuits are introduced, i. e. DNA computing and circuits including genetically modified bacteria strains.

2.1. Current Developments in Bioprinting

With different 3D printing techniques, a large variety of 3D shaped samples at a wide range of length-scales can be produced. In Figure 2.1.1 the main printing techniques that are used in commercial and in custom printers are shown.

While some techniques are advantageous for solid and stiff materials, e.g. laser-sintering for metal and ceramic powders, others like stereo-lithography, direct laser-crosslinking, or direct ink writing are more beneficial to biological materials as the material is handled more gently.

For bioprinting, mainly liquid filament (e.g. hydrogel) is extruded and structural stability can be introduced via a variety of crosslinking mechanisms. The complete bioprinting process is based on the selection of a suitable printing device, but includes also the selction of a biocompatible ink and the corresponding crosslinking mechanism. To generate intelligent hydrogels, synthetic circuits need to be included and their stability throughout the printing process needs to be assured.

2.1.1. Soft Bioprinted Structures

For the artificial bottom-up construction of artificial soft tissues, several printing strategies were already developed. While all approaches commonly employ hy-

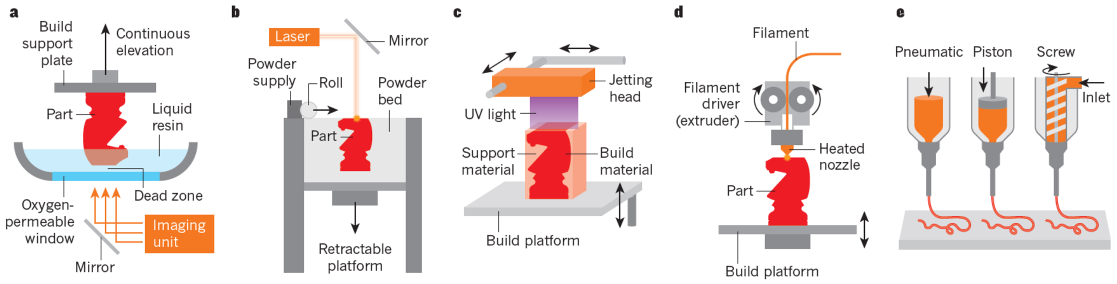

Figure 2.1.1: Printing Methods: *Overview over common 3D printing techniques. a) Light-based stereolithography: Layer-wise production of polymer structures from a monomer bath utilizing lithography masks and photo-crosslinkers. b) Light-based laser sintering: A selective laser beam binds together powdered material to generate the final shape. c) Ink-jet Printing: Photo-curable resin is printed by an ink-jet printer and cured with a laser beam directly after extrusion. d) Fused Filament Fabricatio (FFF): Structures are modeled from singular lines deposited with thermoplastic materials. e) Direct writing of bioinks: similar to the FFF method in d). For bioinks lower temperature and forces are necessary. These can be achieved with pneumatic, piston or screw driven filament drivers. Adapted from Truby et al.* [6]

drogels as main biomaterial to print, as it shows not only a good biocompatibility, but also is widely available and used as cell-laden or scaffold materials, they differ in the selection of printing setup.

Printing of soft amorphous filaments can be performed with a wide variety of techniques: Ink-jet printing [22], [23], [15], [24], stereolithography[25], [26], [27] , laser-assisted bioprinting[28], [29], [30], and extrusion-based bioprinting[19], [31], [32].

Ink-jet printing has advantages in speed and precision, and printers are widely available. During the printing process the hydrogel droplets are exposed to relatively high thermal and mechanical stress. Additionally, the realization of larger z-dimensions is often limited by the printer dimensions and the necessarily low ink viscosity.
Stereolithograpy as well shows extremely high printing precision, but the hydrogel matrix are exposed to intense irradiation during photo-curing and only one gel mixture can be printed per layer as the technique is bath-based.
Similar to stereolithography, **laser-assisted printing** includes a two-photon crosslinking mechanism that allows highly precise structuring at nano scale at high acquisition cost that prevents this technique mainly from wide use.
3D extrusion-based FFF printers are able to construct bioprinted structures from micrometer to centimeter scale at lower mechanical and thermal stress. The relatively straight-forward printer setup generally allows the inclusion of two or more printheads and thus the free patterning of singular layers. For the generation of large or multiple similar structures, multinozzle arrays were developed as extru-

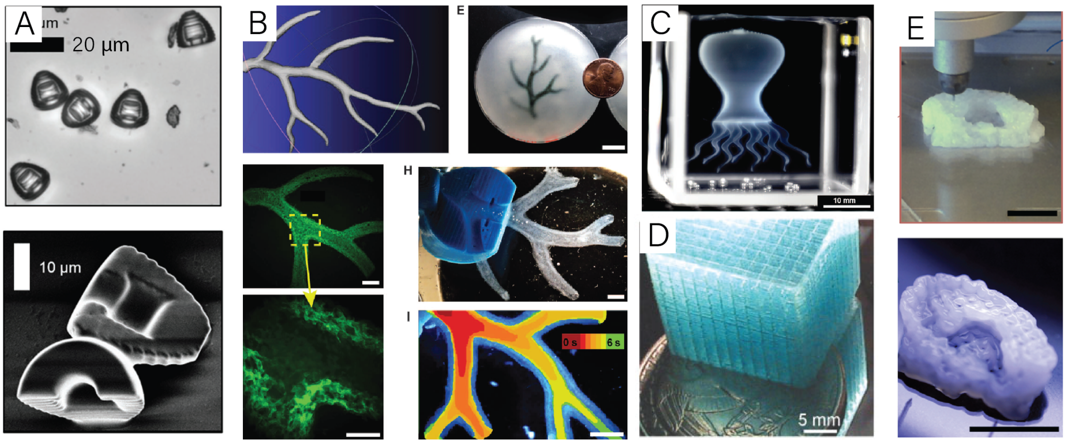

Figure 2.1.2: Soft Printed Structures: *Overview over the different lengthscales that are achieved with different bioprinters. A) Two-photon printing using near-infrared femtosecond lasers allows the fabrication of self-propulisve microswimmers from PEGDA solution. Phase-contrast imaging and SEM imaging of the microswimmers.* [17] *B) Freeform reversible embedding of suspended hydrogels prints fragile 3D structures within a secondary auxilary hydrogel. The 3D model (top left) is printed (top right) with alginate (black) into a gelatin (white) bath. Imaging of the fluorescent alginate print of the same structure (center and bottom left), dark field image (center right) and time-lapse of perfused capillaries (bottom right) are shown.* [18] *C) Writing of solid shells and fragile structures in granular gel medium. The surrounding medium allows to inject modified gel voxels at precise positions forming an octopus that can be crosslinked after printing.* [19] *D) Using a fugitive organic ink 3D scaffolds can be directly printed for more than 100 layers.* [20] *E) 3D bioprint of chondrocyte-laden auricular shape with commercial CELLINK bioink (i.e. 2 % (w/w) nanofibrillated cellulose and 0.5 % (w/w) sodium alginate). Scale bar 1 mm.* [21] *All images adapted from referred original publications.*

sion printhead. [33] Vascular structures can be achieved by concentric nozzle setups [32], [34], and finely-tunable gradients can be generated if microfluidic-mixing printheads are employed [35], [36].

An exemplary overview over the different achievable structures with these techniques is given in Figure 2.1.2 demonstrating the variety in size and shapes. Figure 2.1.3 in the next section additionally gives an overview over successful examples of bacteria containing bioprints.

As laser-based approaches and stereolithography expose integrated synthetic bio-circuits to higher irradiation during photo-crosslinking, and ink-jetting only allows the deposition of rather low viscosity inks resulting in lower structural stability, an extrusion based bio-printing approach is one of the most promising attempts for tissue engineering. The main advantages of extrusion based printing is the possibility to produce 3D objects with a rather high structural stability in sizes applicable within biomedicine at short fabrication and preparation times. [37]

2.1.2. Printing of Living Materials in 3 Dimensions

Within the field of printing soft matter, a major focus lies on the inclusion of living cells within artificially constructed matrices or compartments. Increased effort is drawn to embed human cells within various shapes to replace or reduce malfunctioning tissue. The ultimate goal would be the generation of artificial organoids and bioprinted structures that show a functioning vascular system. As already shown, printing of multilayered skins, [38] artificial bones [39] or bionic ears, [40] as well as vascular tissues [18], [41] and cartilaginous structures [42] was already performed. Other groups worked on the successful print of hollow cell-laden tubes for continuous gas and chemical exchange [43] and artificial hydrogels that are post-crosslinked via nucleid acid adhesives. [44]

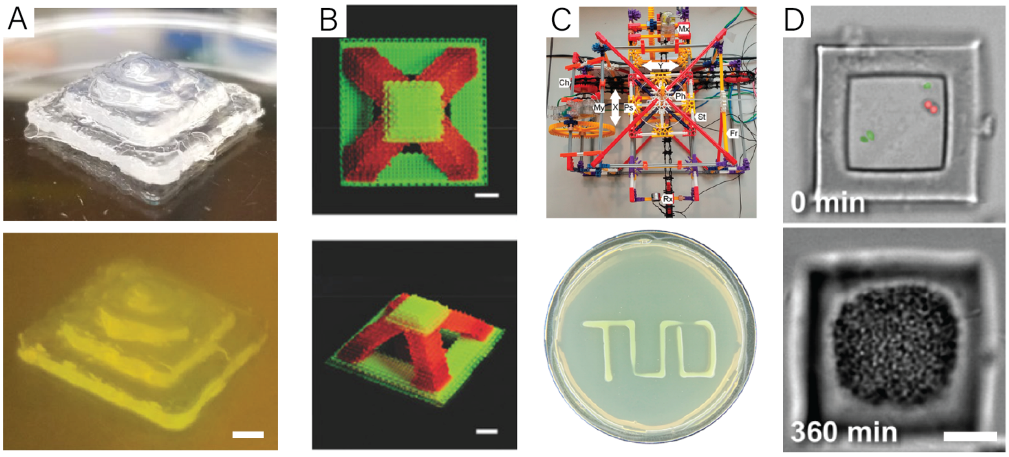

Figure 2.1.3: Printed Bacteria Gel-Structures: *Overview over approaches to immobilize living bacteria in 3 dimensions with different bioprinting techniques. A)Printing of GFP-expressing Bacillus subtilis 168 spores within a 5 % agarose matrix at elevated temperatures (70 °C). Scale bar 5 mm.* [45] *B) Photo-initiated large-scale (3 cm) high-resolution (30 µm) printing of living bacterial networks with 18 - 36 % w|v Pluronic F124 diacrylate micelles, post-crosslinked with Irgacure 2959 following the printing process. Exemplary for the print resolution, plain ink structures with rhodamine B (red) fluorescein (green) labelled gel is shown. Scale bar 5mm.* [46] *C) With a straightforward approach a simple printing unit can be assembled with KNEX components to draw GFP producing E. coli bacteria to 2D structures onto agar plates.* [47] *D) Confinement of polymicrobial communities via laser-based lithography. Single staphylococcus aureus and p. aeruginosa cells (false-colored red and green) are encapsulated within a hydrogel cuboid with inner cavity of 8 pl and 2 µm wall thickness. Bacterial growth could be observed until rupture of cavity walls. Scale bar 10 µm.* [28] *All images adapted from referred original publications.*

However, also the successful immobilization of bacterial cells is of growing interest for the scientific community to generate a variety of self-differentiating intelligent soft materials that are able to react to their surroundings. Closer observation of biofilm formation and cell-cell communication within bacterial communities can be achieved, if the precise positioning of single cells can be controlled. Additionally, a possible field of application would be the combination of both approaches to generate complete *in vitro* models of human tissue inflammations by common bacterial infections can be studied in more detail to screen for mild cures.

Currently, a growing toolbox of bacteria printing machines, inks and crosslinking mechanisms is established that already covers a wide lengthscale from micrometer to centimeter. All procedures allow for different studies, show advantages either in precision or up-scalability (see Figure 2.1.3). However, there are still some gaps within this toolbox that need a closer investigation.

First, there are few printing techniques that can be performed without possible detrimental crosslinking steps including UV-light or chemical crosslinking. The few other possibilities often work only at high (> 50 °C) extrusion temperatures, also inducing heat stress or cell death. Second, some issues e.g. consistent gas supply within extruded hydrogels, for example with oxygen, are not yet solved. And last, many approaches include artificial, or costly chemicals (e.g. hyaluronic acid, fumed silica beads), or cost-intensive (laser-based) bioprinters, that are not widely available in every laboratory.
Therefore, approaches that lower the threshold to apply bioprinting strategies to increase experimental precision and reproducibility would be beneficial to the scientific community.

2.1.3. Bio-Printing Characteristics

For this work an extrusion based FFF printing device is selected. Various mechanical parameters show a major impact on the printing fidelity and structural integrity of the extruded sample, that need to be considered: extrusion pressure, print-speed (i.e. *feedrate*), and the distance between nozzle and print-bed. The selection of the bioink influences the printing result essentially. Depending on the hydrogels used for the ink composition, shear-thinning behaviour is achieved, post-crosslinking methods can enhance structural stability, and printhead temperature influences the viscosity.

Mechanical Printing Parameters

When printing bio-materials the different mechanical properties can have a multitude of effects on the embedded cells. For example, an increase in extrusion pressure shows more detrimental effects on cell viability than a reduction in nozzle diameter. [48] Therefore, a close consideration of the printing parameters is required to reach optimum printing conditions and ensure successful printing.

He et al. [49] assessed the major mechanical parameters for pure alginate and alginate-gelatin bioink compositions for a pressure-driven extrusion printer. As depicted in Figure 2.1.4 two parameters influence the printing quality mainly for this bioink: Feedrate `F` and the initial z offset Δz_0.

The feedrate denotes the technical term for the travel speed of the printhead stemming from the milling origin of xyz-controlled machines and is not to be confused with the flowrate with which the material is extruded. The flowrate cannot be directly manipulated within 3D machine readable gcode, that controls the printer movements (see Chapter 4). In fact, the flowrate is determined by uniform distribution of the desired amount of material being extruded (set via `Exx` [mm]) from start point (`X1 Y1` [mm]) to end point (`X2 Y2` [mm]) at a constant feedrate (`Fxx` [mm/s]). Therefore, this travel speed impacts mainly the line thickness, which is optimized to match the nozzle diameter. Additionally, the travel speed directly effects the residence time of sample ink in the needle, which has been shown to affect cell viability, [50] and is due to these reasons one of the most relevant printing parameters to be considered.

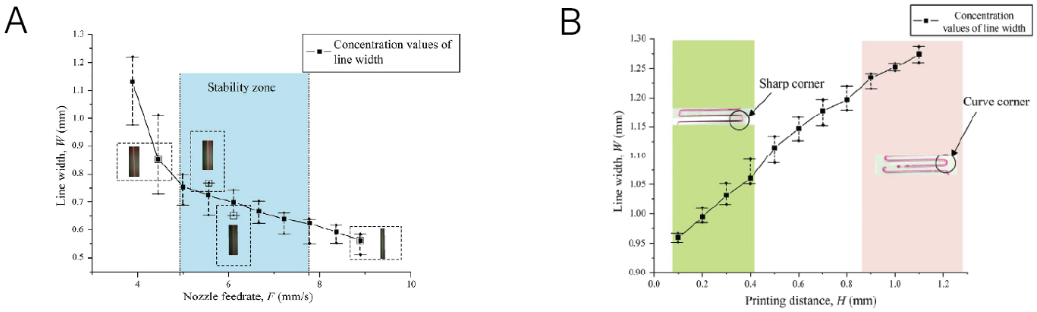

Figure 2.1.4: Influence of Nozzle Feedrate and Nozzle Distance Δz_0: *Screening of the nozzle distance to the printbed and feedrate for print fidelity with a 2.5% alginate and 8 % gelatin mixture in ddH$_2$O at 20 kPa extrusion pressure. A) The print speed (feedrate) was screened for a nozzle with 0.4 mm diameter. A stable line at the range of the extrusion nozzle can only be obtained for an adequate feedrate of approximately 5 - 7 mm/s. For lower feedrates, the line expands, for higher feedrates extruded lines tend to thin until breaks occur. B) Print precision was screened with a nozzle diameter of 0.5 mm. Sharper corners were only obtained for lower distances up to Δz_0 = 0.4 mm. Images adapted from He et al.* [49]

The distance Δz between nozzle and printbed is the crucial geometric factor to enable extrusion. For extremely small Δz_0 (lower than 0.1mm) no filament can be extruded as the material flow is hindered by the high proximity to the printbead. Rather short distances to the printbead from approximately 0.1 mm < Δz_0 < 0.4 mm allow a precise deposition of hydrogel onto the substrate. For higher distances Δz_0 the precision decreases and with increasing distance also rupture of filament increases. For Δz_0 > 0.8 mm also imperfections in the printed path occur for line prints, and single spots appear vacant for voxel prints. While all values determined for the printer used by He et al. may vary with the selection of printer and hydrogel, the influence on printing precision hold true for different FFF bioprinters.

For the generation of not only 2D, but also 3D structures, the layer height Δz_i has to be considered. Due to collapse of the soft extruded shapes (Figure 2.1.5), Δz_i cannot be assumed to equal the nozzle diameter, but needs to be experimentally determined for each hydrogel filament and correction factors derived for increasing z height.

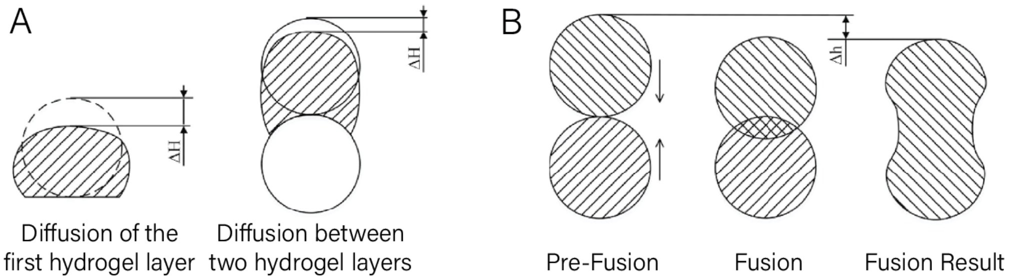

Diffusion of the first hydrogel layer | Diffusion between two hydrogel layers | Pre-Fusion | Fusion | Fusion Result

Figure 2.1.5: Deformation of Hydrogel for all Δz_i: *A) Collapse ΔH of the initial hydrogel layer and successing hydrogel layers. B) Vertical fusion process between layer z_i and z_{i+1} leaving a difference in z height Δh compared to assumed height expected from nozzle diameter. Images adapted from He et al.* [49]

While for extrusion of a low number of layers ΔH and Δh differ only slightly, the deviation in expected layer height Δh increases non-linearly with the number of layers and needs to be addressed accordingly in the generation of print files to compensate.

Additionally, the pressure-induced stresses influence the printing quality and structural integrity. The wall shear stress τ_W within the extrusion nozzle with a radius R and length L at a constant applied pressure P_{appl} can be described with the basic equation relating pressure and shear stress in capillary rheometry at atmospheric pressure P_a: [51]

$$\tau_W = R \cdot \frac{P_{appl} - P_a}{2 \cdot L} \tag{2.1}$$

The Newtonian shear rate $\dot{\gamma}_{Newt}$ can be calculated via the volumetric flow rate Q. With $Q = \pi \cdot r^2 \cdot v$ for feedrate v:

$$\dot{\gamma}_{Newt} = \frac{4Q}{\pi R^3} \tag{2.2}$$

and needs to be corrected for bioinks due to non-Newtonian effects with the Rabinowitch correction: [51]

$$\dot{\gamma}_W = \dot{\gamma}_{Newt} \cdot \frac{3 + b}{4} \tag{2.3}$$

Parameter b can be determined as inverse of the power-law index n which is the best fit for non-Newtonian bioink compositions according to Abdel-Hamid et al. [52]

The power law is defined for shear stress τ, apparent viscosity η, shear rate γ, and flow index n: [52]

$$\tau = \eta \cdot \gamma^n \tag{2.4}$$

From equations 2.1 and 2.4 the apparent viscosity of a bioink can be determined by wall shear stress and corrected volumetric flow rate:

$$\eta_{app} = \frac{\tau_W}{\dot{\gamma}_W} \tag{2.5}$$

From equations 2.1 - 2.4 Suntornnond et al. derived a combined model on the resolution of extrusion bioprinting based on the extrusion pressure and ink-viscosity: [53]

$$d \propto \sqrt{\frac{1}{\dot{v}}} \text{ and } d \propto 4 \cdot r^2 \cdot \sqrt{P_{appl} - P_a} \tag{2.6}$$

It has to be highlighted, that Bruneaux et al. hypothesize that the flow of organic inks is enabled due to slip or lubrication conditions on the syringe wall for non-Newtonian, viscous organic inks, allowing a good printability compared to Newtonian fluids. However, it has to be considered that due to these characteristics a response lag occurs for sudden changes in printing direction. [49]

Hydrogels as Bioprintable Inks

According to Li, *"A hydrogel is defined as the system formed in water through either chemical or physical cross-linking of water-soluble natural or synthetic polymers. A physical hydrogel may be formed through ionic bonding, hydrogen bonding, or hydrophobic association."* [54]

Especially the ability of some physical hydrogels to reversibly form a solid gel from liquid solution upon external stimuli (e.g. temperature, salt, light) is beneficial for the application as bioink material. For this, the selection of an adequate ink mixture for extrusion is the key factor to generate structurally stable amorphous 3D shapes with precise spatial control and the inclusion of biological components. Several attempts have been made in the past years to generate a variety of precisely printed cell-containing structures based on natural and synthetic polymer compositions.

In a comprehensive rewiew, Sanchez et al. [55] assessed hydrogels used as printable paste for extrusion based bioprinting, see Figure 2.1.6. The most common

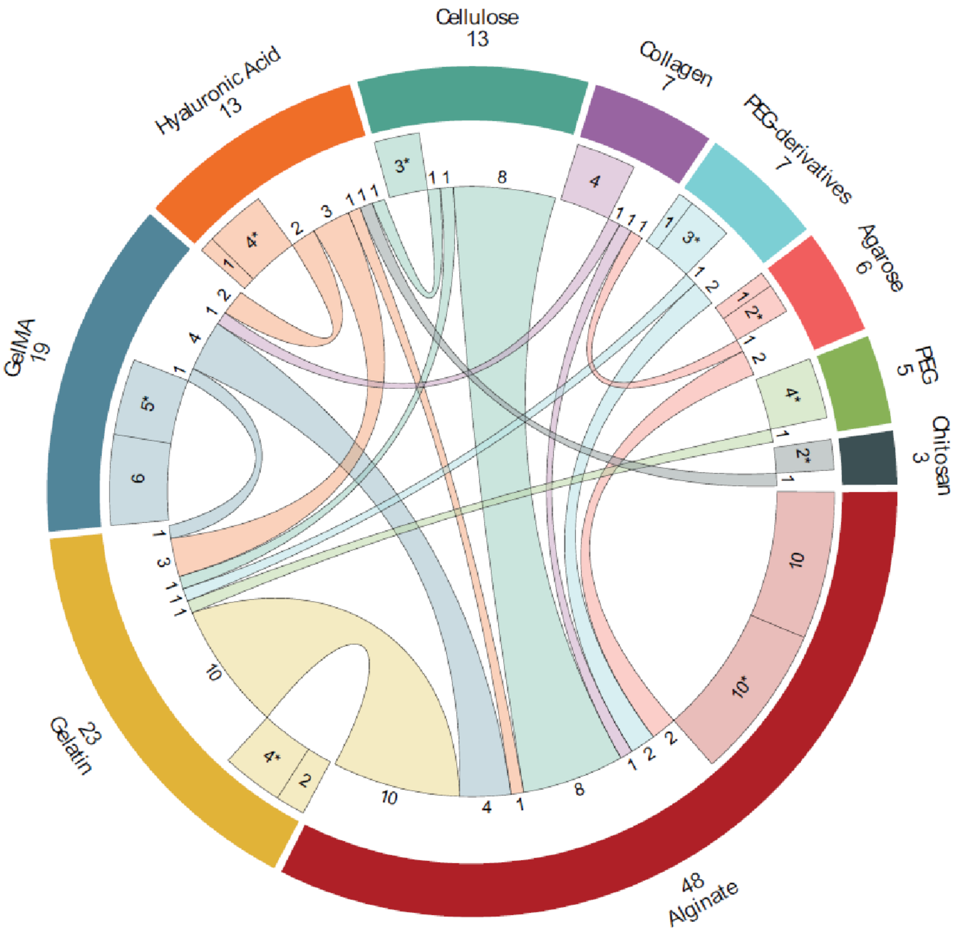

Figure 2.1.6: Most common hydrogels used for bioprinting: *In a 2020 study, all 1774 publications from 2009 to 2019 on extrusion-based bioprinting were evaluated on several criteria and the 118 full paper contributions selected. These were categorized on the hydrogels used as polymers for bioprinting and depicted in a graphical representation. The external ring shows the number of publications including the respective hydrogel, if mixtures of two hydrogels were used, these are connected by the inner lines. (*) indicate mixtures with other components that are less common. Image adapted from Sanchez et al.* [55]

natural (e.g. alginate, collagen, gelatin) and synthetic materials (e.g. Polyethylene Glycol (PEG), Gelatin-Methacryloyl (GelMA)) were examined in respect to their different features and behaviors.

The majority of hydrogel compositions include **alginate**, a polysaccharide isolated from brown algae. [56] Alginate hydrogels show favourable properties due to high viscosity at low percentages (forming pastes already at 6-10%) while maintaining a strong shear-thinning behavior which is vital for extrusion-based printing. [56] These good rheological properties make alginate a singular exception within the group of natural polymers. [57] Additionally, the possibility to strengthen alginate gels by Ca^{2+} ions to form stable structures lead to a high use of this polymer for bioprinting applications [58], [59], [60].

Gelatin is also widely used, while showing poor rheological properties, it is similarly to alginate highly biocompatible and exhibits a fast thermo-gelation [61], [62]. However, if exposed to temperatures above 50 °C the ability to form stable gelatin-hydrogels can diminish drastically.

A synthetically developed version of gelatin that is widely known in the field of bioprinting is **GelMA** [63], [32]. Here, a certain share of the gelatin components are modified with methacrylamide and methacrylate groups to enable crosslinking via UV irradiation. Therefore, in comparison to pure gelatin, GelMA shows improved printability, stability, and shape fidelity. To increase viscosity, GelMA is often used in a combination with alginate to improve the rheology.[43], [34]

A natural polymer extremely suitable to increase the viscosity of bioink-mixtures is **Hyaluronic Acid (HA)** [13], [64]. As HA is a major component of not only neural tissue but also skin, it is mainly employed for skin tissue engineering bioprinting. Additionally, HA can be modified with acrylic or methacrylic groups (similar to gelatin), or other groups (e.g. dopamine-conjugates).

Cellulose is a biological polysaccharide that is widely available and used in bioprinting due to its shear-thinning feature[65], [18]. With the addition of cellulose, the mechanical properties of bioinks can be tuned depending on the chain length to rather stiff materials with high tensile strength to soluble gels.

For bioprinting of materials that mimic the extracellular matrix (ECM) for example cartilage tissues, the most favored material is **collagen**.[18],[66] Similar to gelatin, collagen is one of the extracellular matrix proteins and therefore ideal for the generation of artificial cell laden constructs, but shows low rheologic properties if not mixed to other polymers.

PEG is a highly hydrophilic synthetic polymer that is generated by the polymerization of ethylene oxide. Especially the PEG derivates modified with photo-reactive groups like Polyethylene Glycol Diacrylate (PEGDA), [67] Polyethylene Glycol Tetra-acrylate (PEGTA) [17] and Polyethylene Glycol Methacrylate (PEGMA) [68] can be used to encapsulate biological components in microspheres, but also to generate stiff materials for example for contact-lenses [69] due to the good controllability of photo-crosslinking on that lengthscale.

Agarose shows similar thermal gelation as gelatin and is forming a stable hydrogel within seconds if cooled to room temperature. In contrast to alginate, plain agarose hydrogels exhibit no shear-thinning properties and therefore need to be printed at an adequate temperature to be extrudable. [17]

Another hydrogel from the ECM that is employed for bioprinting is **chitosan**. In contrast to HA, it only exhibits low mechanical stability after a slow gelation phase, and is, therefore, mainly used as component in a mixed bioprintable paste. [70]

The majority of these hydrogels show higher viscosity at lower temperatures and lower viscosity for elevated temperatures, except for methylcellulose [54] and Pluronic F127, [71] a synthetic polaxamer, that both exhibit inverse thermocrosslinking behaviour. With this, the printhead temperature can be critical to allow for a smooth extrusion. For the majority of bioprinting research, the printing temperature was kept around the cell incubation temperature of 37 °C. And, in addition, the printbed temperature can have a strong effect on the gelation speed for high proportions of thermogelating polymers within the bioink mixture, where it is preferentially kept at 0-20 °C, as well as on the viability of cells, for which the printbed temperature is ideally 37 °C. [55]

In addition to simple mixtures of natural and/or synthetic polymers also other molecular crosslinking methods were employed to form hydrogels, for example DNA linkers: Li et al. generated designed structures with a drop-on-drop printer setup with two bioinks. [72] Bioink A consisting of a polypeptide-DNA conjugate formed a hydrogel within seconds whenever bioink B containing the complementary DNA-linkers was present. Buchberger et al. assembled reversible GelMA-DNA hydrogels by replacing inter-GelMA crosslinks with double-stranded DNA, allowing after an initial UV-crosslinking to soften or stiffen the hydrogel via toehold-mediated strand discplacement. [73]

For a straightforward extrusion-based bioprinting platform, several bioink mixtures from literature exhibited relevant features while being based on widely available natural hydrogels: Generally, it has to be highlighted that the combination of alginate and gelatin generates a hydrogel with good rheological properties due to the shear-thinning capability of alginate and a fast thermoresponsive gelation based on the gelatin, making this mixture a widely used choice of ink at different percentages. Agarose-alginate-based hydrogels with 3% agarose and 2 % alginate in 0.15 M PBS were successfully extruded to single lines and cells cultured within the used bioinks for 28 days showing a 70% rate of survival. [74] Extremly viscous pastes of 18% alginate, 4% gelatin, and 12% agar allow the deposition of stiff grids. [62] With 3% alginate mixed to 9% methylcellulose grid structures up to one centimeter could already be achieved. [60]

Rheology of Hydrogels

The main influence on printability and structure fidelity is based on the rheological properties of the liquid ink that is used during the printing process. [75] While for ink-jet printing materials with low viscosity and Newtonian behaviour can be described using the Ohnesorg and Weber number, for extrusion-based printing non-Newtonian fluids are described by Weissenberg and Deborah numbers. [76]

Ink-Jet Printing

Derby [77] summarized the important characteristic equations for ink-jet printing, which are the Reynolds Re, Weber We, and Ohnesorg Oh numbers determining the parameter-space for high printability (Figure 2.1.7):

$$Re = \frac{v \cdot \rho \cdot a}{\eta} \tag{2.7}$$

$$We = \frac{v^2 \cdot \rho \cdot a}{\gamma} \tag{2.8}$$

$$Oh = \frac{\sqrt{We}}{Re} = \frac{\eta}{(\gamma \cdot \rho \cdot a)^{\frac{1}{2}}} \tag{2.9}$$

These numbers are based on density (ρ), dynamic viscosity (η), and surface tension (γ) with velocity v and characteristic drop diameter a.

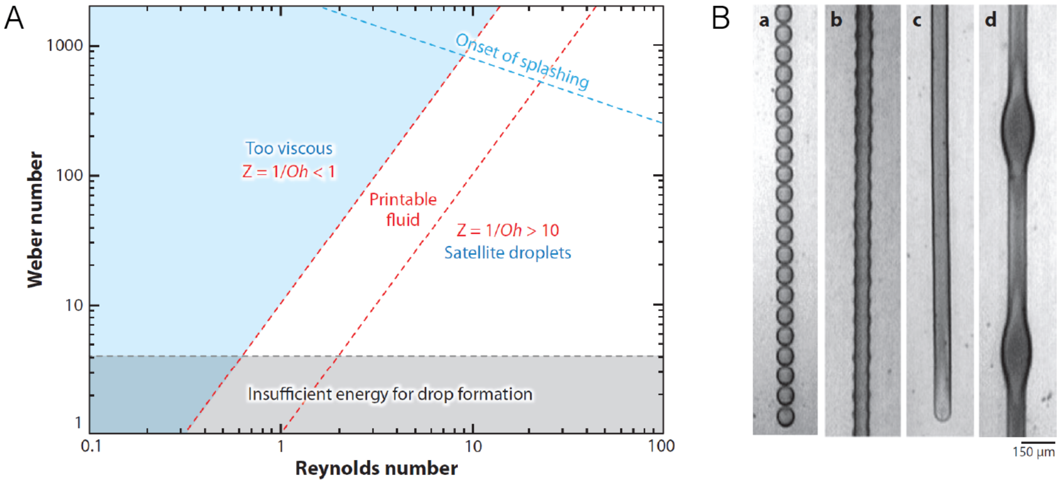

Figure 2.1.7: Range for Stable Ink-Jet Printing: *A) In a plane set up by the Reynolds and Weber number the printable area corresponding to* $1 < Z < 10$ *can be marked clearly. B) Different errors in drop formation lead to non-continuous lines or lines that exhibit bulging. The crucial parameter to achieve straight lines for drop-on-demand printing is the spacing between two successively printed single voxels. Adapted from Derby* [77]

Fromm [78] found the Ohnesorg number to be of major interest to predict good printability, but, all further definitions are based on its inverse $Z = \frac{1}{Oh}$. With numerical simulations Reis and Derby [79] found a stable droplet formation during the printing process only for $1 < Z < 10$.

Extrusion-based Printing

For extrusion-based bioprinting shear-thinning fluids that show high structural stability after extrusion, but low viscosity during the extrusion step are beneficial. Two numbers have proven to be useful to quantify viscoelastic effects: The Deborah and Weissenberg numbers (c.f. Figure 2.1.8). [80]

The Deborah De number was introduced by Reiner [81] as a dimensionless number to compare the time of relaxation λ to the time of observation:

$$De = \frac{\lambda}{T} \tag{2.10}$$

With this the Deborah number allows for a definition of "fluid" materials if the relaxation time after deformation is relatively short in comparison to a characteristic timeframe of such a process T. However, if applied to slow changing conditions or steady flow, the characteristic time is infinite, leading to $De = 0$ and rendering De insufficient as single characterization of viscoelasticity.

The Weissenberg number Wi compares the elastic forces to viscous forces and is defined as:

$$Wi = \frac{\lambda \cdot U}{L} \tag{2.11}$$

for nozzle diameter L and velocity scale U.

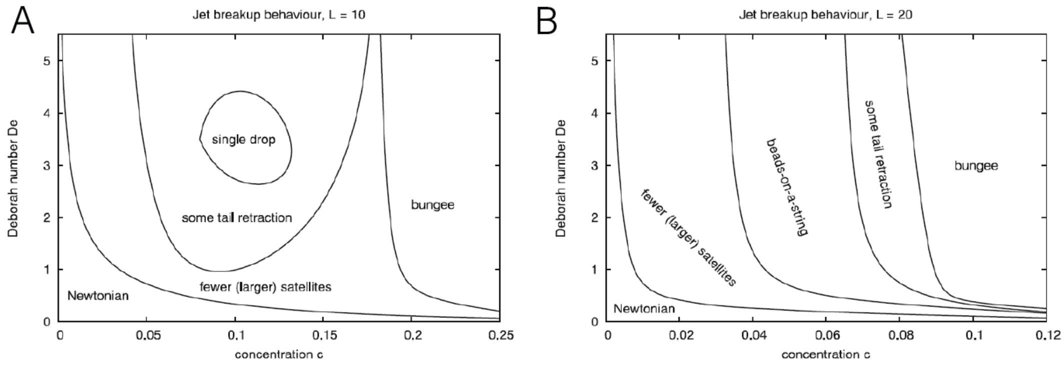

Figure 2.1.8: Deborah Number for Printable Inks: *For two different hydrogels with finite extensibility parameter L = 10 and L = 20 the stream formation after-ink jetting is characterized (L being the ratio of the contour of the polymer chain to the equilibrium coil size) A) "Single drops" can emerge if the tail of the ejected ink fully retracts into the main voxel showing the optimal jet type for most industrial inkjet applications. At a larger parameter space of* De *and concentration* c*, only a fraction of the tails retract to the main voxel, small variations in concentration are suffiecient that the stream breaks up to satellite droplets or a extremely late "bungee" deposition occurs after the retraction step. B) For a twice as high extensibility, no single drop formation is observed, only depending on the concentration comparably strong retraction occurs for higher gel densities or a string of "beads" or even satellite drops occur. Adapted from Morrison et al.* [82]

With this, Wi indicates the degree of anisotropy generated by the deformation. In contrast to De the Weissenberg number is appropriate to describe flows with a constant stretch history, such as simple shear. [83]

Predictability

Emmermacher et al. screened for optimum printing parameters for methylcellulose and pre-gelled agarose in H_2O. [84] They employed the HerschelBulkley law, describing non-Newtonian fluid behavior to run a Computational Fluid Dynamics (CFD) simulation. With this simulation they predicted the printability of a hydrogel composition to screen for optimum printing parameters. The CFD simulation integrated a reduced nozzle model and calculated the rheology of the fluid and the stresses during extrusion for the exact geometry. With the flow parameters for non-Newtonian liquids they found a self-similar solution to describe the fluid flow, valid for their needle geometries and a variety of applied pressures. Generally, such models can be employed in the future for precisely assessed hydrogels to identify optimum printing parameters.

2.2. Dynamic DNA Nanotechnology

Deoxyribonucleic acid (DNA) is a well understood biopolymer that - while carrying the genetic information of all living cells in nature - is now a universally used building block for a large variety of synthetic chemical reaction networks. Within this variety of possible applications, the exact predictability of duplex formation between complementary strands allowed the field of DNA nanotechnology to evolve. Single stranded DNA (ssDNA) molecules show a preference for adequate binding partners to form so called Watson-Crick base-pairs and allow precise predictions on their hybridization kinetics. Based on this hybridization mechanism and strand displacement kinetics, the interactions of short oligonucleotides in promixity to other oligonucleotides can be predicted. In the past, DNA was successfully used as building blocks for nanostructures of a variety of shapes[85], [86], [87] (Figure 2.2.1 A).

Additionally, more complex computational networks were developed, that showed a good programmability and high reliability. These applications included a DNA based solution of the Hamiltonian Path problem by a precise definition of nodes and paths with respective DNA sequences. [88] Further, with the deliberate design of DNA strand displacement, also hydrogel environments could be altered (Figure 2.2.1 B, C). In this thesis DNA circuits are used as synthetic programmable components to realize self-differentiation in bioprinted hydrogel structures.

2.2.1. DNA Hybridization Kinetics

DNA consists of a chain of biopolymer strands that are pairwise wound around another to form a double helical structure. The binding kinetics are due to the preferences of adenine (A) - thymine (T) and guanine (G) - cytosin (C) pairings highly

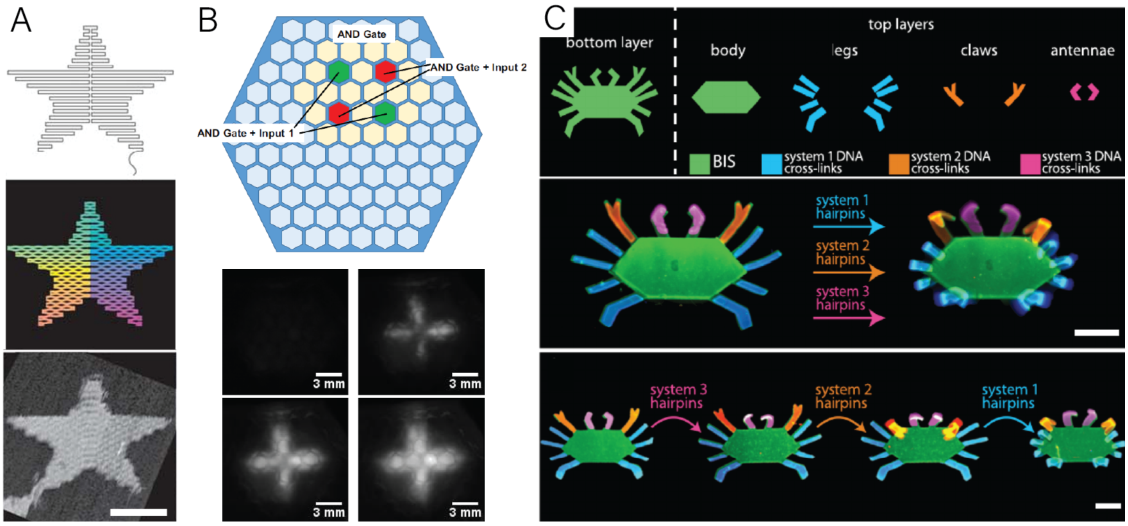

Figure 2.2.1: Applications of DNA Computing: *A) With precise design and routing of short ssDNA staple strands complex 2D and 3D nanostructures can be predefined and reliably folded. Exemplary the star pattern from Rothemund in 2D is shown. Scale bar 100 nm.* [86] *B) Predefined patterns emerge after free diffusion of DNA strands within patterend hydrogel environments.* [89] *C) Shape changes within DNA-crosslinked hydrogels on an exemplary crab structure. Legs, claws, and antennae of the crab are changing shape in response to DNA molecules present. Scale bars 2mm* [90] *All images adapted from referred original publications.*

predictable. On a nucleotide level, the binding energy of a singular basepair not only depends on the individual nucleotides, but also on the nearest-neighbors of the respective strand. SantaLucia and Hicks [91] provide an overview over the average binding energies of nucleobases within an arbitrary neighborhood. They approximate the binding energy of a singular A-T pair with $\Delta\mathrm{G}^\circ_{37} \approx -0.9\ \mathrm{kcal\ mol^{-1}}$ and of a G-C pair with $\Delta\mathrm{G}^\circ_{37} \approx -1.5\ \mathrm{kcal\ mol^{-1}}$ at $T = 37$ °C in 1 M NaCl.

Considering a complete single strand of DNA, a duplex can be formed if the strand is in close proximity to another single stranded DNA that exhibits parts or the complete reverse-complementary sequence to the first strand. If the strand folds back to a reverse-complementary sequence within itself, a secondary structure can be formed, if this is energetically favorable.

For all equilibrium conditions, oligonucleotides prefer the energetically lowest state. Therefore, duplexes are formed whenever possible. The bonds can be melted thermally by heating.

2.2.2. Toehold Mediated Strand Displacement

Zhang and Winfree derived an in detail understanding of the molecular behavior during DNA hybridization. [92] For DNA branch migration, a duplex strand that exhibits a single-stranded so called *toehold* region can be opened up by an invading strand with corresponding sequence. The process is called Toehold-Mediated

Strand Displacement (TMSD) if the duplex exhibits no toehold region afterwards, in which case it is called toehold exchange.

They not only described the procedure but also developed a set of decision tables to gain a fast insight in the expected branch migration dynamics. The association process between two ssDNA strands that show complementary sequence can be described with the rate-constant k_{on}:

$$k_{on} \approx 10^5 \dots 10^7 M^{-1} s^{-1} \tag{2.12}$$

The crucial step for an association process is the nucleation of a small numbers of base pairs (2 - 4) as this step is highly dependent on temperature and salt concentration. Subsequently to the nucleation step, all bases of complementary sequence form bonds fast, in a "zipper"-like manner ($10^7 \frac{\mathrm{bp}}{s}$). [93]

The dissociation rate is determined by breaking of basepairs. With the equilibrium constant K_{eq} and the association constant k_{on} the dissociation rate k_{off} can be calculated:

$$k_{off} = \frac{k_{on}}{K_{eq}} = \left[\frac{1}{s}\right] \tag{2.13}$$

In equilibrium the on-rate must balance the off-rate. Hence the equilibrium constant can be determined via the fraction of the concentration of product and the concentrations of the reagents in solution. Another possibility is to express the equilibrium constant considering the Gibbs free energy G^0:

$$K_{eq} = \exp\left(-\frac{\Delta_r G^0}{R \cdot T}\right) \tag{2.14}$$

Combining both, the Van’t Hoff equation can be derived:

$$K_{eq} = \frac{[A \cdot B]}{[A] \cdot [B]} = \exp\left(-\frac{\Delta_r G^0}{R \cdot T}\right) \tag{2.15}$$

2.3. Synthetic Bacterial Circuits

For protein biosynthesis, a universal mechanism exists within living procaryotic and eucaryotic cells . This gene expression mechanism is based on the transcription from DNA to ribonucleic acid (RNA) via an RNA polymerase and a following translation of this so called messenger RNA (mRNA) via ribosomes to a functional protein. This is possible as the genetic code stored in the succession of nucleotides in the DNA corresponds to the series of amino acids in the encoded proteins. [94]

For bacteria, their complete genome (i.e. the complete set of the genes of an organism) is typically stored on a circular chromosome. Living bacteria are not only able to produce proteins encoded on their chromosome, but gene expression is also possible from additional, smaller circular DNA, so called plasmids. These plasmids carry for example antibiotic resistance or artificially added genes and can be transferred to a bacterium cell via transformation. Within the field of molecular biology a variety of genes were extracted from different organisms and examined. [94]

Over the past decades, in an attempt to standardize parts for synthetic biology, a library of so called BioBricks was developed in a community effort. The main driver here was the international Genetically Engineered Machines (iGEM) competition. These BioBricks can be used as complete functional parts that can be transferred on plasmids and transformed to bacteria cells. [95]

One of the most used model organisms in synthetic biology is the gram-negative bacterium *Escherichia coli* (*E. coli*). This organism is used to produce a fluorescent readout and as more complex sender-receiver system within precisely deposited hydrogel structures.

The following section describes gene expression in this bacterium in general and examines the production of proteins that are relevant for this work. Additionally, cell growth in confined environments - like in a hydrogel matrix - and stress responses that can occur during printing are described.

2.3.1. Gene Regulation in *E. coli*

Transcription within *E. coli* cells starts with the binding of RNA polymerase to a so called σ factor to form a holoenzyme. As such it is able to recognize and bind to promoter regions encoded in the DNA. The complex is able to unwind and separate the DNA by breaking the hydrogen bonds. Complementary nucleotides are added to form a complementary strand by the RNA polymerase that enzymatically ligates the deoxyribose molecules with the phosphate groups already attached to the individual nucleotides. This process is powered by the cleavage of the additional phosphate groups bound to the nucleotide. Such a fresh synthesized RNA strand is called mRNA (messenger RNA), it breaks free from the DNA and can be used for the translation of proteins. [94]

During translation, a ribosome has to reach the ribosome binding site of the mRNA and begins with the protein synthesis at a specific region downstream of the mRNA called start codon to polymerize an amino acid for each base-triplet.

Each of these base-triplets has a corresponding T-RNA, a specific RNA structure connected to an individual amino acid. All newly produced amino acids are added to a continuous chain, until a specific stop codon (either UAA, UAG, or UGA) is reached. Due to the lack of a corresponding T-RNA, the complex of ribosomal subunits, mRNA and the polypeptide dissociates. During the translation process the protein is able to fold into its functional three-dimensional structure. [94]

For this work, four different fluorescent proteins are used as reporters in bacteria. Further, a bacterial sender-receiver system was employed. The gene expression of these constructs is briefly shown in the following.

Fluorescent Protein Production

In this work, several bacteria were immobilized within bioprinted hydrogel matrices. The majority of these bacteria were equipped with an additional gene for the production of fluorescent protein to facilitate readout and allow easy access to the cell viability.

The expression of the fluorescent proteins was either controlled by a lac-promoter (pLac) or a tet-promoter (pTet). The active expression of the corresponding gene is inhibited by LacI/TetR binding to the operator downstream of the promoter sequence. Upon induction with Isopropyl β-D-1-thiogalactopyranoside (IPTG) or anhydrotetracycline (aTc) the bound repressor is released and gene expression enabled.

For all experiments in this work, DH5α cells were used due to the absence of an TetR gene if constitutive protein expression under a pTet promoter was desired. Otherwise, DH5αZ1 bacteria were used. All plasmid maps are depicted in Appendix A.7.

Sender-Receiver Systems

A more complex bacterial circuit was embedded within bioprinted samples with the inclusion of a bacteria sender-receiver system. The sender bacteria are BL21 that produce LuxI under a pLac promoter. LuxI produces the sender molecule N-acyl homoserine lactone (AHL) via an enzymatic reaction, which then can diffuse through the cell membrane due to its small size.

Receptor cells (DH5α) are enabled to produce LuxR constitutively under a pTet promoter. Once the receptor cells take up AHL, these molecules can bind to LuxR and activate the promoter pLux, leading to the expression of green fluorescent protein (GFP).

2.3.2. Bacteria Culturing and Growth in Confined Environments

Bacteria grow by cell division of a mother cell into two genetically identical daughter cells by binary fission. However, the cell growth is not exponential in general.

The bacterial growth can be described as the succession of three dominating phases: First a lag phase occurs during which the bacteria adapt themselves to their surroundings. This phase starts after inoculation or strong environmental influences, e.g. heat shock. After adaption is completed, the exponential phase starts with ideal exponential growth. This phase is mainly characterized by a doubling time t_d for which any cell divides into two new cells. However, during the exponential phase, surrounding medium is used up rapidly and waste products accumulate, leading to the stationary phase. During this phase, cell growth and death rate are equal due to the aforementioned growth-limiting factors. After the medium is completely depleted, cells starts to die, simply called death phase. [96]

For this work, bacterial growth is constricted by confining hydrogel matrices. Männik et al. studied whether given models of bacterial growth can be applied to *E. coli* bacteria for such environments. [97] In their work they observed the ability of *E. coli* with diameters of ≈ 0.8 µm to grow and move through channels as small as their diameter. For even smaller channels, down to 0.4 µm, *E. coli* are able to pass such channels by growth. In their study, they indicated no longer doubling times than for wider channels. They mainly expect the thin 3 nm cell wall and low osmotic pressure to allow *E. coli* cells to be extremely compressible, but also these cells are vulnerable to damage. However, after exiting through the channels, the cell shape differs largely from the regular rod-like *E. coli* shape and some cells are even completely round shaped.

These results lead to the assumption of bacterial growth in hydrogel environments with the same behavior than in unconstricted environments, but that mild printing conditions are necessary to avoid cell death during printing.

For the longest phase observed in the conducted experiments, the exponential phase, a straightforward model for the number of bacteria $N(t)$ with growth rate $\gamma = \frac{ln2}{t_d}$ and doubling time t_d can easily be derived:

$$\frac{dN(t)}{dt} = \gamma \cdot N(t) \tag{2.16}$$

A complete model of bacterial growth can only be described via an adequate sigmoidal models. Of these models, the Gompertz and the logistic model are the best fits for bacterial growth. [98]

The Gompertz model is given for all phases dependent on location r and time t as:

$$N(t) = A \cdot \text{exp}\left(-\text{exp}\left[\frac{\mu_m \cdot e}{A}(\lambda - t) + 1\right]\right) \tag{2.17}$$

and the logistic model as:

$$N(t) = \frac{A}{\left(1 + \text{exp}\left[\frac{4\mu_m}{A}(\lambda - t) + 2\right]\right)} \tag{2.18}$$

for asymptote $A = ln({}^{N_\infty}/{}_{N_0})$, specific growth rate μ_m and lag time λ. [98]

2.3.3. Bacterial Response to Stress

During the printing process the bacteria will have to survive stress conditions, mainly due to heat and hydrostatic pressure. Using signal transduction systems, *E. coli* are able to cope with stress and depending on the stress cause might even improve their survival rate. The signal transduction system can sense environmental changes outside of the cell and adjust the cell behavior by controlling the expression of genes involved in cellular defense mechanisms [99]

Response to Heat Stress

While first observed and studied in *Drosophila busckii*, [100] scientific effort allowed to prove that heat shock proteins are the primary product of protein synthesis during elevated temperatures for every organism yet studied. These proteins are produced to reduce the toxic effects of stress for the cell. The main difference in the production of heat shock proteins between different organisms is the maximum induction temperature as this correlates with the natural environmental temperature of each singular organism. [101] For most organisms extremely adapted to a small range of optimum growth temperature, heat shock is induced at a temperature increase of 5 °C, while for most organisms that are able to grow over a broad range of temperatures this response is only triggered if the organism is exposed to 10 - 15 °C elevated temperatures. [102]

For *E. coli* bacteria an extensive study of the heat shock reaction by Neidhardt et al. revealed a comprehensive understanding of the processes in these cells if exposed to elevated temperatures. [103] Due to the high variability in growth temperatures, in *E. coli* some of the seventeen High-Temperature Production (HTP) proteins (later known as heat shock protein (HSP)) are already transiently induced at temperatures below the optimum growth temperature of 37 °C.

Shifts from low to a moderate temperature range (35-43 °C) lead to a high increase in induction of HSPs but also an increase in protein production in general.

For shifts to higher temperatures of 43-47 °C the cells react with a restricted growth rate, a reduction in general protein synthesis but a stable production of HSPs. Only for temperatures above 47 °C growth will finally stop, even in rich media, and only HSPs are produced as long as the destructed cells are able to. [103]

The seventeen HSPs present in *E. coli* are extremely diverse: while their molecular size range from 10 kDa to 94 kDa (kDalton), two of these proteins are overly present in cells already at normal temperature (3% of cell mass at 37 °C) others only appear at elevated temperatures. Also the proteins are all part of different cell processes at growth temperature: DNA replication, RNA and protein synthesis as well as in protein processing, assembly and degradaton. Specifically the protein produced by the gene *dnaK*, usually a gene used for phage DNA replication, has to be highlighted, as this is a rather universal gene in biology and this gene shares 50 % homology with the hsp70 heat shock protein in Drosophila. [103]

Yamamori et al. and Lemaux et al. proved further that not only the protein synthesis for specific proteins increased dramatically by 5- to 10-fold within the first 5 minutes after increasing the temperature, but also that for *E. coli* K-12 strains the growth and overall protein production rate under heat stress (increase from 30 °C to 42 °C) showed an increase of 50% after 20 - 30 min. [104] [105]

Response to Hydrostatic Stress

External hydrostatic pressure is another factor that cause stress on *E. coli* cultures with the same consequences as other types of external stress: reduction in cell growth, change in nucleoid structure and rate of protein synthesis (see Figure 2.3.1). Welch et al. [106] showed that similar to heat shock proteins the group of proteins produced at high hydrostatic pressure, pressure induced proteins (PIPs), show increased rates of synthesis. The complete set of 55 PIPs shares eleven proteins known from heat shock proteins (HSPs) but also four known from cold shock proteins (CSPs) with a similarity in mobility of HSPs and PIPs.

Further findings include a low effect of short intervals of compression if followed by fast decompression. This might be an effect of a lower high-pressure response (60-90 min for protein synthesis of HSPs) than the fast changes during heat shock within several minutes. [106]

For the bioprinting goal, the impact of heat shock proteins on bacterial resistance against hydrostatic pressure is of major interest. Aertsen et al. [107] examined the influence of preceding heat shock on resistance of pressure shock and vice versa. They focused especially on high hydrostatic pressure (200 to 1.000 MPa), pressures that cause protein denaturation and affect cell growth.

Their major finding was, that previously heat shocked cells showed a higher vitality (up to 100-fold) if exposed to extreme high hydrostatic pressures, leading to the conclusion of a protective effect of heat shock on bacterial cells. However, previously pressure shocked cells showed no increased resistance to subsequent exposure to elevated temperatures.

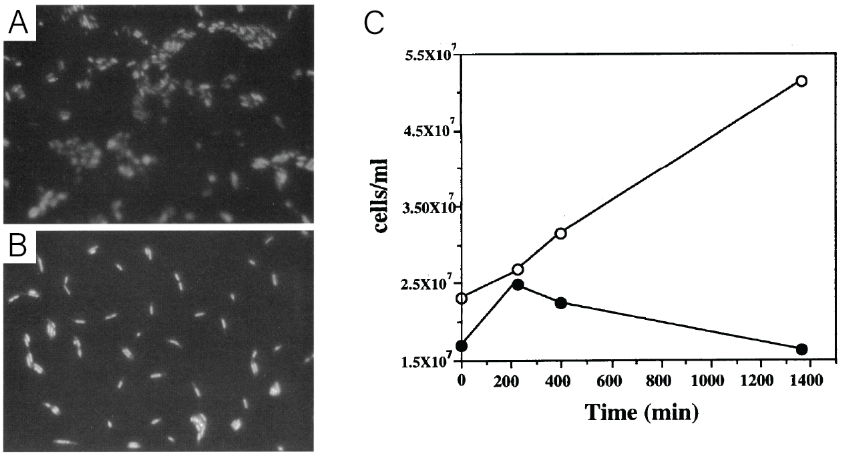

Figure 2.3.1: Pressure Induced Bacterial Growth Change: *A) Epifluorescence microscopy data of stained cells at low pressure growth conditions after 1400min. B) Microscopy data of stained cells from same initial culture but grown at high pressure growth conditions, again after 1400 min. C) The growth of cells at elevated pressure (black) and at atmospheric pressure (white), recorded by epifluorescence direct counts. Adapted from Welch et al.* [106]

A major role comes to the gene *dnaK* where the results showed a high correlation of transcription to pressure resistance. This leads to the conclusion that the expression of this specific protein either prevents cell damage or is of great importance for cell recovery. [107]

Response to Osmotic Stress

Bacterial cells react with *osmoregulation* to external variations in solute concentration. Under normal growth conditions, bacteria maintain a certain turgor pressure - a higher internal pressure compared to their surrounding. Due to semipermeable cell membranes, this turgor pressure can be disrupted if the osmolarity of the surrounding changes and the cell is exposed to an intake of water. [108] During osmoregulation, the ability of cell proliferation is decreased, starvation proteins as well as heat shock proteins are expressed, and the cells accumulate charged solutes. [109]

E. coli, as an example, increase the uptake of glycinebetaine and proline or synthesize glycinebetaine from present choline. [110] In total, the synthesis of around 20 proteins is affected by osmolarity and changes under osmotic stress. [109] Similar to heat shock, acidic shock leads to a higher degree of osmotic stress stability.

For all types of external stress, cross-protection might occur and is stronger, the larger the overlap of the set of proteins produced for both stress types. [108] However, all stress related considerations lead to the conclusion that cell growth is higher for lower stress levels. A mild printing environment, low printing temperatures and extrusion pressure can reduce the amount of stress on bacteria and lead to higher cell viability.

2.4. Reaction-Diffusion Equations

Most spatial dynamic biological circuits are subject to diffusion processes. During diffusion, molecules reach possible reaction partners and trigger a wide variety of processes. This mechanism can be mathematically described with reaction-diffusion equations.

2.4.1. Definition of Reaction-Diffusion Processes

The diffusion flux j_D for a particle occurring due to a gradient of the particle concentration c is described in Fick's first law of diffusion:

$$\vec{j_D} = -D \cdot \nabla c \tag{2.19}$$

with the diffusion coefficient D, which can be also a matrix. Fick's second law of diffusion [111] describes the change of the concentration over time as:

$$\frac{\partial c}{\partial t} = D\Delta c \tag{2.20}$$

With the addition of a reaction term R to this equation, reaction-diffusion of these particles can be modeled:

$$\frac{\partial c}{\partial t} = D\nabla^2 c + R(c) \tag{2.21}$$

2.4.2. Reaction-Diffusion within TMSD-Circuits

Within this thesis DNA-computation is employed as straightforward strand-displacement circuits. Therefore, especially TMSD reactions are considered. All experiments are set up in a central symmetry to allow for the reduction of the mathematical problem to 1D. For one-dimensional diffusion, the reaction term of these reactions is given by:

$$R(c) = \frac{d[A]}{dt} = k_{on} \cdot [A] - k_{off} \cdot [B] \tag{2.22}$$

for a duplex $A : C$ opened by an invading strand B that replaces strand A. The TMSD rate constants k_{on} and k_{off} are explained in more detail in Section 2.2.2.

2.4.3. Reaction Kinetics for Protein Expression

For a complete model of the reaction kinetics, rate constants for all reactions such as transcription factor binding, polymerase binding, and protein folding would be necessary. As these parameters are hard to assess, an approximation of Leveau and Lindow [112] is employed. In their model, the complex pathway of transcription-translation is reduced to a three-step DNA - intermediate (unfolded fluorescent protein) - product (fluorescent protein) setup. The intermediate is directly depending on promoter activity which can be expressed as a Hill equation for promoter strength P, inducer concentration $[I]$, while K indicates the inducer concentration at which P equals ½ P_{max}: [112]

$$P = P_{max} \cdot \frac{[I]^h}{K + [I]^h} \tag{2.23}$$

Reaction-Diffusion for Small Inducer Molecules

For inducer diffusion studies within bioprinted bacteria gels a central symmetric geometry was applied, where the inducer is added to a central cylindrical gel slab (see Chapter 6). Therefore, the problem can be reduced to a 1-dim diffusion problem. For diffusion constant D and a bacterial growth rate $\gamma = \frac{ln2}{t_d}$ with doubling time t_d the following equations are describing the process if the same simplification of the protein maturation process is assumed as in Equation 2.23.

$$\frac{\partial c(r,t)}{\partial t} = \frac{1}{r} \cdot \frac{\partial}{\partial r}\left((r \cdot D \cdot \frac{\partial c(r,t)}{\partial r}\right) \tag{2.24}$$

$$\frac{\partial N(r,t)}{\partial t} = \gamma \cdot N(r,t) \tag{2.25}$$

$$\frac{\partial P(r,t)}{\partial t} = \alpha \cdot \frac{c^n}{c^n + K} \cdot N(r,t) \tag{2.26}$$

These equations describe the fluorescent protein production in dependence on local inducer concentration $c(r,t)$ and a Hill model with threshold concentration K, Hill coefficient n, and maximum production rate α. Depending on the initial conditions, the total number of bacteria $N(r,t)$ and the total amount of protein $P(r,t)$ can be determined. The numerical solution of this set of equations is explained in more detail in Chapter 6.

Reaction-Diffusion for a Sender-Receiver Setup

In contrast to the relatively simple model for reaction-diffusion of small inducer molecules, to model the sender-receiver system mathematically more parameters need to be considered: the growth rates of both sets of bacteria, the production and degradation of the sender-molecule AHL, and the expression and degradation of the observable fluorescent protein GFP produced by the receivers. Additionally, lag time between GFP production and maturation has to be considered.

Sender cells are localized to the central region and produce signaling molecules that can diffuse freely from the center, similar to the inducer experiments. The sender cell growth can be assumed logistic for a cell number N_S and growth rate γ to a maximum cell number N_{max}:

$$\frac{\partial N_S(r,t)}{\partial t} = \gamma \cdot N_S(r,t) \cdot \frac{1 - N_S(r,t)}{N_{max}} \tag{2.27}$$

The number of receiver cells N_R can be modeled similarly, but with respect to a lag time that is due to heat and hydrostatic shock during extrusion. The lag time is approximated with a sigmoidal function $s(t, t_{lag}) := {}^{1}/_{(1+\exp(-\kappa \cdot (t - t_{lag})))}$ with a factor κ to correct the smoothness of the transition.

With this, the number of receiver cells is modeled the following:

$$\frac{\partial N_R(r,t)}{\partial t} = s(t, t_{lag}) \cdot \gamma \cdot N_R(r,t) \cdot \frac{1 - N_S(r,t)}{N_{max}} \tag{2.28}$$

The LuxI production of the sender bacteria is expected to be steady state and that each LuxI generates AHL at a fixed rate. Each sender cell therefore produces AHL with a rate of:

$$\alpha_{AHL} = \frac{1000 {}^{1}/_{s}}{6.022 \cdot 10^{23}/\text{mol} \cdot 2\mu l} \approx 1 \frac{fM}{s} \tag{2.29}$$

With this, the overall reaction-diffusion of the AHL molecules can be expressed as:

$$\frac{\partial [\text{AHL}](r,t)}{\partial t} = \frac{1}{r} \frac{\partial}{\partial r} \cdot (rD \cdot \frac{\partial [\text{AHL}](r,t)}{\partial r}) + \alpha_{AHL} \cdot N_s(r,t) - \delta_{AHL}[AHL] \tag{2.30}$$

The observable protein GFP is expected to be proportional to the number of receiver bacteria: $N_{GFP} \sim N_R$.

$$\frac{\partial N_{GFP}(r,t)}{\partial t} = \\ = \alpha_{GFP} \frac{[AHL]^m}{[AHL]^m + K_{AHL}^m} \cdot s(t, t_{lag}) \cdot N_R(r,t) \cdot (\frac{1 - N_R(r,t)}{N_{max}}) - \delta_{GFP} \cdot N_{GFP}(r,t) \tag{2.31}$$

For AHL and GFP degradation rates have to be considered. The long run-times of the experiments raise the need for considering the reduction of gene expression at stationary phase which is accounted for with a logistic model for the bacteria cell growth.

2.5. Cellular Automata

Already in 1947, John von Neumann developed the idea of an independent kinematic self-reproducing automaton with the goal of a self-replicating machine in mind. [113] Placed in an array of identically programmed other automata and given the possibility to communicate, the *cellular automata* were a novel representation of parallel computing and exhibited self-organizing features.

In 1970, John H. Conway working in the field of game theory [114] published an interpretation of the cellular automata to mimic life which is now known as *Conway's Game of Life*. Depending on the current vital status of neighboring cells, every singular cell evolves. With this simple updating system, complex population dynamics can be simulated. In the 1990s, Green [115] based his considerations of cellular automata models in biology on Stephen Wolfram's description of cellular automata[116],[117]. He stated, that many natural phenomena, for example the pattern formation on mollusc shells, can be modelled as cellular automata. However, most applications of cellular automata are currently found in the field of robotics.

2.5.1. Mathematical Background

Von Neumann's considerations started from the idea of simple computing unit consisting of three modules: a universal constructor, a universal copier, and a control module. For self-replication, the control module sends a command to the universal copier to duplicate the cell description ΦX. Then it commands the universal constructor to build a new automaton X from the description ΦX. In a final step, the replication completes upon splitting of controller and $X + \Phi X$. Such a cell replication can be realized as a finite state machine with 29 logical states. [113] One has to highlight, that this process is extremely similar to the transcription-translation mechanism of living cells, which was only described some years later following the work of Watson and Crick. [118], [119]

Nearest Neighbor Communication

All computers need input parameters to perform calculations. In contrast to classical computing, cellular automata evolve under consideration of their own current status and the states of directly neighboring cells following a unique rule set.

Rule sets determine the updated cell status for the next time interval depending on neighboring cells. Each rule set can be graphically represented (as example Figure 2.5.1 represents rule 60) and transferred to a basic logic function to calculate the next status of a cell depending on the states of itself (c_t) and its right and left neighbors (r_t and l_t).

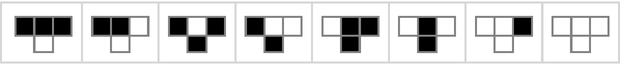

■ 1 | □ 0

Figure 2.5.1: Exemplary Rule Set - Rule 60: *For a one-dimensional cellular array all possible combinations of cell states for a cell c and its left and right neighbors are depicted in binary order. Rule 60 determines, the binary interpretation of the updated states must represent number 60. Depending on the cell states, each cell computes its next status and evolves accordingly.*

Exemplary for rule 60, the logic function is:

$$c_{t+1} = l_t \oplus c_t \tag{2.32}$$

And the mathematical representation can be given as:

$$c_{t+1} = (l_t + c_t) \bmod 2 \tag{2.33}$$

Matrix Representation

The complete cell array can be modeled if the update functions are transferred to matrices. The matrix description allows for the integration of a higher number of states per cell. For the exemplary rule 60, the matrix is given as:

$$R_{60,c} = \begin{pmatrix} 1 & 1 & 0 \end{pmatrix} \tag{2.34}$$

The next state of cell c can now be calculated:

$$c_{t+1} = R \cdot \begin{pmatrix} l_t & c_t & r_t \end{pmatrix}^T \bmod 2 \tag{2.35}$$

For a vector $\vec{c}$ containing all cell states at time t, the updated states at time $t+1$ can be calculated if $R_{60,c}$ is extended to R_{60}, a matrix combining the transition rules for all cells. It follows:

$$\vec{c}_{t+n} = R_{60}^n \cdot \vec{c}_t. \tag{2.36}$$

Self-Assembly

With the mathematical representation of the rule set of each singular cell, the goal is to design a set of rules that lead inevitably from random initial conditions to the assembly of a desired pattern, for example the assembly of an image (see Figure 2.5.2). Programming a desired final pattern can be achieved with the equivalent matrix model by Jones et al.[120], [121]

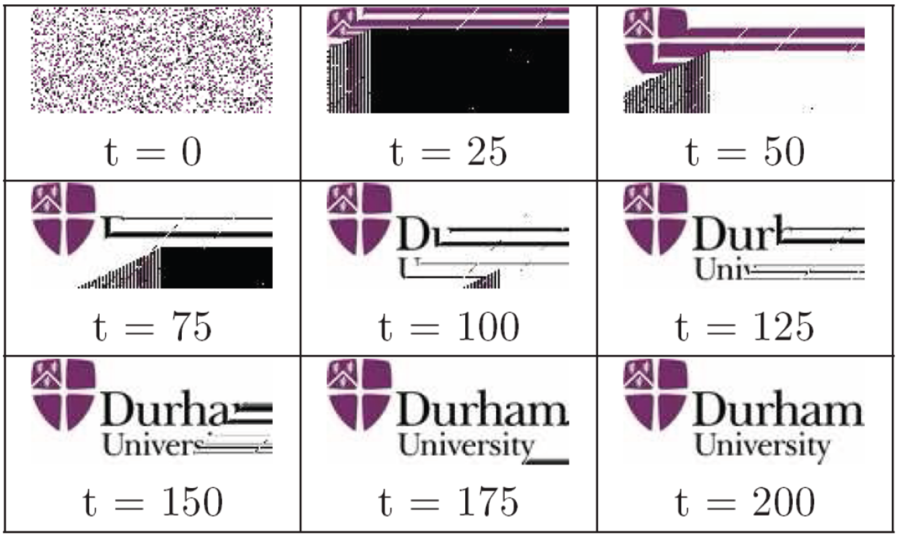

Figure 2.5.2: 2D Self-Assembly: *Starting from random initial conditions (each cell showing one of three possible colors) the university logo self-assembles over time by recursively updating cell states with a predefined uniform algorithm. Adapted from Jones et al.* [121]

The constant matrix D can be added to the transition matrix introduced in equation 2.36 if dim D =dim R.

$$\vec{c}_{t+1} = R \cdot \vec{c}_t + D \tag{2.37}$$

This gives a transition function that fully determines the aimed stable pattern, the so called *steady-state expression* of all singular automata after sufficient steps: [121]

$$\vec{c}_{t+n} = R^n \cdot \vec{c}_t + \frac{(\mathbb{1} - R^{n-1})}{\mathbb{1} - R} \cdot D \tag{2.38}$$

Convergence is given, if the final system of states $c_{\vec{t+n}}$ is independent of the initial conditions. This is true if R is an upper- or lower-diagonal matrix giving:

$$C_n = (\frac{\mathbb{1}}{\mathbb{1} - R}) \cdot D \tag{2.39}$$

2.5.2. Applications

The design principles for cellular automata were successfully applied in informatics and sensoric devices, examples are shown in Figure 2.5.3. Current developments are working on functional self-assembling robots. The integration of cellular automata computing principles on hydrogel - microenvironment would allow more complex pattern formation based on the principles of synthetic biology.

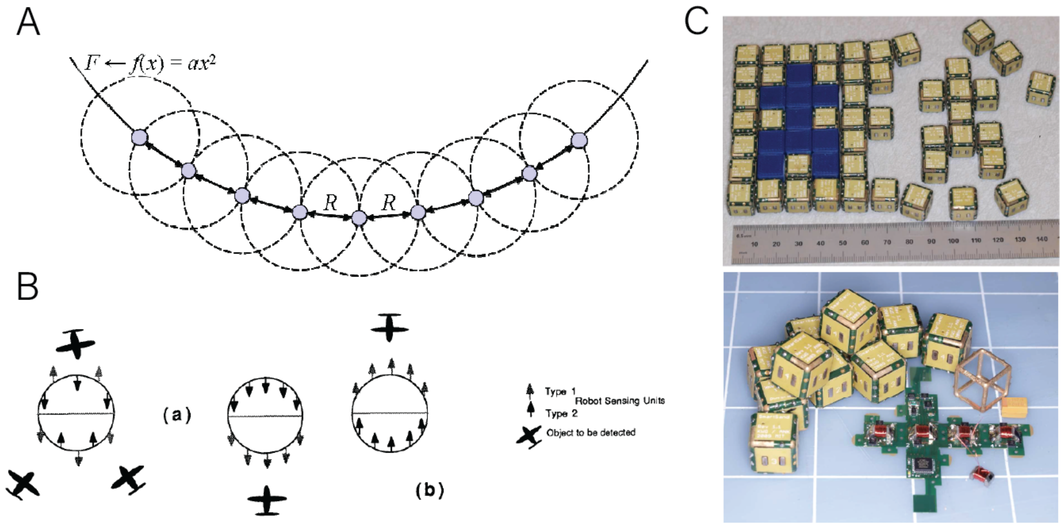

Figure 2.5.3: Cellular Automata Applications: *A) Cellular automata represent a mathematical function. One cell is indicated as seed cell and exhibits an exact function value, all other cells arrange themselves according to their respective location to represent the correct function value.* [122] *B) Depending on the condition of multiple (a) or single (b) airplanes approach an airport, an array of sensors is monitoring either all planes at low resolution, splitting their attendance in coordination with their neighbors or deliver a high resolution monitoring of the singular approaching plane.* [123] *C) Self-assembling pebble robots based on their universal cellular automata rule set. Depending on the rule set, the pebbles organize themselves to form complex shapes, as seen here by recreating the shape of the blue building blocks.* [124] *All images adapted from referred original publications.*

2.6. Photoswitchable Hydrogels

While a majority of hydrogels exhibit stable characteristics once crosslinked, specific chemical modifications allow a feature change upon application of a wide variety of external stimuli. With this feature, hydrogels can be employed for drug delivery by embedding molecules - or even complete proteins protected by the high water amount of the polymer network - to the desired target sites and released there to diffuse. After exposure to their corresponding stimuli hydrogels alter their properties: cross-link density, mechanical strength, hydrophibicity, permeability, and degradability are only some options. External stimuli include for example the addition of chemicals, electric fields, changes in pH or temperature, or irradiation with specific wavelengths (see Figure 2.6.1). [125]

The major advantage of photon based switching mechanics is the decoupling of the stimulus from the sample. Thus, no cross-influence on the used or embedded materials have to be considered. For this work, light-initiated gel-to-sol transitions are employed to generate light-controlled gates to regulate the information exchange between hydrogel compartments.

The functional core of photoresponsive hydrogels is typically a photoreactive moiety, mainly a photochromic chromophore, linked to the chains of a hydrogel. This moiety is able to react to irradiation by photon-driven chemical signals. These signals directly affect the hydrogel properties due to isomerization, cleavage, or dimerization. [125] Some of these reactions are reversible by irradiation with a different wavelength, or upon other stimuli e.g. heat. While photoisomerization and photodimerization are often repeatedly reversible, photocleavage seldom is. Figure 2.6.1 shows an overview over the most frequently used molecular photoswitches in hydrogels.

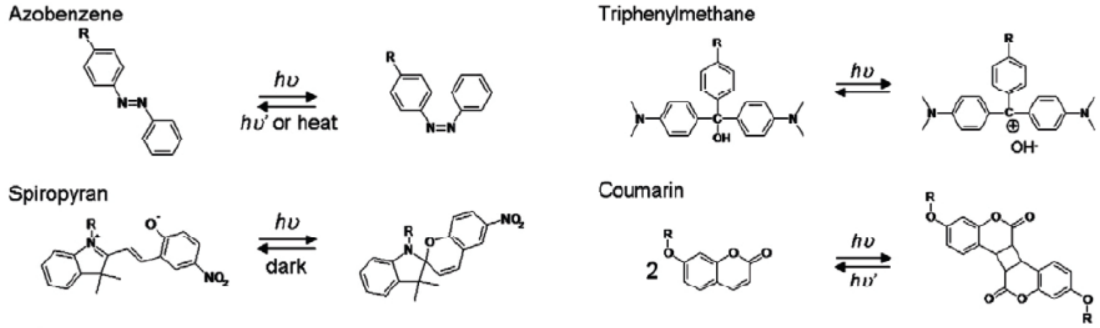

Figure 2.6.1: Reversible Photoactive Groups: *For the modification of hydrogels with photoactive moieties to change the hydrogel properties, a variety of these groups are reversibly switchable. Azobenzenes and spiropyranes are examples of photoactive moieties that exhibit photoisomerization, both molecules show reversible switching. Azobenzenes can be switched back via irradiation with a different wavelength, spiropyranes switch back if the amount of available protons is changed by altering the pH. If irradiated with an UV light source, triphenylmethane dissociates to ion pairs that can be reconnected thermally or under acidic conditions. The switching threshold wavelength for coumarines is 310 nm. Wavelengths longer (i.e. lower energy) initiate dimerization of coumarines that can be decoupled with wavelengths shorter (i.e. higher energy) than the threshold. Adapted from Tomatsu et al.* [125]

Azobenzenes are widely used as molecular switches. Their natural form is in a *trans*-state, where the $-N = N-$ bond between the aromatic residues is at its lowest possible energy level. Upon irradiation with Ultra Violet (UV) light at 350 nm - 360 nm, the bond undergoes photoisomerization and the azobenzene switches to its *cis*-state. In this state, it shows higher polarity, but its main feature is a change in overall conformation. With this, stacking or complexation with host molecules is hindered. Azobenzenes are able to return to the *trans* configuration either by illumination with visible (VIS) light (400 nm - 460 nm) or by thermal equilibration. However, over the last decade, several modifications of azobenzenes were found and the switching wavelengths are largely tunable, for example, complete switching at VIS spectrum is possible. [126]

Stilbenes exhbit a similar chemical structure to azobenzenes, but have a shorter *trans-cis* switching wavelength (high energy UV). This spectrum is less simple to integrate as light sources are rare and the high energy photons are mostly not compatible with biological samples. [125], [126]

Spiropyranes consist of two heterocyclic functional groups as indicated in Figure 2.6.1. These functional groups span orthogonal planes. [127] In contrast to azobenzenes, spiropyranes change the mechanical stability of hydrogels not via molecule-molecule interactions, but the spiropyrane itself exhibits a different protonated state depending on its form. While in acidic environment, these molecules are in their open merocyanine form (i.e. protonated), thus hydrophilic, which results in an uptake of water and a subsequent swelling of the hydrogel. If irradiated with typically blue light, the molecule releases a proton and switches to the closed hydrophobic (i.e. uncharged) form. With this conformational change the corresponding hydrogel releases water and shrinks accordingly. [125], [128]

Triphenylmethane can be dissociated to ion pairs upon irradiation with typically 365 nm. [129] The molecules dissociate into negatively charged hydroxide ions and positively charged polymers. Due to electroneutrality constraints the hydroxide ions are not able to diffuse further away from the positive charge of the polymer until other negatively charged species are nearby. With this dissociation of molecules, a local osmotic field is generated that drives the solvent flow and induces swelling or shrinking of the hydrogel. Recovery can be achieved mainly thermally or if the hydrogel is placed in a high pH solution. Typically, triphenylmethane is colorless in its associated state, the cations are intensely colored after dissociation. [125], [129]

Coumarin dimerizes upon photoirradiation with wavelengths longer than 310 nm and can be reversely decoupled by irradiation with shorter wavelengths than 310 nm. Complexations of coumarine molecular switches with cucurbit[8]uril or γ-cyclodextrins were successfully implemented to tune the mechanical stiffness of hydrogels.[125], [130]

For gated communication between hydrogel compartments, a change in pore size is more desirable than a strong swelling or shrinking response to keep stable conditions in the adjacent hydrogel compartments. Additionally, switching wavelengths $>$ 350 nm are advantagous, as in this area low cost electronic devices are widely available. With this, azobenzenes were selected as molecular switches for the design of a photoswitchable, hydrogel-based communication gate between two adjacent hydrogel compartments.

2.6.1. Guest - Host Interactions

Cyclodextrin (CD) is the most understood and widely used host molecule that can integrate azobenzenes. Cyclodextrins are cage molecules built up from cyclic chains consisting of glucose molecules that can encapsulate other molecules within their hydrophobic cavity. Small molecules form inclusion complexes with the cyclodextrin, for which the CD takes the part of a host molecule and the smaller molecule is incorporated temporarily as guest. [131]

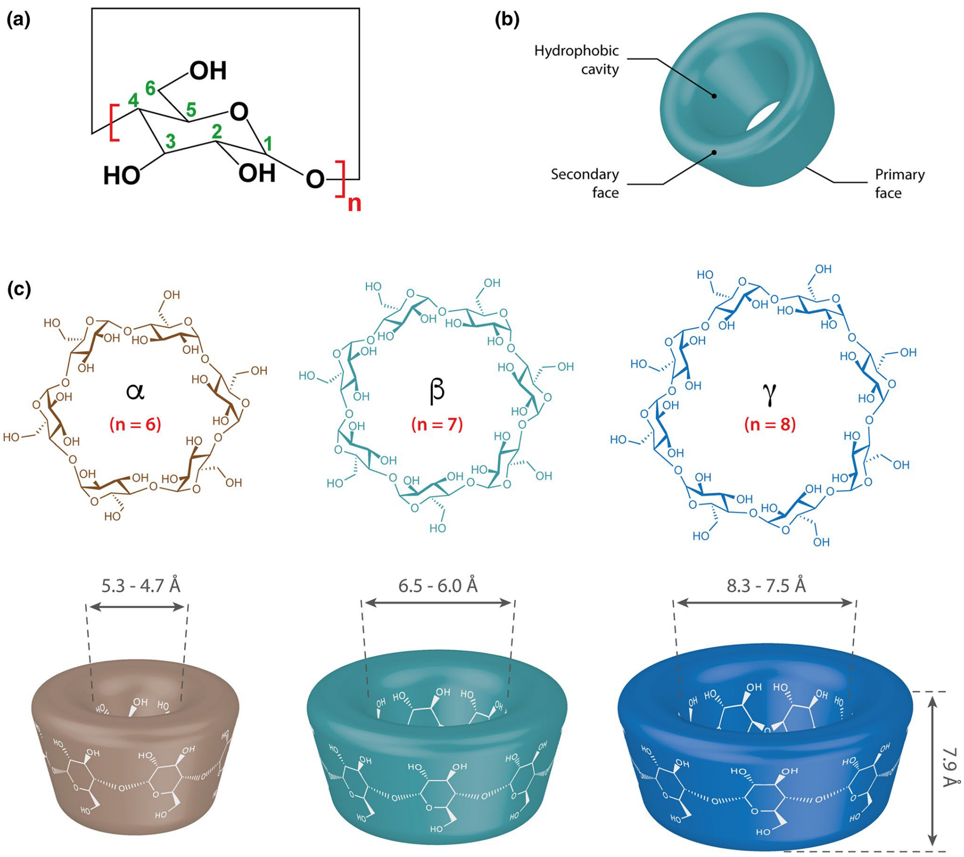

Figure 2.6.2: Cyclodextrin Structure: *A) Structural representation of single 1,4-glycosidically bound glucose subunits of the different cyclodextrins.* n *represents the number of molecules within the structure B) Schematic draft of the spatial structure of a cyclodextrin. The central hydrophobic area is an ideal cavity for the integration of host molecules. C) Spatial structure of α-, β-, and γ - cyclodextrins. The relation of the macro-cyclic molecule size on the number of monomers is clearly visible by the deviations in diameter. Adapted from Crini et al.* [131]

Depending the length of the oligosaccharide, there are three different classes of the most frequently used cyclodextrins: α- CD(six glucose molecules), β- CD(seven glucose molecules), and γ- CD(eight glucose molecules). Of these, β-CD is the most studied and frequently used molecule. A graphical representation of these truncated-cone-shaped molecules is given in Figure 2.6.2. [131]

As an example for successful cyclodextrine-azobenzene hydrogel modification, Wang et al. switched the mechanical stiffness of a Poly-Acrylic-Acid (PAA) hydrogel by grafting azobenzene and β-cyclodextrin via an NH_2 amino linker to a polyacryclic backbone. In their work, they modified the azobenzenes with tetra-*ortho*-methoxy subtitutions to redshift the *trans*-to-*cis* switching wavelength. [132]

For a first test of the guest-host interactions, no color shift was aimed and organic synthesis of the modified PAA molecules was facilitated by purchasing azobenzene with a suitable amino group that can be used for direct N-(3-Dimethylaminopropyl)-N'-ethylcarbodiimid-hydrochloride (EDC) / N-Hydroxysuccinimide (NHS) grafting. [133] As this molecule is roughly at the size of 5 nm while in *trans* configuration, α- and β- cyclodextrins might be applicable hosts.

The azobenzenes can be expected to form stable guest-host complexes with the cyclodexrins while in *trans*-configuration and to disassemble upon irradiation with UV light. As the irradiation induces *trans*-to-*cis* isomerization, the molecules disassemble because of their structural change and change in size from the cyclodextrin cavity and the hydrogel loses mechanical stability.

2.6.2. Available Scaffold Materials

Photoactive moieties can be grafted to a multitude of hydrogel backbones if they exhibit carboxylic groups via a amine coupling reaction including EDC/NHS. [133] Azobenzene - cyclodextrine guest - host modifications have been reported for example on curdlan, [134] PAA[132] [135], dextran, [136] or PEG and alginate. [137]

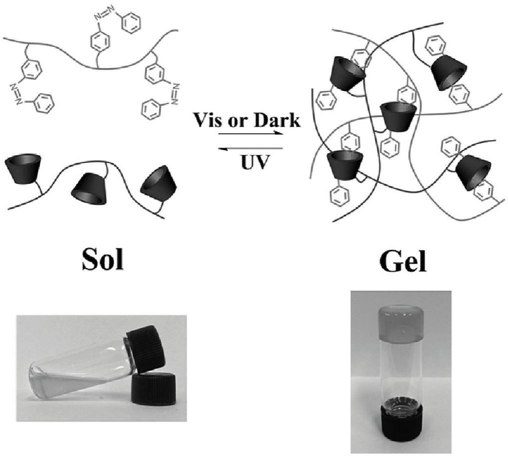

Figure 2.6.3: Photoactivated Change in Hydrogel Stiffness: *α- cyclodextrin grafted to PAA and mixed to azobenzene-modified PAA hydrogel. If the azobenzene exists in cis-configuration, no guest-host interactions stabilize the hydrogel and low viscosity solution is formed. Via VIS irradiation, azobenzenes switch to trans-state and the hydrogel exhibits higher <mechanical stability. Adapted from Wang et al.* [135]

PAA was chosen as backbone due to the following criteria: azobenzene - cyclodextrin interaction driven change in pore size was already reported as shown in Figure 2.6.3. PAA is able to form extremely dense hydrogels with low pore sizes which is beneficial if DNA circuits or even inducer molecules for bacteria circuits should be restrained by the closed gel. Further, azobenzene and cyclodextrin can be modified with a monoamino group that allows both moieties to be synthesized following the same EDC and NHS based synthesis protocol stated by Fischer et al. [133]

3. Materials and Methods

The generation of artificial hydrogel constructs in various shapes and structures is based on a precisely working 3D printer with a bioink that fulfills several requirements (see Chapter 4), and a reliable and observable biological circuit (see Chapters 5 and 6). In this chapter, all protocols are collected and explained.

3.1. Synthetic Circuits as Hydrogel Modifications

3.1.1. DNA Circuits

DNA Circuits were included in printed gel voxels by the addition of free diffusing ssDNA strands to localized ssDNA strands that are linke to the agarose gel.

DNA Preparation

For all bioprints modified with DNA computing circuits, the DNA strands were preprocessed as stated in the following: All DNA strands were prepared at a concentration of 10µM in a 1 M NaCl + 1 × Tris-Acetate-EDTA (TAE) in ddH_2O buffer. If the circuit is designed for the free diffusion of two strands, 2.5 µl of 10 µM DNA strand were mixed to a final concentration of 5 µM each. If the strands are to form a fluorophor-quencher duplex, the duplex formation was initiated following the respective protocol.

For experiments designed for four fluorescently labeled strands, 2.5 µl of 10 µM DNA strand were mixed to a final concentration of 2.5 µM each. For experiments with two fluorophor-quencher duplexes, the respective complementary fluorophor and quencher labeled strands were mixed together as in the experiments for two strands and an annealing step was performed. Then the two fluorophor-quencher duplexes were mixed again with 2.5 µl of each duplex, leading to an end concentration of 2.5 µM per strand and verified fluorophor-quencher bonds. For the diffusion experiments, 3 µl of the respective mixed sample was used for the DNA ink.

Fluorophore-Quencher Duplex Preparation

2.5 µl of 10µM fluorescently labeled strand was mixed with 2.5 µl of the respective 10µM quencher strand in 1 M NaCl + 1 × TAE in ddH_2O buffer. The solution was annealed twice in a thermocycler by heating to 90°C for 5 min and let cool down to 4 °C in 5 min using a linear temperature ramp. Stable duplex formation was verified using a bulk platereader experiment.

Localized DNA Strands

ssDNA can be fixed to agarose chains, if the agarose is modified with propargyl-isothiocyanate (PITC) beforehand. This modification is explained in detail in Aufinger et al. [138] and follows the reaction mechanism established for fluorescein isothiocyanate (FITC) labeled dextrans. [139]

1 mmol (306 ng) of super low melting (SLM) agarose was dissolved in 10 ml of carbonate buffer at pH 10. Dissolution in a Falcon tube was assisted by heating to 90 °C. For further reaction steps, the solution was cooled to room temperature. PITC was dissolved in 5 ml of Dimethyl sulfoxide (DMSO) and 0.25 mmol (22.9 µl) were added under vortexing to the agarose solution. The reaction was allowed for 12 hours at room temperature on a rotator.

Purification of the product was precipitated 4 times with 20 ml of cold (-20 °C) isopropanol, washed with 10 ml methanol, dried for 2 h in a desiccator and re-dissolved in 10 ml ddH_2O . The first precipitation was carried out with 30 ml isopropyl alcohol and the final precipitate was dried overnight. The light brown flakes were stable for storage at 4°C for at least 9 months.

For the linkage of ssDNA strands to PITC agarose, the copper-catalyzed click reaction protocol in Aufinger et al. [138] was followed. 5 mg PITC agarose were dissolved in 250 µl ddH_2O to a concentration of 2% (w|v) in 2 ml round-bottom tubes by heating to 80 °C, stirring and vortexing. To the aqueous solution 100 µl 5 × phosphate-buffered saline (PBS), 50 µl azide-modified ssDNA, 5 µl Tris-(2-carboxyethyl)-phosphine (TCEP), 10 µl Tris(3-hydroxypropyltriazolylmethyl)amine (THPTA), and 5 µl CuSO4 were added. The reaction was allowed to proceed for 1 h at 45 °C on a shaker at 450 rpm.

After completion, uncoupled educts were precipitated by centrifugation for 5 min at 16 000 rpm. The supernatant containing the DNA modified agarose was taken and stored at 4 °C.

3.1.2. Bacteria Circuits

For all bacteria printing experiments, *E. coli* bacteria (DH5α, DH5αZ1, and BL21) were used. All cultures exhibited a resistance to carbenicillin.

Bacterial Culture Conditions

Overnight cultures were prepared prior to printing with 5 ml lysogeny broth (LB) medium and 5 µl carbenicillin (stock concentration: 1000 ×) and bacteria from glycerol stock. The culture was incubated for 16 h at 37 °C.

Pre-Print Bacteria Preparation

Prepared overnight cultures were diluted 1:100 in 5 ml LB medium and 5 µl carbenicillin and grown for at least 2-3 h until OD $\geq$ 0.6 was reached. For printing, the bacteria cultrure was set to exactly OD 0.6 in fresh LB medium. For this the suspension was centrifuged at 4 °C for 2 min at 2000 rcf, the supernatant discarded and the bacteria pellet resuspended with fresh LB media.

Inducer Addition

If bacteria with pTet promoter are used, aTc (stock solution 10000 $\times$) was diluted 1:4 with ddH_2O . This was mixed 1:1 with bacteria-ink and a 5 µl voxel was set to center of printed structure, leading to an end concentration of 2 $\times$ aTc [428 mM]. Bacteria with pLac promoter can be induced via the addition of 1 mM IPTG. The sender bacteria were induced after deposition by the addition of 30 µl [10 mM] IPTG, to ensure a concentration of 1 mM in the complete chamber after diffusion.

3.2. Hydrogel Preparation and Bioprinting

The printing conditions were the same for all DNA-computing and for all bacteria-containing gels and the printing procedure as well as the preparations are stated in the following.

3.2.1. Protocols DNA-Bioink

Bioprinting of DNA modified hydrogels included a paste consisting of gelatin, alginate and super low melt agarose in water. DNA was added to the hydrogel ink via the agarose component using copper-catalyzed click reaction. Due to the high viscosity of the ink, all steps including pipetting were conducted with positive displacement pipettes.

Preparation of blank Bioink

50 ml ddH_2O were heated to 80-100°C. 0.5 g (1 % (w|v)) super low melt agarose was added while stirring at 1400 rpm for $\approx$ 10 min. Subsequently, 1.5 g alginate (3 % (w|v)) were added under continuous stirring for 45 min. Solution can be improved by short sonication intervals (1 - 2 min). When completely dissolved, the solution was cooled down to 50 °C and 5 g (10 % (w|v)) were added and dissolved at 50 °C and 900 rpm. The final gel was degassed either in the sonicator or using a vaccum pump. To avoid the risk of contamination distribute gel to 20 ml aliquots. Bioink can be stored at 4 °C and dissolved in at 50 °C.

Preparation of DNA-Bioink

1% DNA-functionalized agarose was prepared according to the protocol in section 3.1.1. Bioink for mixing was prepared following the aforementioned protocol, with twice the amount of alginate (6 %) and gelatin (20 %), but 1 x agarose (1 %). This mixture and the functionalized super low melt agarose were mixed together 1:1 and sonicated for 1h at 40 - 50 °C.

Pore Size Estimation of DNA-Bioink

For the bio-ink mixture the pore size is expected to be homogeneous within the hydrogel. To assess the pore size, 20 µl FITC dextrans of different sizes were added to 60 µl gelled bioink, while 20 µl of the samples were kept as reference. The samples were equilibrated for $\approx$ 60 hours at room temperature. Due to swelling behaviour the hydrogel adsorbed the supernatant and 20 µl of 1 M NaCl + 1 $\times$ TAE in ddH_2O buffer were added and immediately transferred for fluorescent spectroscopy. For FITC - dextrans of lower size than the pore size, the dextrans are expected to diffuse within the gel and the supernatant is expected to exhibit lower fluorescence than the reference sample.

Fluorescent paticle sizes included: fluorescein as small molecule, 10 kDa dextran ($\varnothing \approx$ 2.3 nm), 50 kDa dextran ($\varnothing \approx$ 5.0 nm), and 500 kDa dextran ($\varnothing \approx$ 10.5 nm) all in 1 M NaCl + 1 $\times$ TAE in ddH_2O buffer.

Printing Process DNA-Bioink

The sample syringe was preheated by an external control unit to 42 °C, the bioink was preheated in an oven to dissolve at max. 50 °C to avoid disintegration of gelatin. 500 µl DNA-bioink was transfered to the sample syringe and placed in the printhead. The desired structure was printed from a `gcode` description on a cover slide. The printed structures were of $\approx$ 70 µl. The printhead was kept at 42 °C in room temperature surroundings (23 °C).

After extrusion, the printed structure was directly wetted with 20 µl ddH_2O to compensate drying. For ideal buffer condition the print was additionally wetted with 20 µl 1 M NaCl and 1 $\times$ TAE in ddH_2O buffer and the samples was let to swell for $\approx$ 10 min. For sample sealing a custom plastic frame (PLA, 3D printed) with an inner cavity of 7.5 mm x 7.5 mm x 4 mm was glued around the print using UV glue. Remaining liquid was pipetted off and the edges of the print covered with 70 - 80 µl blank bioink.

Addition of Free DNA Strands after Bioprinting

After the printing process for diffusion experiments 3 µl DNA were mixed to 3 µl Bioink, centrifuged, and 3 µl pipetted to the center of the print.

For sorting experiments the print was firstly covered with a thin layer of bioink ($\approx$ 30 µl) and 10 µl of the mixed DNA samples in 1 M NaCl and 1 $\times$ TAE in ddH_2O buffer were applied on top. Following the addition of the free DNA strands, the chamber was sealed with a #1 cover slide glued on top of the chamber.

3.2.2. Protocols Bacteria-Ink

To embed living bacteria in 3D printed hydrogel structures a mixture of 2 % agarose and 2 % alginate (w|v) in ddH_2O was used as base. To allow fluorescent readout, sufficient oxygen supply that is crucial for protein maturation was assured by the addition of calciumperoxide and the enzyme catalase to the bacteria-ink. Due to the high viscosity of the ink, all steps including pipetting were conducted with positive displacement pipettes.

Preparation of Bacteria-Ink

50 ml ddH_2O were heated to 100 °C. 1.5 g agarose NEEO quality (2 % (w|v)) were added while stirring at 1400 rpm for $\approx$ 10 min. Subsequently, alginate was slowly added while still stirring (min: 1400 rpm) for 45 min. The hydrogel mixture was degassed at 80 - 100 °C for 1 h. Bacteria-ink can be stored in closed bottles at room temperature and melted in a microwave prior to printing.

Pre-Printing Preparation Bacteria-Ink

Bacteria-ink was dissolved in a microwave and kept warm in an oven at 70 °C. Printhead and sample syringes were heated to the printing temperature of 42 °C. Sample ink was mixed from 2 ml bacteria-ink and 1 ml bacteria at OD 0.6 in LB medium. The oxygen generating system of calcium peroxide and the enzyme catalase was mixed the 2 ml bacteria-ink and 1 ml bacteria solution prior to printing.

200 µl of 0.15 % (w|v) CaO_2 in ddH_2O and 60 µl catalase from a 1 mg/ml stock, corresponding to 60 - 100 units/ml, in potassium phosphate buffer (pH 7.0; 4.68 mg/ml K_2HPO_4, 3.16 mg/ml KH_2PO_4) were added. 1 ml of the final sample mixture was transferred to the preheated sample syringe.

Printing Process Bacteria-Ink

Prints were deposited on cover slides or microscopy slides and a plastic frame was glued for sealing around the printed structures using superglue. The frame consists of PLA, 3D printed, with inner cavity according to print dimensions (circular: $\varnothing = 17$ mm, $h = 4$ mm, rectangular: 24 mm $\times$ 46 mm $\times$ 4mm). 1 ml of LB-ink was added to the round, 6 ml to the rectangular chamber to remove air cavities. Sealing was achieved by gluing a #1 cover slide on top of the plastic chamber.

Bulk Rheology

To measure the temperature dependence of the viscosity of the bioink, a TA-rheometer was used with a 50-mm plate-plate geometry. The sample volume was 750 µl for each measurement. All samples were heated to 70 °C before transferring them onto the rheometer measuring plate. The rheometer was preheated to 60 °C and each sample was measured for 1 min at 60 °C to ensure a constant temperature of 60 °C for the whole sample volume. After this incubation time the measurement was started. The temperature was decreased in 1 °C steps from 60 °C to 20 °C in 4 s intervals.

3.2.3. Epifluorescence Microscopy

Fluorescence intensities were captured for up to 24 h in single images every 10 - 30 min at 37 °C with a P-Apo 4 × NA 0.20, P-Apo 10 × NA 0.45, or P-Apo 60 × oil NA 1.4 objective on a Nikon Ti-2E, equipped with a SOLA SM II LED light source, a motorized stage, perfect focus system, an Andor NEO 5.5 camera and the filter sets listed in Table 3.2.1. Typical settings were 50 % brightness of the fluorescence LED and the exposure time given in Table 3.2.1. Imaging was performed at locations in close proximity with no overlap between neighboring images. The captured images were then stitched together to cover the whole sample area.

Table 3.2.1: Filters and Exposure Times Used in Epifluorescence Microscopy:

Dye	**Dichroic (nm)**	**Excitation (nm)**	**Emission (nm)**	**Exposure (ms)**
DNA Labels				
Alexa 488	495	472/30	520/35	20
Alexa 647N	660	628/40	692/40	200
Atto 425	458	438/24	483/32	200
TAMRA	550	532/10	585/64	100
Fluorescent Proteins				
GFP mut3b	495	472/30	520/35	100
mRFP	550	532/10	585/64	300
mTurquoise2	458	438/24	483/32	50
mVenus	495	472/30	520/35	100

Microscopy Setup DNA - Bioink

For cuboid structures 3 × 3 (Figures 5.2.1 - 5.2.4), for the differentiation experiment 4 × 4 (Figure 5.2.4), and for the TUM logo 4 × 6 (Figure 5.2.3) images were captured and overlaid.

Microscopy Setup Bacteria - Ink

For inducer reaction-diffusion experiments 4 × 4 (Figure 6.2.4), for the sender-receiver experiment 5 × 5 (Figure 6.2.4), and for the artprint 7 × 11 (Figure 6.2.2) images were captured and stitched without overlap.

3.3. Photoswitchable Hydrogel-Channels

The gated hydrogel channels are all PAA based. Modifications of PAA with azobenzene or cyclodextrins were performed with the protocol from Fischer et al.: [133]

Preparation of Azobenzene- or α-Cyclodextrin-Poly-Acrylic-Acid

250 mg of 4-amino azobenzene, 347 mg EDC (10 × excess) and 207 mg NHS (10 × excess) were added under stirring and cooling to 20 ml ddH_2O in a round-bottom flask. The mixture was stirred in an ice bath for 3 h.

Subsequently either 34 mg 4-amino-azobenzene or 181.5 mg 4-monoamino--monodeoxy-α-cyclodextrin were added and the reaction was allowed for 72 h while being permanently stirred. The sample was then purified using dialysis.

Sample Purification

The sample was purified with a 7000 molecular weight cutoff (MWCO) dialysis membrane. The reaction product was dialysed for 3 days against 0.5 l ddH_2O . The dialysis solution was changed every 24h. After dialysis, the sample was freezed to -80 °C and subsequently dried in a vacuum chamber for 8 h.

Pore Size Estimation of Photogel

For the pore size estimation, the protocol is similar to the pore size estimation for DNA-bioink. However, open photogel was mimicked via a PAA - β- cyclodextrin - PAA mixture (2 % (w|v) each), to ensure a fully uncoupled guest - host interaction. Closed gel was mimicked via an azobenzene - PAA - β- cyclodextrin - PAA mixture (2 % (w|v) each) to ensure all guest - host interactions are linked.

Fluorescent particle sizes included: fluorescein as small molecule, 10 kDa dextran ($\varnothing \approx 2.3$ nm), 50 kDa dextran ($\varnothing \approx 5.0$ nm), 70 kDa dextran ($\varnothing \approx 6.0$ nm), 150 kDa dextran ($\varnothing \approx 8.5$ nm), 500 kDa dextran ($\varnothing \approx 10.5$ nm), and 2000 kDa dextran ($\varnothing \approx 38.6$ nm) all in 1 M NaCl + 1 × TAE in ddH_2O buffer.

4. Development of a Bioprinting Platform

During this thesis a bioprinting platform was established. Using the home-built software tool precise point-wise positioning was enabled. Further screening of diverse *bioink* compositions were screened and optimized for good printability and print fidelity among others. With these foundations, synthetic biological circuits based on DNA or bacteria were embedded and characterized.

The following sections cover the printer development and the hydrogel screenings as well as the results of the embedded self-differentiating synthetic structure. Additionally, the development of photoswitchable communication channels to separate circuit-containing voxels and gate communication to implement clear logic levels is introduced.

For the assembly of the bioprinter, hardware and software was developed. First the hardware assembly is explained in detail, covering also the commercial platform and the design considerations. Then, the software tool to generate printable gcodes from .svg design files is explained. At last, this chapter covers the findings on printability of a variety of low cost and widely available hydrogels on their printability and structural stability for bioink use.

4.1. Hardware Development

For the printing platform, a commercial Ultimaker Original+ as depicted in Figure 4.1.1 was used as 3D positioning base. This printer is designed and constructed to deposit plastic filaments of various features (e.g. poly(lactic acid) (PLA), acrylonitrile butadiene styrene (ABS), polycarbonate (PC), or nylon) with a fast filament fabrication (FFF) mechanism.

The Ultimaker Original+ has a precise x-y-positioning with a resolution of 12.5 µm, and a z-positioning resolution of 1.875 µm. A total build volume of 21 cm x 21 cm x 20.5 cm can be used with printing speeds from 30 mm/s - 300 mm/s. While the mainboard supports two extruders, the printer is delivered with a single filament printhead on board. More detailed information on the printer parameters can be found in section A.2 in the appendix.

Plastic filaments are usually delivered as long strings and fed via a tubular supply using a stepper motor to the printhead. The printhead heats the plastic to $\approx 200\,^{\circ}\mathrm{C}$ for extrusion through a 0.4 mm nozzle. This classical filament setup is highly favorable for plastic models, but less adapted to the extrusion of amorphous and viscous inks. Long tubings, no feeding system for liquids, and a singular fitted nozzle are some of the reasons why the plastic-filament printhead is disadvantagous for hydrogel-ink prints, especially if they contain (synthetic) biological samples.

For the implementation of the bioprinting unit, several design aspects were essential. The goals for this bioprinter were compared to existing systems used by other research groups and the following main aims were found:

1. **Biocompatible printing process:** Generally, mild printing conditions are highly favorable. This includes low shear stress, low pressure, temperatures below 45 °C, short interval or no drying, reduction of osmotic stress.
2. **Small volumina:** As biological samples that contain DNA or bacteria might be expensive or extremely vulnerable to external stress, short tubings from reservoir to printing platform were one of the key design parameters.
3. **Precise deposition:** The implementation aimed for a direct control of the extruded amount by the printer mainboard, nearly no slippage at the extruder, as well as the possibility of retraction, to stop sample liquid from afterflow.
4. **Fast and mild curing:** Most bioprinters use post-printing curing steps that include chemicals or UV-radicals. The approach is to generate a precise positioning of thermo-stable inks that solidifies rapidly at room temperature.

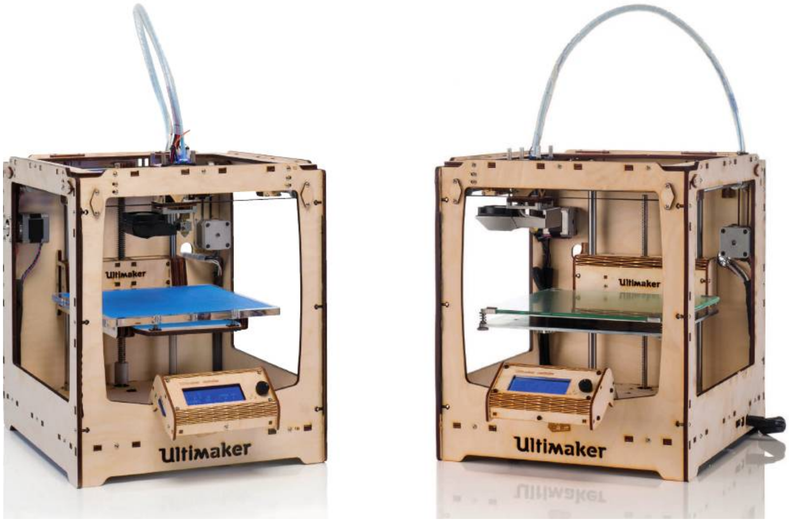

Figure 4.1.1: Commercial 3D Printing Platform: *The printing platform that served as the base for this bioprinter assembly is an Ultimaker Original Plus. This printer is delivered as an assembly kit and all parts can be exchanged or modified. The manual for this printer and further information can be found in A.2. Image taken from the company user manual (see Appendix A.2).*

These considerations lead to an approach where from the Ultimaker base only the x-y-z-positioning mechanism, the gcode interpretation of the mainboard, as well as the output-ports for the feeder motors were used. The complete filament extrusion part was replaced with a custom bioprinting-printhead that extrudes liquids from a printhead mounted sample syringe.

The sample syringe is driven directly from the printer mainboard that operates a syringe pump that is hydraulically coupled to the sample syringe. With this custom printhead the extrusion of small sample volumina at constantly elevated temperatures can be maintained. The major advantage of the direct connection between bio-extrusion unit and the Ultimaker motherboard is the synchronous control.

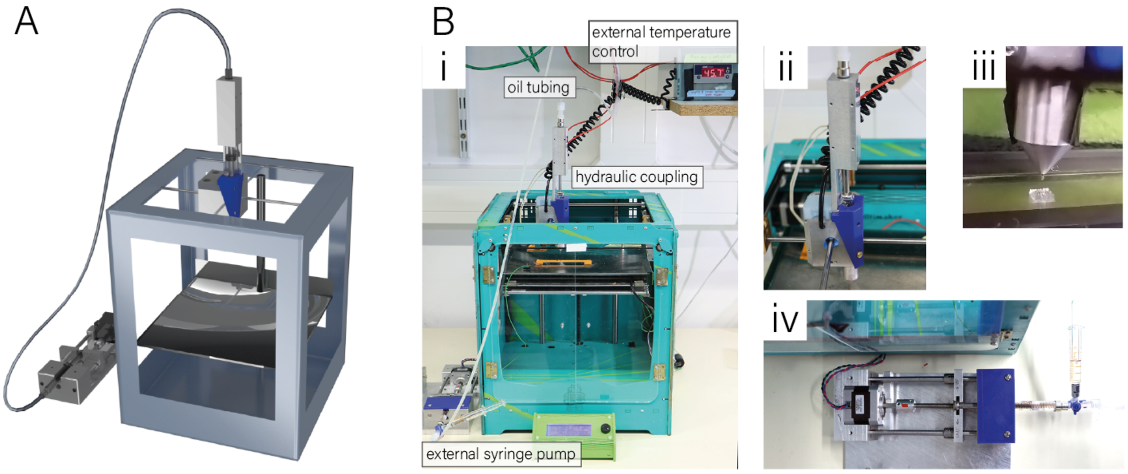

Figure 4.1.2: Bioprinter: *Assembled bioprinting platform on the basis of an Ultimaker Original +. The printer is varnished with acrylic paint to facilitate cleaning. poly(methyl methacrylate) (PMMA) windows are added to reduce air flow within the printing chamber. A) Graphical representation of the complete printer setup with main printing plaform, external syringe pump, custom printhead and hydraulic coupling unit. For all elements except the printing platform the original CAD design files are used. B) Images of the real bioprinter setup: i) Complete setup with singular parts indicated. ii) Hydraulic coupling of sample syringe to receiver syringe of the hydraulic system. iii) Close image of a successfully extruded hydrogel cuboid. iv) External syringe pump with sender syringe of the hydraulic system. Images already published in Müller et al.* [140]

With this direct control, no additional electronics for synchronization arises and the print fidelity of the device is maintained. This further ensures low to no slippage as the hydraulics is filled with incompressible mineral oil and allows for sample volumina as low as 200 µl to be loaded. Further, the coupling of the syringe pump via a hydraulic system allows to reach the printability of small volumina as no long tubing needs to be filled with sample ink (of special interest for samples that need to be maintained at a constant temperature or for cost-intensive samples). The printhead was heated over an external temperature control unit. However possible to heat filament printheads over the printer mainboard, this is not advisable for larger volumes (i.e. the bioprinting printhead) as heating leads to high currents over the mainboard. Figure 4.1.2 shows the final bioprinting setup with the externally placed syringe pump, hydraulic tubing and coupling, and the external printhead thermo-control. All CAD files for the singular parts and a list of components can be found in Appendix Section A.3.

4.2. Software Tool

For the generation of printable code (gcode) a Python script was designed that translates vector graphic .svg files. The script can be customized with an input parameter file, where hardware parameter (e.g. feed rate, travel speed, nozzle diameter) can be adjusted. This allows to use the Python tool to generate gcodes for all available 3D printers that are based on this machine readable protocol. Additionally, the software tool includes the control of a second extruder and therefore allows dual extrusion printing on all printers equipped accordingly.

While the vector graphic file supports 2D structures, also 3D shapes can be determined by the software tool. To indicate the z-dimension in the .svg file, color-coding was employed, a technique known from laser-cutting software. For each path, the stroke color of this element determines at which layer and with which printhead this element will be printed. Each layer and printhead interprets only elements with the respective color. However, colors can be used multiple times to generate the same pattern at multiple layers. The color code is imported to the gcode generator via the input parameter file and controls also the duplex printing tool.

The software tool was published together with the results of the DNA bioprinting experiments that are shown in detail in Chapter 5.
The complete code is available under a Creative Commons License on Github: https://github.com/julia-mueller/bioprinter/

The Python code can be executed as explained in the README section on Github on any platform (Windows, Linux, Mac) if the math library and numpy are included in Python 3.0 on that platform. Example input files for the Python script are also available on Github.

4.2.1. Technical Details

Every .svg file consists of a list of elements, so called paths, that determine the shapes of the graphical representation. These path elements can be directly converted from the path definition to a list of lines and a list of circles, these are further translated to a `G1` command for linear paths or to a `G3` command for arches in gcode. `G1` commands allow linear movement, `G3` circular movements, together these are the main two possibilities to command machine movements and extrusion in 3D printers.

The software tool uses the parameters from the input parameter file to write a header (start_routine) and a footer (end_routine) for the printer to perform all necessary mechanical steps. These steps are similar for all printfiles and deviate only by some parameters (e.g. height of the sample holder). If for all prints the same sample holders, temperatures, nozzles, etc. are used, these parameters only need to be adjusted for the first print and can be stored in the parameterfile.

The main part of the gcode (in the python tool called middleroutine) encodes the determined 3D shape. The .svg file is loaded and all singular paths are extracted. Depending on the path shape, the list of lines or list of circles receives an entry with x-y-coordinates for the start and end point of the element and the color of this element. After scanning all paths, these lists are translated level-wise to `G1` commands for all elements in the list of lines or to a `G3` command for all elements in the list of circles that show the same color as indicated for this layer. For each layer, the lists are screened for elements of the correspnding color and all elements are again translated to `G` commands. During the translation step, all parameters of the parameterfile are taken into all calculations, with this the gcode can be easily manipulated to account for the desired end structure. An exemplary .svg file and the corresponding translated gcode can be found in Appendix A.4

After all layers are translated, the footer is written to the `gcode` file which finishes the printfile. The printfile is subsequently written to a textfile and can be transferred to the 3D printer.

4.2.2. Experimental Parameters

The .svg files were always prepared for point-wise extrusion, as deposition of single voxels exhibited better reproducibility. Voxels were represented by single lines of a length of 0.238 mm. For prints with DNA modified bioink a 0.200 mm (G27) nozzle was used. For stable voxels typically a volume factor of $\times$ 2 was used. Prints with bacteria-ink were typically performed with a 0.330 mm (G23) nozzle and a volume factor of $\times$ 4. Due to the line-by-line translation, the printer receives the command for each voxel in the same sequence as the voxels are generated (or sorted) in the .svg file. This allows for a precise and planned printer path routing and also the exact positioning of a voxel at a single location.

All layer heights were calculated based on the assumption that the voxel assumes a perfect sphere when extruded, followed by a slight deformation as ex-

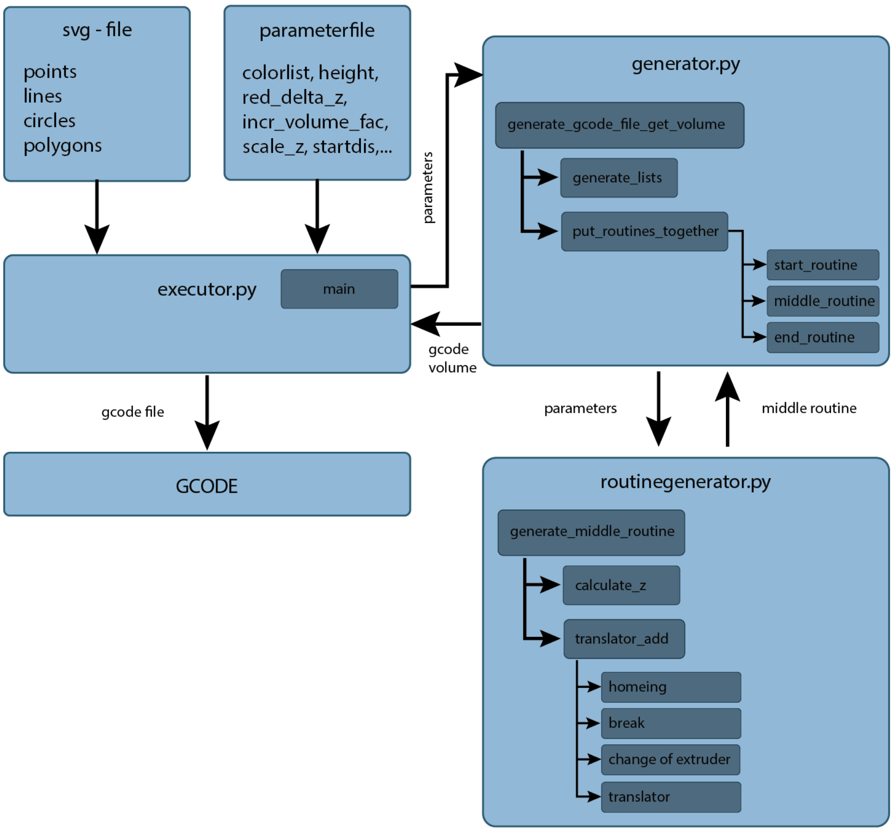

Figure 4.2.1: Flowchart Software Tool: *Graphical representation of the singular processes to transfer simple 2D vector based .svg descriptions together with a parameter file that sets the physical parameters to printable gcode files. The complete translation code was separated to smaller units to facilitate code development. Light blue boxes indicate scripts, dark blue boxes indicate functions within the single scripts.* ***executor.py:*** *Calling this function in a shell with a correct parameterfile starts the generator module and hands over all input parameters and the .svg definitions.* ***generator.py:*** *This python script creates the list of lines from the .svg file, which are used to produce the gcode. Also it calls the function „put routines together", which creates the gcode file and fills it with the routines: start routine, middle routine and end routine.* ***routinegenerator.py:*** *This python script returns the middle routine. At the beginning the height of the layers is calculated and afterwards the single parts of the middle routine are added together for each layer. At the beginning or after an extruder exchange a homing routine, a breaking routine after each layer, a change of extruder if necessary and the most important gcode for the printed structures which are added with the translator function. At the end the option for the addition of a cleaning routine is given.*

plained in Section 2.1.3. The deformation was considered with a factor × 0.8 for the calculations of all layer heights. After 5 layers an additional factor of × 0.8 was added as here also drying effects lead to a stronger deviation from the ideal assumption.

The printhead temperature was controlled externally as stated in Appendix 4.1. The printing temperature was kept at 42 °C with the external controller, leading to a temperature of approximately 36-37 °C within the hydrogel sample. For all prints, the printbead was not cooled and gelation occurred at room temperature (23 °C).

4.3. Bioink

Suitable printable inks - so called *bioinks* - are of major interest for the bioprinting community. Not only the development of a suitable bioprinter is critical for successful bioprinting, but especially the selection of a printable mixture of hydrogels to a bioink is highly important.

Typical bioinks exhibit shear-thinning behavior, are biocompatible, and mimic extra-cellular matrices. During the course of this work a wide range of bioprinters entered the market, some come with suitable bioinks that mainly aim for features that resemble the extracellular matrix, to facilitate tissue engineering. However, the degree of customization within these inks is low, as already small changes in the bioink composition (e.g. addition of modified materials) might lead to extreme changes in printability or structural stability.

With the development of a reliable printer setup completed, a variety of hydrogels and hydrogel mixtures were tested to find the best printable ink for different approaches. The results of these tests are summarized in Table 4.3.1. As only successful mixtures lead to printed samples, there are no images of the other gel compositions. During this thesis, two hydrogel compositions were established that show precise printability. The bioink is customizable with immobilized single stranded DNA oligonucleotide, the bacteria-ink allows the integration of living bacteria.

4.3.1. DNA-Bioink Composition

One major aim was to integrate DNA-computing circuits within deposited hydrogel structures. To reach this goal, localized ssDNA oligonucleotides were desirable. With the copper-click reaction protocol from Aufinger et al. [138] one component of the bioprintable paste was expected to be super-low-melt agarose at a concentration of 1 % w|v.

For a fast solidification, gelatin and agarose are the best candidates within the group of natural polymers. For mild resolving of the gel gelatin was found to be ideal at 10% w|v. However, the gel showed extremely low viscosity if heated to approximately 40 °C, necessary to maintain gelatin in a dissolved state. To increase the viscosity with a shear-thinning component, of the natural polymers mainly alginate and HA are adequate. As alginate is more affordable, a fist approach with alginate resoluted in an ideal addition of 3 % w|v alginate.

Table 4.3.1: Hydrogels For Bioprinting: *The following list of hydrogels were taken into consideration and tested. General features for printing and experimental results are listed. The density column indicates at which percentages each hydrogel is typically used in literature.*

Hydrogel	**Biocompatibility**	**Density**	**Affordability**	**Comments**
Agarose	very good	0.1 - 4	good	High temperatures necessary
Alginate	good	1 - 10 %	good	Good viscosity enhancer, can be crosslinked with $CaCl_2$
Collagen	good	1 - 2 %	good	Not completely tested as provided already only as hydrogel
Gelatin	good	1 - 10 %	good	Needs to be kept below 50 °C
GelMA	good if completely cross- linked	5 - 15 %	medium	Organic synthesis needs freeze-drying step, radical crosslinker necessary, low viscosity without crosslinker
Hyaluronic Acid	good	0.1 - 1 %	expensive	Good water retention
Polyacrylic Acid	good if completely crosslinked	2 - 10 %	good	Extremely low viscosity until initiator added. More suitable for stereolithography.

For a printable, DNA-modified bioink 10 % w|v gelatin, 3 % alginate and 1% w|v super low melt agarose turned out as ideal mixture. The mixture can be deposited pointwise without any post-crosslinking steps necessary. However, if extremely strong gels are desired, the alginate component can be further crosslinked with the addition of Ca^{2+} ions to form stable covalent bonds and enhance the overall structural stability. Sample structures of this ink mixture were stable without shrinking in encapsulation for 10 months.

4.3.2. Bacteria-Ink Composition

In the second group of experiments with the bioprinter, a bacteria-ink was developed to embed bacteria within the bioprinted hydrogel sample. Again a shear-thinning agent and a component that induces fast solidification are necessary. The bioink mixture including gelatin was not suitable as gelatin polymers tend to dissociate randomly if heated to temperatures over 50 °C which would be necessary to sterilize the bacteria-ink before printing.

As there are nearly no natural shear-thinning hydrogels, again alginate was employed with 2% w|v. For fast gelation 2% w|v alginate was used, as this hydrogel is more defined than agar and well developed for bacteria culturing. Higher amounts of alginate tended to solidificate faster, leading to a need for higher extrusion temperatures. The two hydrogel components were dissolved in 0.3 × LB as the salt concentration of higher LB content lead to partial covalent binding of alginate chains and prevented extrusion.

5. 3D-Printed DNA-Functionalized Hydrogels

The custom 3D printing platform introduced in Chapter 4 can be employed to precisely pattern small samples of sizes up to 1 cm with DNA containing bio-ink. Within the samples, reaction - diffusion processes were observed and specific areas could be "adressed" via localized oligonucleotides. The integration of short anchoring strands allowed transient binding of single-stranded DNA and with this control over the diffusion coefficient was achieved.

5.1. Introduction and Motivation

With additive manufacturing tools, 3D shapes and structures can be built nearly freely from a magnitude of printable materials. In contrast to planar lithography, almost arbitrary structures with spatial resolutions down to $\approx$ 100 nm (e.g. laser lithography) in all three dimensions can be built with modern 3D printers. [141] A major goal of additive manufacturing in life science is the artificial construction of living tissue and organs. [6] To reach this goal, cells are allowed to grow into bio-printable scaffolds or are even extruded with materials that mimic the extracellular matrix.[142], [10], [143],[45]

Many of the printable biocompatible material mixtures - *bio-inks* - show excellent shape stability and print fidelity, but lack dynamic behavior. [144], [145] Especially, printed material gradients or dynamic pattern emergence is not yet realized.

On the other hand, with DNA molecules, programmable self-assembly of a wide variety of nanometer-sized shapes was successfully achieved [85], [86], [87]. With the immanent four-valued logic, information storage and processing is possible. More complex molecular machines have been developed with designed DNA hybridization and strand displacement circuits [146] and guide towards future materials including DNA-based mechanical and computational functions. [147]

The application of DNA circuits on a macroscopic level remains challenging although remarkable progress was made with the realization of DNA crystals[148], [149] and larger DNA origami structures. However, the applicability of these materials remains unclear.[150], [151], [152] Different approaches lead to large scale application of DNA hybridization interactions via DNA-mediated colloids [153], [154], [155],[156] where DNA can be programmed to hold nano- and microparticles in a larger crystal-forming lattice [157], [158], [159], or on the creation of amorphous DNA-based hydrogels.

Another possibility to generate macroscopic DNA materials is the integration of these molecules within soft amorphous hydrogels. [160], [161] The hydrogel chains are either based solely on DNA interactions ,[160], [162], [163],[164],[165], [166], [167][168], [169], [170] but also polymer hydrogels modified with DNA molecules to integrate biochemical functionality were developed.[171], [172],[142], [173], [138] Successful integration of DNA molecules to hydrogels led to DNA based shape-memory gels via stimulus-dependent hybridization [174] while inclusion of local hybridization chain reactions allowed shape-morphing swelling and shrinking of the gel sample. [175]

Dynamic pattern formation within DNA-modified hydrogel matrices can be achieved by applying strand displacement principles. For example with the inclusion of a precisely designed DNA circuit, a molecular edge detector marked edges between different gel regions. [44] Another example is the "gellular automata" structure, where DNA strand displacement circuits are localized in 2D gellular arrays. Diffusion is allowed through hydrogel walls and arbitrary patterns were successfully programmed within such arrays. [176]

Until now, only few attempts to combine additive manufacturing techniques such as bioprinting with cell-free circuits were made. Recent approaches include the creation of tissue-like structures from water-in-oil emulsion droplets by bioprinting [177], [8] and millimeter-large 3D-printed DNA colloidal beads, that are stabilized by DNA hybridization interactions.

In this work, DNA-functionalized bioink was printed with a custom refurbished 3D printer to tune diffusibility and allow the development of programmed patterns over time. DNA gives the possibility to design reliable circuits and via a copper click reaction, short single-stranded DNA was localized on super low melt agarose polymer chains. To use this programmable material, a bioink was developed that showed good printability and structural stability while being modified with such short DNA sequences. A three - component bioink mixture was developed, that is fast gelating at room temperature without the need of external crosslinkers to facilitate the printer setup.

As printer, a commercially available Ultimaker Original+ chassis was used and refurbished with custom hardware parts. An external custom syringe pump was developed to drive a sample syringe via hydraulic coupling to drastically reduce the sample volume as no sample filled tubings are necessary. The sample syringe is placed in a temperature - controllable printhead to keep the thermal gelling ink at constant temperature during the print. Additionally a custom software was developed to facilitate the precise and reliable positioning of small hydrogel voxels to predefined positions. The software translates input 2D svg files to single printable layers that are deposited sequentially.

With this setup, experiments were performed to observe the singular reaction-diffusion processes more closely and a self-differentiating structure was evolved. For all prints 20 nucleotide long ssDNA molecules were functionalized to the super low melt agarose component of the bioink. Two different sequences with complete orthogonality were employed to show precise pattern programming if fitting, fluorescently labelled, pre-quenched reporter strands were added. Diffusion coefficients of the free strands within the hydrogel matrix could be observably tuned, if length and complementarity were precisely designed. With the complementarity design, the development of programmed patterns were possible. Experimental results were compared to mathematical simulations to proof the reliability of these results.

Parts of the text and figures in this chapter were already published in Müller et al. *Programming Diffusion and Localization of DNA Signals in 3D-Printed DNA-Functionalized Hydrogels*. [140]

5.2. Results and Discussion

For the depositioning of DNA functionalized hydrogel structures, the bioprinting platform and a custom software tool were developed as explained in detail in Chapter 4. The design goals of the hardware, software and bio-ink are explained briefly in this section. The DNA functionalization is demonstrated and the experimental results are discussed in detail.

5.2.1. Development of Printable DNA-Functionalized Gels

Bioink

The precise deposition of DNA-modified hydrogel samples can be only achieved with printable biocompatible pastes. Such a bio-ink was developed with respect to exhibit high printability, good print fidelity, and also long-term stability. For the mixture only widely available biological hydrogel polymers were considered. With this, biocompatibility can be ensured.

Bioprinting experiments with pure hydrogel polymers at different densities showed in initial experiments to only fulfill one of the mentioned requirements. With a mixture of three natural polymers, good printability and stability, together with the possibility for DNA functionalization has been achieved. The optimized bio-ink mixture consists of 10% gelatin, 3% alginate, and 1% low melting temperature agarose.

This bio-ink can be dissolved at 50 °C and extruded at temperatures of 42 ± 2 °C. Rapid gelation of printed bio-ink voxels lead to solid samples within 5 - 10 sec after depositing at high structural fidelity. To increase the mechanical stability of the bio-ink samples, 100×10^{-3} M $CaCl_2$ solution can be added to covalently crosslink the alginate component of the hydrogel mixture.

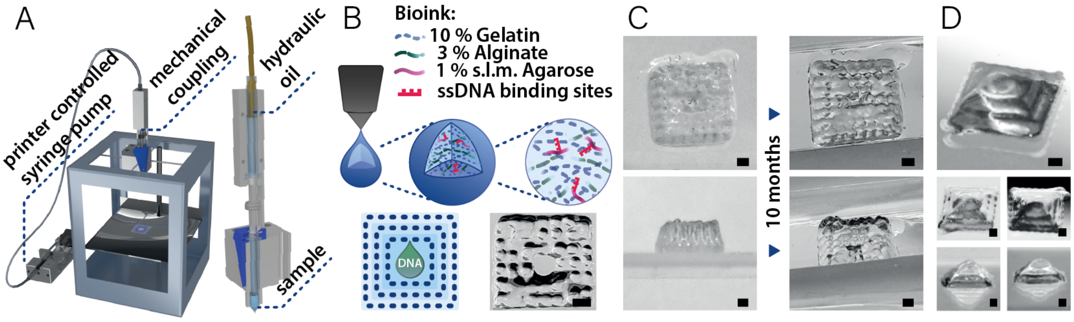

Figure 5.2.1: Overview Bioprinting: *A) Bioprinter setup with an external syringe pump and hydraulic coupling to a syringe containing a small sample volume. The printhead can be equipped with up to four different syringes and functions as a thermoblock. The bioink is held at a constant temperature during extrusion. B) The DNA bioink consists of three different polymer components: gelatin as the main component providing structural stability, alginate as a viscosity enhancer, and super low melt agarose as the DNA-functionalizable component. C) Long-term experiment demonstrating the stability of the bioink and the print: extruded structures remain stable in form and size over 10 months in a sealed container. Scale bar: 1 mm. D) Pyramid structures (I–III) printed with the bioink. Scale bar: 1 mm. Already published in Müller et al.* [140]

Bioprinter

For the realization of DNA-modified 3D structures, the development of an easy-to-use custom bioprinting platform was simultaneously tackled while optimizing a suitable bio-ink mixture. The bioprinter is based on a commercially available 3D FFF printer that was refurbished with custom parts (cf. Figure 5.2.1 A and Section A.3). In contrast to other bioprinters, the major focus was set on a temperature controllable printhead that can be loaded with small sample volumina (0.1 to 1 ml, typically the printer was loaded with 0.5 ml).

The printer is equipped with a mechanical extrusion system that includes an external syringe pump coupled via hydraulics to the sample holder and is controlled directly by the printer board. In contrast to air pressure driven bioprinters, the mechanical setup enables retraction to stop the bio-ink flow and allows the positioning of discrete gel droplets. Best printing results were achieved with nozzles of inner diameters 200 µm (G27) or 150 µm (G30). For more details, see Chapter 4.

Software

In addition to the development of bio-ink and bioprinter, also an adequate software solution was necessary. An open source, Python based software tool was developed that generates machine-readable gcode to precisely route the printer path. The tool asks for an input graphics file (svg) together with a text-based parameter file (see Section A.4). With this, the developed software is independent of CAD tools and software. Typical 3D printing slicing tools create a printable gcode from the 3D CAD model of the desired structure by distributing the model to discrete layers that are routed to optimize the continuous spatial print trajectory. The printer path is selected based on the boundary conditions set by the slicing software and cannot be directly accessed and adjusted. With a voxel based approach, it is possible to place single gel droplets at specific locations that are specified in a vector graphic input file.

In the input file, the 2D vector graphic elements determine the locations of the later printed droplets. The parameter file hands over necessary material and printing parameters, and contains further a record of the printing setup. Printing parameters that can be included are for example extrusion speed (feedrate), nozzle diameter, and print velocity. Further, also correction functions can be included that allow to compensate mechanical deviations or the deformation of deposited droplet spheres.

This approach enables the precise arrangement of single voxels during printing. Specific locations can thus be reached and the printer pathway is defined by the order of the single points in the vector graphics file. Details on the bioprinting platform and software can be found in the Chapter 4 and examples for input and output file are presented in Appendix A.4. The source code (Python 3.0) is available on Github including example files: https://github.com/julia-mueller/bioprinter/.

Gel Structures

Bio-ink samples were printed at 42 °C from the sample syringe and in pico-liter voxels. The singular droplets exhibited rapid solidification upon extrusion on glass substrates at room temperature. Shrinking of the printed hydrogel matrixes occurred due to drying processes within the first 24 h after printing. If the hydrogel samples were sealed in small glass and plastic containers, they showed to sustain in shape and structure for at least 10 months (see Figure 5.2.1).

Printed samples reached heights of up to $\approx$ 10 mm if $\approx$ 20 layers were printed subsequently. Plain areas of 50 mm × 24 mm were patterend with up to two different bio-ink samples (containing either different DNA modifications or being unmodified).

Functionalization of the Bio-Ink with Sequence-Addressable DNA Anchors

The developed bio-ink was "programmed" via modification with short oligonucleotides that work as sequence addressable "anchor" molecules within the hydrogel matrix. Addressability was reached via the modification of the bio-ink super-low-melt agarose component that is functionalized with alkyne groups using PITC, and then coupled to azide-modified oligonucleotides using coppercatalyzed azide-alkyne cycloaddition ("click chemistry"). [138]

With the previous estimation of 0.1 % terminal alkynes per agarose subunit, that corresponds to a 25 × 10^{-6} M alkynes in 1 wt% agarose, [138] bio-ink containing 1% super-low-melt agarose is expected to exhibit a similar functionalization density.

The pore size of printed bio-ink samples was assessed by evaluating the uptake of fluorescently labeled dextran molecules of different molecular sizes. These experiments showed a MWCO between 10 and 50 kDa, that corresponds to a pore diameter in the range of 5 nm - 10 nm (data shown in Appendix A.6.1).

5.2.2. Free Diffusion of DNA Signals in Printed Gel Structures

First, the free diffusion of single-stranded DNA molecules inside of 3D-printed gels was characterized. Fluorescently labeled ssDNA strands were added to a rectangular window (≈ 1.5 mm × 1.5 mm) of a cuboid 10 mm × 10 mm 3D hydrogel print by mixing them to blank bio-ink and applying the mixture to the central location.

For the experiment, two 10 nucleotide (nt) and 20 nt long DNA strands, $\overline{Y}_{10}$ and $\overline{Y}_{20}$, were labeled with Alexa 488 and Alexa 647, respectively (see Figure 5.2.2 A). Diffusion of the strands into the surrounding gel structures was then recorded over a time course of 24 h at room temperature. The diffusion coefficients were estimated from the variance of the corresponding fluorescence intensity profiles at different time points (Figure 5.2.2 B).

For $\overline{Y}_{20}$ a diffusion coefficient D ≈ 12 $\mu m^2\ s^{-1}$ and for $\overline{Y}_{10}$ a correspondingly larger coefficient of D ≈ 43 $\mu m^2\ s^{-1}$ were derived. Simulations of diffusion profiles in cylindrical geometry using these diffusion coefficients showed very good agreement with the experimentally obtained fluorescence profiles (cf. Figure 5.2.2 C; Appendix A.6.4). Comparison with diffusion coefficients shown in literature (130 - 180 $\mu m^2\ s^{-1}$ for 20 - 10 nt long strands [178]) raise the estimation of a strong retardation of diffusion within bio-ink matrices due to small pore sizes. While the small pores decrease diffusibility strongly, it is not completely suppressed as the size of the diffusing DNA molecules is of the same order as the estimated pore size.

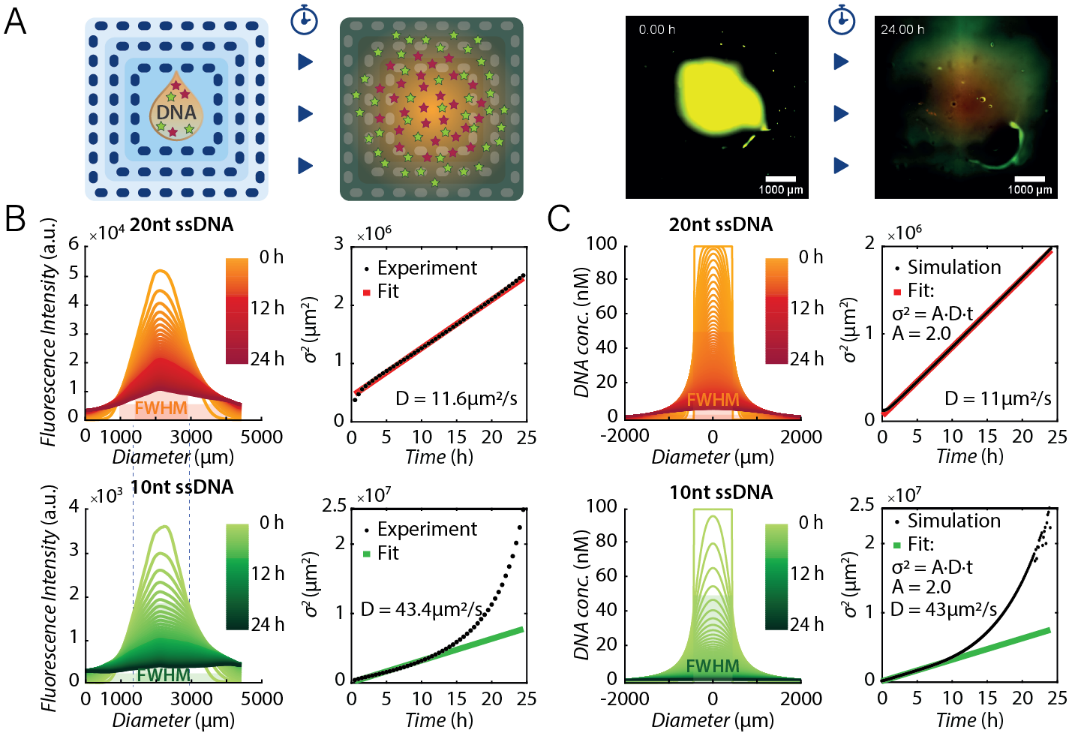

Figure 5.2.2: Diffusion of DNA molecules in a 3D-printed gel structure: *A) Experimental setup: A drop of bioink containing DNA strands of 10 and 20 nt length (fluorescently labeled in Alexa 488 (green) and Alexa 647 (red), respectively) is added to the center of a 3D-printed cuboid test structure and the fluorescence intensities in the green and red channels are monitored over 24 h. B) Fluorescence profiles obtained from rectangular sections through the center of the print are analyzed as a function of time. The variances (σ^2) of Gaussian fits to the experimental data are taken as approximate measures for the mean-squared displacement (MSD) of the diffusing molecules. Linear fits to $\sigma^2 = 2\,Dt$ yield the diffusion coefficients for the 20 and 10 nt long DNA strands (11.6 and 43.4 $\mu m^2\ s^{-1}$). C) Simulated fluorescence profiles obtained from numerical solutions of the diffusion equation in cylindrical geometry using the experimentally obtained diffusion coefficients. The striking deviation of the variance of the 10 nt long strands from the linear fit after $\approx$ 10 h is reproduced in the simulation and results from DNA strands reaching the boundaries of the printed structure. Adapted from Müller et al.* [140]

5.2.3. Toehold-Mediated Strand Displacement and Localization of DNA in the Gel

With these experiments, the setup to position singular voxels of DNA-labeled bioink to pre-defined locations has been shown to function in the desired manner. In further experiments, simple DNA-circuits were introduced to the hydrogel structures utilizing the sequence-programmable hybridization interactions of this molecules. Localized DNA sequences clicked to agarose polymers can be assumed immobile in the printed hydrogel structures and interact with freely diffusing DNA molecules depending on the amount of strand complementarity. The strands for all experiments were designed in such a way, that free DNA strands were captured by localized complementary strands temporarily or permanently, and to perform DNA strand displacement reactions if applicable. This design lead to the sequence-based control of diffusion and to sequence-directed molecular sorting.

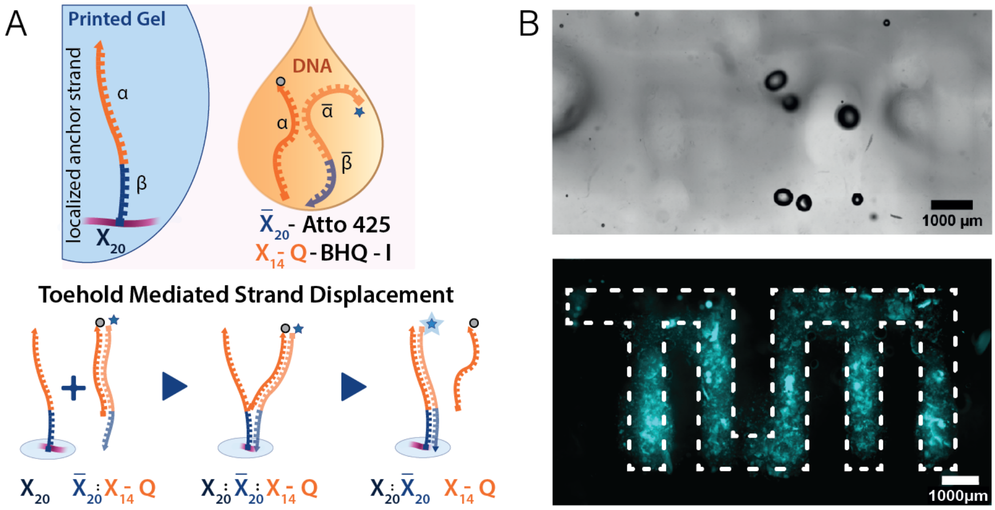

Figure 5.2.3: Spatially organized toehold-mediated strand displacement reactions inside a printed gel structure: *A) Experimental scheme: The 20 nt long DNA anchor strands* X_{20} *are covalently immobilized in the printed gel. As diffusing signal molecules, DNA complexes composed of fluorescently labeled signal strands* $\overline{X}_{20}$ *hybridized to quencher-labeled strands X14-Q are added to the gel. The* $\overline{X}_{20}$:X_{14}*-Q complexes have a 6 nt long ssDNA toehold, which facilitates TMSD of the quencher by the anchor strands. As a result, signal strands* $\overline{X}_{20}$ *light up as soon as they are immobilized in the gel. B) Top: Microscopy image of a 3D-printed test structure with embedded anchor strand pattern (bottom view). Distinct areas are successively printed with unmodified and anchor modified bioink, respectively. Bottom: DNA signal complexes are added to the gel structure and allowed to freely diffuse through the gel. As a result, a fluorescent pattern (TUM University logo) emerges in the anchor modified regions (shown is an average image of four individual prints). Adapted from Müller et al.* [140]

For a straightforward experiment, the shape of the TUM Logo was printed with bio-ink containing localized anchoring strands embedded into a frame of unmodified bio-ink in sequential printing processes. In Figure 5.2.3 A the localized DNA circuit is depicted: Within the gel matrix, DNA "anchor" strands X_{20} are programmed to target the toehold area of freely diffusing double-stranded DNA constructs ("signal complexes"). The duplexes consist of a 20 nt fluorescently labeled DNA reporter $\overline{X}_{20}$ and a 14 nt complementary strand modified with a quencher complex, X_{14}-Q, exposing a 6 nt long single-stranded toehold. If the signal complexes are free, the fluorescence of the constructs remains completely quenched, showing only low background signal. If signal complexes are in close proximity to anchor strands, TMSD reactions can start and the quencher molecule unbinds while the reporter bind permanently to the anchors leading to sequence-specific immobilization of the fluorescent signals within the gel print (Figure 5.2.3 B).

For the TUM logo experiment, DNA signal complexes were added in bulk solution centrally on top of the printed sample, after a thin layer of unmodified bio-ink was applied to the whole structure for sealing purposes. If signal complexes were captured by the anchor strands, quencher-DNA was unbound by TMSD interactions and fluorescence increased locally. As central areas are faster reached by the freely diffusing signal complexes, a slightly inhomogeneous increase in fluorescence intensity within the gel was observed, that lead to lower fluorescence at outer voxels of the letters T and M compared to central areas of the logo.

5.2.4. Sorting DNA Signals to Distinct Addresses

The DNA bioprinting setup is programmed to deposit bio-ink voxels that can be functionalized with different DNA anchor strands at specific locations. With such a setup, more elaborate immobilization patterns can be printed with sequence-programmable DNA anchor strands localized within the hydrogel voxels.

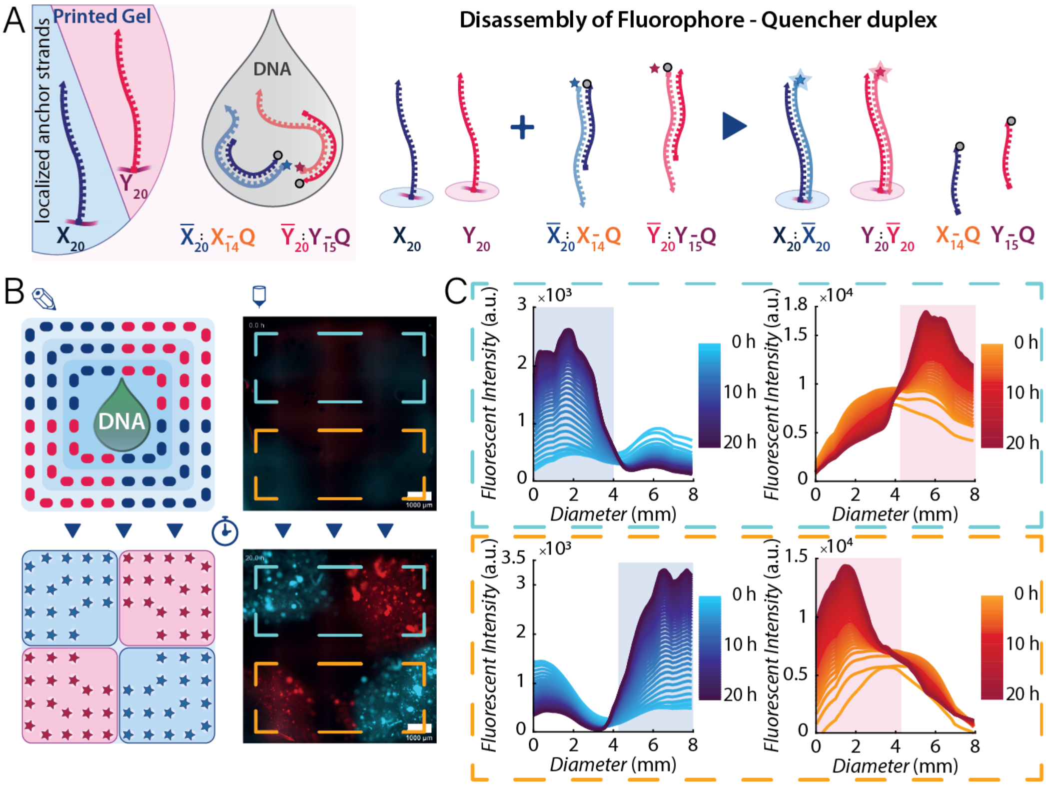

Figure 5.2.4: Sorting of DNA molecules to differently addressed gel regions: *A) Experimental scheme similar to Figure 5.2.3, but with two orthogonal anchor sequences (X_{20} and Y_{20}), and two differently labeled signal complexes $\overline{X}_{20}$:X_{14} and $\overline{Y}_{20}$:Y_{15}, resulting in a localization of the labeled strands to different regions. B) Differently modified bioinks were printed in a 2×2 checkerboard pattern. Quenched DNA signal complexes were added to the print and allowed to diffuse into the gel over 20 h. C) Fluorescence profiles corresponding to the gel regions highlighted with the blue and orange boxes, showing sequence-programmed molecular sorting of the DNA signals over time. Adapted from Müller et al.* [140]

Exemplary a 2×2 cuboid structure was printed from two orthogonal ssDNA anchor strands in a miniature checkerboard structure: every corner contained one of the orthogonal anchor strands X_{20} and Y_{20}. Similar to the experimental setup for the TUM logo (shown in Figure 5.2.3), the structure was printed and sealed with a thin layer of unmodified bio-ink. Subsequently, two orthogonal fluorophore-quencher complexes ($\overline{X}_{20}$:$X_{14} - Q$ and $\overline{Y}_{20}$:Y_{14}) were applied in bulk solution on top of the printed gel structure. Over the course of 10 h, the DNA solution unmixed and the DNA signals were sorted to their respective addresses (Figure 5.2.4).

5.2.5. Sequence-Dependent Differential Diffusion

For the generation of dynamic applications, such as spatio - temporal patterns via reaction-diffusion mechanisms, permanent localization alone is insufficient. Here, tunability of diffusion coefficients is necessary to obtain more control over the reaction dynamics.

Mechanical solutions include the change of gel density, pore size, or viscosity, which are all constrained by the printability of the hydrogel. However, changing the mechanical parameters influence diffusion coefficients on a global level and cannot be adjusted for specific DNA strands. A more elaborate option is the retardation of diffusing DNA strands by transient hybridization to immobile DNA anchor strands. With the precise design of hybridization interactions, travel times through the hydrogel can be controlled for all ssDNA molecules. [44]

In the experimental setup, gel-immobilized X_{20} anchor strands were deposited with the bioprinter in the established cuboid structure. As free ssDNA strands, 10 nt long fluorescently labeled DNA strands with complementary subsequences of 4, 6, 8, and 10 nt to the anchor strand were applied as equimolar mixture in bio-ink to the center of the printed structures ($\overline{X}_{10}$-Alexa 647, $\overline{X}_{8}$+(dA)$_2$-Alexa 488,$\overline{X}_{6}$+(dA)$_4$-Atto 425, $\overline{X}_{4}$+(dA)$_6$6-TAMRA).

Diffusion was allowed for 20 h while fluorescent intensities were recorded with in the microscope. As can be seen in Figure 5.2.5, larger sequence complementarity indeed reduced the diffusability due to longer transient hybridization of the free ssDNA molecules. This lead to the development of a dynamic pattern (see also Figure A.6.3). Shorter complementary regions lead to larger off-rates of the bound strands and vice versa, therefore, $\overline{X}_{10}$-Alexa 647 with the highest complementarity showed a very low effective diffusion coefficient of D ≈ 1.4 µm^2 s^{-1}. The diffusion coefficients of the other strands increase with decreasing complementarity to ≈ 30 µm^2 s^{-1} for $\overline{X}_{8}$ strands over ≈ 40 µm^2 s^{-1} for $\overline{X}_{6}$ strands to ≈ 120 µm^2 s^{-1} for $\overline{X}_{4}$ strands that can bind with a maximum of four basepairs.

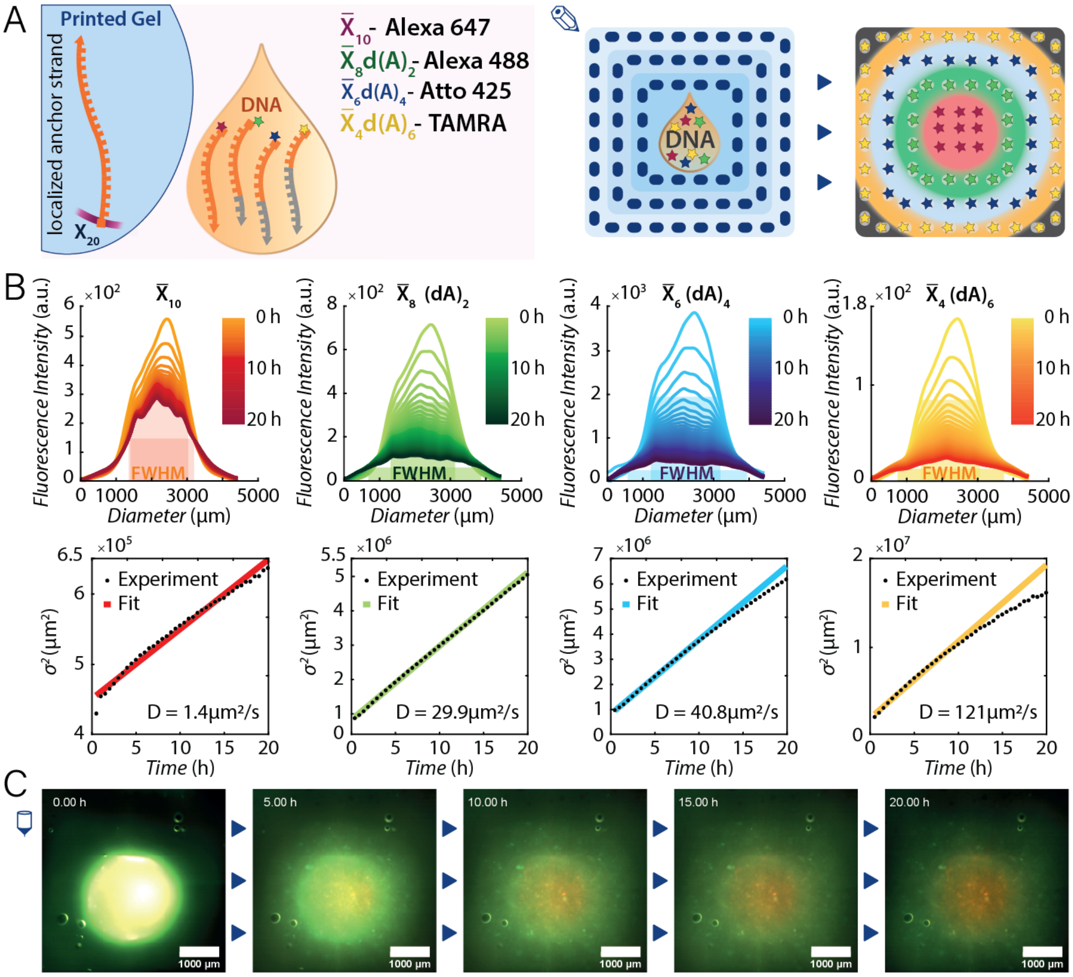

Figure 5.2.5: Sequence-tunable diffusion coefficients: *A) In order to study how transient hybridization of DNA sequences to immobilized X_{20} anchor strands affects diffusion, a mixture of fluorescently labeled DNA strands with partial complementarity to the anchors was added in the center of a printed test structure. As indicated, the strands with shorter complementarity regions were expected to diffuse faster than those with longer regions, which is indeed observed in the experiments. B) Fluorescence profiles for the different DNA strands for different times and variation of the variance as a function of time. As expected, higher binding affinity leads to a lower diffusion coefficient and a more localized distribution of the respective DNA strands. In (C), microscopy images of the gel print for the indicated time points are shown in a superposition of all fluorescence channels (cf. Figure A.6.3 in the Appendix for the separate fluorescence channels). Adapted from Müller et al.* [140]

With this experiment, the tunability of the diffusion coefficient by sequence design was shown to span almost two orders of magnitude. It has to be mentioned that the diffusion coefficient for $\overline{X}_4$ is larger than that of the freely diffusing 10 nt strand in Figure 5.2.2, which might be due to potential secondary structure but also due to slight variances in the hydrogel density of single printed structure.

With the regular short binding interactions, the strands in Figure 5.2.5 have a considerably lower free energy in the gel than outside, leading to confinement in this area in contrast to the free diffusion experiments shown in Figure 5.2.2. This leads to low concentration of DNA molecules at the gel boundaries (Figure 5.2.5 B) and causes the variance for the faster diffusing species to saturate at a value corresponding to the gel dimensions rather than to diverge as in Figure 5.2.2.

5.2.6. TMSD-Mediated Pattern Formation

In addition to permanent and transient binding experiments, also toehold-mediated strand displacement processes can be integrated to the localized DNA circuits within the hydrogel. Similar to the experiments described in the anchor localization experiments (Figures 5.2.3 and 5.2.4), ssDNA strands that exhibit a longer sequence of complementary nucleotides can unbind shorter complexes by a TMSD mechanism. With a specifically designed DNA circuit, simple pattern formation processes can be integrated to DNA modified hydrogel samples.

Figure 5.2.6 shows the pattern formation of a ring like structure from an equimolar mixture of free 10 and 20 nt long signal strands ($\overline{X}_{10}$ labeled with Alexa 647 and $\overline{X}_{20}$ with Atto 425 fluorophores) applied to the central area of a cuboid structure with X_{20} anchor strands. After the reporter strands are applied to the hydrogel sample, the distribution within the bioink is monitored over 20 h.

Already after 6 h, a ring of $\overline{X}_{10}$ - Alexa 647 DNA molecules establishes around the center. In contrast to the experiments based solely on temporary binding, the shorter DNA strands not only move faster into the gel, but are further displaced by longer $\overline{X}_{20}$ - Atto 425 strands with stringer binding affinity, indicated by a lack of fluorescent Alexa 647 at the center of the structure. In contrast to the shorter $\overline{X}_{10}$ strands, the $\overline{X}_{20}$ strands barely diffuse into the gel, but are captured close to the center of the structure. This behavior is "demixing" the two species from its bulk solution and a simple sequence-programmed reaction-diffusion pattern is formed.

To support the assumption of demixing by binding affinity, for the next experiment, two 20 nt long DNA strands $\overline{X}_{20}$ and $\overline{X}_{10}$ + (dA)$_{10}$ of expectable similar diffusion coefficients were employed. Again, after $\approx$ 6 h a ring of fluorescently labeled DNA emerged around the center of the cuboid structure (Figure 5.2.6 C). While the $\overline{X}_{10}$ + (dA)$_{10}$ strands diffuse into the gel more slowly than the comparable $\overline{X}_{10}$ strands (cf. Figure 5.2.6 B), again the $\overline{X}_{20}$ strands displayed nearly no diffusion and barely entered the printed gel. With this, again a ring structure established over time, with increased contrast compared to the first experiment. Simple reaction-diffusion models incorporating hybridization and TMSD, reproduced these experimentally observed patterns very well (see Figures A.6.4 and A.6.5).

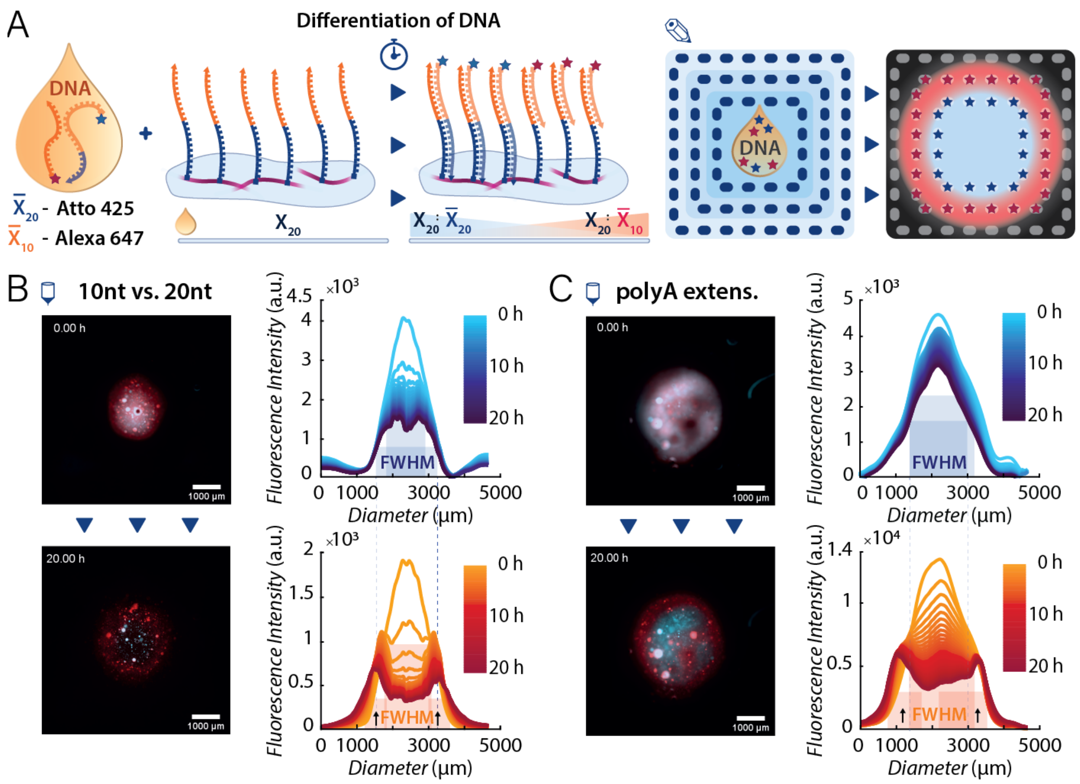

Figure 5.2.6: TMSD-based pattern formation in 3D-printed gels: *A) Again, X_{20} anchor strands are immobilized in the printed gel. DNA strands with different lengths of complementarity to X_{20} are then applied to the center of the gel print. Shorter, less complementary $\overline{X}_{10}$ strands are expected to diffuse into the gel faster than $\overline{X}_{20}$ strands. Furthermore, $\overline{X}_{20}$ are expected to displace anchor-bound $\overline{X}_{10}$ via TMSD, resulting in different gradients for $\overline{X}_{20}$ and $\overline{X}_{10}$ strands throughout the gel. B) Microscopy images (bottom view) of reaction-diffusion patterns generated by $\overline{X}_{10}$ and $\overline{X}_{20}$ strands in a 3D-printed hydrogel structure with homogeneously attached X_{20} anchors and corresponding fluorescence profiles for different time points. Due to the larger diffusion coefficient and reduced affinity to the anchor, a circular ring structure is created by $\overline{X}_{10}$-Alexa647 (red) after a few hours. C) The same experiment as in (B) performed with two DNA signals of the same length ($\overline{X}_{20}$ and $\overline{X}_{10}$ + (dA)$_{10}$), but with different binding affinities to the anchors. The diffusion of the $\overline{X}_{10}$ + (dA)$_{10}$ strands into the gel is reduced compared to the $\overline{X}_{10}$ strands of (B), and thus the ring is more localized to the center. In consequence, diffusion of $\overline{X}_{20}$ into the gel is reduced, resulting in a more sharply defined localization pattern. Adapted from Müller et al.* [140]

5.3. Conclusion and Outlook

In this part of the work, the developed low cost bioprinter was employed to pattern 3D samples of DNA modified bio-ink with a point-wise positioning. This precise positioning facilitates the creation of DNA-labeled gel structures of small hydrogel voxels. The setup was optimized for printing bio-ink, a DNA functionalizable hydrogel mixture of the natural polymers gelatin, alginate and super-low-melt agarose.

This bio-ink can be printed at relatively low temperatures (42 °C) and exhibits rapid solidification after deposition at room temperature. Functionalization of the bio-ink is possible via a click-chemistry reaction of azide-DNA to the agarose component of the mixture.

The DNA functionalized bio-ink can be used to create larger hydrogel structures that can capture and immobilize DNA molecules, but also larger molecules that are modified with short DNA strands. With this, a hydrogel exhibiting a variety of anchoring sequences can be used to demix and immobilize molecules via their "addresses". This approach to combine bioprinting with programmable molecular circuits allows to enlarge the application area of DNA nanotechnology at larger length scales up to several 100 µm.

Additionally, this work showed not only the sequence-programmable immobilization of DNA molecules, but with the clicked anchor strands also demixing, localization, and diffusion control of free ssDNA over at least two orders of magnitude was achieved. The development of dynamic diffusion patterns were observed and could be reproduced in simulations.

In future applications, self-differentiating amorphous biomaterials that can be precisely structured and programmed could be possible. Further, DNA-functionalized scaffold structures to capture and localize DNA-labeled molecules at specific regions while being fully biocompatible are thinkable. With the development of more elaborate reaction-diffusion systems and with the application of enzymatic processes, more possibilities to employ 3D bioprinting for the generation of complex patterns in soft structures come into reach.

6. 3D-Printed Hydrogels Containing Living *E. coli* Bacteria

With the successful integration of a programmable DNA circuit to extrude bioink structures, the next aim was to integrate living bacterial circuits during the printing process for a precise deposition within the printed matrix. *E. coli* bacteria were selected as model system for integration, as this bacteria are well characterized, their behavior described, and they show the widest use of all bacteria strains in synthetic biology.

6.1. Introduction and Motivation

Over the past years, additive manufacturing of biocompatible scaffold structures for the integration of mammalian and human cells became popular among biomedical researchers. The integration of cells at specific locations within 3D printed hydrogel matrices enabled the generation of spatially differentiated cell cultures and models of living tissues[45], [14].

In this part of the thesis, the comparably less developed integration of bacterial systems within artificial amorphous structures was targeted. Until now, development was mainly focused on the handling of eukaryotic cells in 3D printed structures but not on prokaryotic cells. However, the engineering of spatially organized bacterial communities could ultimately lead to the realization of living, bacteria-based biomaterials [45], [143], [179], [180].

Study and control of bacterial interactions with their environment, other cells, or communities can be facilitated if well-defined and highly reproducible experimental conditions are set for example within bioprinted structures. For applications in synthetic biology, which involve spatially distributed synthetic cell-cell communication and division of labor between different types of genetically engineered bacteria, such approaches are of specific interest. Precise arrangement of engineered bacteria in 3D matrices allows the control of initial and boundary conditions. The spatial evolution of localized genetically programmed dynamic systems in the presence of designable and controllable constraints can thus be observed and studied. Especially the ability to precisely pattern a three-dimensional amorphous structure with bacteria and the control of external stimuli (e.g. medium, inducer molecules, local gas supply) allows the generation of a large variety of hypothetical biological niches. Natural environments are additionally seldom completely homogeneous, but environmental parameters such as gas supply, nutrients, or stress factors, influence larger bacterial communities. This in turn can lead to noticeable gradients over thicker biofilm structures, which can also provide positional information [181] and therefore facilitate autonomous differentiation within the printed structures.

Functional biomaterials with biosensing [182],[183] or biocatalytic capabilities [184] have been previously realized by immobilizing bacteria within various hydrogel-based support matrices, which in some cases also allowed a rough positioning of the bacteria in 3D. At a more macroscopic scale, bacteria laden extrusion-printed hydrogel biofilms were generated for the degradation of pollutants, [31] the realization of self-healing structures, [143] and even bacterial electrodes. [185]

3D bioprinting techniques were utilized more recently to achieve better spatial control over bacteria-laden structures via a variety of different printing approaches: With laser-based lithography, bacterial cells were enclosed in bulk within pico-liter-sized gel compartments. This confinement enabled the observation of cell-cell interactions and bacterial signaling between small populations. [186] Bioink from Pluronic F127 diacrylate containing bacteria was extruded with a FFF printer and photo-crosslinked by UV curing to enforce structural stability of printed bacteria-based biosensors.. [46] Again with a FFF printing approach, [45] agarose bioink was mixed to *B. subtilis* that sporulated at the necessarily high printing temperatures for agarose (70 °C). Upon cooling to 37 °C the agarose-ink solidified and the spores started new bacterial colonies during subsequent incubation. While this printing approach is successful for bacteria strains that sporulate, the high temperatures would be detrimental if living bacteria should tolerate the printing procedure. An often used alternative to circumvent high printing temperatures includes alginate-based inks. With these bacterial, e.g. *E. coli* , biofilms with few layers can be printed that solidify upon contact with a calcium-containing substrate[47], [58].

Until now, the majority of bacteria-printing approaches result in homogeneous two-dimensional bacteria-laden structures with only a single bacterial clone. Further, most bacteria-laden bioprintable inks require a curing step after extrusion either using a chemical crosslinker [143], [185], [47], [58] or via photo-crosslinking [186], [46]. All approaches have in common that printability and biocompatibility need to be carefully adjusted to find printable inks and materials that are not detrimental to cell viability.

Hydrogel mixtures to extrude and immobilize bacteria with a bioprinter need to be optimized for printing at low temperatures to ensure cell viability and prevent sporulation. [31] The amount of radicals within the hydrogel structures throughout the crosslinking process should be minimized to reduce stress for the enclosed bacteria. All previously discussed strategies were not capable of printing live *E.*

coli bacteria into voxel-defined 3D hydrogel structures, and were not used to execute engineered genetic functions within the used bacteria. However, especially the integration of *E. coli* to artificial amorphous structures is of interest for synthetic biology as *E. coli* is the most thoroughly analyzed model organism with a broad genetic toolbox already developed.

In this part of the thesis, specifically the integration of genetically modified *E. coli* within almost arbitrary 3D hydrogel structures with a gentle voxel-based bioprinting approach was addressed. After intensive screening for an ideal bacteria-ink composition, a mixture of the natural hydrogels alginate and agarose was found, that exhibits mild printing conditions at a comparably low extrusion temperature of 42 °C. The mixture solidifies within seconds if extruded at room temperature, without the need for chemical crosslinking. Addition of slowly decaying molecule calcium-peroxide (CaO_2, CPO) and the enzyme catalase [188] [189] [190] to the bioink ensured a continuous supply of the embedded bacteria with oxygen over a time course of at least 24 hours. With the integration of these components, good growth conditions and the production of fluorescent protein as an optical readout within the hydrogel structures were established. Sufficient oxygen supply is crucial for the maturation of fluorescent proteins such as GFP and red fluorescent protein (RFP) and one of the issues known from previous projects incorporating bacteria within hydrogels. [45] Embedding an oxygen suppliant facilitated proof of cellular growth, observation of cell viability, and localization within the printed hydrogel structures over longer time intervals. Exemplary, in Figure 6.1.1 a clear increase in RFP produced by embedded *E. coli* cells can be seen after incubation for 24 h.

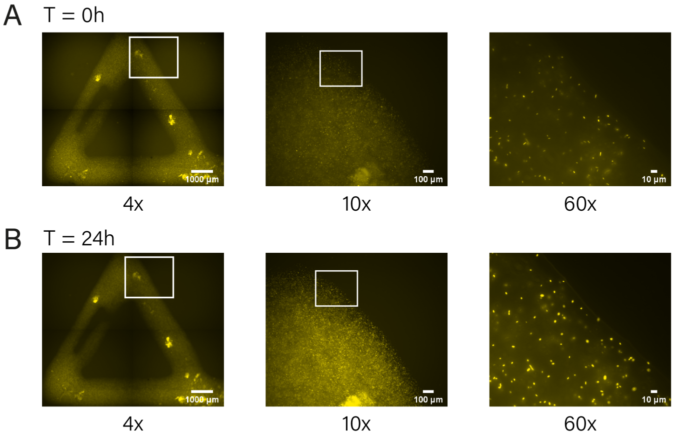

Figure 6.1.1: Immobilization within a Hydrogel Matrix: *E. coli bacteria producing mRFP constitutively were printed with bac-ink and sealed after print. A) The top part of the triangular shape was imaged directly after printing with 4x, 10x and 60x magnification. B) After 24h of incubation at 37°C, the same area was imaged again. The edges of the printed shape were largely preserved during incubation and singular bacteria remained on their respective locations. Adapted from Müller et al.* [191]

While precise localization of bacteria can be observed best in fluorescent imaging, the bacterial growth itself is monitored in brightfield as during growth and cell division the fluorescent proteins are not shared evenly between the successor cells. Cell growth was thus assessed by averaging over multiple bacterial colonies in separately printed structures that were incubated for different time intervals (1 h steps for up to 12 hours) after protein maturation was allowed at 4 °C for at least 24 hours. With this, the cell division within the printed hydrogel scaffold could be observed to occur every 50 - 60 min.

Printed bacterial structures reached sizes up to 24 mm $\times$ 36 mm in x-y plane and up to 10 mm in z-direction. With sequential printing, three different bacteria clones were printed to the same plane and showed a reproducible print fidelity of 50 µm to 500 µm with voxels of $\approx$ 70 µm diameter. Dual extrusion printing further allowed to print three-dimensional structures with a singular or two separated bacteria containing layers.

Within this work, bacterial growth, protein maturation and cell-cell interactions in the gel matrix were studied closely. For induction of fluorescent protein production after the printing process, Tet and Lac operons with the respective inducer molecules aTc and IPTG were employed. For the inducer molecule aTc, diffusion studies were conducted and compared to mathematical models.

In general, the ability to bioprint bacterial communities opens up the possibility to precisely define the boundary and initial conditions of dynamical systems composed of bacteria with genetically programmed interactions [192], [193], [194], [195], [196]. This potentially allows to combine the advantages of top-down patterning with self-organized spatio-temporal differentiation for the realization of living biomaterials.

To demonstrate this capability, a bacteria-based quorum sensing communication system was deposited at defined locations in a printed scaffold structure. Bacterial communication between engineered sender and receiver bacteria was observed by fluorescent readout. The sender bacteria produce the signal molecule AHL which diffuses through the hydrogel sample until individual receiver cells are reached. Upon uptake of AHL, the receiver cells can activate a pLux promotor and GFP signal is generated.

Further it was shown that bioink containing non-motile bacteria can be used to create living boundaries that cannot be crossed by chemotactic bacteria. With this, bacterial chemotaxis was guided on the surface of soft agar with such printed bacterial boundaries. While bacteria-ink without the addition of bacteria showed no influence on the path of chemotactic bacteria, the edges of precisely positioned bacteria held back migrating cells for at least 12 hours.

With this work, the spatial organization of living *E. coli* bacteria equipped with genetically modified gene circuits and the validation of cellular growth and gene expression within printed three-dimensional structures was achieved. With extremely low stress on the bacteria, local oxygen supply, and the possibility to combine several bacteria-laden bioinks, a convenient platform for the close study of cellular processes within bacteria biofilms was developed. In contrast to previous publications, high levels of fluorescent proteins produced by immobilized bacteria - which were induced after the printing process - were observed. High spatial control over the printed structures was achieved via a point-wise deposition mechanism and the implementation of a real dual-extrusion system.

Parts of the text and figures in this chapter were already published in Müller et al. *Bacterial growth, communication and guided chemotaxis in 3D bioprinted hydrogel environments* [191]

6.2. Results and Discussion

Similar to the development of the bio-ink printing setup in Chapter 5, a number of challenges need to be considered to establish a reliable and reproducible bacteria printing setup. First and of highest importance is the design of a mild printing process to induce only minimal stress on the bacteria. Especially low printing temperatures, low pressure and independence of radical crosslinkers are favorable printing conditions. Second, the hydrogel composition needs to be non-toxic, exhibit good printability, rapid solidification and high structural fidelity, similar to the bio-ink. Third, the hydrogel mixture needs to be sterilized prior to printing, to reduce contamination. This requirement hinders the addition of gelatin as solidification agent and prevents the use of bio-ink, as gelatin cannot withstand autoclave temperatures. Lastly, after extrusion, the printed bacterial gels have to stay in solid phase at incubation temperature (37 °C) for recovery and growth of the embedded bacteria. If the printed structures cannot be incubated at high humid conditions, the structures are best embedded in a supporting environment that prevents shrinking, drying, or depletion of nutrients.

6.2.1. Encapsulation of Living *E. coli* Bacteria in Printable Hydrogel Matrices

For the custom-built bioprinter [140] (Chapter 4 and Figure 6.2.2 A) a printable hydrogel composition that fulfills the stated requirements was developed. The printable bacteria-ink necessarily needs to be compatible with a moderate temperature printing process in which the highest continuously applied temperature does not exceed approx 42 °C to reduce cell death (cf. Appendix 6.2.1) Furthermore it must enable fast post-print solidification by cooling to room temperature without the need for a crosslinking step. *E. coli* bacteria show strongly reduced cell growth after being exposed to elevated temperatures during growth [197], [198], even if some strains sustain temperatures of up to 48.5 °C. [199] Higher temperatures generally result in bacterial cell death as *E. coli* are non-spore-forming bacteria and cannot be printed via the sporulation at elevated temperatures, in contrast to e.g. *B.subtilis*. [45]

After screening a variety of natural hydrogels, a mixture of 2 % (w|v) agarose and 2 % (w|v) alginate meet all requirements for a suitable bacteria-ink (see also Section 4.3). Both hydrogels are shown to be compatible with cell culture conditions and are at a 2 % - 2 % mixture compatible with printing at 42 °C. [74] Again, alginate is employed as a viscosity enhancer, while agarose provides fast solidification after extrusion and supports a good spatial resolution.

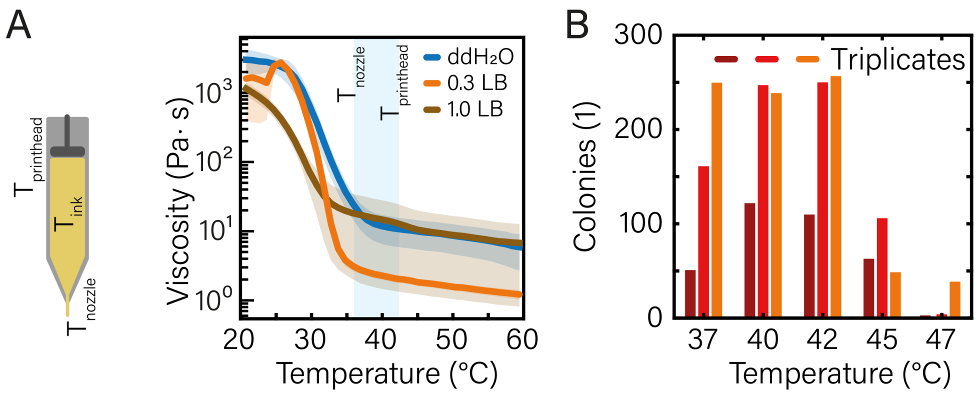

Figure 6.2.1: Viscosity of bacteria ink: *A) Viscosity of bacteria ink prepared in either pure ddH$_2$O , 0.3 × LB, or 1 × x LB medium. The region of interest is the temperature range between nozzle (≈ 36 °C) and printhead (≈ 42 °C) temperature. Fast solidification at all temperatures below the nozzle temperature is beneficial while solidification during the print leads to clogging. For bacteria ink in 1.0 × LB medium the viscosity is significantly lower at room temperature than for ddH$_2$O or up to 0.3 × LB medium in ddH$_2$O . This leads to low printability and less stability of extruded structures. B) Bacterial growth after short 2 min heat shock at 60 °C and longer 30 min heat shock at a variety of possible printing temperatures (37 °C - 47 °C). Up to printing temperatures of 42 °C the bacterial growth is similar or better than for the incubation temperature (37 °C). Printing temperatures higher than 47 °C appear to be not compatible with survival of the cells. These temperatures are consistent with earlier findings for heat stressed E. coli bacteria. Adapted from Müller et al.* [191]

The assumption of the strong influence of LB content on the printability was validated with viscosity measurements in a bulk rheometer. The experiments indicate that the LB content change the temperature-dependent viscosity of the bacteria-ink mixture, which shows a steep decline in the temperature range from 20 - 35 °C (see Figure 6.2.1).

For a reduction in osmotic stress, the bacteria-ink was prepared with 0.3 × LB medium. Higher LB concentrations led to pre-crosslinking of the alginate due to calcium and other bivalent ions in the medium and a subsequent clogging of the printing nozzle. Additionally, the uncontrolled crosslinking leads to a larger variability in viscosity at printing temperature, and lower viscosities at room temperature (Appendix Figure A.8.1). The strong temperature dependence of the bacteria-ink viscosity is exploited to achieve rapid solidification after extrusion, but raises the need to enclose the gel in a temperature controlled printhead.

Heat shock experiments were conducted with *E. coli* bacteria cultures. For this, overnight cultures were prepared and diluted 1:100 after incubation for 16 h and grown to OD 0.6. Then, heat shock was induced on the cells in bulk in a thermocycler mimicking the temperature impact during printing: a short 2 min intense heat shock at 60 °C, representing the mixing to preheated bacteria-ink, is followed by a 30 min exposure to elevated temperatures from 37 °C to 47 °C to screen possible printing temperatures. The cultures are plated after the heat shock and colony forming units (CFU) were counted. As shown in Figure 6.2.1 B, printing temperatures up to 42 °C only show slightly lower cell viability, while temperatures of 45 °C and above, are not advisable.

With this, the printhead is kept at 42 °C throughout the print, keeping the temperature of the bacteria-ink to 42 ± 1.5 °C within the sample syringe. In comparison to the inner temperature of the printhead, the tip of the nozzle is continuously cooled due to its exposition to room temperature and the gel in this area is exposed to 36 ± 1.5 °C during the printing procedure.

With a final bacteria-ink composition of 2% agarose and 2% alginate in 0.3 × LB medium, *E. coli* -laden hydrogel structures up to 30 mm in x-y and 10 mm in z dimension could be reliably printed. Larger structures are in theory printable, but limited by longer printing times that come with drying of extruded structures during the ongoing printing process.

Expression and maturation of fluorescent proteins inside the printed hydrogel structures was supported by an addition of the oxygen-generating system composed of calcium peroxide and catalase. This system is explained in detail in Section 6.2.3.

6.2.2. Bioprinting of Living Bacteria in 2D and 3D

The bacteria-ink was employed in first experiments to assess the printing performance, the spatial positioning precision, and the degree of immobilization. Triangular structures with bacteria-containing edges are imaged with 4 ×, 10 × and 60 × magnification at a single position directly after printing and after 24h of incubation and shown in Figure 6.1.1. After one day of incubation the fluorescence measurements indicate that printed bacteria remain in close proximity to their initial positions over this time interval. The overall fluorescence signal increases due to cell growth and protein production of mRFP.

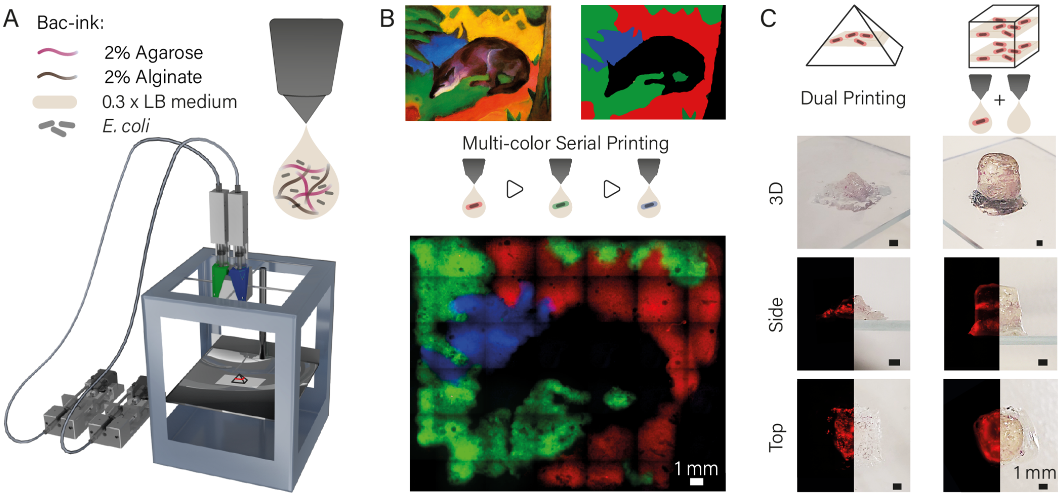

Figure 6.2.2: Overview Bacteria Printing: *A) Schematic image of the custom-built dual extrusion gel printer* [140] *refined for bacteria printing. Two printer driven syringe pumps were placed next to the printer and hydraulically connected to a print head holding two syringes filled with bacteria-ink. The print head was heated to 42 °C, and the gel quickly solidified upon cooling to room temperature upon deposition on a object slide on the base plate. B) Three E. coli DH5α bacteria clones expressing either mRFP, mVenus, or mTurquoise were printed sequentially into 2D hydrogel layers. The structure was incubated over night and high levels of fluorescent protein render a representation of the painting "Blue Fox". With this the high printing precision and reproducibility of bacteria-ink deposition at specific locations is demonstrated. C) The new dual extrusion mechanism enables to structure three-dimensional gel objects with blank and bacteria-ink, that contain single layers with confined bacteria. Images of the 3D structures (top and side view) were taken using a Canon 80D camera, fluorescence images were obtained with a Nikon Ti2-E microscope from the bottom and from slices of the structures. Adapted from Müller et al.* [191]

For the demonstration of spatial resolution and reproducibility of the bioprinting procedure, another 2D structure was designed with three bacteria clones that are printed sequentially to the same plane. To distinguish the singular clones, bacteria were selected that are genetically modified to constitutively express the fluorescent proteins mVenus (green), mTurquoise (cyan), and mRFP (red) that can be observed in orthogonal channels. The printing pattern was designed to resemble a simplified, three-colored version of the famous artwork "Blue Fox" by Munich expressionist Franz Marc (see Figure 6.2.2 B). After printing all three bacterial clones, incubation was allowed for 24 h at 37°C. The desired pattern is clearly visible in all three fluorescent channels and overlapping signals from two fluorescence channels were found only in the border regions between subsequent printed layers. Overlaps exhibited widths between 50-500 µm, indicating a high alignment accuracy of sequential prints.

Extending the patterning of hydrogel structures to 3D is achievable with the integration of a second extruder and a dual-extrusion printing protocol. With the integration of the dual-extrusion capability, 3D structures with one (pyramid structure) or two (cuboid structure) bacterial bands were fabricated within a single print job (Figure 6.2.2 C). For the main structure, "blank" bacteria-ink was loaded to the first sample syringe, for the bacteria bands, mRFP producing bacteria were prepared and loaded into a separate glass syringe. The two syringes were loaded to the same printhead and the two gels were printed alternatingly to form 3D shapes with a base area of 6 mm x 6 mm each and a height of 5mm (pyramid) and 10mm (cuboid), respectively. Bacterial bands consisted of two layers printed with bacteria containing ink directly onto "blank" ink.

Printed 3D structures were sealed in chambers emerged in LB medium containing 10% Pluronic F127 to preserve structural integrity and incubated at 37 °C. After 24h of incubation, the printed structures were released from the Pluronic encapsulation by dissolving this inversely thermal gelating hydrogel by 15 min storage at 4°C. The overall 3D structures remained stable in shape without considerable shrinking or swelling. In all prints, bacterial bands showed high RFP production and are clearly colored red. Precise deposition of the bacterial layers within the complete gel structure was observed in photography and microscopy images from the bottom, side and in slices of the print.

6.2.3. Growth Conditions in the Hydrogel Matrix

Confocal microscopy was employed to study size and shape of the printed colonies for the first 8h after extrusion more closely to gain a better understanding of the bacterial growth conditions inside the hydrogel matrices.

As depicted in Figure 6.2.3 A, colonies typically are of ellipsoidal, in some cases spherical shapes, whose volume grew exponentially over time. Estimations of the colony cell count were derived from the colony volume and the volume of single cells. The bacteria cells printed showed an average volume of 1.5 µm^3 per cell, determined via microscopy. An exponential fit to the cell number as a function of time resulted in a mean generation time of 55 ± 6 min (see Figure A.8.2 for experimental replicates).

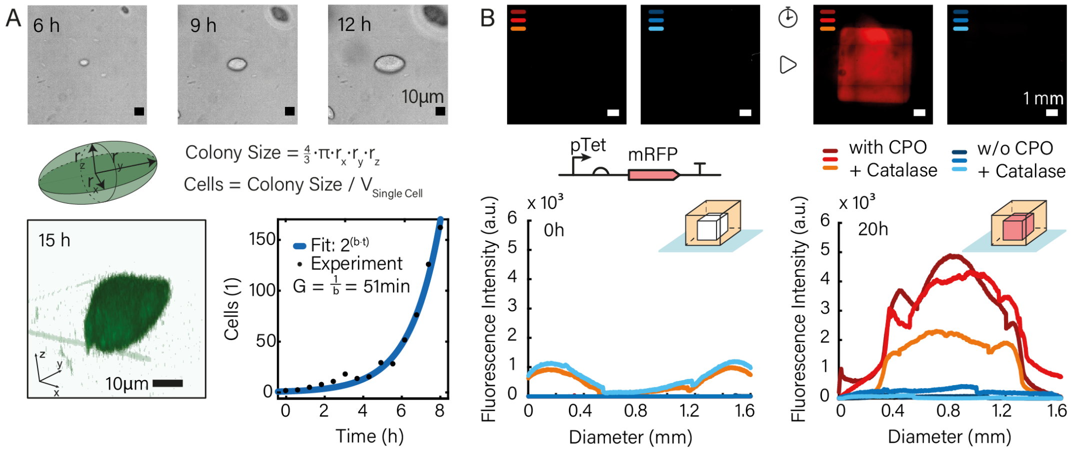

Figure 6.2.3: Bacterial Growth and Protein Production: *A) Bacterial growth was observed by confocal microscopy for 12 hours after printing. Bacterial colonies were generally found to exhibit ellipsoidal shapes. The sizes of these shapes were used to determine bacterial numbers and derive growth curves for colonies inside the printed hydrogel matrix. The bacteria displayed exponential growth over at least 8 hours after printing. B) Good fluorescence readout generated from protein production of embedded bacteria within the hydrogel matrix is dependent on continuous oxygen supply in the gel. Without oxygen present, the maturation of the majority of fluorescent proteins is hindered* [185], [200], [201]*. Cuboid structures were casted and sealed in 1 × LB and 2% (w|v) agarose, 2 % (w|v) alginte (as "blank" bacteria-ink) to mimic the procedure applied for printed structures. In the structures where 0.15 % (w|v) calcium peroxide and 0.3 mg/ml of the enzyme catalase were added, the fluorescence signal strongly increased during 20 h of growth at 37°C. In the absence of any oxygen generator, no fluorescence could be detected. Adapted from Müller et al.* [191]

Within this work, the lack of fluorescent readout within bioprinted bacterial structures as mentioned in literature [45] was also addressed. Fluorescent protein maturation requires oxygen for one (GFP [201]) or two (RFP [200]) folding processes and thus was only observed at gel-air interfaces in previous work. Proof of the successful immobilization of genetically modified *E. coli* deep within bioprinted hydrogels is largely facilitated, if fluorescent monitoring is available. To achieve observable fluorescent readout, a calcium peroxide-based oxygen generation system was utilized, which is known as an additive from conventional cell culture. [188] After printing, CPO degrades to hydrogen peroxide within the hydrogel matrix. As high levels of hydrogen peroxide are detrimental to cell viability, the conversion of hydrogen peroxide to oxygen and water is therefore mediated by addition of the enzyme catalase.

Hydrogel bacteria-ink cubes were casted with bacteria containing the plasmid pTet-mRFP, that encodes mRFP under the control of a pTet promoter. The fluorescent protein production was only induced via addition of aTc directly before casting, to reduce background fluorescence due to premature induction. Cubes were casted either with or without the addition of CPO and catalase and incubated for 20 h at 37 °C. After incubation, all cubes without CPO did not provide a considerable increase in fluorescence signal. In contrast, all hydrogel cubes containing the oxygen generating CPO - catalase system showed a clear fluorescence signal in all triplicates (Figure 6.2.3 B).

Diffusion of Genetic Inducers

With the previous experiments, the capability to print multiple clones of living *E. coli* bacteria in two and three dimensions and observe cell activity via fluorescent readout is confirmed.

In the next experiments, more elaborate systems are studied in immobilized bacteria. First, diffusion of inducer molecules and resulting spatio-temporal gene expression response of bacteria embedded in the bioprinted gel is studied. In these experiments, aTc-inducible DH5αZ1 cells, again carrying the plasmid pTet-mRFP, were employed as they showed reliable fluorescent output in the casting experiments (Figure 6.2.4 A and B).

For the diffusion experiments, bacteria cells were printed into a circular shape with a diameter of 12 mm. Following extrusion, a 2 µl bacteria-ink voxel containing 1 µg/ml aTc (final concentration in the reaction chamber 0.2 µg/ml (or 0.43 µM)) was added to the center of the circular structure. The printed structure was then sealed with blank LB-containing ink in a plastic and glass container and imaged during incubation for 12 h at 37 °C with 4 × magnification.

The fluorescence signal started to rise in the center after incubation for 3–4 h and small colonies became visible in the brightfield images. This timing is expectable in respect to bulk measurements that showed strong increase in fluorescence signal after 4-5 h (see Appendix A.8.4). After 10 h large bacterial colonies became visible in the brightfield channel and the expression rate of RFP within the cells was observable, looking at the increasing fluorescence intensities.

The spatio-temporal dynamic pattern is based on the combination of the inducer diffusion through the gel, the growth of the single bacterial colonies and the inducer-dependent gene expression in the immobilized bacteria. Figure 6.2.4 B further shows that with a mathematical model of these processes, the spatio-temporal change in fluorescence signal can be emulated with a numerical simulation.

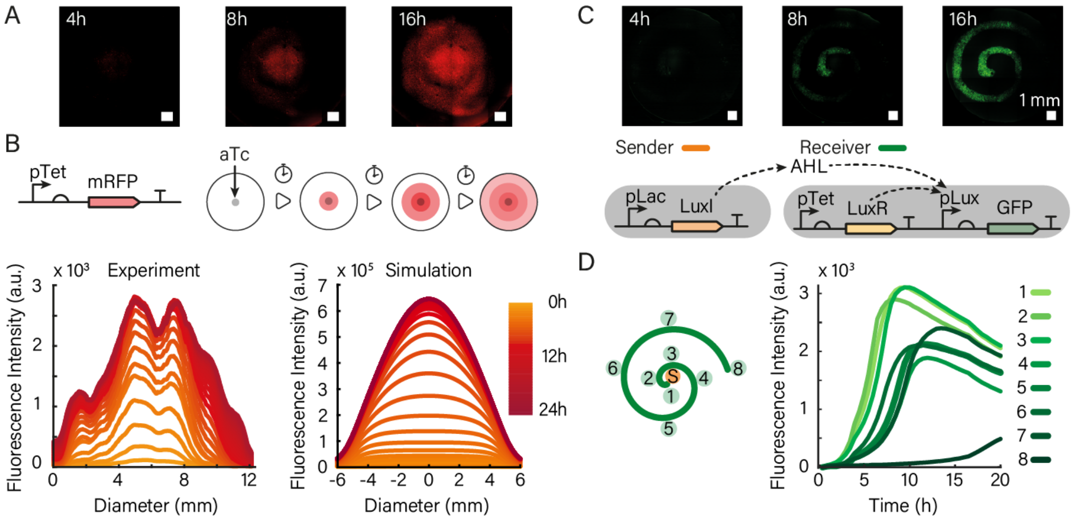

Figure 6.2.4: Diffusion of Inducers: *A) Diffusion of the genetic inducer aTc from the center of a printed gel and subsequent expression of mRFP by bacteria contained in the gel (scale bar 1 mm). B) mRFP was expressed under the control of a pTet promoter and thus responds to aTc diffusion. The graph on the left shows the fluorescence intensity measured along the diameter of the bioprint for different timepoints. Simulations (right) that model aTc diffusion, bacterial growth and gene expression are in good agreement with the experimental observations. C) Fluorescence channel of 4 × microscopy images of a sender-receiver system at 4h, 8h, and 16h after the start of the experiment. The increase in fluorescence intensity is synchronous (time intervals of 10 min showed no differences) upon induction of the sender bacteria with IPTG and consequently with high AHL production. The corresponding gene circuit is shown below the micrographs. D) Fluorescence time traces (right) corresponding to the locations indicated on the left for an experiment, in which the sender bacteria were not induced, and thus only a small amount of AHL is produced by leaky expression of LuxI from the Lac promoter. Adapted from Müller et al.* [191]

For bacterial growth rate and expression dynamics, realistic parameters from the conducted experiments were employed (see Appendix A.8.7). With the simulations, values for the diffusion coefficient for aTc in bacteria-ink were screened, which indicate a diffusivity on the order of 200 $\mu m^2/s$ within the gel (Figure A.8.8).

6.2.4. Bacterial Communication in a Bioprinted Environment

Reliable bioprinting with bacteria-laden inks opens up the possibility to arrange different types of interacting bacteria into well-defined spatial patterns, with which communication pathways can be planned.

In synthetic biology, an advantageous feature is the precise control of boundary conditions and sample patterning. With such setups, spatio-temporal development in structures containing genetically engineered bacteria can be directed or manipulated [192],[193],[194],[195].

A first approximation to such more complex setups was performed with the integration of a synthetic bacterial sender-receiver system embedded in a bioprinted gel structure. As sender cells, DH5αcells were employed which are equipped with a plasmid coding for the AHL synthase LuxI under the control of a Lac promoter. Sender cells express LuxI upon induction with IPTG, as explained in Section 2.3.1, LuxI consecutively produces the quorum sensing signal AHL that can freely diffuse out of the bacteria. Receiver cells contain a plasmid coding the constitutive production of the AHL-dependent transcriptional activator LuxR, which in turn controls the expression of GFP via the pLux promoter. Before printing sender and receiver cells, bulk experiments were conducted to verify the sender-receiver system (see Figure A.8.5). The system showed a robust behavior and fluorescent readout was only generated for active sender cells. If sender cells are induced with IPTG a high fluorescence intensity was detected within the first 3 hours. But also uninduced senders showed "leaky" AHL expression due to lactose residuals in LB medium, which lead to a fluorescence signal.

Receiver cells were printed to form an Archimedean spiral, defined by $r(\Phi) = a{\cdot}\Phi$, where r and Φ are polar coordinates, and a is a constant. In contrast to the typically used logarithmic spiral, more revolutions of an Archimedean spiral can be printed to a sample slide as printed voxels are of $\approx$ 1 mm size and central space is kept free for the sender voxel at r = 0.

As expected from bulk measurements, induced sender cells activate the GFP production of the receiver cells at their respective locations by sending out AHL (Figure 6.2.4 C). With nearly all receiver cells starting to produce fluorescent proteins at the same time, the sender-receiver output exhibited a different behavior compared to the aTc-driven RFP-expressing system in Figure 6.2.4. A possible explanation is the much higher sensitivity of LuxR activation to AHL with a K_d on the order of only 10 nM.

The performed bulk experiment suggested possible "leaky" AHL production by the sender cells, therefore experiments were conducted with printed sender-receiver samples without the addition of IPTG to compare the spatio-temporal development of fluorescence output signals for reduced "sender strength". [202] For these samples, in some cases a clear differentiation in spatial response of the bacteria was observable. There receiver bacteria closer to the sender cells showed faster response after printing than more remote cells (Figure 6.2.4 C). However, for other uninduced samples, no clear spatial order could be derived, or similar to induced sender-receiver samples, the complete spiral showed synchronous increase in fluorescence intensity (Figure A.8.6).

A possible explanation for this behavior can be found with simulations. There, such response can be observed if the AHL concentration throughout the gel had already reached nanomolar concentrations before the receivers started to grow appreciably (Figure A.8.9).

For all sender-receiver samples, independent of induced or uninduced senders, GFP signal can be observed to increase over 10 - 16 h until nutrient and possibly oxygen depletion and bleaching effects set in, followed by a decay in GFP fluorescence. For all sender-receiver experiments, a considerable variability was noticeable as shown in Figure A.8.6. These deviations are likely related to the high sensitivity of the dynamics with respect to variations in bacterial growth and the very low AHL concentration required for induction (cf. discussion in Section A.8.7).

6.2.5. Guiding Chemotaxis with Printed Boundaries

The second example to spatially control bacterial dynamics with a bioprinting approach included the artificial guidance of chemotactic bacteria in an engineered environment by printed bacterial boundaries. Chemotactic bacteria typically move on the surface of soft agar gels [203] towards areas of more favorable environmental conditions, e.g. higher nutrient content.

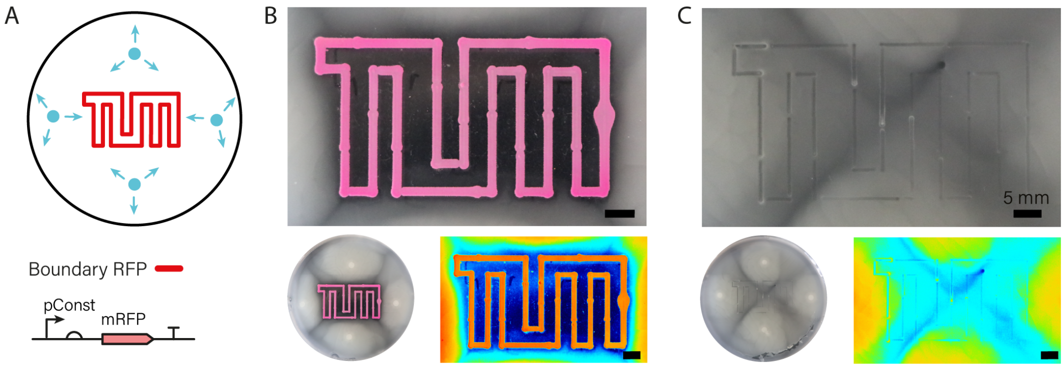

Figure 6.2.5: Artificial Boundaries Guide Bacterial Growth: *A) Artificial boundaries in the form of a TUM logo were printed into soft agar using non-motile bacterial cells constitutively expressing RFP. Directly after printing, chemotactic cells were inoculated on four locations and grown at 37°C. B) After 20h of incubation, the printed boundaries showed a high intensity of RFP fluorescence. The chemotactic cells successfully spread over the whole surface outside of the boundaries, but could not enter the interior of the logo. The small images show a view of the whole plate (left) and a high contrast image of the apparent bacterial density in heatmap coloring (right). C) For comparison, the TUM logo was printed with bioink not containing any bacteria. In this case the bacteria spread over the whole plate without hindrance. Adapted from Müller et al.* [191]

As suitable environment for chemotactic bacteria, the experiments were performed on the surface of soft agar plates with agar concentrations of 0.22-0.24% (w|v). With the bioprinter the shape of the logo of the Technical University of Munich (TUM) was deposited on top of these agar plates (Figure 6.2.5 A). Due to the soft nature of the plates, the non-motile, RFP-producing boundary bacteria are mixed to 1 % (w|v) alginate, as the developed bacteria-ink shows a much higher gel density and would itself hinder chemotactic bacteria to perpetrate the boundary.

After printing the TUM logo shaped boundaries, the plates were inoculated with four 2 µl aliquots of a suspension of a chemotactic *E. coli* strain (MG1655) at OD 0.2 placed at approximately equal distances from the outline of the logo.

After 20 h of incubation at 37 °C, chemotactic cells showed to have grown into a thick bacterial lawn covering the agar surface with the exception of the enclosed logo areas and small spaces between printed borders (Figure 6.2.5 B). This lead to the conclusion that the presence of printed bacterial borders prevented the chemotactic bacteria from propagating into the interior of the logo, where only singular cells were found to be present.

Control experiments with bacteria-free 1 % (w|v) alginate boundaries, the chemotactic bacteria showed to be able to overgrow the complete agar surface within 20 h (Figure 6.2.5 C). As result, it can be mentioned that chemotactic bacteria unlikely enter border and enclosed regions of immobilized bacteria, probably due to unfavorable nutrient conditions potentially combined with the physical obstruction caused by the non-motile bacteria themselves.

6.3. Conclusion

With the development of a suitable bacteria-ink mixture, the 3D printing of living bacteria within hydrogel matrices was facilitated. The approach is based on widely available, inexpensive, and non-toxic hydrogels and is independent of post-printing crosslinking steps. It further enables a mild extrusion at comparably low temperatures and ensures bacterial survival throughout the printing process. Embedded genetically modified *E. coli* cells were also shown to reach exponential growth into extended microcolonies within the printed gel during incubation after extrusion. The printer was equipped with a dual-extrusion mechanism controlled directly by the printing protocol. With this, two different bacteria-inks can be printed into predesigned voxel-defined 3D shapes. Sequential extrusion of bacteria-laden hydrogels can be used to pattern areas with different bacteria types enclosed in 70 µm voxels at a 50-500 µm spatial resolution. The integration of the continuous oxygen supply from the degradation of calcium peroxide assisted by the enzyme catalase supports the maturation process of fluorescent proteins and enables fluorescence readout deep within the gel.

Together, these developments open up the possibility to pattern arbitrary 3D structures with precisely deposited genetically engineered, communicating and interacting bacterial communities in a programmable and reproducible manner. First demonstrations of such a spatial arrangement are given with the inducer controlled spatio-temporal gene expression in deposited bacteria and the printed bacterial sender-receiver system. In the last experiment also guidance of chemotactic bacteria on the surface of soft agar by patterned non-motile bacteria were shown. With this, the creation of living boundaries that are impenetrable for motile bacteria to engineer biofilms is possible.

For future applications, the spatial organization of living bacteria with a bioprinter in 3D shapes and structures will facilitate the generation of smart living biomaterials that are capable of simple forms of differentiation or other types of information processing [192], [193]. Within such living materials, bacteria can be employed to sense environmental stimuli and mutual presence at their respective locations and produce local response accordingly. The dual-extrusion of the developed bioprinter further assists the local arrangement of systems of communicating bacteria that might develop into spatial organization. Possible applications include not only the spatial positioning of bacteria of the same species containing different types of genetic circuits, but also extrusion of different bacteria species to spatially arranged co-cultures which can perform more complex biosynthetic tasks. With this, co-culturing of bacteria with conflicting growth requirements – e.g., *E. coli* and cyanobacteria – can be achieved.

To this end, many existing biomaterials can be easily modified and with a precisely programmed bioprinter, 3D structures and geometries can be patterned with the desired hydrogel during the printing process to integrate a variety of stimuli at programmed regions.

With the nearly free patterning of 3D shapes, natural biofilms and bacterial niches can be mimicked and studied in a reproducible and controlled environment. In such an environment also antimicrobial agents could be tested under close to realistic conditions. Other applications are plausible if bioprinting of mammalian and microbial cells are performed simultaneously, which might be of high interest for pathogen-host interactions and screening for adequate personalized cures.

7. Cellular Automata Realized as Electro-Bio-Hybrid Circuit

The last project of this thesis considers the physical implementation of a combination of an electronic circuit that is controlled by the output signals of a biological circuit and can itself take control over the evolution within the biological network via photo-coupling.

7.1. Motivation

Cellular automata are of high interest for programmers as with this approach real parallel computing is possible. [117] To reach this ambitious goal, no complex code has to be established, rather than short algorithms that are executed by multiple distributed computing units that are only sharing data with their directly assigned *nearest neighbors*. With this, all units can perform their computation at the same time and only share the results. [117]

As already stated in Section 2.5 the applications of this computing mechanism are promising in the field of robotics and intelligent sensor design. A famous field of application is the emergency evacuation routing for high buildings based on a cellular automata network of sensors [204],[205]. Also in modeling the spread of infectious diseases, cellular automata is a known approach [206] and became more popular with the recent covid-19 pandemic. [207] Within the field of chemistry and biochemistry, cellular automata based models are employed to simulate diffusion, dissolution, hydration, and chemical transformations. [208]

Another toolbox that is capable of real parallel computing can be found in biological circuits, for example in DNA circuits, where all processes are physically occurring simultaneously. One of the most well known approaches was published by Adleman already in 1994 and shows an elegant way to solve the np-complete Hamiltonian path problem of the traveling salesman. [88] In his work, precisely labeled ssDNA were used to encode possible paths between the locations the salesman wants to visit. However, biological circuits often have the major disadvantage to lack in clear logic levels. For simple readout systems, for example reporter - binding or a singular gene expression, high logic levels are easily achieved. However, for oscillating synthetic circuits (e.g. Elowitz and Leibler [209]), high logic levels are mainly observed for the first iterations, but are likely decreasing over time due to several processes, e.g. diffusion or degradation.

With the stated electro-bio hybrid circuit, the stability of logic levels within hydrogel compartments should be improved by controlled gating of diffusion in and out of the compartment. The soft gates will remain closed if no clear logic levels can be indicated. The closed state is achieved via a photoswitchable hydrogel in its gel - state, where it exhibits a small pore size that prevents, or strongly decreases diffusion. If high logic levels (e.g. high fluorescent intensity) is detected in the hydrogel compartment, communication channels can be opened to allow diffusion. To open the gate, irradiation with the respective wavelength switches the photoreactive gel to its sol - state which increases the pore size.

For the realization of a complete logic block, like an "and" or "nand" gate, the synthetic circuit needs to be designed accordingly and ideally a two-value logic is desirable, to achieve clear zeros and ones. In this first approach, however, the biological circuit will be implemented as a proof of principle circuit and includes a single readout value (= logical one) by a singular fluorescent reporter.

To reach the goal of gated communication between hydrogel compartments, several building blocks need to be considered: First, a suitable hydrogel with photoswitchabel gel-sol transition has to be found, synthesized and fully characterized. Second, the design and testing of a synthetic biological circuit to include to the hydrogel compartments is necessary. Here, a DNA computing circuit is employed that relies on fueled TMSD fluorophore - quencher unbinding. Then, the pore size of the photoswitchable gel needs to be adjusted to fit the sizes of the synthetic biological molecules in the adjacent hydrogel compartments. The fully working gated setup can be linked in a last step to the electronic setup which is coupled via a light - matrix and camera sensors to the hydrogel compartments. Parallel to the development of the biological components, such an electric circuit needs to be developed.

7.2. Results and Discussion

During this work, the separate building blocks of the complete electro-bio hybrid setup were completed. The overall working principle was planned and distributed to five major tasks: Design and verification of a suitable DNA readout circuit, synthesis and characterization of photoswitchable hydrogels, hardware and software development of an electronic readout circuit, and an alignment platform. The last task is to combine all separate components to a working hybrid. The four separate tasks were successfully realized during this work and will be described in the following sections. Until the end of this thesis, the setup of the complete hybrid structure was not yet finished.

7.2.1. Electro - Bio Setup Overview

A network of hydrogel compartments containing synthetic biological circuits can be coupled best to an electronic irradiation and readout circuit, if both networks are structured as matrices. As shown in Figure 7.2.1, the hydrogel compartments are all equally sized and distributed. Hydrogel compartments are linked to direct neighbors via a channel containing photoswitchable hydrogel. This setup resembles the von-Neumann neighborhood. [114]

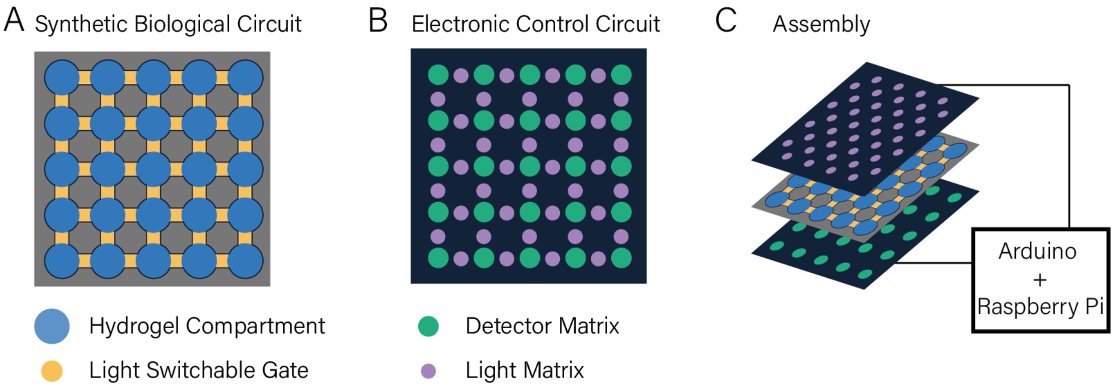

Figure 7.2.1: Design Electro-Bio Circuits: *The complete setup contains two matrices, one including a synthetic biological readout circuit and one containing electronic components for irradiation and fluorescence detection. A) Hydrogel compartments containing functionalized bioink are linked together with photoswitchable channels. The channels can be opened upon irradiation with UV light and closed either via irradiation with VIS light or by thermal relaxation. If gates are opened, diffusion between the two linked compartments is enabled, if the gates are closed, diffusion is limited or even completely prevented. With this, catalytic or fueled reactions will be allowed to continue until high logic levels are reached without fast diffusion of fuel strands. B) The electronic circuit is equipped with a light matrix and a detector (LEDs with a wavelength of* λ *= 350 nm and a camera). The light matrix is switched on either via a pre-defined pattern, for example following an external clock signal, e.g. all LEDs are on for 2 min every 30 min, or depending on the signals detected with the camera. CMOS cameras are able to detect fluorescent signals and therefore can be employed to sense the fluorescence intensity within the bioink compartments. If a certain threshold of fluorescence is reached, the logic level for the corresponding compartment is interpreted as a logical one. Following a cellular automata computing algorithm, gates can be switched on. As an example, a gate might only be switched on, if exactly one of the adjacent hydrogel compartments shows a logical one. C) For the complete experimental setup, these matrices need to be aligned. The light matrix needs to reach the photo-gates and the detection matrix must be placed in close proximity to the hydrogel compartments. Signals are evaluated with a RasperryPi which also controls the light matrix.*

In a similar way, a light-matrix of the same geometry is designed, to allow the irradiation of singular photo-channels. The light matrix is driven by an external computing unit. For this, an Arduino was employed that is able to drive multiple outputs. For the integration of CMOS camera data, a Raspberry Pi is connected, that sends the measured fluorescence intensities to the Arduino. The Raspberry Pi camera will detect fluorescence in the singular hydrogel compartments at specific time intervals (similar to the signal edge of a clock signal) and send the logic level (high fluorescence = one, low fluorescence = zero) to the computing unit. With a cellular automata setup, only the logic levels of a singular hydrogel compartment and the logic levels of the four direct neighbors are used as input, to calculate if the photo - gate will be switched open or not. If the computer decides to switch a gate open, the corresponding light emitting diode (LED) is switched on for an exact interval at the next clock.

Closing of the photo-gates can be realized with a second light - matrix, that emits at the relaxation wavelength of the azobenzene moiety. For this work, gates are only opened as only a singular logic is realized within the DNA readout circuit. For complete logic gates and a complete realization of e.g. a resemblance to the game-of-life, the dual - logic and the second light - matrix need to be included.

7.2.2. DNA Based Readout Circuit

Within the hydrogel compartments a DNA circuit was localized that resembles the circuit in Chapter 5 but was altered slightly, to allow certain modifications. [140] The reporter strand Z_{20} consists of 40 bases and exhibits a 20 nt region, that binds strongly to the complementary 20 nt anchoring strands that are linked via a copper - catalyzed click reaction to the hydrogel (c.f. Figure 7.2.2). The 20 spare bases allow for the binding of a 15 nucleotide quencher $\overline{Z}_{15}$. With this, the fluorophore - quencher duplex is not allowed to diffuse freely as in Chapter 5, but is localized to the super low melt agarose chains. The fuel strands $\overline{Z}_{20}$ are free in solution and able to replace the quencher strands via TMSD with a toehold region of 5 nucleotides.

The free fuel strands are modified with a biotin with a size of $\approx$ 3 nm. The biotin is larger than the single-stranded oligonucleotides and additionally allow to bind streptavidin coated polystyrene or gold - nano - beads via biotin - streptavidin binding to increase its size. With this, not only the pore size of the photogel, but also the size of the fuel strand can be adapted to alter the switching of diffusability. The circuit was tested in bulk experiments and worked as expected. For this work, only fuel strands with biotin modification were tested without the addition of larger streptavidin coated polystyrene or gold beads.

With the validation of the suitable DNA readout circuit, the photoswitchable gate hydrogel must be synthesized and tested to adjust the pore size accordingly.

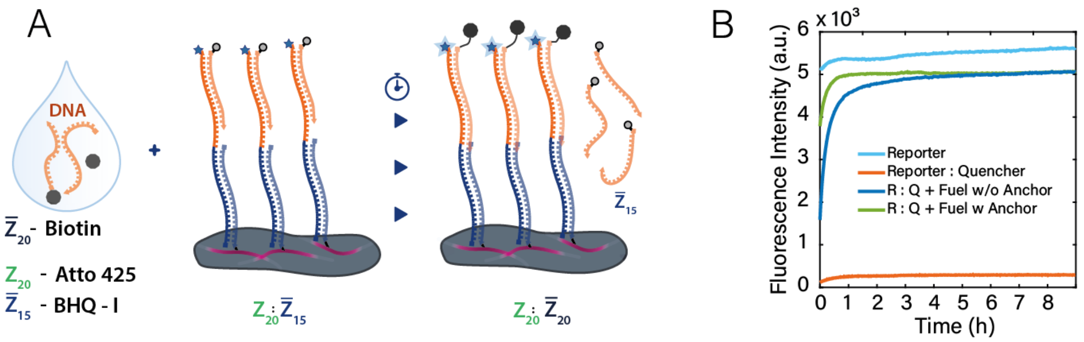

Figure 7.2.2: DNA Readout Circuit: *The DNA readout circuit was designed to be adaptable to different pore sizes for a sol-gel photoswitchable hydrogel. A) Similar to the DNA circuit already introduced in Section 5.2.2 the reporter duplex (15 bp) reduces fluorescence to a low background noise if the fuel strand is not present. However, the duplex here is localized via a stable 20 bp binding to anchor strands that are immobilized on the SLM agarose chains via a copper-click reaction. Therefore, the fuel strands need to reach the duplexes to release the quencher strands via a 5 nt toehold. The fuel strands are modified with biotin, to allow a variation in size and adjust the diffusion coefficient. B) Experimental results of a bulk experiments in a fluorescence spectrometer show the correct functioning of the circuit. Complexes of fluorophore-quencher strands ($Z_{20} : \overline{Z}_{15}$) only showed low background fluorescence. If fuel strands were present ($Z_{20} : \overline{Z}_{15} + \overline{Z}_{20}$), the fluorescence intensity increased until levels close to the positive control containing only fluorescently labeled Z_{20} strands.*

7.2.3. Photoswitchable Hydrogel Gates

The hydrogel chains exhibit carboxylic groups that can be used for amine coupling through EDC/NHS. [133] Azobenzene and α- cyclodextrin were purchased with a single amine group and grafted separately to the poly - acrylic polymer backbone via this coupling mechanism and the protocol stated in Section 3.3. The synthesis products were dialyzed for 7 days against ddH$_2$O and freeze-dried. Synthesis results were verified via nuclear magnetic resonance (NMR) spectroscopy and showed a substitution of $\approx$ 2-3 % (cf. Figure 7.2.3).

Pore size determination of the photoswitchable gel was performed with PITC-dextrans according to the protocol in Appendix A.6.1 (cf. Figure 7.2.4). Completely closed pores were achieved with azobenzene - PAA and β- cyclodextrin - PAA (at 2% + 2%, w|v), as azobenzenes can always integrate to the slightly larger β-cyclodextrin cavity.

For measurements with open photogel, PAA and β-cyclodextrin-PAA (at 2% + 2%, w|v) were used to prevent azobenzenes from base stacking. Further, if irradiated with UV light for several hours to keep azobenzenes in *cis*-state, the fluorescently labeled dextrans would bleach and results distorted. Closed gel holds back all available FITC-dextrans and therefore most likely has a pore size of less than $\approx$ 2.3 nm.

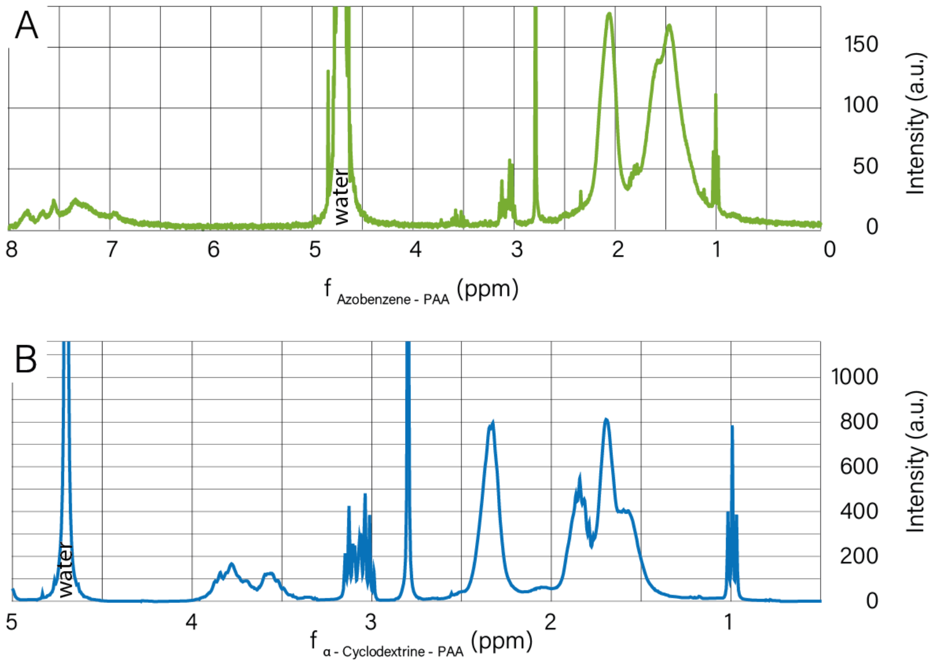

Figure 7.2.3: NMR Data Photogel: *Free induction decay of modified polymer backbones were measured in* D_2O *in a NMR. Spectra were Fourier transformed and phase corrected. The water peak is always at 4.7 ppm. A) NMR data of azobenzene - PAA. Characteristic peaks of PAA are visible from 1.0 - 2.0 ppm, azobenzenes at 3.0 ppm. Due to 7 d dialysis, unlinked azobenzenes are unlikely and the amine - carboxyl binding can be assumed successful. B) Similarly, α- cyclodextrin - PAA shows the PAA peaks at 1.0 - 2.2 ppm. The peaks at 3.6 - 3.9 are characteristic for α- cyclodextrin. Again dialysis reduces free cyclodextrins and again the binding can be assumed successful. NMR spectra of the reactands are supplied in Appendix A.9.2. Grafting densities are assumed on the NMR data to be 2%-3%.*

Dextrans up to 2000 k Da were able to diffuse through open photo gel and a pore size of more than 30 nm is expected for disintegrated guest - host complexes.

For azobenzene - PAA the switching time was determined via absorption spectroscopy (data in Appendix A.9.2). The *trans* - *cis* switching time t_{on} was determined via increasing time intervals of irradiation with 356 nm. Irradiation times of more than 30 s showed no stronger deviation in the absorption spectrum and was determined as t_{on}.

Similarly, after a switchting time t_{off} = 45 min, it is estimated that most *cis* - azobenzenes switched back to *trans* - configuration, as no stronger changes in the absorption spectra were detected for longer irradiation times. It has to be mentioned, that the reverse switching time deviates from literature largely, where 5 - 10 min are typical, which might be due to stronger light sources or a lower room temperature of 20 - 22 °C. [135]

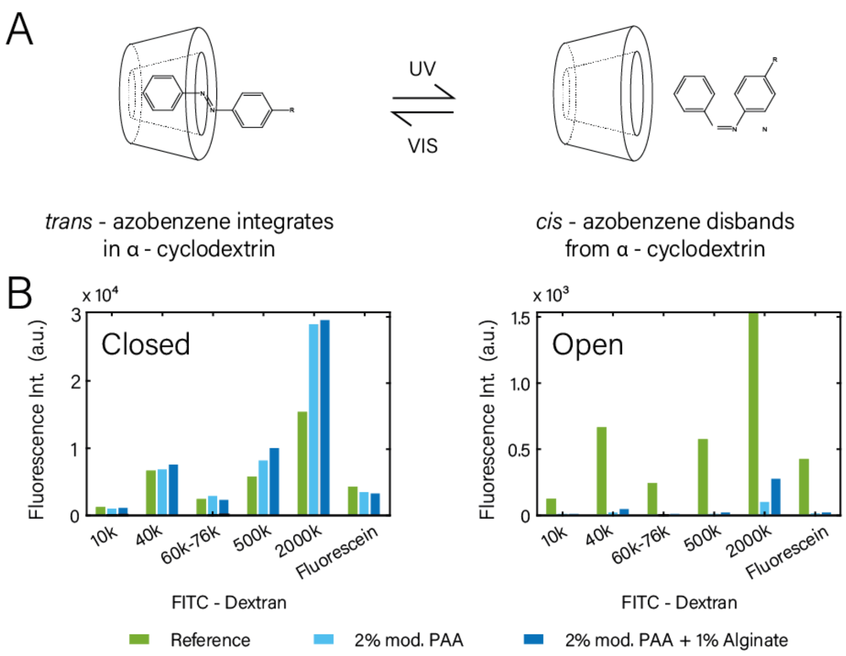

Figure 7.2.4: Photoswitchable Hydrogel Gate: *A) Schematic representation of the guest-host interaction of azobenzene and α- cyclodextrin. For azobenzenes in the equilibrium trans-state, a guest-host complex is formed, if switched to cis-state, the complex disassembles. With this, polymer chains grafted to the molecules can be linked temporarily and the pore size increased upon irradiation. B) The pore size was determined again with the application of differently sized FITC-dextrans on hydrogel samples. Diffusion was allowed for 72 h and residual fluorescence of the supernatant was compared to reference samples. For closed gel, only the small molecule fluorescein was able to diffuse into the small hydrogel pores. The majority of FITC-dextrans remained in the supernatant for all samples, concluding a pore size lesser than 2.3 nm. Open gel allowed all dextrans to perfuse into the hydrogel, which gives a pore size estimate larger than 38.6 nm.*

7.2.4. Photoswitchable Gating of DNA Circuits

With the verification of the DNA readout circuit and the photoswitchable hydrogel, the biological circuit components are present and a combined setup can be prepared. Before the biological circuit can be coupled to the electronic circuit, proof-of-principle experiments with a reduced 2×1 biological matrix and a singular switchable channel were performed.

The pore size experiments suggest that biotinylated ssDNA molecules are held back by 2 % (w|v) *trans*-azobenzene-PAA + 2 % (w|v) α-cyclodextrin-PAA forming a tight gel. Therefore, no larger polystyrene- or gold-nano-beads were added to increase the molecule size.

Of the 2×1 matrix, one compartment is filled with free fuel strands mixed to bioink, the other with pre-quenched reporter complexes anchored to the bioink. The channel is filled with switchable hydrogel, mixed 1 : 1 to bio-ink (see Figure 7.2.5).

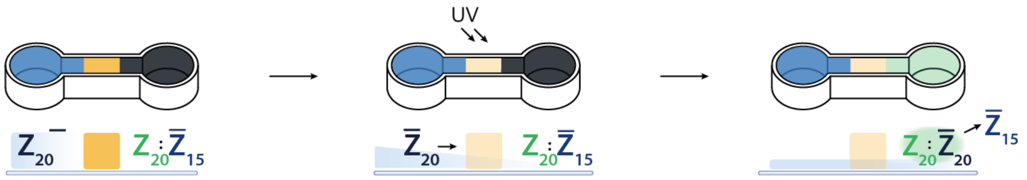

Figure 7.2.5: Photoswitchable Gating of DNA: *Schematic representation of a proof-of-principle 2 × 1 structure with a start compartment containing free biotinylated fuel-strands (indicated in blue) and a reporter compartment with localized fluorophore-quencher duplexes (indicated in black). The connecting channel is filled with photoswitchable azobenzene-cyclodextrin-PAA (indicated in orange). Upon irradiation, the guest-host complexes disassemble and allow the fuel strand to diffuse through the channel to the second compartment. Fluorescence readout can be detected if fuel strands disassemble the quencher complex via TMSD.*

The hydrogel channel is opened via irradiation for 60 s with 254 nm and 356 nm and kept open as the sample is placed in a dark environment. With this, the fuel strands are enabled to perfuse through the channel to the second compartment. Control experiments were performed with closed channel hydrogel mixtures (no irradiation). After addition of fuel strands, diffusion was allowed for 16 h at room temperature. Fluorescence intensity was measured every 30 min. Background subtraction was performed before data analysis, to reduce noise.

Figure 7.2.6 shows the microscopy data of the first and last time step and a histogram over the average fluorescence intensity in the reaction chamber over time. If the gate remains closed, only few fuel strands reach the reporter duplexes in the right chamber and low fluorescence intensity is detected. In contrast, if the gate was opened for the experiment, fuel strands are able to pass the gate and reach the signal complexes, leading to a strong fluorescence signal over time.

Detectable fluorescence signal can be observed already shortly after starting imaging, due to preparation times of approx 10-15 min. It is noticeable, that the highest fluorescence signal within the signal champer is close to the channel, suggesting a depletion of the 5 × fuel strands excess already at the reporter complexes close to the gate area. Technical triplicates are shown in Appendix A.9.5.

7.2.5. Electronic Control and Sensor Unit

The light matrix consists of LEDs, as low energy light sources at a suitable wavelength (350 nm). Every single LED is driven by the computing unit depending on the input signals measured at the hydrogel compartments. For a proof of principle experiment, the circuit is tested with a set of given input "sensor data" to mimic the switching behavior.

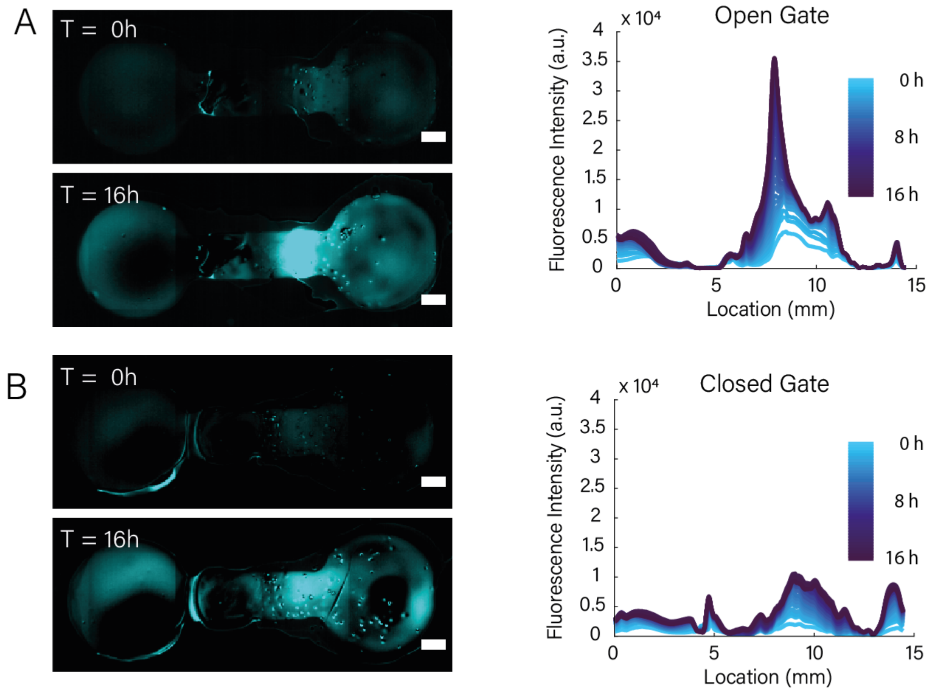

Figure 7.2.6: Experimental Data for Photoswitched Gate: *Microscopy data acquired in CFP channel after correction of the low fluorescent background by subtraction of the first image. A) For the opened photoswitchable channel, fluorescence signal is detected in the reporter compartment already in the first time step and increasing over time. This leads to the assumption, that the fuel strands are able to pass the channel, if the guest-host complexes disassemble. (Scale bar 1 mm) B) Closed channels hold back fuel strands and only low fluorescence intensity can be detected in the reporter compartment, suggesting strong guest-host interactions of azobenzene and α-CD being able to reduce the pore size to hold back biotinylated ssDNA.*

Similar to the rules for Conway's *Game of Life*, a hydrogel channel will be switched open, if a compartment with low fluorescence (logical 0) is linked via this channel to a neighbor with high fluorescence (logical 1). For this, the LED is set on for 30 sec to switch the gate open and subsequently off, to omit photobleaching of the azobenzene moiety.

The electronic circuit is completely assembled for grids up to 3 × 3 hydrogel compartments (12 gates). For simple testing of the gate, an electronic circuit and the Arduino program code to switch the gate of a 2 × 1 compartment setup is provided (see Appendix A.9.4).

Direct integration of the LED lights within the hydrogel channel is necessary as most materials absorb more than 90% within the UV region (e.g. PMMA, glass). For this, the sample cavities can be redesigned to allow the insertion of the LED body directly. A future possibility is the usage of SMD components to reduce the overall size.

7.3. Conclusion

With the designed setup, delayed or even completely stopped diffusion of short DNA strands from one hydrogel compartment to an adjacent compartment has come into reach. This would allow for fueled or catalytic circuits to establish stronger logic levels as the reactants are in an enclosed environment and less likely to diffuse faster than the reaction might start.

The biological circuit, consisting of a DNA fluorescent readout circuit and a photoswitchable hydrogel - gate, was shown to be a promising approach to generate stronger logic levels. Additionally, this setup could also be completely "clocked" like in a processing unit, where logic levels are set valid at signal edges. In such a setup, all connection channels could be switched open simultaneously at specific intervals to allow communication for a dedicated time. During a following closed period, signals within the singular hydrogel compartments can equilibrate, reactions occur, and valid logic levels derived. With an adequate biological circuit integrated to the hydrogel compartments, a full biological computing unit could be implemented, where all calculations are performed by a synthetic molecular circuit and outputs can be detected by e.g. fluorescent signals.

The electronic circuit was implemented and tested independently of the biological circuit. For a given set of provided input data, the switching behavior of the LED matrix resembled the expected irradiation. Channel opening or closing is performed, if the light matrix is coupled within the channel geometry, to reduce photon losses.

For the complete implementation, several experiments need to be performed and parameters optimized: The gel density of the photoswitchable gate is expected to be ideal with 2% azobenzene - PAA and 2% - α- cyclodextrin - PAA (w|v) according to literature. However, the density could be screened for optimum parameters and the consideration of viscosity enhancers (e.g. alginate, hyaluronic acid) for the facilitation of sample preparation could be useful. Reverse switching of the photo-gel must be optimized, possibly by increasing the irradiation energy. UV-matrix and biological matrix need to be aligned and switching behavior verified. Further, correct alignment must be verified to reduce unintended bleaching of the fluorophores. Additionally, the VIS-matrix needs to be integrated to the setup. At last, the sensor matrix must be placed close to the hydrogel compartments to enable fluorescent readout. If a more complex biological computing unit is achieved, the integrated DNA circuit could be replaced by a more complex and two-valued circuit.

8. Conclusion and Outlook

During this thesis a low-cost custom 3D bioprinter was designed and built. Hardware components as well as a suitable software for the generation of point-wise defined printfiles was developed. With this printer setup, reliable print results were achieved. Major advantages of this design are the small sample volumes and the heatable printhead, that also allows retraction to decrease dripping. After intensive screening of hydrogels and hydrogel mixtures, two kinds of bioinks were developed that suit the demands of DNA or *E. coli* bacteria bioprinting. Within these hydrogels, self-differentiating pattern formation was established and observed by fluorescence microscopy.

8.1. Conclusion

Amorphous 3D printing opens up a variety of new possibilities for precise 2D and 3D patterning and structuring of soft materials. Embedding synthetic circuits in artificial gel structures allows the integration of dynamic patterns to evolve over time. In this work, DNA circuits and genetically modified bacterial circuits were embedded within 3D printed hydrogel structures and the evolution of programmed patterns over time was observed.

To achieve these goals, a commercial 3D printer was refurbished with custom hardware parts. The parts include a temperature controllable printhead that can hold up to four sample syringes, an external syringe pump connected to the printer mainboard and a hydraulic coupling mechanism to avoid large sample volumes. For a precise control of the hydrogel deposition, a custom python software was developed that translates svg files in a layer-wise manner and integrates the control of two printheads.

For the design of both bioinks, the focus was set on the usage of solely biological hydrogels that allow mild printing conditions. Both mixtures - bioink and bacteria-ink - can be printed at a low extrusion temperature of 42 °C, and showed rapid gelation if exposed to room temperature. Additionally, the printing process is independent of any crosslinking agents and occurs solely by thermal gelation within seconds. The bioink gel structures consist of picoliter voxels that can be placed with a precision of 50 - 500 µm. Sample sizes measured up to 3 cm × 5 cm in x - y planes with maximum heights up to 1 cm. The bioink structures showed to last up to 10 months, if sealed within small chambers. Within the bacteria - ink, *E. coli* were shown to survive at least 20 hours immobilized within gel structures, if sufficient culture medium and oxygen supply is provided.

With the integration of localized DNA molecules to bioprinted structures, artificial differentiation within the 3D structures can be achieved. This enables the tunability of diffusion coefficients within the gel matrix and allows to program areas to capture specific ssDNA strands from bulk to demix the solution. This bioink consists of gelatin for fast gelation and alginate to increase viscosity and shear-thinning behavior, the super low melt agarose hydrogel is entangled between the aforementioned hydrogel chains and can be modified with short single stranded DNA to label specific areas.

The integration of living genetically modified *E. coli* bacteria within printed 3D structures is a versatile tool for future studies on bacteria-based biomaterials. During this work, present difficulties in bacteria printing were overcome by the usage of the developed bacteria - ink. Extremely mild extrusion is enabled at temperatures that induce nearly no heat stress within the bacteria. Both components, agarose and alginate, are well established in bacteria culturing and are known to be not disadvantageous to cell viability. Adding blank LB containing bacteria - ink to seal the print, ensures long term nutrient support for the immobilized bacteria. With the addition of calciumperoxide and catalase, the oxygen-dependent maturation process of fluorescent proteins can be supported and fluorescent readout is increased within the extruded samples. The developed setup supports reproducible experiments at confined environments and facilitates the study of bacterial growth and cell - cell communication.

Gated communication between hydrogel compartments containing biological synthetic circuits, is further examined as a powerful tool to support stronger logic levels as diffusion processes become controllable. For such a setup, a DNA based readout circuit was designed and tested. A photoswitchable hydrogel was synthesized and characterized. The switching wavelengths were verified and switching times determined. To open the gate, irradiation for $\approx$ 30 sec at 350 nm is necessary, while the reverse switching time is $\approx$ 45 min at 470 nm. The reverse switching time determined is untypically long compared to literature, possibly due to a low energy light source. Further, an electronic circuit was developed that switches the channels via an output - light - matrix, dependent on measured fluorescent intensity of the grid of hydrogel compartments. The output matrix is computed via a cellular automata algorithm, that only considers direct neighbors of any hydrogel compartment. Until the end of this thesis, the singular parts were developed and biological circuits as well as electronic circuit were tested. The complete assembly is not finalized yet and has to be considered in future work.

8.2. Future Work

With a reliable and precisely programmable bioprinter, a great variety of applications become possible. While clinical groups aim for better structuring of artificial organs and tissues, basic research could gain specific insights into communication pathways, diffusion and proliferation within 3D matrices as embedded cells can be monitored closely. Integration of localized DNA molecules within printed hydrogel samples allows addressing of certain regions which can support demixing and dynamic pattern evolution. DNA circuits that include more than one readout can be employed to "print" logic circuits which might also enable the deposition of soft logic gates that can be combined to basic computing units.

A large toolbox to bioprint human cells has been developed recently. With the developed bacteria - ink, co-deposition of common bacteria to human tissue samples is possible. With such heterogeneous samples, *in vitro* models of bacterial inflammations of human tissue could be achieved, a step towards more personalized medicine and treatments. More complex bacterial biofilms can be constructed for closer examination of the internal processes. Artificial differentiation within these extruded geometries dependent on external stimuli are possible. The stimuli might introduce local gradients in density, vitality or protein production and lead to a overall differentiation within the bacteria - sample.

A long term goal would be the generation of a printed photoswitchable hydrogel matrix. By printing extremely small dimensions of hydrogel compartments only separated by singular photoswitchable voxels directly adjacent to each other, small scale bio-computers could be achieved. Within these computers, an external clock or a signal - based gating can be introduced to amplify output signals.

To resume, bioprinting has become a resourceful tool, to generate a multitude of fine, reproducible, and highly programmable and customizable experiments. With this work, the toolbox of bioprinting was enlarged by a low cost - custom printer hardware, a simple software tool, and two bioprintable pastes that allows integration of DNA and living bacteria. This work should help lowering the threshold for other synthetic biological laboratories and groups to employ bioprinting as an experimental process as no expensive or hardly available components are used.

Publications

During the course of this thesis two publications on the results in bioprinting with DNA and bacteria modified gels were submitted:

Programming Diffusion and Localization of DNA Signals in 3D-Printed DNA-Functionalized Hydrogels

Julia Müller, Anna C. Jäkel, Dominic Schwarz, Lukas Aufinger and Friedrich C. Simmel, Small, Wiley, Volume 16, Issue 31 2001815 (2020) under licence CC BY 4.0

Bacterial Growth, Communication and Guided Chemotaxis in 3D-Bioprinted Hydrogel Environments

Julia Müller, Anna C. Jäkel, Jonathan Richter, Markus Eder, Elisabeth Falgenhauer and Friedrich C. Simmel, ACS Applied Materials & Interfaces, Volume 14 (14) (2022)

List of Figures

List of Tables

Glossary

E. coli	*Escherichia coli*
ABS	Acrylonitrile butadiene styrene
AHL	N-(β-ketocaproyl)-L-Homoserine lactone
aTC	Anhydrotetracycline
bp	Basepair
CAD	Computer-Aided Design
CD	Cyclodextrin
CFD	Computational Fluid Dynamics
CFU	Colony Forming Unit
CPO	Calciumperoxide
CSP	Cold Shock Protein
DMSO	Dimethyl sulfoxide
DNA	Deoxyribonucleic Acid
ECM	Extracellular Matrix
EDC	N-(3-Dimethylaminopropyl)-N’-ethylcarbodiimid-hydrochloride
EDTA	Ethylenediaminetetraacetic Acid
FDS	Fused Deposition Modelling
FFF	Fused Filament Fabrication
FITC	Fluorescein Isothiocyanate
GelMA	Gelatin-Methacryloyl
GFP	Green Fluorescent Protein
HA	Hyaluronic Acid
HSP	Heat Shock Protein
HTP	High-Temperature Production
iGEM	international Genetically Engineered Machines
IPTG	Isopropyl β-D-1-thiogalactopyranoside
LB	Lysogeny Broth
LED	Light Emitting Diode
mRNA	messenger RNA
MWCO	Molecular Weight Cutoff
NHS	N-Hydroxysuccinimide

NMR	Nuclear Magnetic Resonance
nt	Nucleotide
PAA	Poly-Acrylic-Acid
PBS	Phosphate-buffered saline
PC	Polycarbonate
PEG	Polyethylene Glycol
PEGDA	Polyethylene Glycol Diacrylate
PEGMA	Polyethylene Glycol Methacrylate
PEGTA	Polyethylene Glycol Tetraacrylate
PIP	Pressure Induced Protein
PITC	Propargyl-isothiocyanate
PLA	Poly (Lactic Acid)
PMMA	Poly (Methyl Methacrylate)
RFP	Red Fluorescent Protein
RNA	Ribonucleic Acid
SLM	Super Low Melting
ssDNA	single stranded DNA
ssDNA	double stranded DNA
TAE	Tris-Acetate-EDTA
TCEP	Tris-(2-carboxyethyl)-phosphine
THPTA	Tris(3-hydroxypropyltriazolylmethyl)amine
TMSD	Toehold-Mediated Strand Displacement
UV	Ultra Violet
VIS	Visible

Bibliography

[1] Johannes F Gottwald. *Liquid metal recorder*. US Patent 3,596,285. July 1971.

[2] Charles W Hull. “Apparatus for production of three-dimensional objects by stereolithography”. In: *United States Patent, Appl., No. 638905, Filed* (1984).

[3] Emanuel Sachs, Michael Cima, and James Cornie. “Three-dimensional printing: rapid tooling and prototypes directly from a CAD model”. In: *CIRP annals* 39.1 (1990), pp. 201–204.

[4] S Scott Crump. “Fused deposition modeling (FDM): putting rapid back into prototyping”. In: *The 2nd International Conference on Rapid Prototyping. Dayton, Ohio*. 1991, pp. 354–357.

[5] Sean V Murphy and Anthony Atala. “3D bioprinting of tissues and organs”. In: *Nature biotechnology* 32.8 (2014), pp. 773–785.

[6] Ryan L Truby and Jennifer A Lewis. “Printing soft matter in three dimensions”. In: *Nature* 540.7633 (2016), pp. 371–378.

[7] Aurore Dupin and Friedrich C Simmel. “Signalling and differentiation in emulsion - based multi-compartmentalized in vitro gene circuits”. In: *Nature chemistry* 11.1 (2019), pp. 32–39.

[8] Mariam Bayoumi et al. “Multi-compartment encapsulation of communicating droplets and droplet networks in hydrogel as a model for artificial cells”. In: *Scientific reports* 7.1 (2017), pp. 1–11.

[9] Luciano P Silva. “Current trends and challenges in biofabrication using biomaterials and nanomaterials: future perspectives for 3D/4D bioprinting”. In: *3D and 4D Printing in Biomedical Applications: Process Engineering and Additive Manufacturing* (2019), pp. 373–421.

[10] Sean V Murphy and Anthony Atala. “3D bioprinting of tissues and organs”. In: *Nature biotechnology* 32.8 (2014), pp. 773–785.

[11] Ursula Hopfner et al. “Development of photosynthetic biomaterials for in vitro tissue engineering”. In: *Acta biomaterialia* 10.6 (2014), pp. 2712–2717.

[12] Joselle M McCracken et al. “Ionic Hydrogels with Biomimetic 4D-Printed Mechanical Gradients: Models for Soft-Bodied Aquatic Organisms”. In: *Advanced Functional Materials* 29.28 (2019), p. 1806723.

[13] Shinji Sakai et al. “Differentiation potential of human adipose stem cells bioprinted with hyaluronic acid/gelatin-based bioink through microextrusion and visible light-initiated crosslinking”. In: *Biopolymers* 109.2 (2018).

[14] Madhuri Dey and Ibrahim T Ozbolat. *3D bioprinting of cells, tissues and organs*. 2020.

[15] Cameron J Ferris et al. “Bio-ink for on-demand printing of living cells”. In: *Biomaterials Science* 1.2 (2013), pp. 224–230.

[16] Giuseppe Arrabito et al. “Artificial biosystems by printing biology”. In: *Small* 16.27 (2020), p. 1907691.

[17] Hakan Ceylan, Immihan Ceren Yasa, and Metin Sitti. “3D chemical patterning of micromaterials for encoded functionality”. In: *Advanced Materials* 29.9 (2017), p. 1605072.

[18] Thomas J Hinton et al. “Three-dimensional printing of complex biological structures by freeform reversible embedding of suspended hydrogels”. In: *Science advances* 1.9 (2015), e1500758.

[19] Tapomoy Bhattacharjee et al. “Writing in the granular gel medium”. In: *Science advances* 1.8 (2015), e1500655.

[20] Daniel Therriault et al. “Fugitive inks for Direct-Write assembly of Three-Dimensional microvascular networks”. In: *Advanced Materials* 17.4 (2005), pp. 395–399.

[21] Héctor Martínez Ávila et al. “3D bioprinting of human chondrocyte-laden nanocellulose hydrogels for patient-specific auricular cartilage regeneration”. In: *Bioprinting* 1 (2016), pp. 22–35.

[22] Makoto Nakamura et al. “Biocompatible inkjet printing technique for designed seeding of individual living cells”. In: *Tissue engineering* 11.11-12 (2005), pp. 1658–1666.

[23] Brian Derby. “Bioprinting: inkjet printing proteins and hybrid cell-containing materials and structures”. In: *Journal of Materials Chemistry* 18.47 (2008), pp. 5717–5721.

[24] Paul C Duineveld et al. “Ink-jet printing of polymer light-emitting devices”. In: *Organic Light-Emitting Materials and Devices V*. Vol. 4464. International Society for Optics and Photonics. 2002, pp. 59–67.

[25] Busaina Dhariwala, Elaine Hunt, and Thomas Boland. “Rapid prototyping of tissue-engineering constructs, using photopolymerizable hydrogels and stereolithography”. In: *Tissue engineering* 10.9-10 (2004), pp. 1316–1322.

[26] Karen Dubbin et al. “Projection Microstereolithographic Microbial Bioprinting for Engineered Biofilms”. In: *Nano Letters* 21.3 (2021), pp. 1352–1359.

[27] Karina Arcaute, Brenda Mann, and Ryan Wicker. “Stereolithography of spatially controlled multi-material bioactive poly (ethylene glycol) scaffolds”. In: *Acta biomaterialia* 6.3 (2010), pp. 1047–1054.

[28] Jodi L Connell et al. “3D printing of microscopic bacterial communities”. In: *Proceedings of the National Academy of Sciences* 110.46 (2013), pp. 18380–18385.

[29] Fabien Guillemot et al. “High-throughput laser printing of cells and biomaterials for tissue engineering”. In: *Acta biomaterialia* 6.7 (2010), p. 2494.

[30] Ruitong Xiong et al. “Freeform drop-on-demand laser printing of 3D alginate and cellular constructs”. In: *Biofabrication* 7.4 (2015), p. 045011.

[31] Manuel Schaffner et al. “3D printing of bacteria into functional complex materials”. In: *Science advances* 3.12 (2017), eaao6804.

[32] Ratima Suntornnond et al. “A highly printable and biocompatible hydrogel composite for direct printing of soft and perfusable vasculature-like structures”. In: *Scientific reports* 7.1 (2017), pp. 1–11.

[33] Christopher J Hansen et al. “High-throughput printing via microvascular multinozzle arrays”. In: *Advanced Materials* 25.1 (2013), pp. 96–102.

[34] Weitao Jia et al. “Direct 3D bioprinting of perfusable vascular constructs using a blend bioink”. In: *Biomaterials* 106 (2016), pp. 58–68.

[35] Thomas J Ober, Daniele Foresti, and Jennifer A Lewis. “Active mixing of complex fluids at the microscale”. In: *Proceedings of the National Academy of Sciences* 112.40 (2015), pp. 12293–12298.

[36] James O Hardin et al. “Microfluidic printheads for multimaterial 3D printing of viscoelastic inks”. In: *Advanced materials* 27.21 (2015), pp. 3279–3284.

[37] Tomasz Jungst et al. “Strategies and molecular design criteria for 3D printable hydrogels”. In: *Chemical reviews* 116.3 (2016), pp. 1496–1539.

[38] Vivian Lee et al. “Design and fabrication of human skin by three-dimensional bioprinting”. In: *Tissue Engineering Part C: Methods* 20.6 (2014), p. 473.

[39] Susmita Bose, Sahar Vahabzadeh, and Amit Bandyopadhyay. “Bone tissue engineering using 3D printing”. In: *Materials today* 16.12 (2013), p. 496.

[40] Manu S Mannoor et al. “3D printed bionic ears”. In: *Nano letters* 13.6 (2013), pp. 2634–2639.

[41] Cyrille Norotte et al. “Scaffold-free vascular tissue engineering using bioprinting”. In: *Biomaterials* 30.30 (2009), pp. 5910–5917.

[42] S Mayer-Wagner et al. “Scaffold-free 3D cellulose acetate membrane-based cultures form large cartilaginous constructs”. In: *Journal of tissue engineering and regenerative medicine* 5.2 (2011), pp. 151–155.

[43] Wanjun Liu et al. “Coaxial extrusion bioprinting of 3D microfibrous constructs with cell-favorable gelatin methacryloyl microenvironments”. In: *Biofabrication* 10.2 (2018), p. 024102.

[44] Peter B. Allen et al. “3D Printing with Nucleic Acid Adhesives”. In: *ACS Biomaterials Science & Engineering* 1.1 (2015), pp. 19–26. DOI: `10.1021/ab500026f`.

[45] Lina M González, Nikita Mukhitov, and Christopher A Voigt. “Resilient living materials built by printing bacterial spores”. In: *Nature chemical biology* 16.2 (2020), pp. 126–133.

[46] Xinyue Liu et al. “3D printing of living responsive materials and devices”. In: *Advanced Materials* 30.4 (2018), p. 1704821.

[47] Dominik T Schmieden et al. “Printing of patterned, engineered E. coli biofilms with a low-cost 3D printer”. In: *ACS synthetic biology* 7.5 (2018), pp. 1328–1337.

[48] Amit Panwar and Lay Poh Tan. “Current status of bioinks for micro - extrusion-based 3D bioprinting”. In: *Molecules* 21.6 (2016), p. 685.

[49] Yong He et al. “Research on the printability of hydrogels in 3D bioprinting”. In: *Scientific reports* 6.1 (2016), pp. 1–13.

[50] Minggan Li et al. “Modeling process-induced cell damage in the biodispensing process”. In: *Tissue Engineering Part C: Methods* 16.3 (2010), p. 533.

[51] Julien Bruneaux, Daniel Therriault, and Marie-Claude Heuzey. “Micro-extrusion of organic inks for direct-write assembly”. In: *Journal of Micromechanics and Microengineering* 18.11 (2008), p. 115020.

[52] Sameh M Abdel-Hamid et al. “Formulation of an antispasmodic drug as a topical local anesthetic”. In: *International journal of pharmaceutics* 326.1-2 (2006), pp. 107–118.

[53] Ratima Suntornnond et al. “A mathematical model on the resolution of extrusion bioprinting for the development of new bioinks”. In: *Materials* 9.9 (2016), p. 756.

[54] Lin Li. “Thermal gelation of methylcellulose in water: scaling and thermoreversibility”. In: *Macromolecules* 35.15 (2002), pp. 5990–5998.

[55] Enrique Mancha Sánchez et al. “Hydrogels for bioprinting: a systematic review of hydrogels synthesis, bioprinting parameters, and bioprinted structures behavior”. In: *Frontiers in Bioengineering and Biotechnology* 8 (2020).

[56] Alexander D Augst, Hyun Joon Kong, and David J Mooney. "Alginate hydrogels as biomaterials". In: *Macromolecular bioscience* 6.8 (2006), p. 623.

[57] Kuen Yong Lee and David J Mooney. "Alginate: properties and biomedical applications". In: *Progress in polymer science* 37.1 (2012), pp. 106–126.

[58] Benjamin AE Lehner, Dominik T Schmieden, and Anne S Meyer. "A straightforward approach for 3D bacterial printing". In: *ACS synthetic biology* 6.7 (2017), pp. 1124–1130.

[59] Ana P Piedade. "4D printing: the shape-morphing in additive manufacturing". In: *Journal of Functional biomaterials* 10.1 (2019), p. 9.

[60] Kathleen Schütz et al. "Three-dimensional plotting of a cell-laden alginate/-methylcellulose blend: towards biofabrication of tissue engineering constructs with clinically relevant dimensions". In: *Journal of tissue engineering and regenerative medicine* 11.5 (2017), pp. 1574–1587.

[61] Shinji Sakai et al. "Drop-On-Drop Multimaterial 3D Bioprinting Realized by Peroxidase-Mediated Cross-Linking". In: *Macromolecular rapid communications* 39.3 (2018), p. 1700534.

[62] Waeljumah Aljohani et al. "Three-dimensional printing of alginate-gelatin-agar scaffolds using free-form motor assisted microsyringe extrusion system". In: *Journal of Polymer Research* 25.3 (2018), pp. 1–10.

[63] David B Kolesky et al. "3D bioprinting of vascularized, heterogeneous cell-laden tissue constructs". In: *Advanced materials* 26.19 (2014), p. 3124.

[64] Liliang Ouyang et al. "3D printing of shear-thinning hyaluronic acid hydrogels with secondary cross-linking". In: *ACS Biomaterials Science & Engineering* 2.10 (2016), pp. 1743–1751.

[65] Kajsa Markstedt, Johan Sundberg, and Paul Gatenholm. "3D bioprinting of cellulose structures from an ionic liquid". In: *3D Printing and Additive Manufacturing* 1.3 (2014), pp. 115–121.

[66] Tun Yuan et al. "Collagen hydrogel as an immunomodulatory scaffold in cartilage tissue engineering". In: *Journal of Biomedical Materials Research Part B: Applied Biomaterials* 102.2 (2014), pp. 337–344.

[67] Nils Frederik Hasselmann, Michael Jona Hackmann, and Wolfgang Horn. "Two-photon fabrication of hydrogel microstructures for excitation and immobilization of cells". In: *Biomedical microdevices* 20.1 (2018), p. 8.

[68] Yuanqing Xiang and Dajun Chen. "Preparation of a novel pH-responsive silver nanoparticle/poly (HEMA–PEGMA–MAA) composite hydrogel". In: *European Polymer Journal* 43.10 (2007), pp. 4178–4187.

[69] Chien-Hong Lin et al. “Novel silicone hydrogel based on PDMS and PEGMA for contact lens application”. In: *Colloids and Surfaces B: Biointerfaces* 123 (2014), pp. 986–994.

[70] Tuğrul Tolga Demirtaş, Gülseren Irmak, and Menemşe Gümüşderelioğlu. “A bioprintable form of chitosan hydrogel for bone tissue engineering”. In: *Biofabrication* 9.3 (2017), p. 035003.

[71] James PK Armstrong et al. “3D bioprinting using a templated porous bioink”. In: *Advanced healthcare materials* 5.14 (2016), pp. 1724–1730.

[72] Chuang Li et al. “Rapid formation of a supramolecular polypeptide–DNA hydrogel for in situ three-dimensional multilayer bioprinting”. In: *Angewandte Chemie* 127.13 (2015), pp. 4029–4033.

[73] Alex Buchberger et al. “Reversible Control of Gelatin Hydrogel Stiffness by Using DNA Crosslinkers”. In: *ChemBioChem* 22.10 (2021).

[74] Gabriel R Lopez-Marcial et al. “Agarose-based hydrogels as suitable bioprinting materials for tissue engineering”. In: *ACS Biomaterials Science & Engineering* 4.10 (2018), pp. 3610–3616.

[75] Naomi Paxton et al. “Proposal to assess printability of bioinks for extrusion-based bioprinting and evaluation of rheological properties governing bioprintability”. In: *Biofabrication* 9.4 (2017), p. 044107.

[76] Zhengyi Zhang et al. “Evaluation of bioink printability for bioprinting applications”. In: *Applied Physics Reviews* 5.4 (2018), p. 041304.

[77] Brian Derby. “Inkjet printing of functional and structural materials: fluid property requirements, feature stability, and resolution”. In: *Annual Review of Materials Research* 40 (2010), pp. 395–414.

[78] JE Fromm. “Numerical calculation of the fluid dynamics of drop-on-demand jets”. In: *IBM Journal of Research and Development* 28.3 (1984), p. 322.

[79] N Reis and B Derby. “Ink jet deposition of ceramic suspensions: Modeling and experiments of droplet formation”. In: *MRS Online Proceedings Library (OPL)* 625 (2000).

[80] R. J. Poole. “The Deborah and Weissenberg numbers”. In: *Rheology Bulletin* 53.2 (2021), pp. 32–39.

[81] Marcus Reiner. “The deborah number”. In: *Physics today* 17.1 (1964), p. 62.

[82] Neil F Morrison and Oliver G Harlen. “Viscoelasticity in inkjet printing”. In: *Rheologica acta* 49.6 (2010), pp. 619–632.

[83] Jun Yin, Dengke Zhao, and Jingyi Liu. “Trends on physical understanding of bioink printability”. In: *Bio-Design and Manufacturing* 2.1 (2019), pp. 50–54.

[84] Julia Emmermacher et al. “Engineering considerations on extrusion-based bioprinting: interactions of material behavior, mechanical forces and cells in the printing needle”. In: *Biofabrication* 12.2 (2020), p. 025022.

[85] Matthew R Jones, Nadrian C Seeman, and Chad A Mirkin. “Programmable materials and the nature of the DNA bond”. In: *Science* 347.6224 (2015).

[86] Paul WK Rothemund. “Folding DNA to create nanoscale shapes and patterns”. In: *Nature* 440.7082 (2006), pp. 297–302.

[87] Shawn M Douglas et al. “Self-assembly of DNA into nanoscale three-dimensional shapes”. In: *Nature* 459.7245 (2009), pp. 414–418.

[88] Leonard M Adleman. “Computing with DNA”. In: *Scientific american* 279.2 (1998), pp. 54–61.

[89] Masami Hagiya et al. “On DNA-based gellular automata”. In: *International Conference on Unconventional Computation and Natural Computation*. Springer. 2014, pp. 177–189.

[90] Angelo Cangialosi et al. “DNA sequence–directed shape change of photopatterned hydrogels via high-degree swelling”. In: *Science* 357.6356 (2017), pp. 1126–1130.

[91] John SantaLucia and Donald Hicks. “The Thermodynamics of DNA Structural Motifs”. In: *Annual Review of Biophysics and Biomolecular Structure* 33.1 (2004), pp. 415–440. ISSN: 1056-8700. DOI: `10.1146/annurev.biophys.32.110601.141800`.

[92] David Yu Zhang and Erik Winfree. “Control of DNA strand displacement kinetics using toehold exchange”. In: *Journal of the American Chemical Society* 131.47 (2009), pp. 17303–17314.

[93] V.A. Bloomfield, D.M. Crothers, and I. Tinoco. *Nucleic Acids: Structures, Properties, and Functions*. University Science Books, 2000. ISBN: 9780935702491.

[94] Yinghui Li and Dingsheng Zhao. “Basics of Molecular Biology”. In: *Molecular Imaging: Fundamentals and Applications* (2013), pp. 541–601.

[95] iGEM Foundation. *Registry of Standard Biological Parts*. URL: `http://parts.igem.org/` (visited on 09/20/2021).

[96] Allen G Marr. “Growth rate of Escherichia coli”. In: *Microbiological reviews* 55.2 (1991), pp. 316–333.

[97] Jaan Männik et al. “Bacterial growth and motility in sub-micron constrictions”. In: *Proceedings of the National Academy of Sciences* 106.35 (2009), pp. 14861–14866.

[98] MH Zwietering et al. “Modeling of the bacterial growth curve”. In: *Applied and environmental microbiology* 56.6 (1990), pp. 1875–1881.

[99] Peter J Kennelly and Malcolm Potts. “Fancy meeting you here! A fresh look at" prokaryotic" protein phosphorylation”. In: *Journal of bacteriology* 178.16 (1996), pp. 4759–4764.

[100] Ferruccio Ritossa. “A new puffing pattern induced by temperature shock and DNP in Drosophila”. In: *Experientia* 18.12 (1962), pp. 571–573.

[101] Milton J Schlesinger. “Heat shock proteins.” In: *Journal of Biological Chemistry* 265.21 (1990), pp. 12111–12114.

[102] Susan Lindquist. “The heat-shock response”. In: *Annual review of biochemistry* 55.1 (1986), pp. 1151–1191.

[103] FC Neidhardt, RA VanBogelen, and V Vaughn. “The genetics and regulation of heat-shock proteins”. In: *Annual review of genetics* 18.1 (1984), p. 295.

[104] T Yamamori et al. “Transient regulation of protein synthesis in Escherichia coli upon shift-up of growth temperature”. In: *Journal of Bacteriology* 134.3 (1978), pp. 1133–1140.

[105] Peggy G Lemaux et al. “Transient rates of synthesis of individual polypeptides in E. coli following temperature shifts”. In: *Cell* 13.3 (1978), p. 427.

[106] Timothy J Welch et al. “Stress response of Escherichia coli to elevated hydrostatic pressure”. In: *Journal of bacteriology* 175.22 (1993), pp. 7170–7177.

[107] Abram Aertsen et al. “Heat shock protein-mediated resistance to high hydrostatic pressure in Escherichia coli”. In: *Applied and Environmental Microbiology* 70.5 (2004), pp. 2660–2666.

[108] HJ Chung, W Bang, and MA Drake. “Stress response of Escherichia coli”. In: *Comprehensive reviews in food science and food safety* 5.3 (2006), p. 52.

[109] Laszlo N Csonka. “Physiological and genetic responses of bacteria to osmotic stress”. In: *Microbiological reviews* 53.1 (1989), pp. 121–147.

[110] Laszlo N Csonka and Andrew D Hanson. “Prokaryotic osmoregulation: genetics and physiology”. In: *Annual review of microbiology* 45.1 (1991), p. 569.

[111] Palghat A Ramachandran. *Mass transfer processes: modeling, computations, and design*. Prentice Hall, 2018.

[112] Johan HJ Leveau and Steven E Lindow. “Predictive and interpretive simulation of green fluorescent protein expression in reporter bacteria”. In: *Journal of bacteriology* 183.23 (2001), pp. 6752–6762.

[113] John von Neumann and Arthur W Burks. “Theory of self-reproducing automata”. In: (1966).

[114] John H Conway. *On Numbers and Games*. London Mathematical Society Monographs, No. 6, Academic Press, London-New-San Francisco, 1976.

[115] DG Green. “Cellular automata models in biology”. In: *Mathematical and Computer Modelling* 13.6 (1990), pp. 69–74.

[116] Stephen Wolfram. “Universality and complexity in cellular automata”. In: *Physica D: Nonlinear Phenomena* 10.1 (1984), pp. 1–35.

[117] Stephan Wolfram. “Cellular automata as models of complexity”. In: *Nonlinear Physics for Beginners: Fractals, Chaos, Solitons, Pattern Formation, Cellular Automata, Complex Systems* 311 (1998), p. 197.

[118] James D Watson and Francis HC Crick. “Molecular structure of nucleic acids: a structure for deoxyribose nucleic acid”. In: *Nature* 171.4356 (1953), p. 737.

[119] Francis HC Crick. “On protein synthesis”. In: *Symp Soc Exp Biol*. Vol. 12. 138-63. 1958, p. 8.

[120] David H Jones, Richard McWilliam, and Alan Purvis. “Designing convergent cellular automata”. In: *Biosystems* 96.1 (2009), pp. 80–85.

[121] D Jones, Richard McWilliam, and Alan Purvis. “Design of selfassembling, self-repairing 3d irregular cellular automata”. In: *New Advanced Technologies (A. Lazinica, ed.)* (2011), pp. 373–394.

[122] Ross Mead. “Cellular Automata for Control and Interactions of Large Formations of Robots”. PhD thesis. Southern Illinois University, 2008.

[123] Susan Hackwood and Jing Wang. “The engineering of cellular robotic systems”. In: *Intelligent Control, 1988. Proceedings., IEEE International Symposium on*. IEEE. 1988, pp. 70–75.

[124] Kyle Gilpin, Ara Knaian, and Daniela Rus. “Robot pebbles: One centimeter modules for programmable matter through self-disassembly”. In: *Robotics and Automation (ICRA), 2010 IEEE International Conference on*. IEEE. 2010, pp. 2485–2492.

[125] Itsuro Tomatsu, Ke Peng, and Alexander Kros. “Photoresponsive hydrogels for biomedical applications”. In: *Advanced drug delivery reviews* 63.14-15 (2011), pp. 1257–1266.

[126] Zbigniew L Pianowski. “Recent implementations of molecular photoswitches into smart materials and biological systems”. In: *Chemistry–A European Journal* 25.20 (2019), pp. 5128–5144.

[127] Silvia Scarmagnani et al. “Polystyrene bead-based system for optical sensing using spiropyran photoswitches”. In: *J. Mater. Chem.* 18 (42 2008), pp. 5063–5071. DOI: `10.1039/B810080B`.

[128] Wayne Francis et al. “Spiropyran based hydrogels actuators—Walking in the light”. In: *Sensors and Actuators B: Chemical* 250 (2017), pp. 608–616.

[129] Jiehao Chen et al. “A photoresponsive hydrogel with enhanced photoefficiency and the decoupled process of light activation and shape changing for precise geometric control”. In: *ACS Applied Materials & Interfaces* 12.34 (2020), pp. 38647–38654.

[130] Anthony Tabet et al. “Modulating stiffness with photo-switchable supramolecular hydrogels”. In: *Polymer Chemistry* 10.4 (2019), pp. 467–472.

[131] Grégorio Crini et al. “Cyclodextrins, from molecules to applications”. In: *Environmental chemistry letters* 16.4 (2018), pp. 1361–1375.

[132] Dongsheng Wang et al. “Supramolecular hydrogels constructed by red-light-responsive host–guest interactions for photo-controlled protein release in deep tissue”. In: *Soft Matter* 11.38 (2015), pp. 7656–7662.

[133] Marcel JE Fischer. “Amine coupling through EDC/NHS: a practical approach”. In: *Surface plasmon resonance*. Springer, 2010, pp. 55–73.

[134] Shingo Tamesue et al. “Photoswitchable supramolecular hydrogels formed by cyclodextrins and azobenzene polymers”. In: *Angewandte Chemie International Edition* 49.41 (2010), pp. 7461–7464.

[135] Mingwei Wang et al. “Photo-reversible supramolecular hydrogels assembled by α-cyclodextrin and azobenzene substituted poly-(acrylic acid)s: effect of substitution degree, concentration, and tethered chain length”. In: *Macromolecular Materials and Engineering* 301.2 (2016), pp. 191–198.

[136] Ke Peng, Itsuro Tomatsu, and Alexander Kros. “Light controlled protein release from a supramolecular hydrogel”. In: *Chemical communications* 46.23 (2010), pp. 4094–4096.

[137] Xinyu Zhao et al. “Light-tuning amphiphility of host-guest Alginate-based supramolecular assemblies for photo-responsive Pickering emulsions”. In: *Carbohydrate polymers* 251 (2021), p. 117072.

[138] Lukas Aufinger and Friedrich C Simmel. “Artificial gel-based organelles for spatial organization of cell-free gene expression reactions”. In: *Angewandte Chemie International Edition* 57.52 (2018), pp. 17245–17248.

[139] AN De Belder and Kirsti Granath. “Preparation and properties of fluorescein-labelled dextrans”. In: *Carbohydrate Research* 30.2 (1973), pp. 375–378.

[140] Julia Müller et al. “Programming Diffusion and Localization of DNA Signals in 3D-Printed DNA-Functionalized Hydrogels”. In: *Small* 16.31 (2020), p. 2001815.

[141] Mohammad Vaezi, Hermann Seitz, and Shoufeng Yang. “A review on 3D micro-additive manufacturing technologies”. In: *The International Journal of Advanced Manufacturing Technology* 67.5-8 (2013), pp. 1721–1754.

[142] Chuang Li et al. “Rapid formation of a supramolecular polypeptide–DNA hydrogel for in situ three-dimensional multilayer bioprinting”. In: *Angewandte Chemie* 127.13 (2015), pp. 4029–4033.

[143] Jiaofang Huang et al. “Programmable and printable Bacillus subtilis biofilms as engineered living materials”. In: *Nature chemical biology* 15.1 (2019), p. 34.

[144] Amer B. Dababneh and Ibrahim T. Ozbolat. “Bioprinting Technology: A Current State-of-the-Art Review”. In: *Journal of Manufacturing Science and Engineering* 136.6 (2014). ISSN: 1087-1357. DOI: `10.1115/1.4028512`.

[145] Katja Hölzl et al. “Bioink properties before, during and after 3D bioprinting”. In: *Biofabrication* 8.3 (2016), p. 032002.

[146] Friedrich C Simmel, Bernard Yurke, and Hari R Singh. “Principles and applications of nucleic acid strand displacement reactions”. In: *Chemical reviews* 119.10 (2019), pp. 6326–6369.

[147] Friedrich C Simmel and Rebecca Schulman. “Self-organizing materials built with DNA”. In: *MRS Bulletin* 42.12 (2017), pp. 913–919.

[148] Jianping Zheng et al. “From molecular to macroscopic via the rational design of a self-assembled 3D DNA crystal”. In: *Nature* 461.7260 (2009), p. 74.

[149] Evi Stahl et al. “Impact of heterogeneity and lattice bond strength on DNA triangle crystal growth”. In: *ACS nano* 10.10 (2016), pp. 9156–9164.

[150] Hao Qi et al. “DNA-directed self-assembly of shape-controlled hydrogels”. In: *Nature communications* 4.1 (2013), pp. 1–10.

[151] Klaus F Wagenbauer, Christian Sigl, and Hendrik Dietz. “Gigadalton-scale shape-programmable DNA assemblies”. In: *Nature* 552.7683 (2017), p. 78.

[152] Tao Zhang et al. “3D DNA origami crystals”. In: *Advanced Materials* 30.28 (2018), p. 1800273.

[153] Anthony J Kim, Paul L Biancaniello, and John C Crocker. “Engineering DNA-mediated colloidal crystallization”. In: *Langmuir* 22.5 (2006), pp. 1991–2001.

[154] Dmytro Nykypanchuk et al. “DNA-guided crystallization of colloidal nanoparticles”. In: *Nature* 451.7178 (2008), pp. 549–552.

[155] Mirjam E Leunissen et al. “Switchable self-protected attractions in DNA-functionalized colloids”. In: *Nature materials* 8.7 (2009), pp. 590–595.

[156] Matthew R Jones et al. “DNA-nanoparticle superlattices formed from anisotropic building blocks”. In: *Nature materials* 9.11 (2010), pp. 913–917.

[157] Yu Wang et al. “Crystallization of DNA-coated colloids”. In: *Nature communications* 6.1 (2015), pp. 1–8.

[158] W Benjamin Rogers and Vinothan N Manoharan. “Programming colloidal phase transitions with DNA strand displacement”. In: *Science* 347.6222 (2015), pp. 639–642.

[159] Yin Zhang et al. “Sequential self-assembly of DNA functionalized droplets”. In: *Nature communications* 8.1 (2017), pp. 1–7.

[160] Jason S Kahn, Yuwei Hu, and Itamar Willner. “Stimuli-responsive DNA-based hydrogels: From basic principles to applications”. In: *Accounts of chemical research* 50.4 (2017), pp. 680–690.

[161] Feng Li et al. “Polymeric DNA hydrogel: Design, synthesis and applications”. In: *Progress in Polymer Science* 98 (2019), p. 101163.

[162] Yougen Li et al. “Controlled assembly of dendrimer-like DNA”. In: *Nature materials* 3.1 (2004), pp. 38–42.

[163] Soong Ho Um et al. “Enzyme-catalysed assembly of DNA hydrogel”. In: *Nature materials* 5.10 (2006), pp. 797–801.

[164] Nokyoung Park et al. “A cell-free protein-producing gel”. In: *Nature materials* 8.5 (2009), pp. 432–437.

[165] Jong Bum Lee et al. “A mechanical metamaterial made from a DNA hydrogel”. In: *Nature nanotechnology* 7.12 (2012), pp. 816–820.

[166] Yongzheng Xing et al. “Self-Assembled DNA Hydrogels with Designable Thermal and Enzymatic Responsiveness”. In: *Advanced Materials* 23.9 (), pp. 1117–1121. DOI: `https://doi.org/10.1002/adma.201003343`.

[167] Chuang Li et al. “A supramolecular hydrogel with identical cross-linking point density but distinctive rheological properties”. In: *Mater. Chem. Front.* 1 (4 2017), pp. 654–659. DOI: `10.1039/C6QM00176A`.

[168] Zhongyang Xing et al. “Microrheology of DNA hydrogels”. In: *Proceedings of the National Academy of Sciences* 115.32 (2018), pp. 8137–8142.

[169] Chi Yao et al. “Double rolling circle amplification generates physically cross-linked DNA network for stem cell fishing”. In: *Journal of the American Chemical Society* 142.7 (2020), pp. 3422–3429.

[170] Jianpu Tang et al. “Super-Soft and Super-Elastic DNA Robot with Magnetically Driven Navigational Locomotion for Cell Delivery in Confined Space”. In: *Angewandte Chemie International Edition* 59.6 (2020), pp. 2490–2495.

[171] David C Lin, Bernard Yurke, and Noshir A Langrana. “Mechanical properties of a reversible, DNA-crosslinked polyacrylamide hydrogel”. In: *J. Biomech. Eng.* 126.1 (2004), pp. 104–110.

[172] Tim Liedl et al. “Controlled trapping and release of quantum dots in a DNA-switchable hydrogel”. In: *small* 3.10 (2007), pp. 1688–1693.

[173] Julian Thiele et al. “DNA-functionalized hydrogels for confined membrane-free in vitro transcription/translation”. In: *Lab on a Chip* 14.15 (2014), p. 2651.

[174] Yuwei Hu et al. “Reversible modulation of DNA-based hydrogel shapes by internal stress interactions”. In: *Journal of the American Chemical Society* 138.49 (2016), pp. 16112–16119.

[175] Angelo Cangialosi et al. “DNA sequence–directed shape change of photopatterned hydrogels via high-degree swelling”. In: *Science* 357.6356 (2017), 1126–1130.

[176] Takuto Hosoya et al. “Pattern Formation on Discrete Gel Matrix Based on DNA Computing”. In: *New Generation Computing* 37.1 (2019), pp. 97–111. ISSN: 1882-7055. DOI: `10.1007/s00354-018-0047-1`.

[177] Gabriel Villar, Alexander D Graham, and Hagan Bayley. “A tissue-like printed material”. In: *Science* 340.6128 (2013), pp. 48–52.

[178] Sören Doose, Hannes Barsch, and Markus Sauer. “Polymer properties of polythymine as revealed by translational diffusion”. In: *Biophysical journal* 93.4 (2007), pp. 1224–1234.

[179] Srikkanth Balasubramanian, Marie-Eve Aubin-Tam, and Anne S Meyer. *3D printing for the fabrication of biofilm-based functional living materials*. 2019.

[180] Charlie Gilbert et al. “Living materials with programmable functionalities grown from engineered microbial co-cultures”. In: *Nature materials* 20.5 (2021), pp. 691–700.

[181] Julien O Dubuis et al. “Positional information, in bits”. In: *Proceedings of the National Academy of Sciences* 110.41 (2013), pp. 16301–16308.

[182] F Bettaieb et al. “Immobilization of E. coli bacteria in three-dimensional matrices for ISFET biosensor design”. In: *Bioelectrochemistry* 71.2 (2007), pp. 118–125.

[183] Hae Ja Shin. “Agarose-gel-immobilized recombinant bacterial biosensors for simple and disposable on-site detection of phenolic compounds”. In: *Applied microbiology and biotechnology* 93.5 (2012), pp. 1895–1904.

[184] Jorge A Trelles et al. “Immobilized Escherichia coli BL21 as a catalyst for the synthesis of adenine and hypoxanthine nucleosides”. In: *Chemistry & biodiversity* 1.2 (2004), pp. 280–288.

[185] Megan C Freyman et al. “3D printing of living bacteria electrode”. In: *Nano Research* 13.5 (2020), pp. 1318–1323.

[186] Jodi L Connell et al. “3D printing of microscopic bacterial communities”. In: *Proceedings of the National Academy of Sciences* 110.46 (2013), p. 18380.

[187] Evita Ning et al. “3D bioprinting of mature bacterial biofilms for antimicrobial resistance drug testing”. In: *Biofabrication* 11.4 (2019), p. 045018.

[188] Se Heang Oh et al. “Oxygen generating scaffolds for enhancing engineered tissue survival”. In: *Biomaterials* 30.5 (2009), pp. 757–762.

[189] Eileen Pedraza et al. “Preventing hypoxia-induced cell death in beta cells and islets via hydrolytically activated, oxygen-generating biomaterials”. In: *Proceedings of the National Academy of Sciences* 109.11 (2012), p. 4245.

[190] Neslihan Alemdar et al. “Oxygen-generating photo-cross-linkable hydrogels support cardiac progenitor cell survival by reducing hypoxia-induced necrosis”. In: *ACS biomaterials science & engineering* 3.9 (2017), pp. 1964–1971.

[191] Julia Müller et al. “Bacterial Growth, Communication, and Guided Chemotaxis in 3D-Bioprinted Hydrogel Environments”. In: *ACS Applied Materials & Interfaces* 14.14 (2022), pp. 15871–15880.

[192] Jeffrey J Tabor et al. “A synthetic genetic edge detection program”. In: *Cell* 137.7 (2009), pp. 1272–1281.

[193] Alvin Tamsir, Jeffrey J Tabor, and Christopher A Voigt. “Robust multicellular computing using genetically encoded NOR gates and chemical ‘wires’”. In: *Nature* 469.7329 (2011), pp. 212–215.

[194] Paul K Grant et al. “Orthogonal intercellular signaling for programmed spatial behavior”. In: *Molecular systems biology* 12.1 (2016), p. 849.

[195] Yolanda Schaerli et al. “A unified design space of synthetic stripe-forming networks”. In: *Nature communications* 5.1 (2014), pp. 1–10.

[196] Javier Santos-Moreno et al. “Multistable and dynamic CRISPRi-based synthetic circuits”. In: *Nature communications* 11.1 (2020), pp. 1–8.

[197] Anne M Bronikowski, Albert F Bennett, and Richard E Lenski. “Evolutionary adaptation to temperature. VIII. Effects of temperature on growth rate in natural isolates of Escherichia coli and Salmonella enterica from different thermal environments”. In: *Evolution* 55.1 (2001), pp. 33–40.

[198] Vaughn S Cooper, Albert F Bennett, and Richard E Lenski. “Evolution of thermal dependence of growth rate of Escherichia coli populations during 20,000 generations in a constant environment”. In: *Evolution* 55.5 (2001), pp. 889–896.

[199] Birgit Rudolph et al. “Evolution of Escherichia coli for growth at high temperatures”. In: *Journal of Biological Chemistry* 285.25 (2010), p. 19029.

[200] Rita L Strack et al. “Chromophore formation in DsRed occurs by a branched pathway”. In: *Journal of the American Chemical Society* 132.24 (2010), p. 8496.

[201] Roger Y Tsien. “The green fluorescent protein”. In: *Annual review of biochemistry* 67.1 (1998), pp. 509–544.

[202] Tiago Ramalho et al. “Single cell analysis of a bacterial sender-receiver system”. In: *PLoS One* 11.1 (2016), e0145829.

[203] Ottavio A Croze et al. “Migration of chemotactic bacteria in soft agar: role of gel concentration”. In: *Biophysical journal* 101.3 (2011), pp. 525–534.

[204] Leandro A Pereira et al. “Emergency evacuation models based on cellular automata with route changes and group fields”. In: *Physica A: Statistical Mechanics and its Applications* 473 (2017), pp. 97–110.

[205] Nuria Pelechano and Ali Malkawi. “Evacuation simulation models: Challenges in modeling high rise building evacuation with cellular automata approaches”. In: *Automation in construction* 17.4 (2008), pp. 377–385.

[206] S Hoya White, A Martin Del Rey, and G Rodriguez Sánchez. “Modeling epidemics using cellular automata”. In: *Applied mathematics and computation* 186.1 (2007), pp. 193–202.

[207] Sayantan Mondal, Saumyak Mukherjee, and Biman Bagchi. “Mathematical modeling and cellular automata simulation of infectious disease dynamics: Applications to the understanding of herd immunity”. In: *The Journal of chemical physics* 153.11 (2020), p. 114119.

[208] Natalia V Menshutina, Andrey V Kolnoochenko, and Evgeniy A Lebedev. “Cellular Automata in Chemistry and Chemical Engineering”. In: *Annual Review of Chemical and Biomolecular Engineering* 11 (2020), pp. 87–108.

[209] Michael B Elowitz and Stanislas Leibler. “A synthetic oscillatory network of transcriptional regulators”. In: *Nature* 403.6767 (2000), pp. 335–338.

[210] Rodrigo Alvarenga Rezende et al. “Rheological behavior of alginate solutions for biomanufacturing”. In: *Journal of applied polymer science* 113.6 (2009), pp. 3866–3871.

[211] Marta Portolés, Miguel F Refojo, and Fee-Lai Leong. “Poloxamer 407 as a bacterial abhesive for hydrogel contact lenses”. In: *Journal of biomedical materials research* 28.3 (1994), pp. 303–309.

[212] Benjamin AE Lehner, Dominik T Schmieden, and Anne S Meyer. “A straightforward approach for 3D bacterial printing”. In: *ACS synthetic biology* 6.7 (2017), pp. 1124–1130.

[213] César Mateo et al. “Glyoxyl agarose: a fully inert and hydrophilic support for immobilization and high stabilization of proteins”. In: *Enzyme and Microbial Technology* 39.2 (2006), pp. 274–280.

[214] Valeria Grazu et al. “Glyoxyl agarose as a new chromatographic matrix”. In: *Enzyme and microbial technology* 38.7 (2006), pp. 960–966.

[215] Jorge A Trelles et al. “Immobilized Escherichia coli BL21 as a catalyst for the synthesis of adenine and hypoxanthine nucleosides”. In: *Chemistry & biodiversity* 1.2 (2004), pp. 280–288.

[216] Sina Naficy et al. “4D printing of reversible shape morphing hydrogel structures”. In: *Macromolecular Materials and Engineering* 302.1 (2017), p. 1600212.

[217] Bin Zhang et al. “3D bioprinting: an emerging technology full of opportunities and challenges”. In: *Bio-design and Manufacturing* 1.1 (2018), pp. 2–13.

[218] Honglei Jian et al. “3D bioprinting for cell culture and tissue fabrication”. In: *Bio-Design and Manufacturing* 1.1 (2018), pp. 45–61.

[219] Roberta Gentilini et al. “Polysaccharide-based hydrogels with tunable composition as 3D cell culture systems”. In: *The International journal of artificial organs* 41.4 (2018), pp. 213–222.

[220] Joseph T Muth et al. “Embedded 3D printing of strain sensors within highly stretchable elastomers”. In: *Advanced materials* 26.36 (2014), pp. 6307–6312.

[221] Shweta AnilKumar et al. “The applicability of furfuryl-gelatin as a novel bioink for tissue engineering applications”. In: *Journal of Biomedical Materials Research Part B: Applied Biomaterials* 107.2 (2019), pp. 314–323.

[222] T Ahlfeld et al. “Development of a clay based bioink for 3D cell printing for skeletal application”. In: *Biofabrication* 9.3 (2017), p. 034103.

[223] Guoliang Ying et al. “Three-dimensional bioprinting of gelatin methacryloyl (GelMA)”. In: *Bio-design and Manufacturing* 1.4 (2018), pp. 215–224.

[224] Dominik T Schmieden et al. “Printing of patterned, engineered E. coli biofilms with a low-cost 3D printer”. In: *ACS synthetic biology* 7.5 (2018), pp. 1328–1337.

[225] Dorothy Jordan Lloyd and Winnifred Bertha Pleass. “The absorption of water by gelatin”. In: *Biochemical Journal* 21.6 (1927), pp. 1352–1367.

[226] Michael Müller et al. “Nanostructured Pluronic hydrogels as bioinks for 3D bioprinting”. In: *Biofabrication* 7.3 (2015), p. 035006.

[227] Guo-Liang Ying et al. “Aqueous two-phase emulsion bioink-enabled 3D bioprinting of porous hydrogels”. In: *Advanced materials* 30.50 (2018), p. 1805460.

[228] Jason W Nichol et al. “Cell-laden microengineered gelatin methacrylate hydrogels”. In: *Biomaterials* 31.21 (2010), pp. 5536–5544.

[229] Barbara J Klotz et al. “Gelatin-methacryloyl hydrogels: towards biofabrication-based tissue repair”. In: *Trends in biotechnology* 34.5 (2016), pp. 394–407.

[230] Charles W Peak et al. “Nanoengineered colloidal inks for 3D bioprinting”. In: *Langmuir* 34.3 (2018), pp. 917–925.

[231] N Stephanopoulos. “Reversible Control of Gelatin Hydrogel Stiffness using DNA Crosslinkers.” In: *Chembiochem: a European Journal of Chemical Biology* (2021).

[232] Itsuro Tomatsu, Ke Peng, and Alexander Kros. “Photoresponsive hydrogels for biomedical applications”. In: *Advanced drug delivery reviews* 63.14-15 (2011), pp. 1257–1266.

[233] I-Ning Lee et al. “Photoresponsive hydrogels with photoswitchable mechanical properties allow time-resolved analysis of cellular responses to matrix stiffening”. In: *ACS applied materials & interfaces* 10.9 (2018), pp. 7765–7776.

[234] Maximilian Hörner et al. “Phytochrome-based extracellular matrix with reversibly tunable mechanical properties”. In: *Advanced Materials* 31.12 (2019), p. 1806727.

[235] Ramiz Daniel et al. “Synthetic analog computation in living cells”. In: *Nature* 497.7451 (2013), pp. 619–623.

[236] Marvin Whiteley, Stephen P Diggle, and E Peter Greenberg. “Progress in and promise of bacterial quorum sensing research”. In: *Nature* 551.7680 (2017), pp. 313–320.

[237] John Zenk et al. “Stable DNA-based reaction–diffusion patterns”. In: *RSC advances* 7.29 (2017), pp. 18032–18040.

[238] Karen Alim. “Fluid flows shaping organism morphology”. In: *Philosophical Transactions of the Royal Society B: Biological Sciences* 373.1747 (2018), p. 20170112.

[239] Thanapop Rodjanapanyakul et al. “Diffusion modulation of DNA by toehold exchange”. In: *Physical Review E* 97.5 (2018), p. 052617.

[240] Sifang Chen and Georg Seelig. “Programmable patterns in a DNA-based reaction–diffusion system”. In: *Soft matter* 16.14 (2020), pp. 3555–3563.

[241] Hao Zeng et al. “Light-driven, caterpillar-inspired miniature inching robot”. In: *Macromolecular rapid communications* 39.1 (2018), p. 1700224.

[242] Thomas Drepper et al. “Reporter proteins for in vivo fluorescence without oxygen”. In: *Nature biotechnology* 25.4 (2007), pp. 443–445.

[243] Elisabeth Falgenhauer et al. “Evaluation of an E. coli Cell Extract Prepared by Lysozyme-Assisted Sonication via Gene Expression, Phage Assembly and Proteomics”. In: *ChemBioChem* (2021).

A. Appendix

All additional experimental data and documentations can be found in this chapter.

A.1. Bioprinter Hardware

As already stated in Section 4.1, the printer is based on an Ultimakter Original + chassis (Section A.2). The extrusion system was replaced by an hydraulically coupled external syringe pump driven by the printer mainboard and connected to the sample syringe in the printhead. CAD files for all parts can be found in Section A.3. The syringe pump is driven by the Ultimaker stepper motor (Nema 17, 3200 microsteps).

For the mechanical coupling two precise PTFE-sealed glass syringes with luer lock adapters were linked with a PTFE tubing. As a reservoir, a 2 ml luer lock glass syringe was used, integrated via a 3-way-junction. The system was filled with incompressible mineral oil. One PTFE-sealed syringe is placed permanently in the syringe pump and the other PTFE-sealed syringe is placed in a custom aluminum syringe coupler that can be mounted on the printhead and couples the syringe pump to the sample syringe (fastening via tape).

The printhead is a custom part that can be heated via an external temperature control to keep the sample temperature constant during extrusion.

In the following sections the printer chassis, the hardware partlists and the technical drawings of all custom parts are collected.

A.2. Documentation Ultimaker Original +

The complete documentation of the commercial 3D finite filament fabrication printer can be found in the **Ultimaker Original User Manual** (same specifications for Ultimaker Original and Original Plus). Assembly instructions can be found in the **Ultimaker Original Plus Assembly Manual**. The most important device specifications are given on page 6 of the user manual (see next page); The manual can be downloaded from www.ultimaker.com/pages/support/manuals

A2. Specification of the Ultimaker Original

Printing

Print technology	Fused filament fabrication (FFF)	
Build volume	21 x 21 x 20,5 cm	
Layer resolution	Ultra high	20 micron
	High	60 micron
	Medium	100 micron
	Low	200 micron
Position precision	X 12,5 micron Y 12,5 micron Z 1.875 micron	
Filament diameter	2.85 mm (generally known as 3 mm filament)	
Nozzle diameter	0.4 mm	
Print speed	30 mm/1 - 300 mm/s	
Travel speed	30 mm/1 - 350 mm/s	

Software

Software package	Cura - Official Ultimaker
File types	STL / OBJ / DAE / AMF
Supports	Windows (XP 32 bit/7+) Ubuntu Linux (12.04+) Mac OS X (10.6 64bit +)
Connectivity	Stand-alone printing from SD-card USB (firmware)

Physical dimensions

Frame Dimension	X 35.7 cm Y 34.2 cm Z 38.8 cm
Operating dimension with UltiController, spoolholder and the max height filament guide tube	X 54.4 cm Y 34.2 cm Z 56.5 cm

Temperature

Ambient Operating Temperature	15°- 32° C
Storage Temperature	0° - 32° C
Operating nozzle temperature	180° - 260°
Operating Bed temperature	50° - 110°

Electrical

AC INPUT	100 – 240 V, 2.0 AMPS, 50 – 60 HZ 120 watt max.
Power Requirements	19V DC @ 6.32 AMPS

Electrical with heated bed

AC INPUT	100 – 240 V, 4.0 AMPS, 50 – 60 HZ 221 watt max.
Power Requirements	24V DC @ 9.2 AMPS

WARNING: The Ultimaker Original generates high temperatures and has hot moving parts that can cause injury. Never reach inside of the Ultimaker Original while it is in operation. Always control the Ultimaker Original from the push wheel on the UltiController or with the power-switch on the back. Allow the Ultimaker Original to cool down for at least 5 minutes before reaching inside.

CAUTION: When opening the Ultimaker Original for service, ensure that the power supply is turned off and the cord is disconnected from the wall socket.

CAUTION: Only use the power supply provided with your Ultimaker Original.

A.3. Hardware Components

Technical drawings of all custom hardware components and the partlists for the printer assembly can be found here for reproduction.

Custom Printhead:
Milled parts were made of aluminum (syringe pump, printhead, nozzle holder, coupler) with either bearings or brass elements (no bearing needed) and a threaded rod with the corresponding nut (M6) as ball screw. The syringe pump consists of milled aluminum parts, linear bearings, threaded rod and nut, and a SETonic custom syringe that is linked via a three-way-cock to the tubing connected to the coupled syringe forcing the sample syringe. The upper coupling part was also milled from aluminum. The lower coupling part was 3D printed from PLA with settings: printhead temperature 215 °C, bed temperature 60 °C, print speed 70 mm/s, on an Ultimaker 3 extended.

The following pages include the technical drawings in the following order:

- Technical drawing of custom SETonic 2.5 ml glass syringes (SETonic, Germany)
- Aluminum printhead to hold custom 2.5 ml glass syringes with PTFE sealing (aluminum, Workshop physics department)
- PLA coupler part to fix aluminum coupler to printhead (PLA Innofil, 3D printed with Ultimaker 3 extended)
- Aluminum coupler part to hold custom 2.5 ml glass syringes with PTFE sealing for hydraulic force coupling onto sample syringe (aluminum, Workshop physics department)
- Nozzle heating segment for SETonic syringes (aluminum, workshop physics department)

Tubing from the syringe pump to the printhead was constructed with a three-way-junction, luer-lock adapters, and pneumatic tubings.

Partlist Printhead:

- Pneumatic tubing, outer diameter = 4.0 mm (Reichelt Chemietechnik, Germany)
- Luer-lock adapter, outer diameter = 4.0 mm (Reichelt Chemietechnik, Germany)
- Stopcock-3-way, luer-lock adapters (Romed, Netherlands)
- Klauenkupplungsnabe- und stern (rigid central coupling), type 07, GESF07F05S (Conrad, Germany)

- Silberstahl Welle (linear shaft), ∅ = 6 mm (Conrad, Germany)
- HK Nadellager (linear bearing), ∅ = 5 mm (Conrad, Germany)
- M6 Gewindestange und Mutter (threaded rod and nut), (Material Supply Physics Department TUM, Germany)
- Nema 17 stepper motor, bipolar 200 steps, rev 42 × 38 mm, 2.8 V, 1.7 A phase (Polulu, USA)

External Heating:

An external heating was employed to keep the custom aluminum printhead to a desired temperature. To avoid high currents on the printer motherboard, the included thermo-components were disregarded. For heating, a thermo-controller (230 V, mounting base) was equipped with a PT100 sensor and a heating cartridge that were connected to the aluminum printhead and secured via M3 screws. The thermo-control unit was mounted within an isolated box and connected via an IEC power connector and a separated fuse.

Partlist External Heating:

- Anzeiger Jumo di eco digital indicator, CCCN 90303330 (RS Components GmbH, Germany)
- Cartridge Heater, 1/4” x 1-1/2”, 50 W, CCCN 73229000 (RS Components GmbH, Germany)
- Jumo Pt100 mit Spiralleitung, CCCN 90251980 (RS Components GmbH, Germany)
- Sicherungshalter (fuse socket) 5 mm x 20 mm (Conrad, Germany)
- Feinsicherung (fuse) 5 mm x 20 mm, 0.315 A (Conrad, Germany)

Home Step:

All 3D printers need a home step to initialize x-, y-, and z-axes similar to milling machines. For the x-y-plane the original end switches were used. For the z axis the nozzle indicates zero if a small switch is pressed at (X|Y) = (0|0). As switch a micro miniature pushbutton switch was used (TE Connectivity 1977223-3).

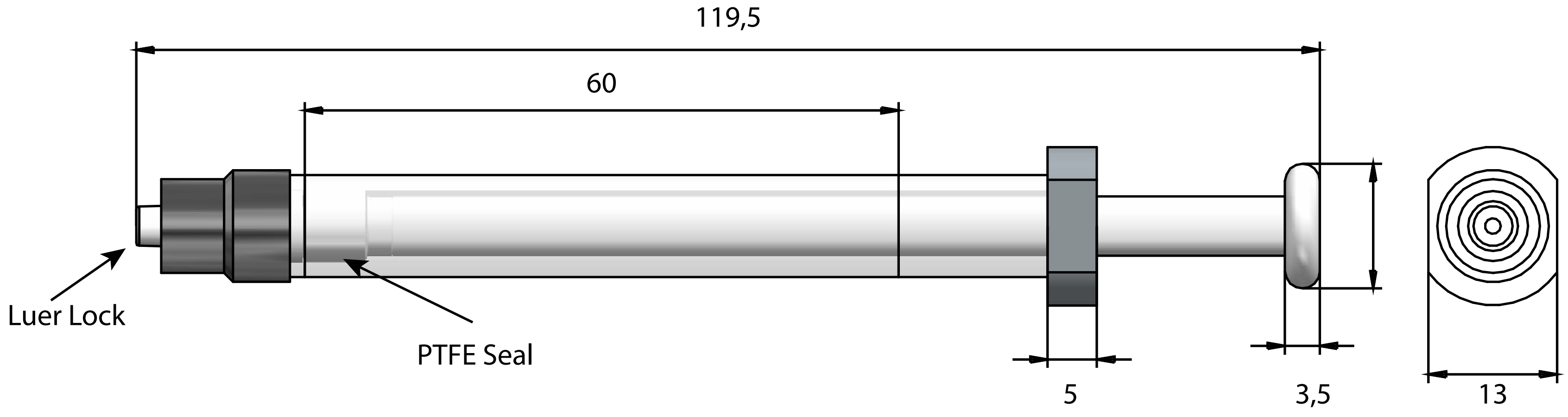

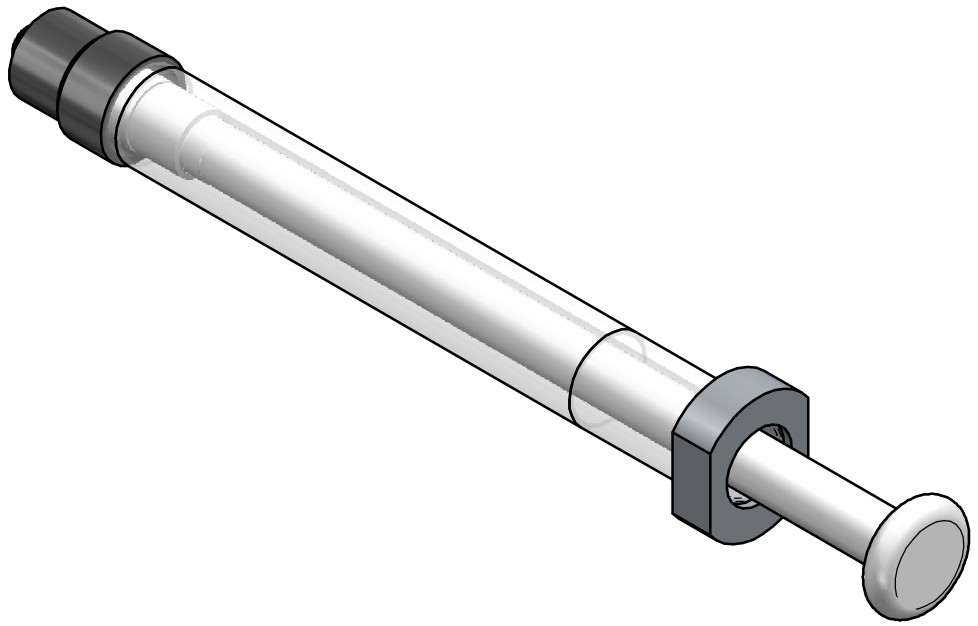

SETonic GmbH
Am Vogelherd 30
98693 Ilmenau

17.04.2018 Schultheiß

SYR 2,5 ml SYR TLL

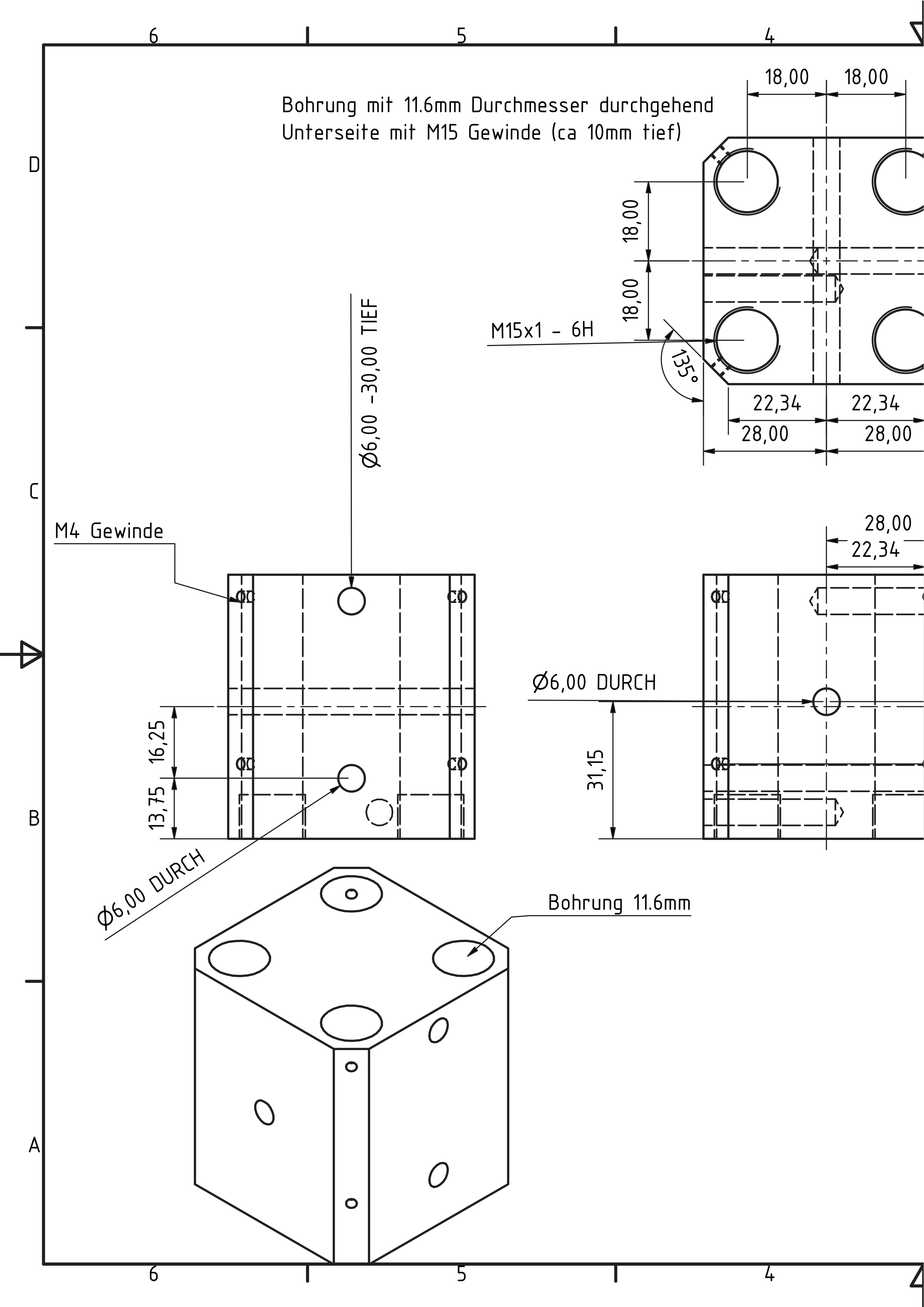

Bohrung mit 11.6mm Durchmesser durchgehend
Unterseite mit M15 Gewinde (ca 10mm tief)

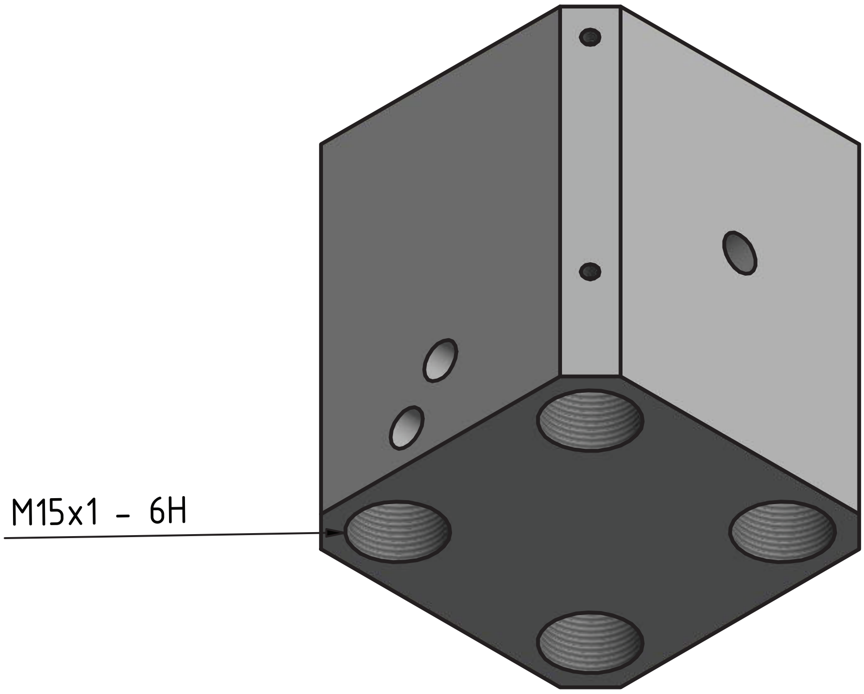

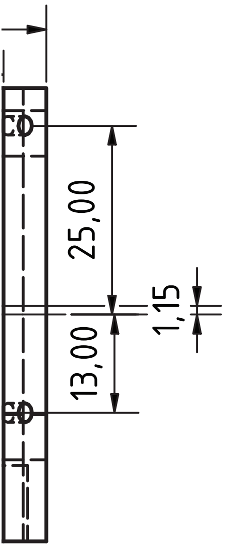

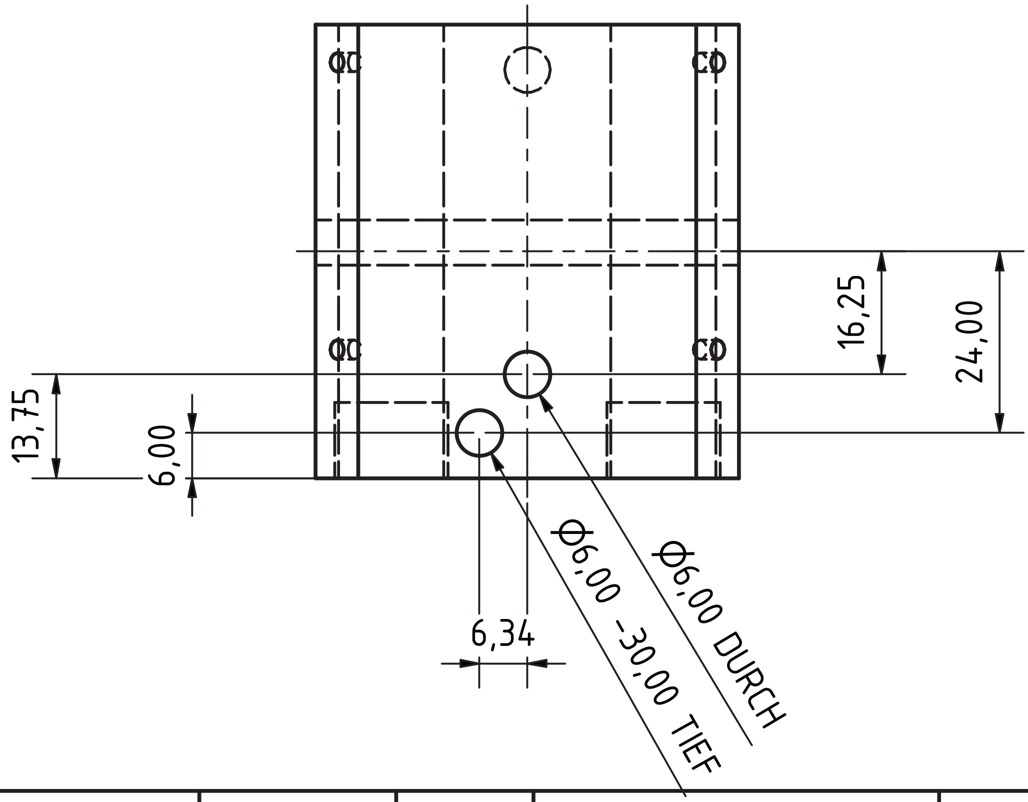

	Datum	Name
Gezeichnet	22.07.2020	Julia Müller
Kontrolliert		
Norm		

Status	Änderungen	Datum	Name

Druckkopf_Setonic

1

A3

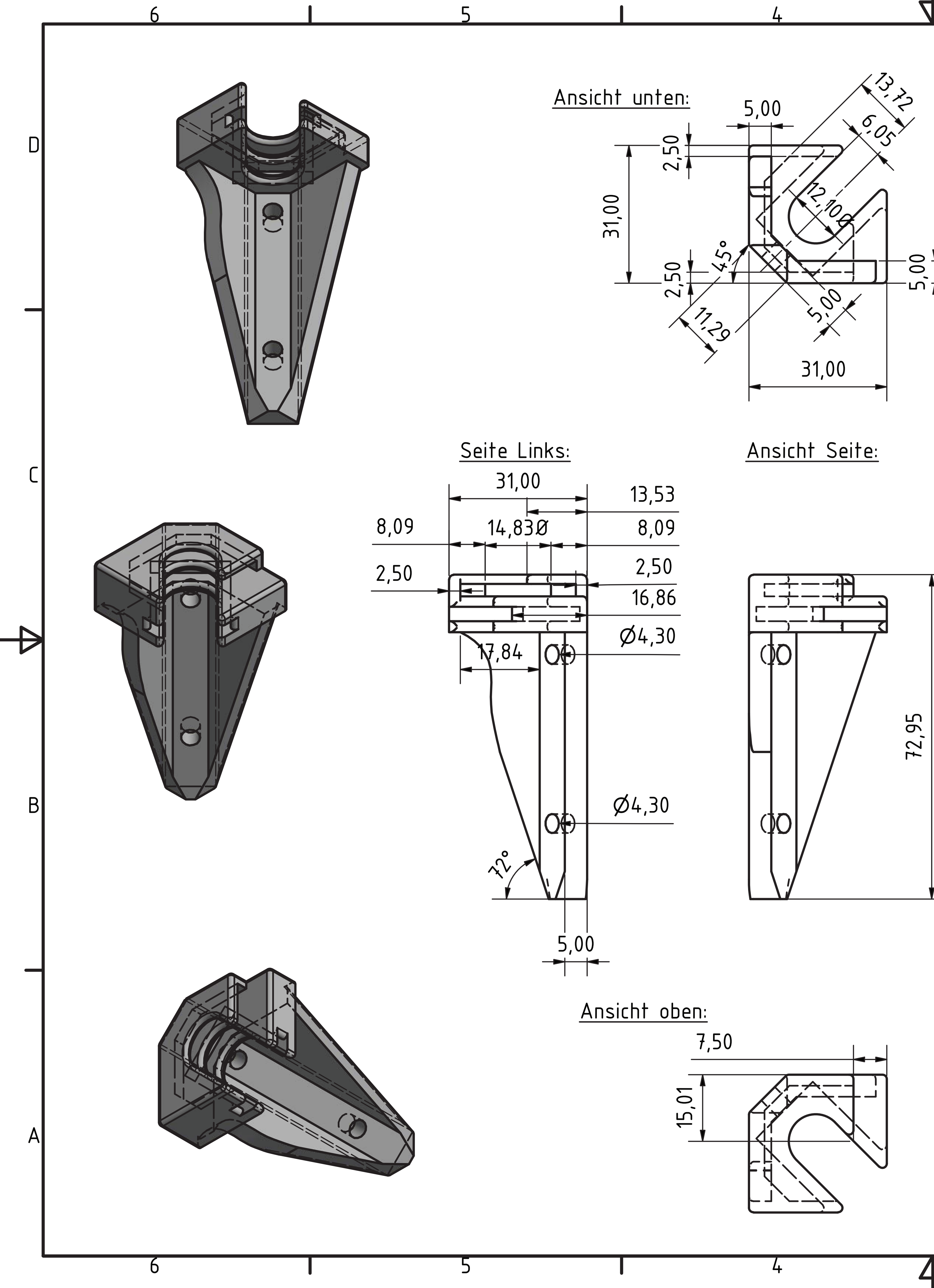
6
5
4
D
C
B
A
Ansicht unten:
13,72
5,00
6,05
2,50
31,00
12,10Ø
45°
2,50
11,29
5,00
5,00
5,0
31,00
Seite Links:
31,00
13,53
8,09
14,83Ø
8,09
2,50
2,50
16,86
Ø4,30
17,84
Ø4,30
72°
5,00
Ansicht Seite:
72,95
Ansicht oben:
7,50
15,01
6
5
4

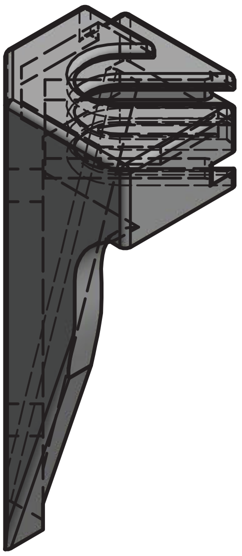

B (1 : 1)

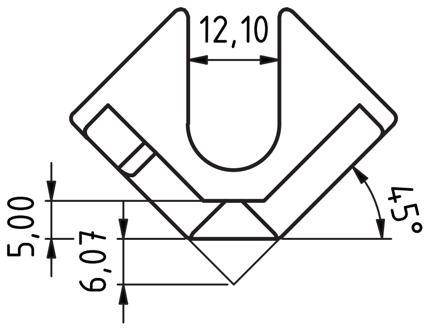

Seite Rechts:

Einschub Innen:

A (1 : 1)

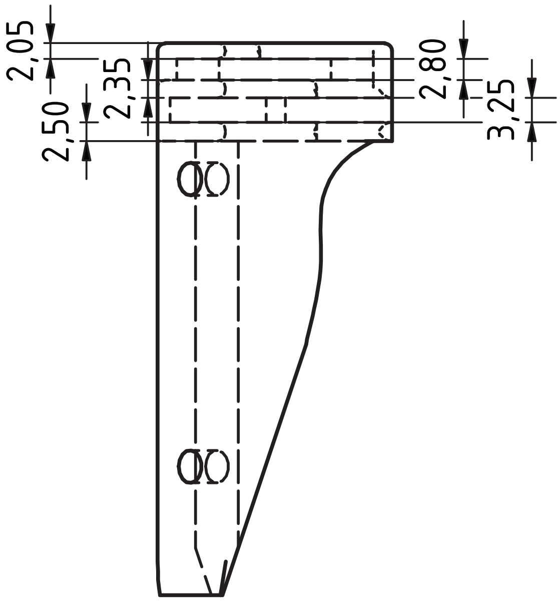

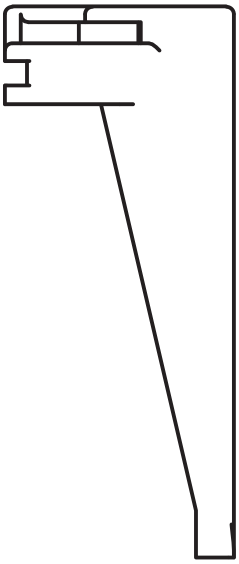

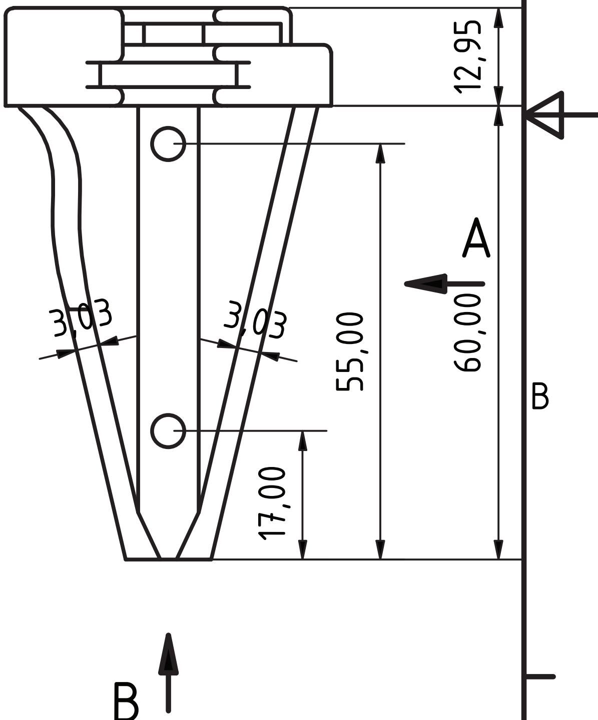

				Datum	Name
			Gezeichn	24.06.2020	Julia Müller
			Kontroll		
			Norm		
Status	Änderungen	Datum	Name		

Coupler_Printhead_Block

1

A3

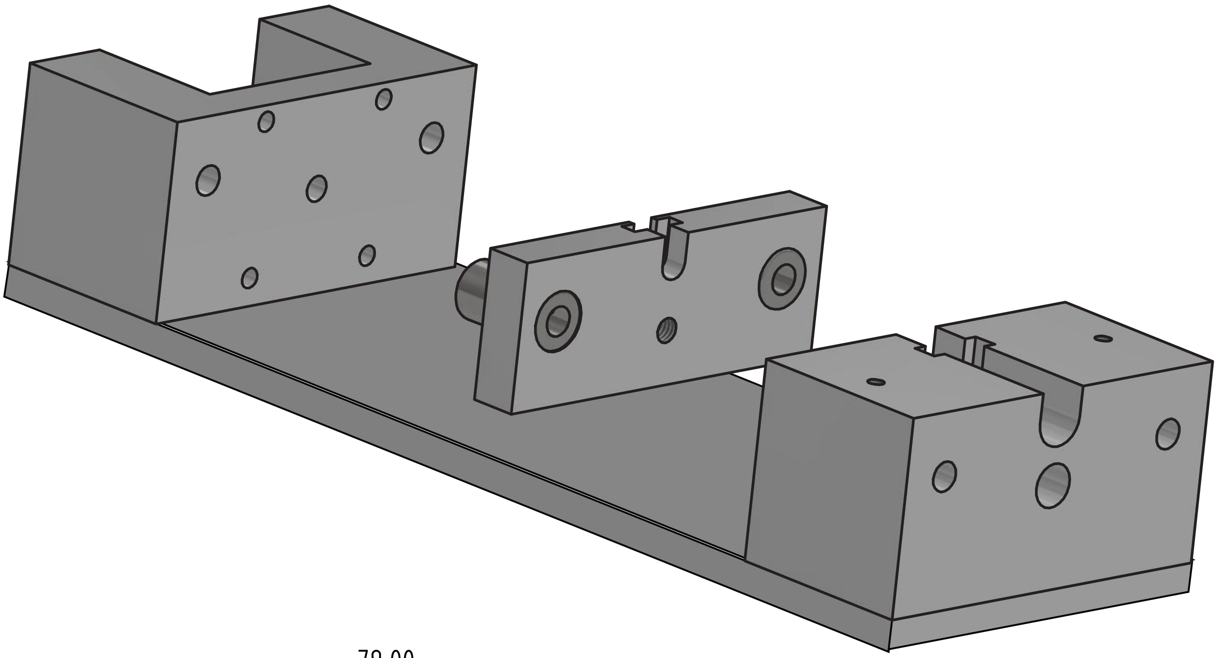

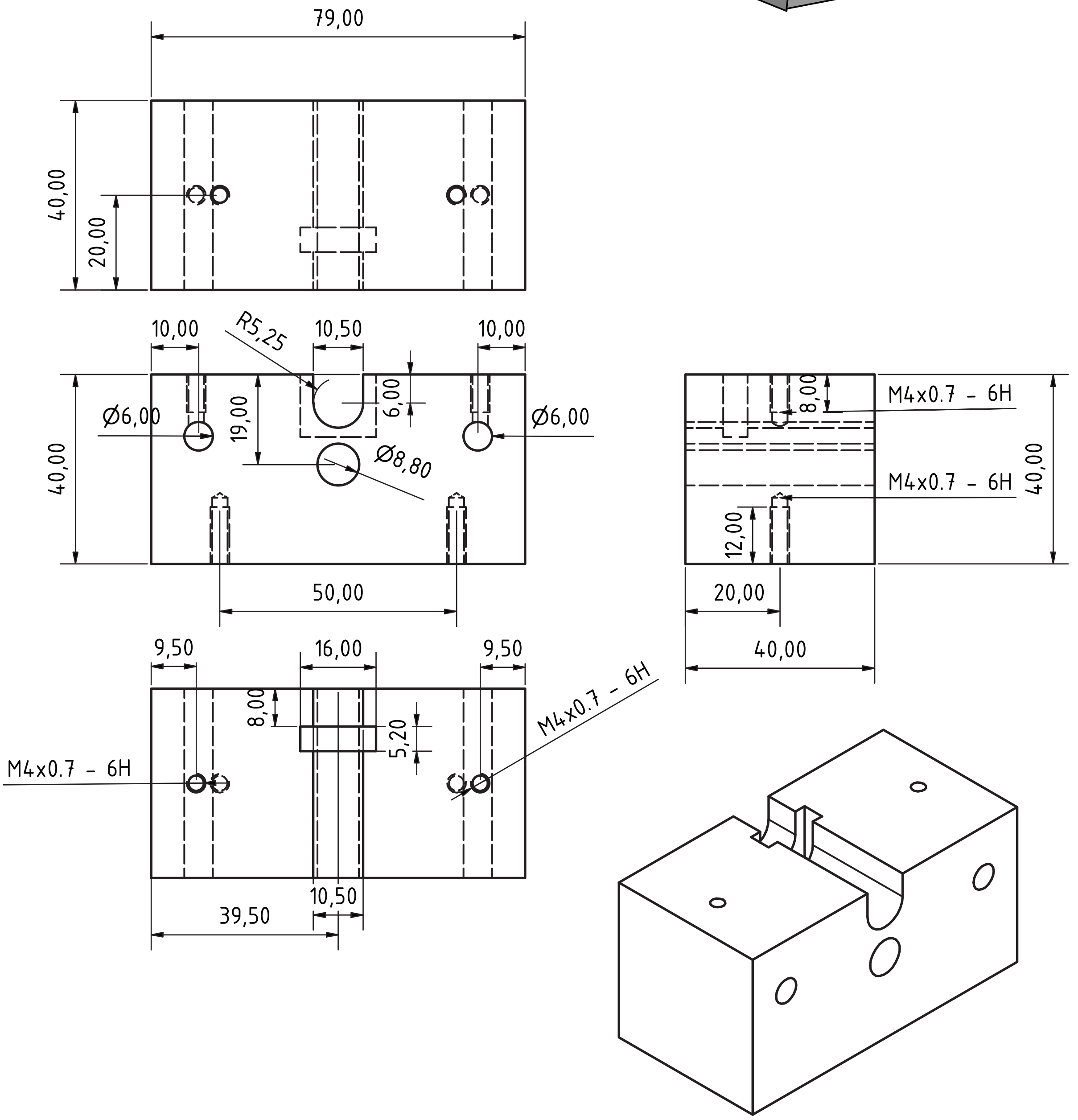
79,00
40,00
20,00
10,00
R5,25
10,50
10,00
Ø6,00
19,00
6,00
Ø6,00
Ø8,80
40,00
50,00
8,00
M4x0.7 - 6H
M4x0.7 - 6H
40,00
12,00
20,00
40,00
9,50
16,00
9,50
8,00
5,20
M4x0.7 - 6H
M4x0.7 - 6H
39,50
10,50


40,00
M4
20,00
40,00

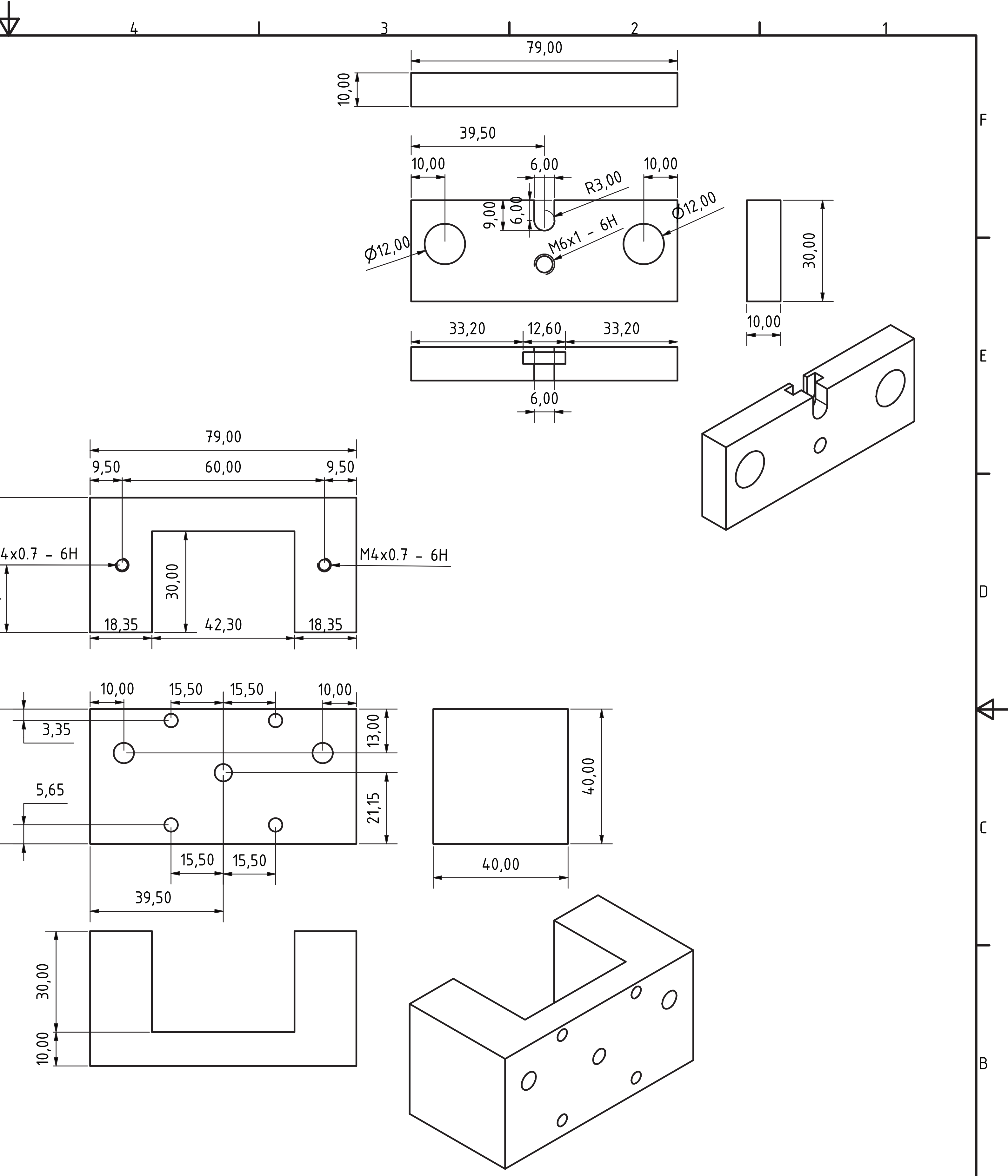

	Datum	Name
Gezeichnet	01.06.2018	Julia Müller
Kontrolliert		
Norm		

Status	Änderungen	Datum	Name

spritzenpumpe_zeichnung

1

A2

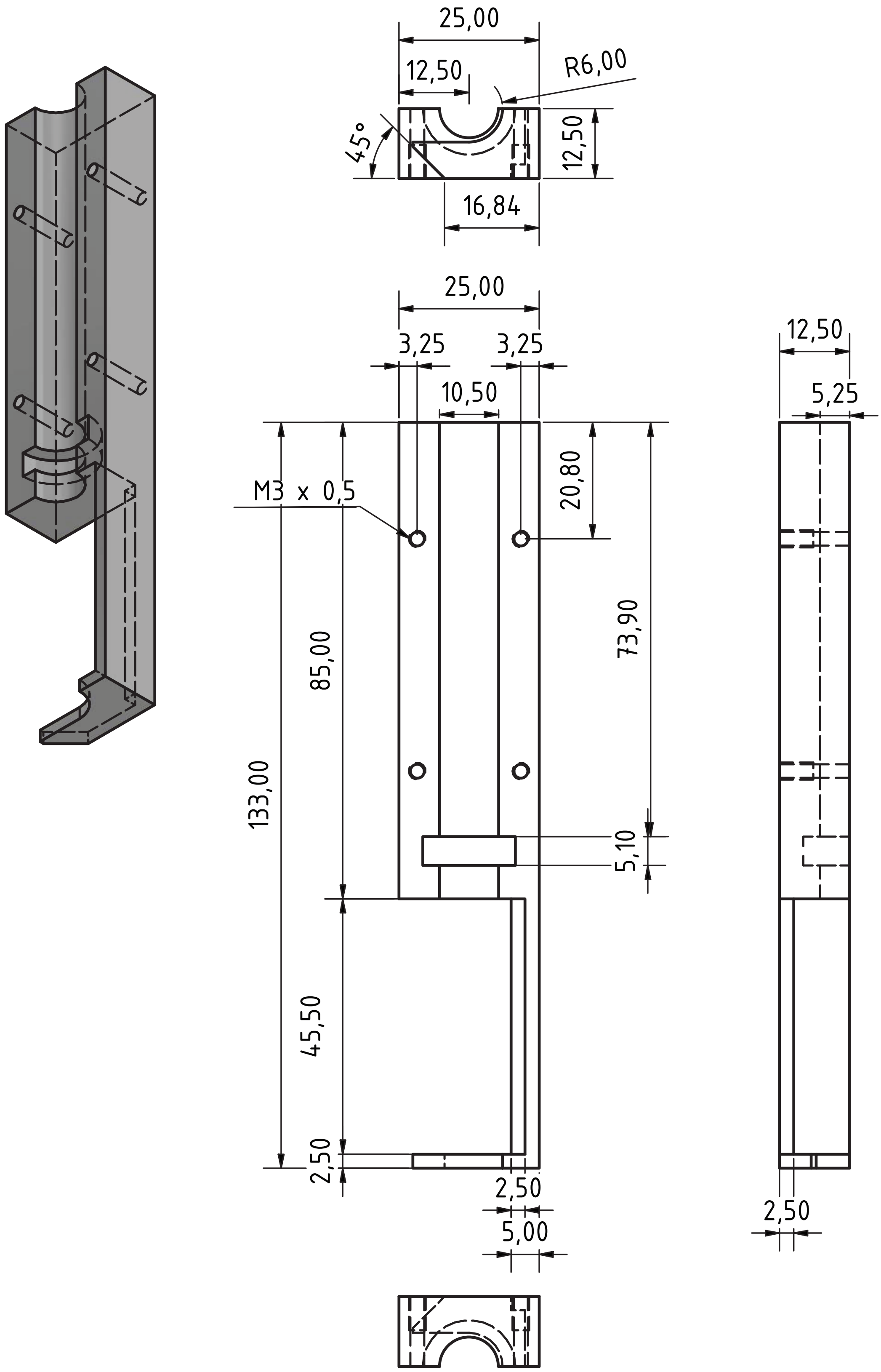

	Datum	Name
Gezeichnet	12.06.2018	Julia Müller
Kontrolliert		
Norm		

Status	Änderungen	Datum	Name

Coupler_setonic

1

A4

Bitte 2x

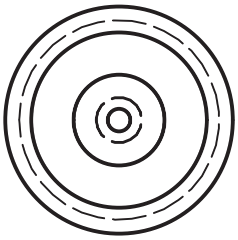

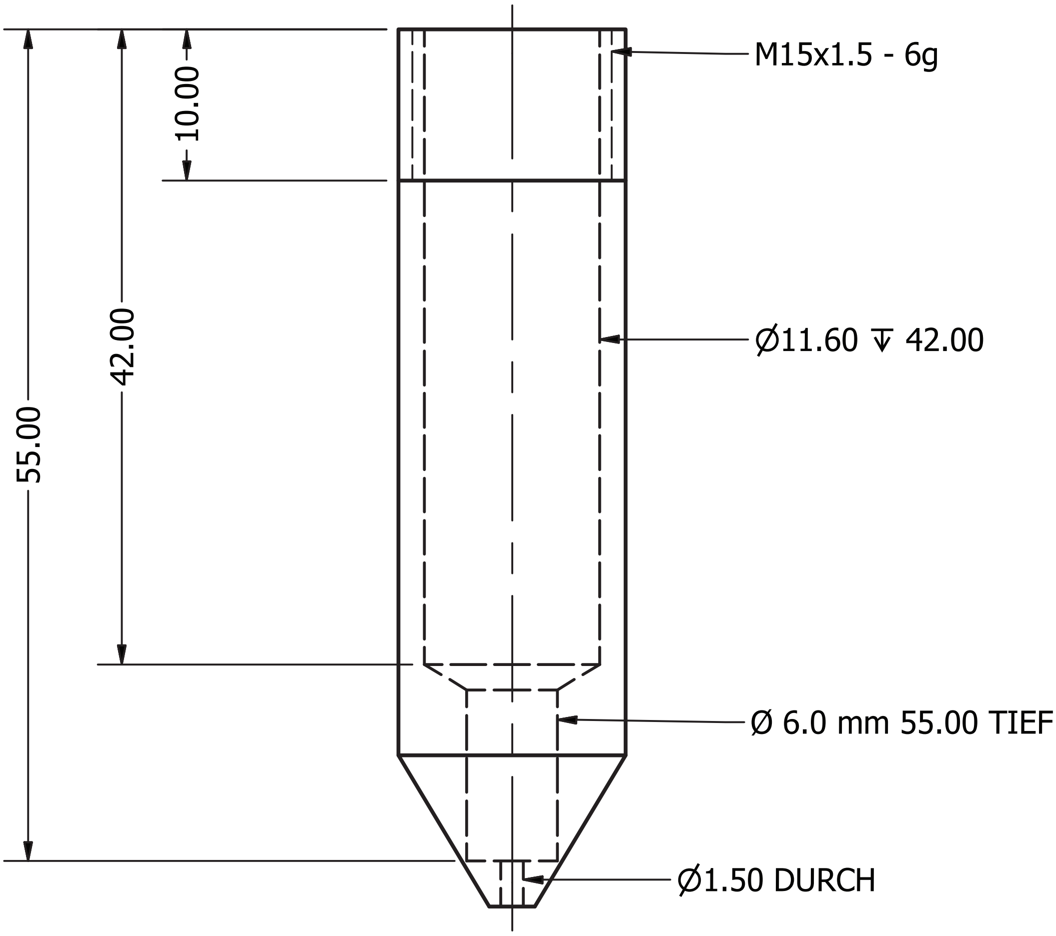

DRAWN Julia Müller	22.07.2020				
CHECKED		TITLE			
QA					
MFG					
APPROVED					
		SIZE A4		DWG NO Druckkopf_Heizdüse_Setonic-1	REV
		SCALE	2 : 1		SHEET 1 OF 1

A.4. Printer Software

For a brief overview over the Python tool, code samples are given for the input svg file and the output gcode file in Figures A.4.1 and A.4.2.

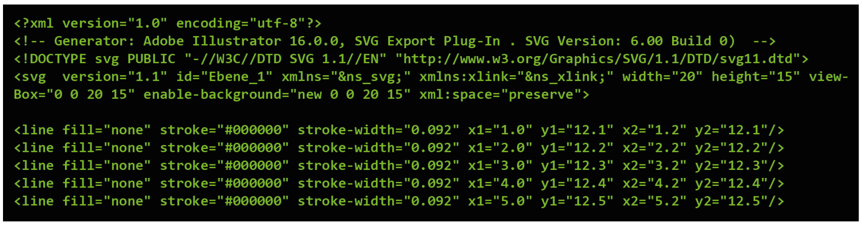

```
<?xml version="1.0" encoding="utf-8"?>
<!-- Generator: Adobe Illustrator 16.0.0, SVG Export Plug-In . SVG Version: 6.00 Build 0)  -->
<!DOCTYPE svg PUBLIC "-//W3C//DTD SVG 1.1//EN" "http://www.w3.org/Graphics/SVG/1.1/DTD/svg11.dtd">
<svg  version="1.1" id="Ebene_1" xmlns="&ns_svg;" xmlns:xlink="&ns_xlink;" width="20" height="15" view-
Box="0 0 20 15" enable-background="new 0 0 20 15" xml:space="preserve">

<line fill="none" stroke="#000000" stroke-width="0.092" x1="1.0" y1="12.1" x2="1.2" y2="12.1"/>
<line fill="none" stroke="#000000" stroke-width="0.092" x1="2.0" y1="12.2" x2="2.2" y2="12.2"/>
<line fill="none" stroke="#000000" stroke-width="0.092" x1="3.0" y1="12.3" x2="3.2" y2="12.3"/>
<line fill="none" stroke="#000000" stroke-width="0.092" x1="4.0" y1="12.4" x2="4.2" y2="12.4"/>
<line fill="none" stroke="#000000" stroke-width="0.092" x1="5.0" y1="12.5" x2="5.2" y2="12.5"/>
```

Figure A.4.1: Exemplary svg File: *The input svg file consists of multiple short lines that are defined by a starting point (X_1 | Y_1) and an end point (X_2 | Y_2). These will be the limits for the gcode. The amount of ink that should be extruded is calculated from the start to end distance and can be modified with a volume factor in the parameter file. Already published in Müller et al.* [140]

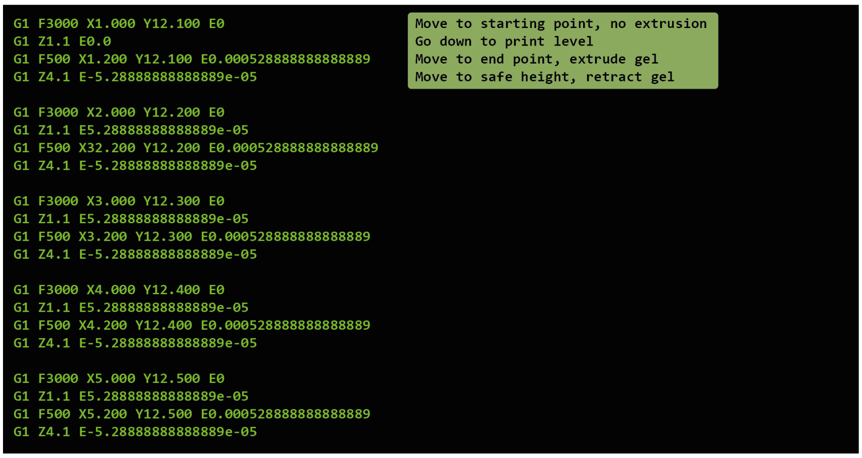

```
G1 F3000 X1.000 Y12.100 E0                              Move to starting point, no extrusion
G1 Z1.1 E0.0                                            Go down to print level
G1 F500 X1.200 Y12.100 E0.000528888888888889            Move to end point, extrude gel
G1 Z4.1 E-5.28888888888889e-05                          Move to safe height, retract gel

G1 F3000 X2.000 Y12.200 E0
G1 Z1.1 E5.28888888888889e-05
G1 F500 X32.200 Y12.200 E0.000528888888888889
G1 Z4.1 E-5.28888888888889e-05

G1 F3000 X3.000 Y12.300 E0
G1 Z1.1 E5.28888888888889e-05
G1 F500 X3.200 Y12.300 E0.000528888888888889
G1 Z4.1 E-5.28888888888889e-05

G1 F3000 X4.000 Y12.400 E0
G1 Z1.1 E5.28888888888889e-05
G1 F500 X4.200 Y12.400 E0.000528888888888889
G1 Z4.1 E-5.28888888888889e-05

G1 F3000 X5.000 Y12.500 E0
G1 Z1.1 E5.28888888888889e-05
G1 F500 X5.200 Y12.500 E0.000528888888888889
G1 Z4.1 E-5.28888888888889e-05
```

Figure A.4.2: Exemplary gcode File: *The printer travels at higher speed (F) with a first* `G1` *command to the start point (X_1 | Y_1) without extrusion (E = 0) and subsequently moves down to the build plate with a Z movement (again without extrusion). At the correct height for extrusion, the printer uses a lower feedrate (F) to extrude the amount indicated with E to the end point (X_2 | Y_2). Last, the nozzle moves up to reduce collision with already printed hydrogel and performs a retraction step with 10% of the extruded amount to prevent the printer from dripping. Already published in Müller et al.* [140]

A.5. DNA Sequences and Modifications

The DNA sequences employed for the DNA computation circuit (see Chapter 5) within a gel environment are given in Table A.5.1. Identity or complementarity to X is indicated in red, to Y indicated in blue. Poly-A extensions are black.

Y_{20} has an additional 10 nt poly-A extension as in TMSD experiments of a corresponding fluorophore-quencher pair a strong increase in fluorescence signal was observed when bases were used as spacers between the strand and the gel.

Table A.5.1: DNA Sequences and Modifications for Controlled Diffusion:

Name	Strand	Length	Modification	Source
Anchors				
Y_{20}	AAAAAAAAAATGCCACCTGACGTCTAAGAA	30	5AzideN	IDT
X_{20}	ATTACCGCCTTTGAGTGAGC	20	5AzideN	IDT
Free Strands				
$\overline{Y}_{20}$	TTCTTAGACGTCAGGTGGCA	20	5Alexa647	eurofins
$\overline{Y}_{10}$	TCAGGTGGCA	10	5Alexa488	IDT
$\overline{X}_{20}$	GCTCACTCAAAGGCGGTAAT	20	5Atto425	biomers
$\overline{X}_{10}$	AGGCGGTAAT	10	5Atto647N	IDT
$\overline{X}_{10}$ + (dA)$_{10}$	AAAAAAAAAAAGGCGGTAAT	20	5Atto647N	biomers
$\overline{X}_{4}$+(dA)$_{6}$	AGGCAAAAAA	10	5TAMRA	IDT
$\overline{X}_{6}$+(dA)$_{4}$	AGGCGGAAAA	10	5Atto425	biomers
$\overline{X}_{8}$+(dA)$_{2}$	AGCGGTAATA	10	5Alexa488	IDT
Quencher				
Y_{15}-Q	CCTGACGTCTAAGAA	15	3BlackBerry-Quencher650	biomers
X_{14}-Q	GCCTTTGAGTGAGC	14	3BlackHole-Quencher-I	biomers

The sequences were checked to have no secondary structure using NUPACK-(http://www.nupack.org/). Only $\overline{Y}_{20}$ (probability 0.2-0.3, stem 2nt, loop 5nt) and X_{20} (probability 0.0-0.1, stem 3nt, loop 6nt) had a low propensity for hairpin formation. Note that in contrast to the strands $\overline{X}_4$+(dA)$_6$ and $\overline{X}_6$+(dA)$_4$ for strand $\overline{X}_8$+(dA)$_2$ additional dA bases were attached separately at both ends of the strands. With this it could be avoided that $\overline{X}_8$+(dA)$_2$ would hybridize to X_{20} over a stretch of 9 contiguous bases rather than 8, as intended.

As readout for the photoswitchable channels in Chapter 7, a DNA circuit similar to the circuit for the diffusion experiments of Chapter 5 were designed based on the same sequences X_{20} and Y_{20} with slight deviations. The exact sequences and modifications can be found in Table A.5.2.

The sequences were again checked for secondary structure using NUPACK. While the duplex formation for fluorophor-anchor ($\overline{X}_{20} + \overline{Y}_{20} : X_{20}$) as well as fluorophor-quencher ($\overline{X}_{20} + \overline{Y}_{20} : \overline{Y}_{15}$-Q), and fluorophor-fuel ($\overline{X}_{20} + \overline{Y}_{20} : Y_{20}$-Biotin) is stable for temperatures up to 37 °C with a probability of 1, the single-stranded $\overline{X}_{20} + \overline{Y}_{20}$ can exhibit a 3bp toehold stem with a probability of 0.3 at room temperature.

Table A.5.2: DNA Sequences and Modifications for Controlled Channeling:

Name	Strand	Length	Modification	Source
Anchor				
X_{20}	ATTACCGCCTTTGAGTGAGC	20	3AzideN	IDT
Quenched Duplex				
$\overline{X}_{20}+\overline{Y}_{20}$	GCTCACTCAAAGGCGGTAATGCCACCTGACGTCTAAGAA	40	3Alexa488	IDT
$\overline{Y}_{15}$-Q	TTCTTAGACGTCAGG	15	5BlackHole-Quencher-I	biomers
Free Fuel Strand				
Y_{20}-Biotin	AAAAAAAAAAAAAAATTCTTAGACGTCAGGTGGCA	20	5Biotin	biomers

A.6. Additional Data Printing DNA - Bioink

A.6.1. Pore Size Estimation

With the protocol stated in 3.2 the pore size of DNA - bioink was assessed experimentally with the application of FITC-dextrans (see Figure A.6.1).

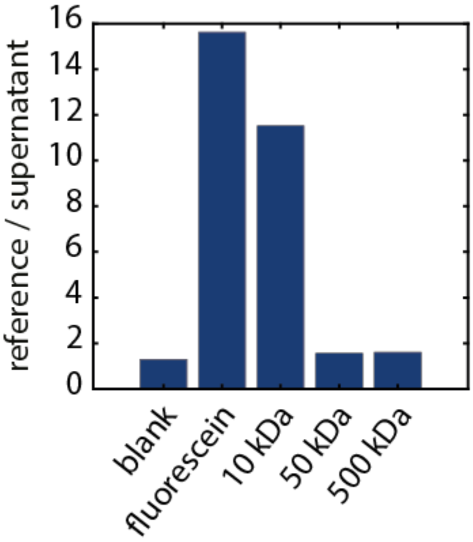

Figure A.6.1: Pore Size DNA - Bioink: *The fluorescence of the reference sample is expected to be similar to the fluorescence of the supernatant if the corresponding fluorescently labeled particles are larger than the pore size:* $f = F_{ref}/F_{sup} \approx 1$. *If the fluorescence of the supernatant is much lower than the reference sample, this indicates an adsorption of fluorescent particles to the hydrogel sample. With the fluorescent intensities measured, the gel pore size is estimated to be* $\approx$ *5 - 10 nm. Already published in Müller et al.* [140]

A.6.2. Printing Reproducibility

The TUM logo print in Figure 5.2.3 is an average of four separate prints shown in Figure A.6.2 that were captured independently. All individual images were taken after at least 16 hours of free diffusion of reporter - quencher DNA duplexes within the extruded structure of DNA functionalized bioink.

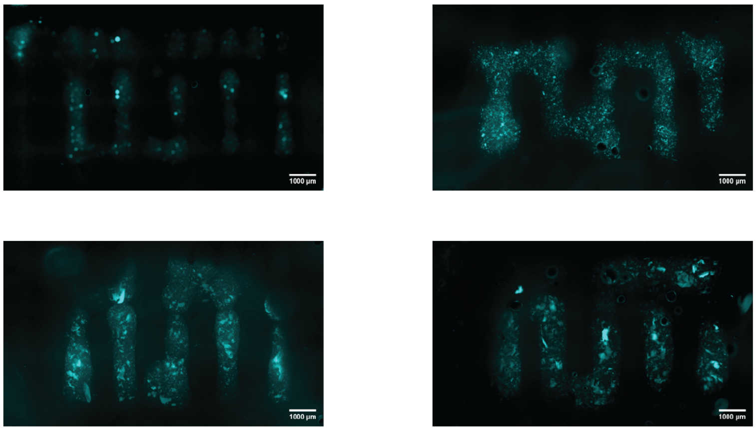

Figure A.6.2: Reproducibility DNA Bioink Print: *Four independently printed TUM logo patterns with DNA modified bioink. The cyan fluorescence channel of all experiments is shown. Already published in Müller et al.* [140]

A.6.3. Sequence-dependent Diffusion: Single Fluorescence Channel Images

In Figure 5.2.4 the tunability of the diffusion constant of short ssDNA oligonucleotides by temporary binding to the anchoring strands localized on the bioink is shown.

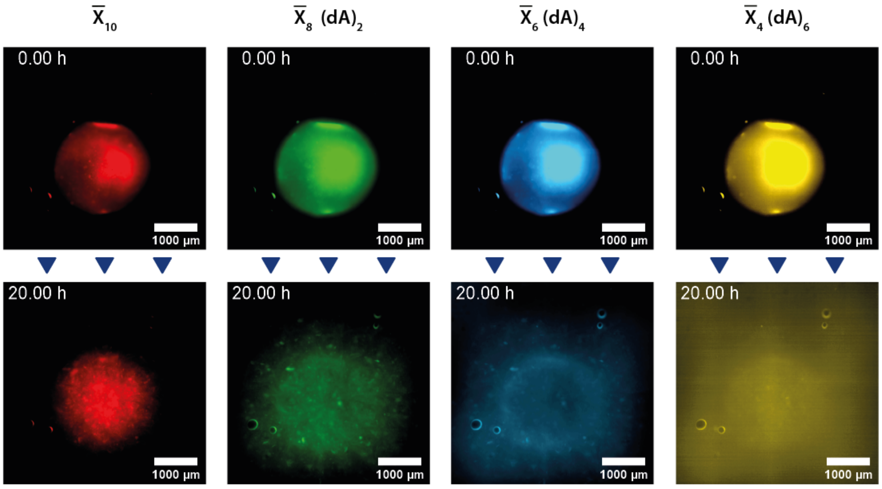

Figure A.6.3: Differential Diffusion - Single Channels: *Microscopy images of single fluorescent channels. The variation in diffusion constant is visible by the comparison of start and end distribution of the fluorophore. While the distribution of all DNA molecules is at the same spot at the start of the experiment, the end distributions differ as easily detectable. Already published in Müller et al.* [140]

The different binding affinity is achieved via a different length of complementary base-pairing sequences within 10 nucleotide long short single strands. In Figure A.6.3 the single fluorescence channels are depicted to allow a closer investigation of the diffusion of each ssDNA strand after 20 hours.

A.6.4. Mathematical Models

Estimation of the Diffusion Coefficients

In order to determine diffusion coefficients, the diffusion profiles generated by the fluorescently labeled DNA molecules were fitted using Gaussian distributions. These are not the analytic solutions of the diffusion equation for the geometry of the printed gels (which is more complicated for the approximately cylindrical geometry), but gives a reasonable estimate for the diffusion coefficient. The fluorescent intensity was recorded of the rectangular region of interest centered around the spot where the DNA sample was applied initially. Then, a Gaussian function was fitted using MATLAB over the fluorescence intensities at each time step (after background subtraction using the same background for all time steps based on the first time step). The fit function was:

$$\frac{a}{2\pi} \cdot \text{exp}(-\frac{(x-\mu)^2}{2\sigma^2}) \tag{A.1}$$

The diffusion constant D is connected to the standard deviation σ via:

$$\sigma^2 = 2 \cdot D \cdot t \tag{A.2}$$

Figures 5.2.2 and 5.2.5 show plots of the variance σ^2 as function of t, which are used to derive the diffusion coefficient from fits with this Equation.

Reaction - Diffusion Processes

The ring structures of the sequence-dependent differential diffusion experiment in Figure 5.2.5 follow the reaction diffusion equations, in which hybridization as well as displacement of shorter by longer strands via TMSD was considered (here δ denotes the Laplace operator):

$$\begin{aligned}
\frac{\partial[\overline{X}_{10}]}{\partial t} &= D_{\overline{X}_{10}} \cdot \Delta\overline{X}_{10} - k_{on,10}[X_{20}][\overline{X}_{10}] + +k_d[X_{20}:\overline{X}_{10}][\overline{X}_{20}] \\
\frac{\partial[\overline{X}_{20}]}{\partial t} &== D_{\overline{X}_{20}} \cdot \Delta\overline{X}_{20} - k_{on,20}[X_{20}][\overline{X}_{20}] - k_d[X_{20}:\overline{X}_{10}][\overline{X}_{20}] \\
\frac{\partial[X_{20}]}{\partial t} &= -k_{on}[X_{20}][\overline{X}_{20}] - k_{on}[X_{20}][\overline{X}_{10}]
\end{aligned}$$

For free strands $\overline{X}_{10}$ and $\overline{X}_{20}$ and locally fixed strands X_{20}. These equations were numerically solved with experimentally derived diffusion constants D, and on-rates and TMSD rates similar to rates typically observed for TMSD reactions in solution (see next section).

Simulations

All simulations were performed using the MATLAB pdepe function with cylindrical symmetry (m=1), and no-flux boundary conditions $\frac{\partial c_i}{\partial r}|_{r=R} = 0$ at $R = 4000$ µm for all reaction species . Initial conditions for diffusing species were set to 100 nM for R $<$ 500 µm and 0 nM elsewhere, while immobilized species were homogeneously distributed at 30 nM.

Unless otherwise noted, hybridization on-rates were set to $k_{on} = 10^6 M^{-1} s^{-1}$, toehold mediated strand displacement rates were set to $k_{TMSD} = 10^5 M^{-1} s^{-1}$, dissociation reactions for stable duplexes were assumed to be negligible and diffusion coefficients for mobile species were set to $D = 10$ µm ^{2} s $^{-1}$. For Figure 5.2.2 there is no reaction term and the experimentally estimated diffusion coefficients of 43 and 12 µm ^{2}s^{-1} for the 10 and 20 nt strands were used respectively. To verify the experimental procedure, the resulting diffusion profiles were fitted with a Gaussian (as described in experimental section). The steep increase in σ^2 after 10 hours for the 10 nt strand is caused by the influence of the no-flux boundary. When Dirichlet boundary conditions (with concentrations clamped to zero outside of the gel) are chosen, σ^2 saturates at a value corresponding to the gel dimensions, as experimentally observed for the fastest diffusing species in Fig. 5.2.5B. This can be explained by that fact that in comparison to Fig. 5.2.2, the free energy of the strands used in Fig. 5.2.5B is reduced in the gel by binding interactions with the anchors, effectively localizing the strands to the gel region.

For Figure 5.2.6 B and C the reaction terms are:

$$\begin{aligned}
\dot{c_1} &= -k_{on} c_1 c_3 + k_{off} c_4 + k_{TMSD} c_4 c_2 \\
\dot{c_2} &= -k_{on} c_2 c_3 - k_{TMSD} c_4 c_2 \\
\dot{c_3} &= -k_{on} c_1 c_3 + k_{off} c_4 - k_{on} c_2 c_3 \\
\dot{c_4} &= +k_{on} c_1 c_3 - k_{off} c_4 - k_{TMSD} c_4 c_2 \\
\dot{c_1} &= +k_{on} c_2 c_3 + k_{TMSD} c_4 c_2
\end{aligned}$$

The k_{off} rate was varied as specified in the plot to investigate the effect of temporary immobilization on the final pattern. As expected, in the limit of low k_{off} rates the formation of a sharp ring was observed. For higher k_{off} rates the 10 nt strand is depleted quickly from the center.

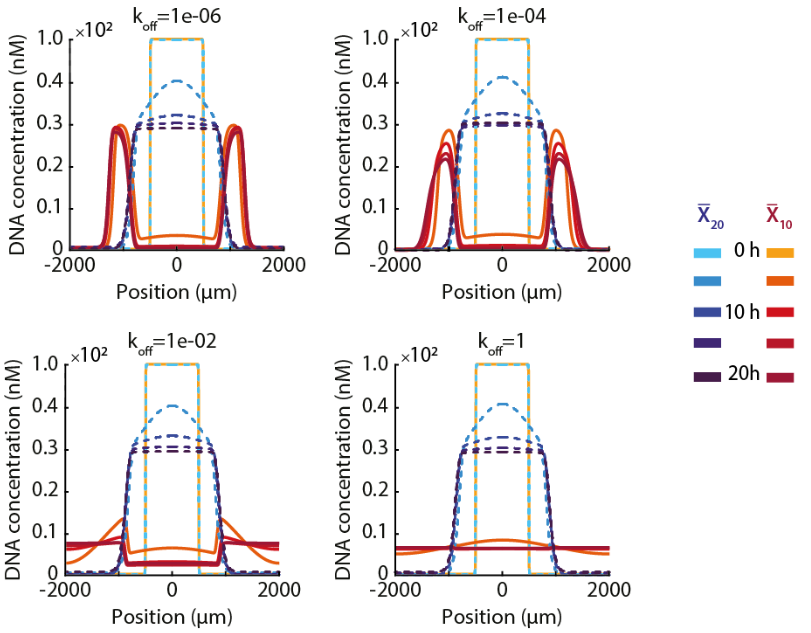

Figure A.6.4: Simulation $\overline{X}_{10}$ and $\overline{X}_{20}$: *Simulated behavior of $\overline{X}_{10}$ and $\overline{X}_{20}$ for different rate coefficients k_{off}. Again, coefficients in the range of 10*$^{-6}$*/s to 10*$^{-4}$*/s show a behavior observable in the experiments (cf. Figure 5.2.6B). For higher off-rates, no rings would be visible. Already published in Müller et al.* [140]

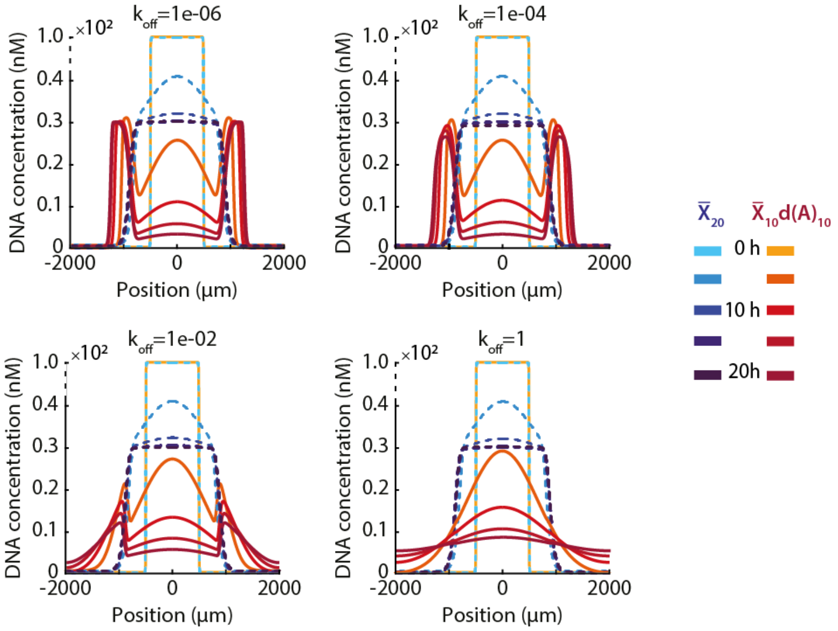

Figure A.6.5: Simulation$\overline{X}_{10+10}$ and $\overline{X}_{20}$: *Simulated reaction-diffusion of $\overline{X}_{10} + (dA)_{10}$ and $\overline{X}_{20}$ for different rate coefficients k_{off}. When using off-rates in the range of 10*$^{-6}$*/s to 10*$^{-4}$*/s, the simulations show a similar behavior as in the experiments (cf. Figure 5.2.6C). As in the experiment, the longer $\overline{X}_{10} + (dA)_{10}$ moves out of the center less quickly than the $\overline{X}_{10}$ strand. Higher rate constants lead to broader rings with more blurry boundaries. Already published in Müller et al.* [140]

A.7. Bacteria Strains

Bacteria strains were DH5α, DH5αZ1 and BL21. DH5α, DH5αZ1 were modified with iGEM plasmid pSB1A3-I13521 and DH5αwith iGEM plasmid pSB1A2-K116638. BL21 was modified with iGEM plasmid pSB1A3-T9002. [95]

DH5αwere modified with plasmids containing the sequence pSB1A3-J23106--B0034-mTurqouise2-B0015 and pSB1A3-J23106-B0034-mVenus-B0015, that were kindly supplied by E. Falgenhauer. [243] Plasmid maps are supplied in Figures A.7.1 - A.7.5

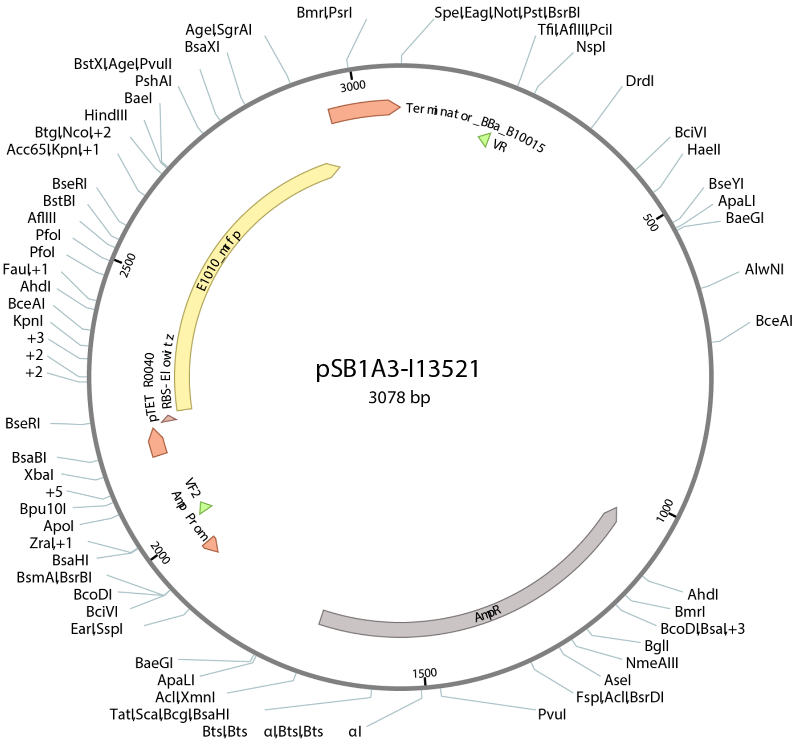

Figure A.7.1: Plasmid Map pSB1A3-I13521: *With this high copy number plasmid, mRFP can be expressed under a pTet promoter constitutively in DH5α and for DH5αZ1 in the presence of aTc.* [95]

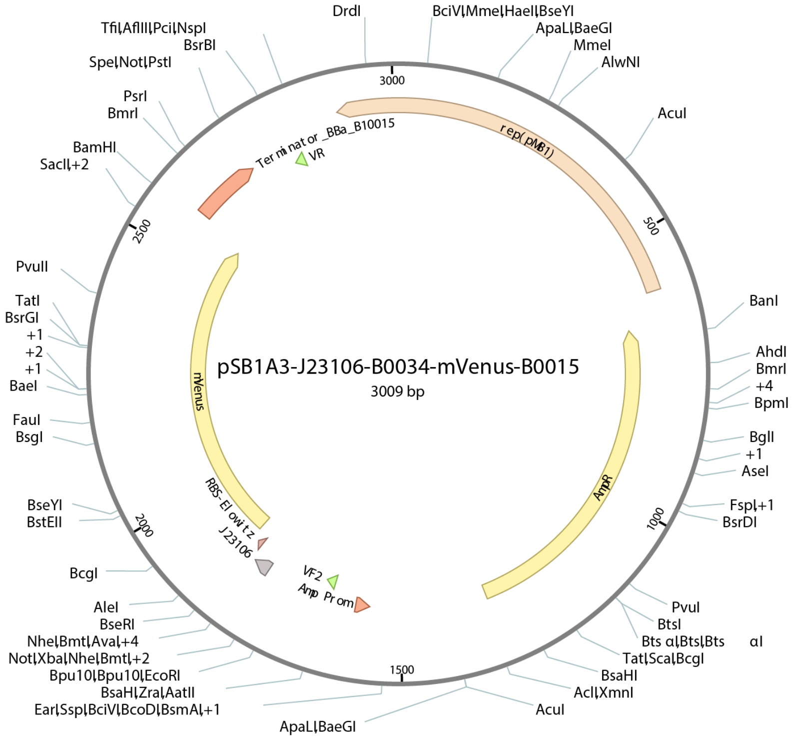

Figure A.7.2: Plasmid Map pSB1A3-J23106-B0034-mVenus-B0015: *With this high copy number plasmid, mVenus cen be expressed under a constitutive promoter.* [243]

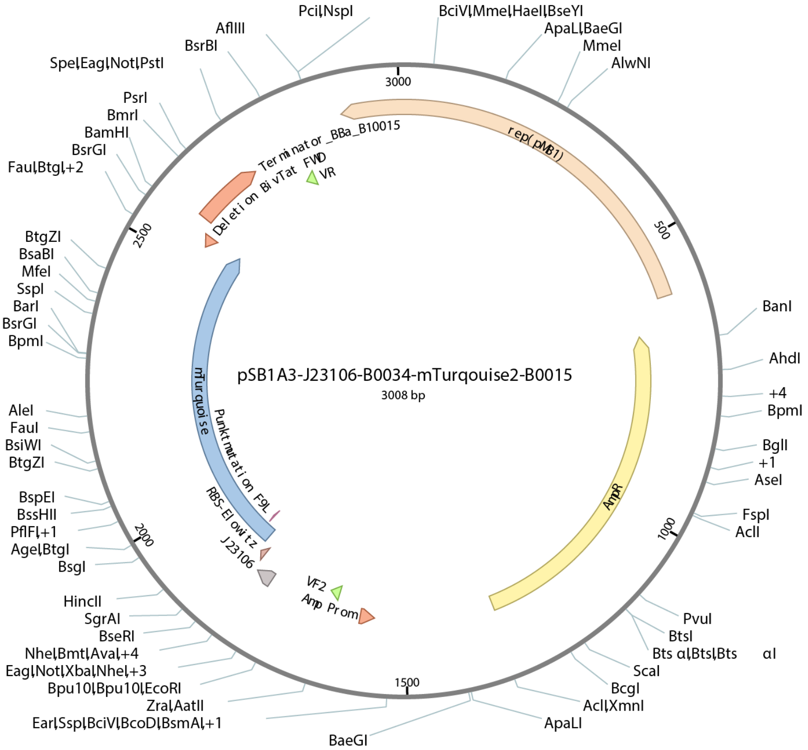

Figure A.7.3: Plasmid Map pSB1A3-J23106-B0034-mTurqouise2-B0015: *With this high copy number plasmid, mTurquoise cen be expressed under a constitutive promoter.* [243]

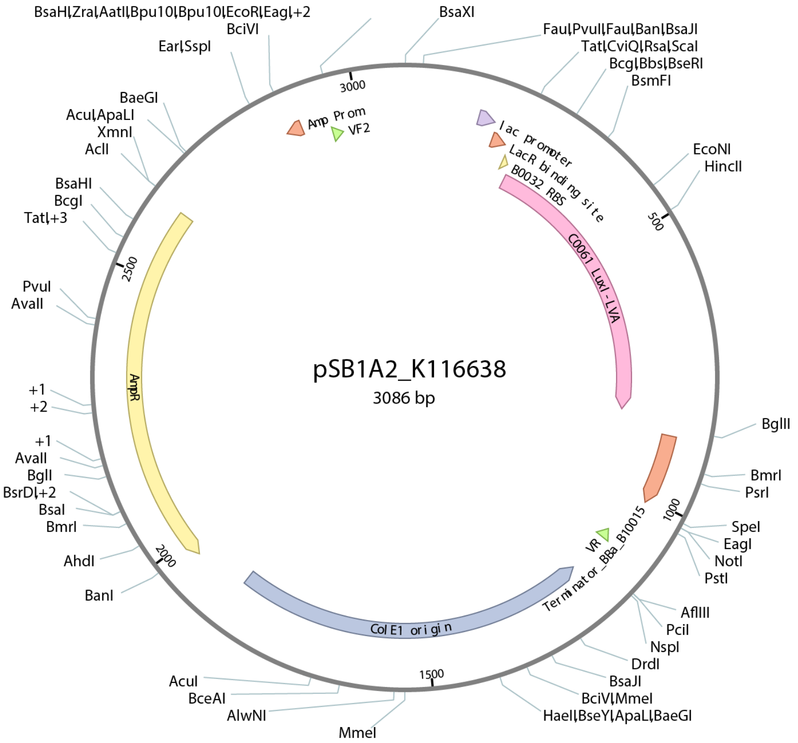

Figure A.7.4: Plasmid Map Sender Cells - pSB1A2-K116638: *In this high copy number plasmid, luciferase activase LuxI under a pLac promotor. LuxI produces the sender molecule AHL that can diffuse through the cell membrane.* [95]

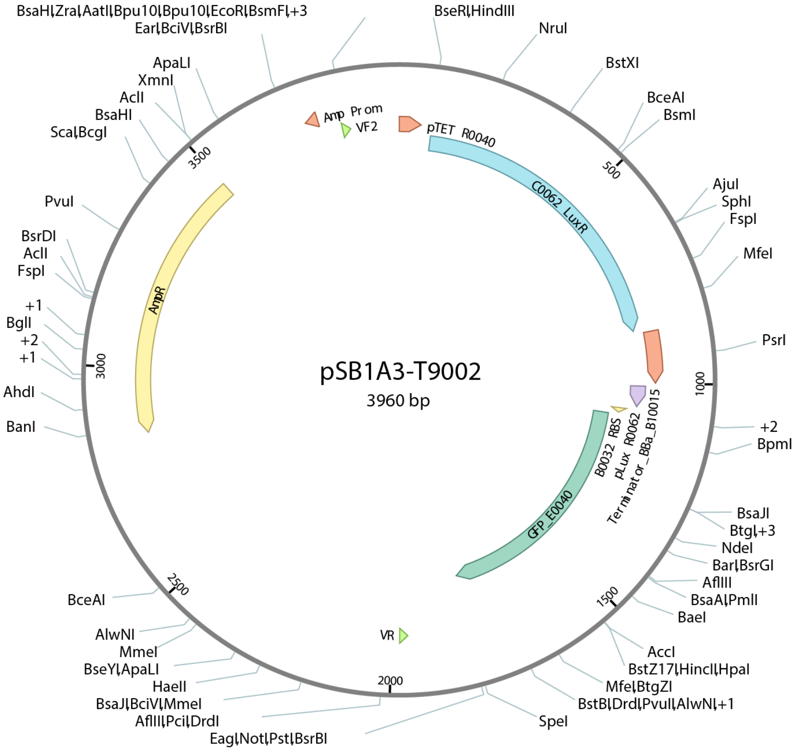

Figure A.7.5: Plasmid Map Receiver Cells - pSB1A3-T9002: *In DH5a cells, the pTet promoter of this high copy number plasmid is constitutively expressing LuxR. If AHL is taken up by the receiver cells, these molecules bind to LuxR and can active the pLux promoter leading to the expression of mGFP.* [95]

A.8. Additional Data Printing Living Bacteria

A.8.1. Bulk Rheometer Data

Fast thermal gelation was verified with bulk rheometer experiments for bacteria-ink prepared in ddH_2O, 0.3 × LB medium and 1.0 × LB medium (see Figure A.8.1).

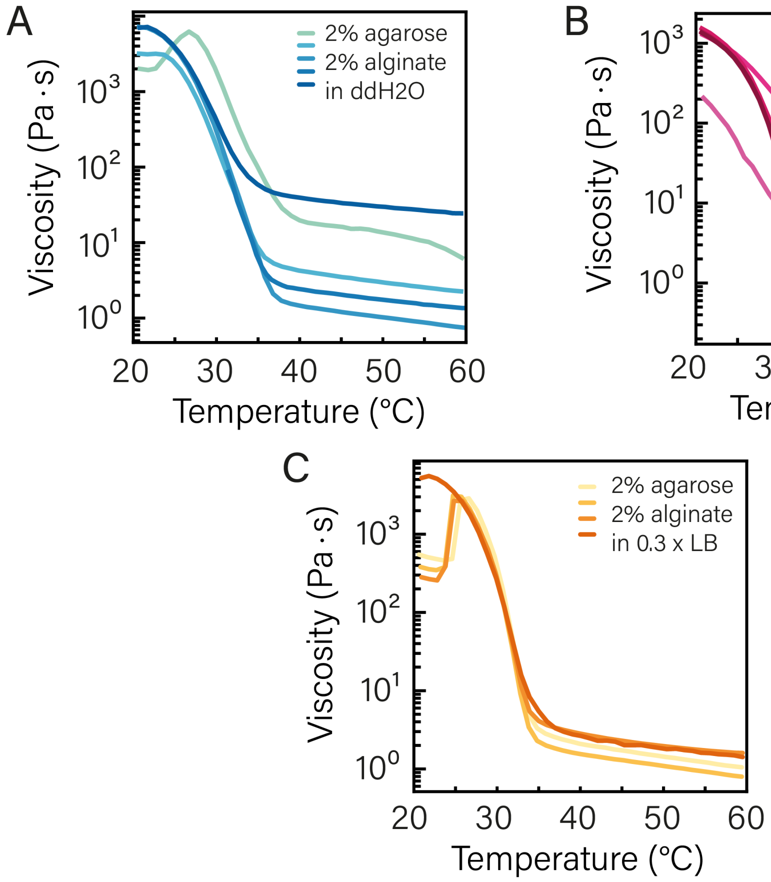

Figure A.8.1: Triplicates Viscosity Measurements: *Experimental triplicate data for viscosity measurements on bac-ink in ddH_2O, 0.3 × LB and 1 × LB medium (cf. Fig. 6.2.1). The temperature dependence of the viscosity has a clear transition temperature for all conditions, which in all cases is below 35 ± 2 °C. Hence, the gels solidify at room temperature. For ddH_2O and 1 × LB medium the batch-to-batch variation is higher than for 0.3 × LB medium, which also performed best in all prints. Adapted from Müller et al.* [191]

For easier comparison, averaged values are plot together in Figure 6.2.1 in Chapter 6. All bacteria-inks show a strong increase in viscosity if cooled to roomtemperatures, however for 0.3 × LB medium the mixture exhibits lowest viscosity for elevated temperatures.

A.8.2. Colony Growth Data

Colony growth was observed by analysis of the colony size of four colonies per 1 h time step. The colony sizes were averaged and fitted with an exponential function to determine the generation time.

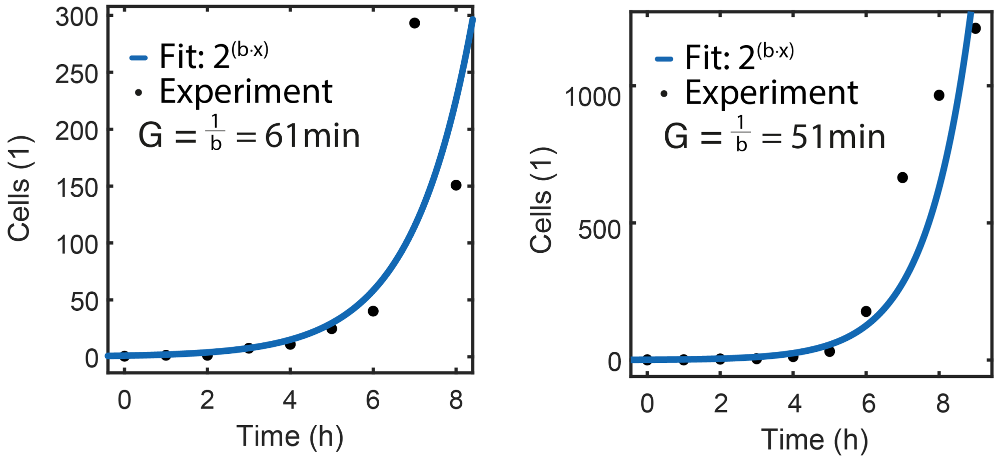

Figure A.8.2: Triplicates Growth Measurements: *Data of two additional biological replicates of colony growth measurements over 0 h – 10 h in printed bacteria - ink. Together, the experiments resulted in a mean generation time of 55 ± 6 min. Adapted from Müller et al.* [191]

The colony shapes are assumed to be ellipsoids, the axes x, y, and z were determined and the number of cells was calculated from the colony volume and an assumed average *E. coli* cell size of 1.5 μm^3.

All triplicates showed generation times ranging from 50 min – 60 min (see Figure A.8.2).

A.8.3. Gene Induction with aTc

For the experiments on spatiotemporal gene induction by diffusing aTc inducers, *E. coli* DH5αZ1 bacteria containing the plasmid pSB1A3-I13521 were used. For bulk characterization of the bacterial gene expression response (without bacteria-ink), measurements of 300 µl sample volumes were performed in a 96-well plate using a Fluostar Plate Reader (Figure A.8.4).

In the diffusion experiment shown in Figure 6.2.4, a 2 µl volume of bacteria-ink--aTc (500x) placed in the center of the print corresponds to a final concentration of 2.0 × aTc in the closed gel chamber, which expected to results in full induction of the bacteria.

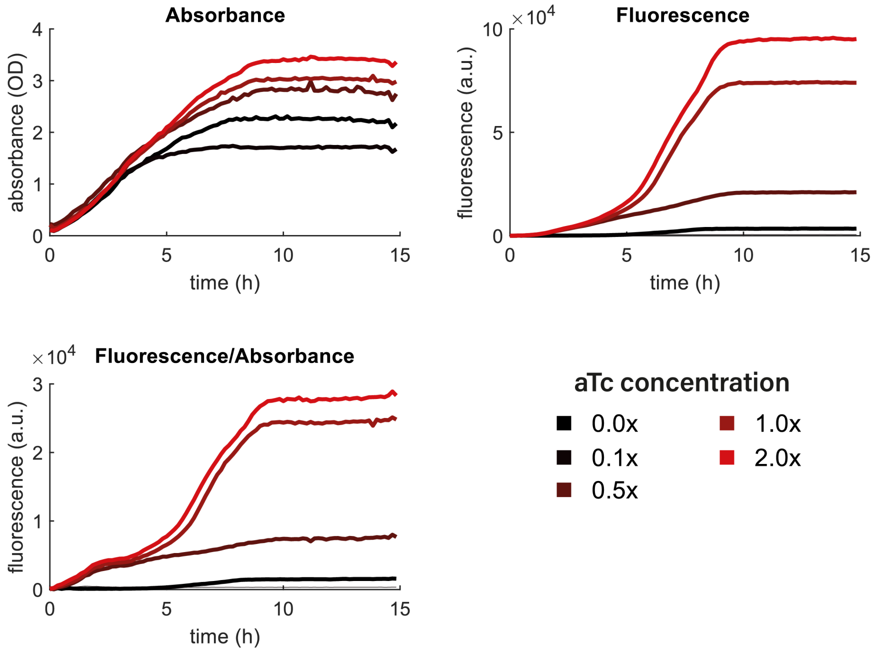

Figure A.8.3: Gene Induction with aTc: *Absorbance, mRFP fluorescence and fluorescence/absorbance data for different aTc concentrations in bulk were determined in a plate reader experiment. A concentration of 1 × aTc corresponds to* $0.1\,{}^{\mu g}/_{ml}$*. In the diffusion experiment, a 2 × (final) concentration is used, which is expected to result in full induction after equilibration of the inducer. Adapted from Müller et al.* [191]

A.8.4. Gene Expression in Response to Diffusing aTc Inducers

Triplicate data of the RFP expression within bioprinted hydrogel strctures containing *E. coli* DH5αZ1 bacteria with the plasmid pSB1A3-I1352 upon central induction with a 1 µl voxel of bacteria-ink- aTc (500x).

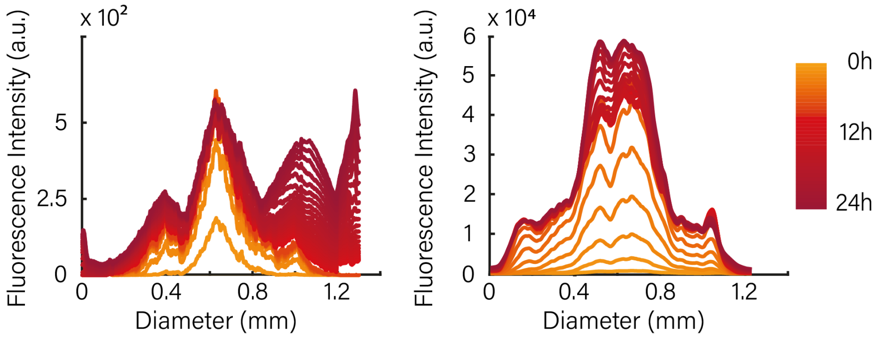

Figure A.8.4: Gene Induction with aTc: *Spatiotemporal gene expression in response to aTc inducers diffusing from a spot in the center of a bioprint - data for additional biological replicates (cf. Figure 6.2.4 B). The substructure in the curves results from irregularities in the print and from stitching of the fluorescence micrographs. Adapted from Müller et al.* [191]

A.8.5. Sender-Receiver Characterization and Triplicates

The sender-receiver system was tested in a bulk experiment and measured with a 96-well plate in a Fluostar Plate Reader with a total sample volume of 300 µl. (see Figure A.8.5.

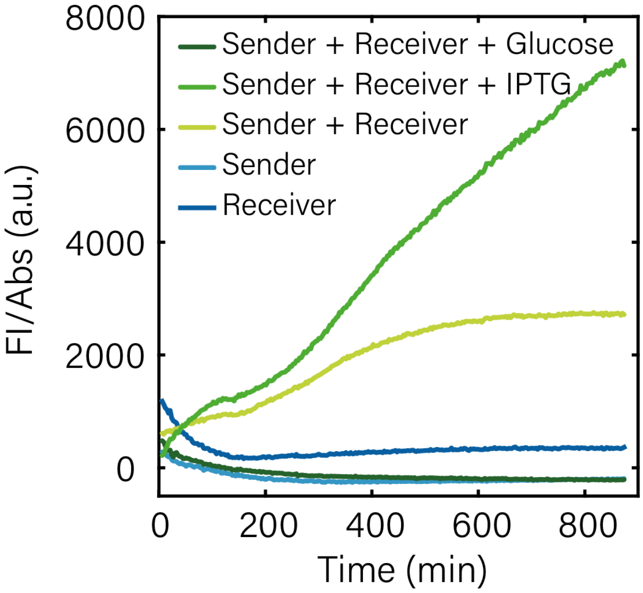

Figure A.8.5: Sender-Receiver Characterization in Bulk: *Sender-Receiver performance in plate reader measurements (Fluorescence/OD). GFP is generated only in the presence of senders and receivers. In the absence of IPTG, leaky expression of LuxI from the pLac promoter generates enough AHL to result in an appreciable GFP signal. Induction with 1 mM IPTG increases the signal. Leaky expression can be suppressed by the addition of glucose. Senders and receivers alone do not show any fluorescence in the GFP channel. Adapted from Müller et al.* [191]

In the absence of IPTG, receivers show a low fluorescence signal, which results from leaky AHL expression by the senders. A correspondingly higher signal is obtained, when senders are induced with IPTG (1 mM).

Highest receiver levels are achieved by complete induction of the receiver cells with externally added AHL (200 nM). As negative controls, receiver cells without the addition of AHL or only sender cells were studied, which both showed no fluorescence.

In Figure A.8.6 triplicates of the experiments shown in Figure 6.2.4 exhibit a comparable behavior. Leaky sender activity generated more likely a sequential fluorescence signal at the receiver locations. IPTG induced sender showed high AHL expression and nearly all receiver locations showed strong increase in fluorescence signal at the same time.

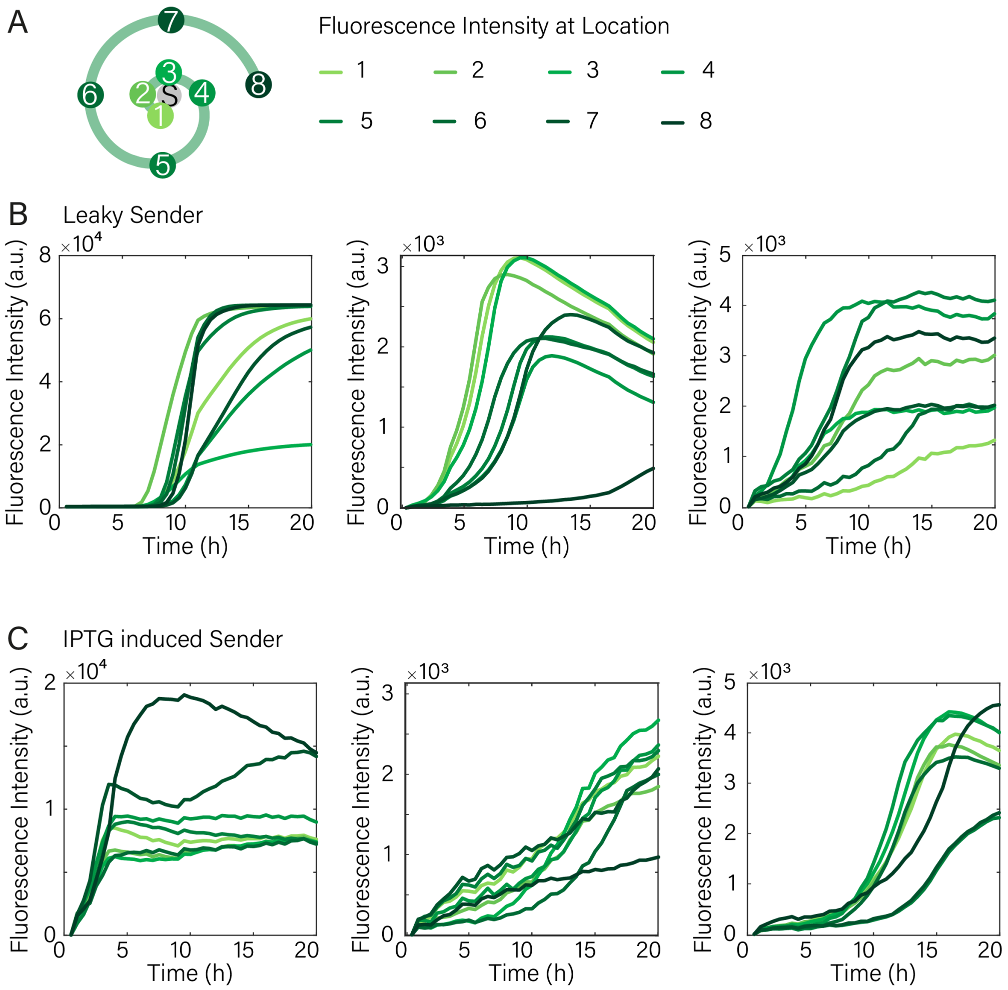

Figure A.8.6: Sender-Receiver Triplicates: *Fluorescence Data of triplicates with either leaky (low sender strength) and IPTG induced (full sender strength) sender cells (cf. Figure 6.2.4 D). Adapted from Müller et al.* [191]

A.8.6. Guiding Chemotaxis with Bacterial Boundaries

Experiments with printed E. coli boundaries were performed with pConst-mRFP bacteria mixed to 1 % (w|v) alginate in 0.5 × LB medium, while printing with plain 1 % (w|v) alginate was used as a negative control.

In all experiments the chemotactic cells were able to cover the complete agar surface over the course of 20 h after inoculation at four locations surrounding the logo. Bacterial lawn was only reduced to singular bacteria within the enclosed area of the printed logo, when the logo was printed with non-motile bacteria.

In the negative controls, the logo shape was printed by blank alinate. The chemotactic bacteria were not affected by the printed structure and covered the complete plate with thick lawn for all triplicates (Figure A.8.7).

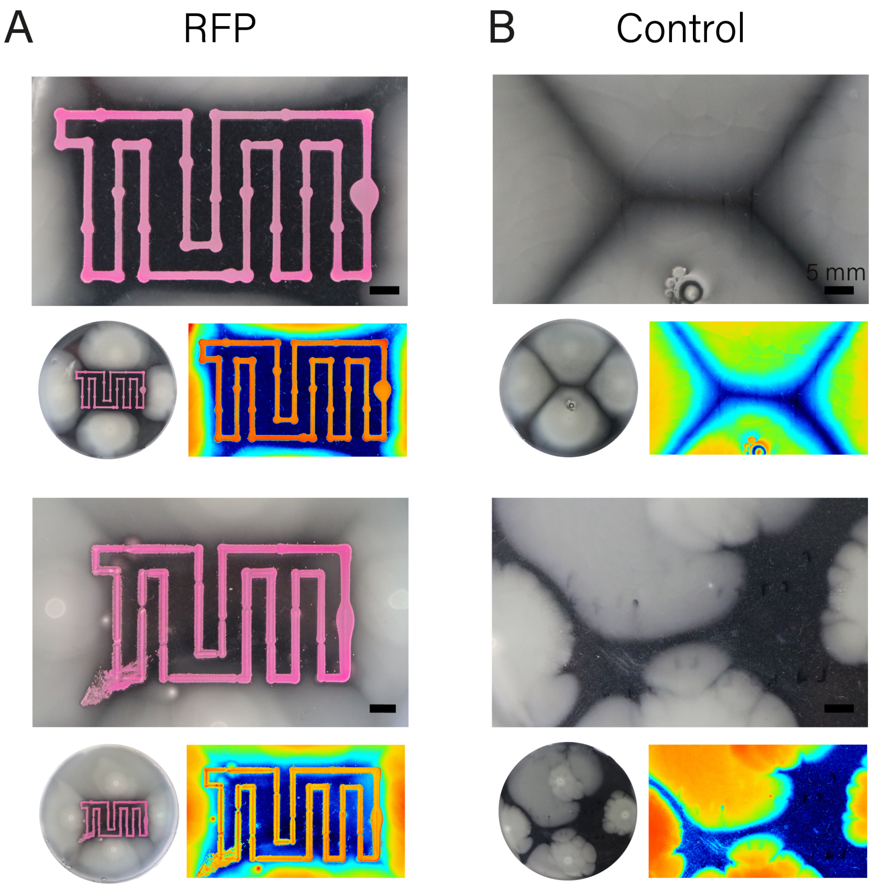

Figure A.8.7: Sender-Receiver Triplicates: *Experimental replicates for printed boundary experiments with A) mRFP producing non-motile bacteria in the boundary and B) with boundaries printed with alginate. Adapted from Müller et al.* [191]

A.8.7. Computer Simulations of Printed Bacteria

The spatiotemporal gene expression dynamics observed in the experiments discussed in Figure 6.2.4 were modeled using a simple reaction-diffusion model. The bioprint can be considered as a cylindrical gel slab with height h = 4.0 mm and radius R = 10 mm, where the diffusing inducer (or sender bacteria) is initially confined to the region $r < R_0$. The inducer then diffuses isotropically within the gel with diffusion coefficient D.

The bacteria are assumed grow exponentially with growth rate $\gamma = ln2/t_d$, where t_d is the doubling time, consistent with the observations of Figure 6.2.3 A. Bacteria produce fluorescent proteins depending on the local inducer concentration, which is modeled with a Hill function with a threshold concentration of K, Hill coefficient n, and maximum production rate α.

This leads to the following differential equations for inducer concentration $c(r,t)$, bacteria number $N(r,t)$ and total amount of protein $P(r,t)$ (as the experimental observable is total fluorescence, the total protein number is modeled):

$$\frac{\partial c(r,t)}{\partial t} = \frac{1}{r}\frac{\partial}{\partial r}(r \cdot D \cdot \frac{\partial c(r,t)}{\partial r}) \tag{A.3}$$

$$\frac{\partial N(r,t)}{\partial t} = \gamma \cdot N(r,t) \tag{A.4}$$

$$\frac{\partial P(r,t)}{\partial t} = \alpha \cdot \frac{c^n}{c^n + K^n} \cdot N(r,t) \tag{A.5}$$

The equations were solved numerically using the Matlab pde solver pdepe with no-flux boundary conditions for c.

Diffusing Inducer

For the experiments with diffusing aTc, as an initial condition a 0.39 mM concentration of aTc confined to a cylinder with radius R_0=0.4 mm was assumed. The other parameters were set to α = 1, n = 2, K = 40 nM. A screen of the diffusion coefficient showed the best match with the experimental data for a value of D = 200 µm^2/s (Figure A.8.8).

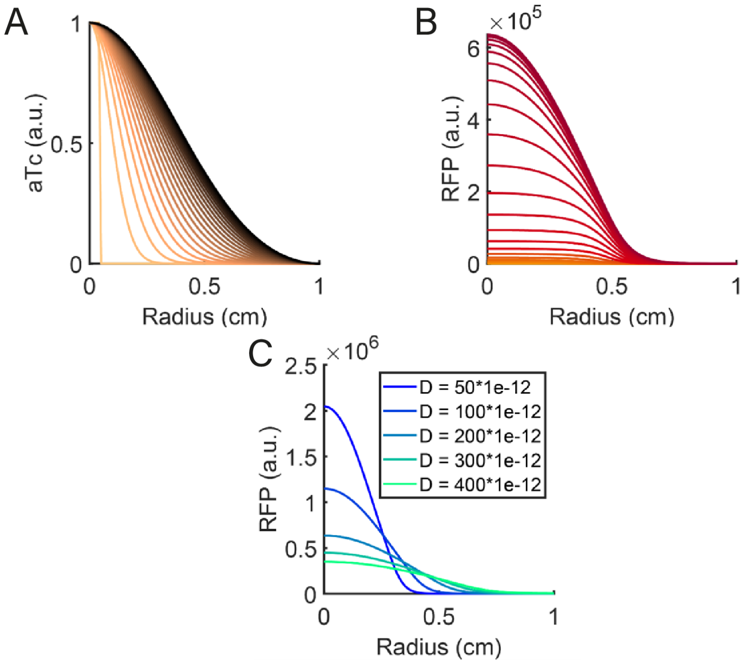

Figure A.8.8: Simulation of Inducer Diffusion: *A) shows diffusion of aTc away from the center ($r = 0$), while B) shows the expected RFP signal at different positions. The color gradients indicate the progress over time. C) shows how the aTc diffusion coefficient influences the RFP profile. The expected RFP intensity is depicted after 10 h for diffusion coefficients ranging from 50 µm^2 /s to 400 µm^2/s . Further model parameter values are $n = 2$ and $K = 0.01495$ µg/l. Adapted from Müller et al.* [191]

Sender-Receiver Simulations

The sender-receiver system requires a more complex model that incorporates growth of the senders and receivers, production of the signal AHL by the senders, and GFP expression by the receivers in response to AHL. In order to qualitatively capture the experimental observations made in Figures 6.2.4 D and A.8.6, the degradation of AHL and GFP needs to be considered, also.

Furthermore, the experiments indicate a time lag between growth/expression of the senders and growth/expression of the receivers. This parameter appears to vary between experiments and is expected to have a strong impact on the spatiotemporal dynamics of GFP expression. It is actually reasonable to assume such a lag as the receivers are printed in the experiments (and thus are exposed to a brief high temperature "shock"), while the senders are simply applied to the center of the printed structure.

Sender Cells:
The senders are assumed to be confined to the central region ($r < R_0$ = 0.4 mm) of a cylindrical gel with R = 10 mm. Initially, a 2 µl volume of bacteria ink with cells at a concentration of $\approx 2 \cdot 10^8$ cells / ml is applied to the center, i.e., the initial number of senders is $4 \cdot 10^5$ sender cells. Based on bulk growth experiments, the cell number can be expected to saturate at a ≈ 20 × higher value, i.e., $N_{max} = 8 \cdot 10^6$ cells. For simplicity, logistic growth of the senders was assumed, i.e.,

$$\frac{\partial N_S(r,t)}{\partial t} = \gamma N_S(r,t) \cdot (1 - N_S(r,t)/N_{max}) \tag{A.6}$$

with γ as above.

Receiver Cells:
Receiver cells, which are only present for $r > R_0$, are modeled just as the sender cells, but now explicitly a time lag via the sigmoidal function was modeled $s(t, t_{lag}) := 1/(1 + \exp(-\kappa(t - t_{lag}))$, where κ controls the smoothness of the transition to growth and is set to the (arbitrary) value 10^{-3}. Hence,

$$\frac{\partial N_R(r,t)}{\partial t} = s(t, t_{lag}) \cdot \gamma \cdot N_R(r,t) \cdot (1 - N_R(r,t)/N_{max}) \tag{A.7}$$

AHL Turnover:
Further, steady state production of LuxI by the senders is assumed at a concentration of 1 µM (or a copy number of 1000). Each LuxI enzyme will generate AHL at a rate of ≈ 1 molecule / second. The contribution to the AHL production of each sender bacterium within the sender volume 2 µl is thus

$$\alpha_{AHL} = \frac{1000 \cdot 1/s}{6.022 \cdot 10^{23}/\text{mol} \cdot 2\mu l} \approx 1 fM/s \tag{A.8}$$

The overall reaction-diffusion dynamics of AHL is then given by the equation:

$$\frac{\partial[AHL](r,t)}{\partial t} = \frac{1}{r}\frac{\partial}{\partial r}(r \cdot D \cdot \frac{\partial[AHL](r,t)}{\partial r}) + \alpha_{AHL} \cdot N_S(r,t) - \delta_{AHL}[AHL] \quad \text{(A.9)}$$

The degradation rate of AHL is set to $\delta_{AHL} = 0.5 \cdot 10^{-5} s^{-1}$, while its diffusion coefficient is set to $D = 1000 \mu m^2/s$ (for simulations with different diffusion coefficients see Figure A.8.10.

GFP Production:
Just as in the simple induction experiment 6.2.2, the production of the total number of fluorescent proteins N_{GFP} is assumed to be proportional to the number of bacteria. Due to the longer run-time of the experiments, it has to be explicitly accounted for a reduction of gene expression in the stationary phase (phenomenologically modeled via logistic growth as for the bacteria themselves). Further, the degradation of GFP cannot be neglected, which is assumed to occur roughly within 1 day, i.e., $\delta_{GFP} = 10^{-5}/s$:

$$\frac{\partial N_{GFP}(r,t)}{\partial t} = \\ = \alpha_{GFP} \frac{[AHL]^m}{[AHL]^m + K_{AHL}^m} \cdot s(t, t_{lag}) \cdot N_R(r,t) \cdot (1 - N_R(r,t)/N_{max}) - \delta_{GFP} N_{GFP}(r,t) \quad \text{(A.10)}$$

The Hill coefficient for AHL induction is set to m=1, K_{AHL} = 10nM. For this purpose, the expression rate α_{GFP} is an arbitrary scaling parameter and is set to 1/s.

These equations can reproduce the various fluorescence time courses observed in the sender-receiver experiments quite well (cf. Figure A.8.9). Specifically, they capture the observation that longer lag times tend to sharpen the transition – at later times AHL has already distributed in the gel, and all bacteria are induced above threshold without any spatial dependence.

The model further explains that at low sender strength and without time lag there is a stronger differentiation than at high sender strength without lag, or, alternatively, at low sender strength, but with time lag. The simulations also suggest that within one print bacteria at different positions might show slightly different growth behavior, leading to the variability observed in the curves displayed in Figure A.8.6.

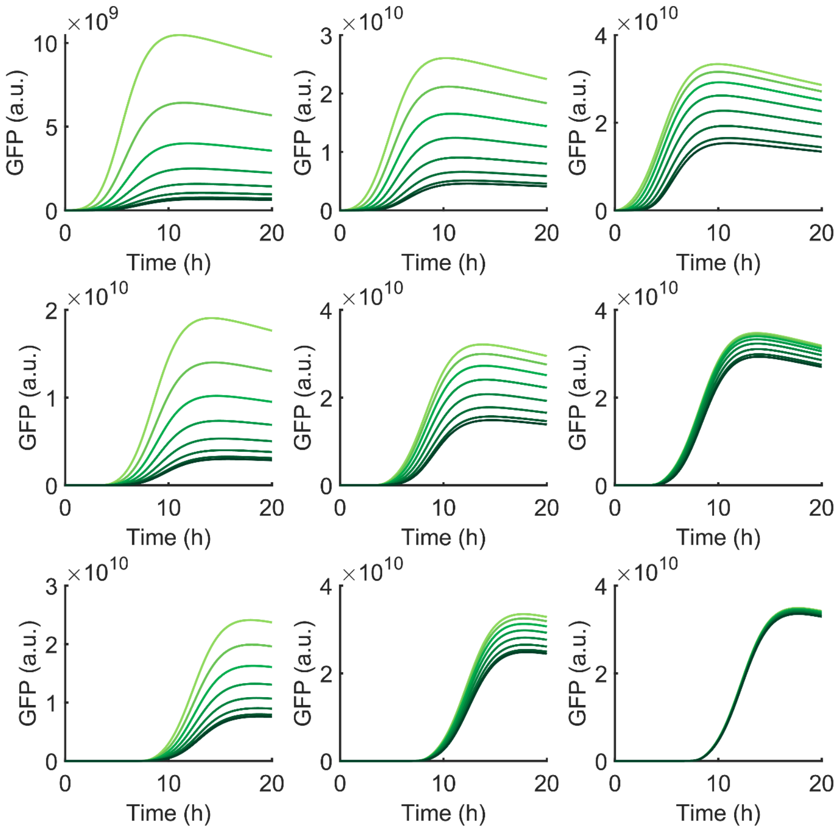

Figure A.8.9: Sender-Receiver Simulation: *Simulated GFP intensities for the sender-receiver experiments. The response by the receiver bacteria is strongly dependent on sender strength and the time lag between sender and receiver growth. From left to right, the sender expression rate is varied uninduced to induced, i.e.,* α_{AHL} *= 0.01 , 0.1, and 1 fM / s / cell. From top to bottom the lag time is varied from 0 over 4 h to 8 h. Both higher expression and larger lag time sharpen the response. Adapted from Müller et al.* [191]

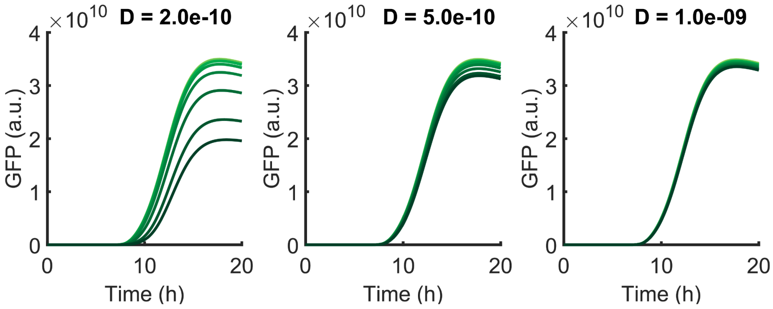

Figure A.8.10: Simulated Influence of Diffusion Coefficient on Sender-Receiver System: *Influence of diffusion coefficient on sender-receiver dynamics for a lag time of 8 hours. Faster diffusion has a sharpening effect (D is given in units of m* ^{2} */ s) similar to lag time and expression strength (see Figure A.8.9). Adapted from Müller et al.* [191]

A.9. Additional Data Electro - Bio Hybrid Circuit

A.9.1. NMR Spectra

Grafting of the guest and the host complex to the poly acrylic chains were verified with NMR (Figures A.9.1-A.9.3). With this, the chemical structure can be determined by the changes in nuclear spin orientation if exposed to strong magnetic fields.

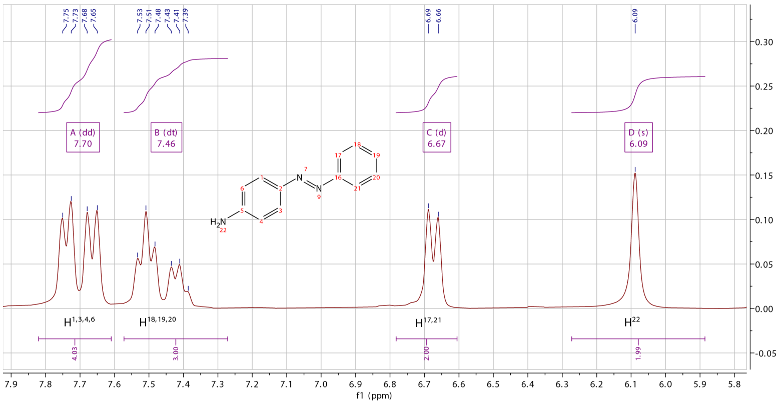

Figure A.9.1: NMR Spectrum 4-Amino-Azobenzene: *^{1}H NMR spectrum of 4 - amino - azobenzene molecules in DMSO were determined.*

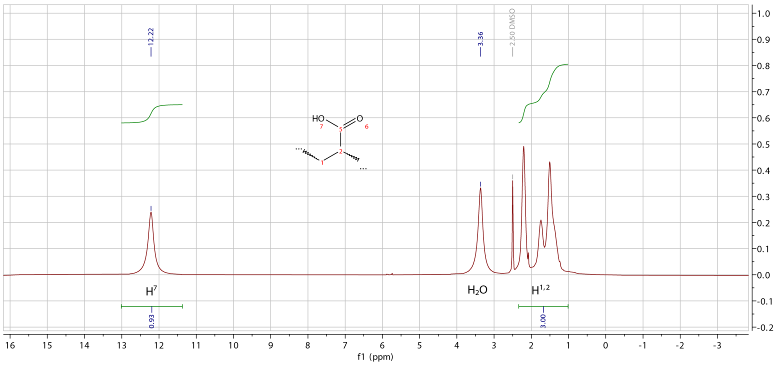

Figure A.9.2: NMR Spectrum Poly-Acrylic-Acid: *^{1}H NMR spectrum of poly-acrylic-acid chains in DMSO were determined.*

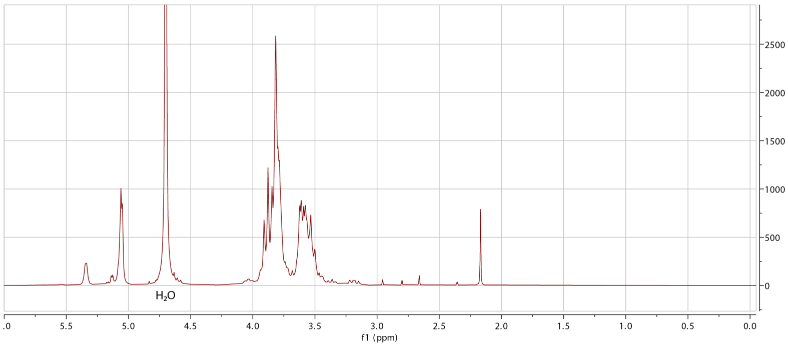

Figure A.9.3: NMR Spectrum α-Cyclodextrin: *^{1}H measurements NMR spectrum of 6-monoamino-6-monodeoxy-α-cyclodextrin in D_2O were determined.*

A.9.2. Absorption Spectra Azobenzene

For the exact determination of the switchting times of azobenzene grafted to PAA chains, absorption spectra were measured. As indicated in Figure A.9.4, *trans* - and *cis* - azobenzene exhibit specific absorption spectra that deviate largely at the UV spectrum. With this, to determine the t_{on} time, the gel was irradiated with a 356 nm lamp and absorption spectra were measured for 15 sec to 5 min. For the determination of the closing time, the sample was irradiated within the absorption spectrometer at a constant wavelength of 470 nm.

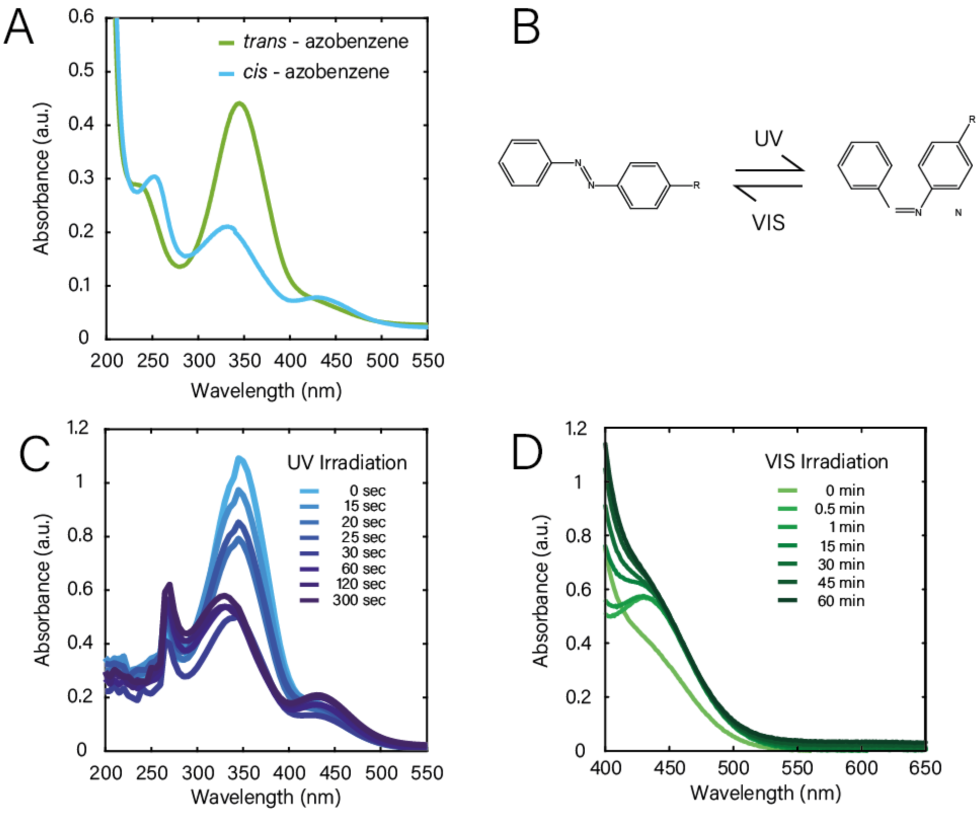

Figure A.9.4: Absorption Spectrum Azobenzene - PAA: *A) Absorption spectra of trans - azobenzenes show a strong peak at 350 nm. This peak is decreased and shifted to 325 nm for cis - azobenzene, while the peak at 250 nm increases. With this, absorption spectra are typically used to determine the azobenzene configuration. B) Schematic representation of trans - and cis - azobenzene. Due to the geometrical change, the absorption spectra differ slightly in the UV region. C) Switching time from trans to cis configuration,* t_{on}*, was determined via irradiation with a 356 nm lamp and consequent absorption spectra recording. While for shorter time intervals, the peak at 350 nm decreases clearly with increasing irradiation time, after 30 s the cis - spectrum is reached and no change in absorption spectrum can be achieved with longer irradiation intervals. D)The reverse switching time from cis to trans configuration,* t_{off}*, was measured for irradiation with 470 nm. Irradiation times were longer than in literature and a complete reverse switch was only detected after 45 min.*

A.9.3. Additional Data Switched Gate

Triplicates were measured for the azobenzene-α-cyclodextrin gated DNA circuit (c.f. Figure A.9.5).

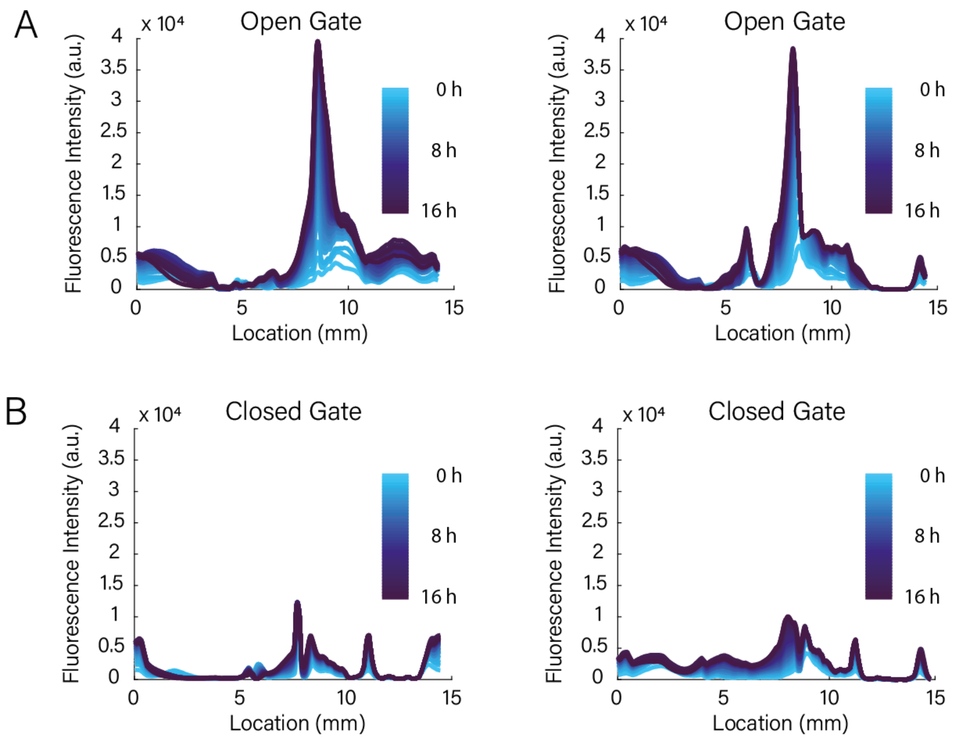

Figure A.9.5: Triplicate Data for Photoswitched Gate: *Experimental setup as in Figure 7.2.6. The triplicates show comparable behavior to the data shown in the main text. A) For the opened photoswitchable channel, strong fluorescence signal is again detected in the reporter compartment over time. B) Closed channels hold back fuel strands and only again low fluorescence intensity can be detected in the reporter compartment. (Scale bar 1mm)*

A.9.4. Source Code Electro Matrix

The source code for the reduced 2 × 1 matrix is provided which can be used to control the setup examined in Chapter 7. The code for a 3 × 3 matrix is based on the same principles, and considers more biological compartments and hydrogel gates. In the following, the code for the smaller 2 × 1 matrix that runs on Arduino is provided:

```
#include <stdio.h>
#define MAX_Y 1
#define MAX_X 2
#define MAX_MILLIS_TO_WAIT 30000  // change to adjust
const int BUFFER_SIZE = 2;
byte buf[BUFFER_SIZE];
byte buf_2[BUFFER_SIZE];
unsigned long starttime;
int timeinterval = 13000;
// Save two iterations of detected matrixes
int detectgrid[MAX_Y][MAX_X];
int detectgrid_2[MAX_Y][MAX_X];
bool new_grid[MAX_Y][MAX_X] = {{0,0}};
/// LED struct with the following parameters
typedef  struct{
  int brightness;
  int adjustPin;
  int Ledstate;
  unsigned long lastTime = 0;
  int LastState;
  int control = 1;
  }Led;
/// Channel struct with two LEDs to open and close the channel
typedef struct  {
    Led led_UV;
  Led led_VIS;
  }channel;
/// Declare 1 channel, containing 2 types of LEDs inbetween two cells
channel channel1;
int play_gol();
void apply_gol();
int LED_VIS(int OnTime, channel *which_led);
int LED_UV(int OnTime, channel *which_led);
int loop_ = 1;
void setup() {
/// Set up all channel parameters (pins, brightness, start-states)
channel1.led_UV.adjustPin = 2;
channel1.led_UV.brightness =200;
channel1.led_UV.Ledstate = LOW;
```

```
channel1.led_VIS.adjustPin = 3;
channel1.led_VIS.brightness = 200;
channel1.led_VIS.Ledstate = LOW;
///Set LEDs as output pins
pinMode(channel1.led_UV.adjustPin, OUTPUT);
pinMode(channel1.led_VIS.adjustPin, OUTPUT);
/// Assign the initial brightness values of the LEDs to the respective pins: logic HIGH: "channelx.led_XX.brightness" else "0"
analogWrite(2, 0);
analogWrite(3, 0);
//Define constant VIS LEDs for fluorescence, brightness_max = 200
analogWrite(4,200);
analogWrite(5,200);
Serial.begin(9600);
Serial.setTimeout(1);}
void loop() {
if(loop_==1){
    play_gol();
    apply_gol();
    Serial.println("new grid");
    loop_ = 0;
    for(int i = 0 ; i < MAX_Y; i++){
        for(int j = 0 ; j < MAX_X; j++){
            Serial.println(new_grid[i][j]); } }
 Serial.println("end new grid");}}
int play_gol() {
/*1. Any live cell with < 2 neighbours dies (loneliness).
  2. Any live cell with > 3 neighbours dies (overcrowding).
  3. Any live cell with 2 || 3 neighbours lives.
  4. Any dead cell with = 3 neighbours comes to life.
Compute detect grid in Raspi , send to Arduino. Execute python code only when needed, send call data from Arduino to Pi. Only call is received, Pi takes a photo and calculates matrix.*/
  Serial.write(18);
  starttime = millis();
  // stay in loop until either all bytes set, or t>1s
  while ( Serial.available() < BUFFER_SIZE ){}
  if(Serial.available() == BUFFER_SIZE){
// all bytes received, read serial port, save bytes in buffer array
      for(int n=0; n < (MAX_Y * MAX_X); n++){
         buf[n] = Serial.read();
         Serial.println(buf[n]);}
      for(int y = 0; y < MAX_Y; y++){
       for(int x = 0; x < MAX_X; x++){
// Save elements of 1D buffer in 2D detectgrid
         detectgrid[y][x] = buf[y*MAX_X + x];
         Serial.println(detectgrid[y][x]); } } }
```

```
// if cell=1 next to a cell=0, open channel at next iteration
if(detectgrid[0][0] != detectgrid[0][1]){
    new_grid[0][0] = 1;
    new_grid[0][1] = 1;}
else{new_grid[0][0] = detect_grid[0][0];
    new_grid[0][1] = detect_grid[0][1];}
  return new_grid[MAX_Y][MAX_X];}
void apply_gol(){
// cell changes 0 to 1, the function opens the channel inbetween
    int a;
    int b;
    int *giver_pointer;
  while(millis() < timeinterval){
  for (int y = 0; y < MAX_Y; y++) {
   for (int x = 0; x < MAX_X; x++) {
    if(detectgrid[y][x]==0 && new_grid[y][x]==1){
      Serial.println("Open channel 1");
        LED_UV(1000, &channel1);
// after channel open, cells are checked (photo) for signal propagaion
    ok: close channel
        Serial.write(18);
        starttime_2 = millis();
// stay in loop until 9 databytes received or t>1s
         while ( Serial.available() < BUFFER_SIZE ){ }
          if(Serial.available() == BUFFER_SIZE){
// if 9 bytes received, read serial port and save each byte
              for(int n=0; n < (MAX_Y * MAX_X); n++){
                  buf_2[n] = Serial.read();
                  Serial.println(buf_2[n]); }
          for(int y = 0; y < MAX_Y; y++){
              for(int x = 0; x < MAX_X; x++){
// Save elements of 1D buffer in 2D detectgrid
                  detectgrid_2[y][x] = buf[y*MAX_X + x];
                  Serial.println(detectgrid_2[y][x]);
                  } } }
      if(detectgrid_2[y][x] == 1){
      LED_VIS(1000, &channel1); }
      else{
  // if signal not propagated yet, rerun UV code to keep channel open
      LED_UV(1000, &channel1);
      LED_VIS(1000, &channel1);
        } } } } }
  channel1.led_VIS.control = 1;
  channel1.led_UV.control = 1;}
/* Switch UV led on/off in a given time interval, to open channels */
 int LED_UV(int OnTime, channel *which_led){
   Led temp_UV = which_led->led_UV;
```

```
  if((temp_UV.Ledstate == HIGH) && (millis() - temp_UV.lastTime >=
   OnTime))
  { temp_UV.Ledstate = LOW;          // Turn UV off
    temp_UV.lastTime = millis();   // Remember the time
    analogWrite(temp_UV.adjustPin, 0);
    Serial.println("UV closed");}
  else if ((temp_UV.Ledstate == LOW) && (temp_UV.control == 1))
  { temp_UV.Ledstate = HIGH;         // turn UV on
    temp_UV.control = 0;
    temp_UV.lastTime = millis();    // Remember the time
    analogWrite(temp_UV.adjustPin, temp_UV.brightness);
    Serial.println("UV opened");}
    which_led->led_UV = temp_UV;
    return temp_UV.Ledstate; }  // Update actual LED
// Switch VIS led on/off to close channels
 int LED_VIS(int OnTime, channel *which_led){
   Led temp_VIS = which_led->led_VIS;
  if((temp_VIS.Ledstate == HIGH) && (millis() - temp_VIS.lastTime >=
   OnTime))
  { temp_VIS.Ledstate = LOW;         // Turn VIS off
    temp_VIS.lastTime = millis();   // Remember the time
    analogWrite(temp_VIS.adjustPin, 0);
    Serial.println("VIS closed");}
  else if ((temp_VIS.Ledstate == LOW) && (temp_VIS.control == 1))
  { temp_VIS.Ledstate = HIGH;     // turn VIS on
    temp_VIS.control = 0;
    temp_VIS.lastTime = millis();   // Remember the time
    analogWrite(temp_VIS.adjustPin, temp_VIS.brightness);
    Serial.println("VIS opened"); }
    which_led->led_VIS = temp_VIS;
    return temp_VIS.Ledstate; // Update the actual LED
  }
```

Acknowledgements

The first thank you goes to Friedrich Simmel for giving me the possibility to work on bioprinting at his chair.

Also a big thank you to Helene Budjarek, Susanne Kinzel and Daniela Härtwig for their support in all lab and non-lab related questions. A special thanks to Susanne for her dedicated work on iGEM 2018 and ECCSB2.

I want to thank all of my colleagues at ZNN, it was a great time working with all of you. Especially to Elisabeth Falgenhauer for her support in mechanical workshop skills and her introduction to bacteria culturing. The hours caring for her/my/our cyanos, her constant feedback and help with all the synbio topics. And, of course, for the kind supply with her bright mVenus and mTurquoise bacteria.

To Thomas Frank, for his constant personal support, not being irritated by alternating moods and being a neverending source of weird biological facts (we will find the beavers someday!). For long discussions about the world in general and introducing me to hardstyle (which allows to work focused in nearly all circumstances). Thank you Kilian Vogele, Marisa Götzfried, and Florian Katzmeier for support in all random (un-)lab-related questions. To Enzo Kopperger, because thanks to his supervision, I had a great start at this chair during my Master's Thesis. Special thanks to Lukas Aufinger for the kind supply with PITC-Agarose and to Markus Eder for the supply with chemotactic bacteria.

I want to thank Johannes Seitz, Nick Schröder and Hubert Riedl from the WSI for introducing me to mills and lathes, explaining me a lot about mechanics and manufacturing, and for producing and assembling all the aluminum parts for my bioprinter setup.

iGEM 2018 for sleepless nights, the stressful wiki freeze, the European Meetup, and the experience to reach extreme goals if working together. Special props to Dominic Schwarz, Quirin Emslander, Johann Brenner and Keno Eilers for powering the wiki on night shifts.

A big thank you to Dominic Schwarz, for being my strongest critic, bringing up good ideas for the project and creating the slickest designs. To Jonathan Richter for finding CPO, introducing me to organic chemistry, and teaching me a lot about biochemistry. To Anna Jäkel, Izlen Erenoglu, Franziska Kotsch, and Hannes Ehlert (and interesting topics). To all of my students for their dedicated work, their ideas and input, to generate an even nicer project and learn a lot about myself.

And absolutely a big thank you to the FSEI people. Especially Florian Wilde, because he told me what-not-to-do, bringing my attention to the didactic courses, and always reminded me of keeping my labbook straight. To Sebastian Gebhard for being my IT-expert of all issues. To Michael Brambach for being a great person to talk about 3D printing with all materials one can think of.

And over all, I want to thank my parents Luise and Josef for constant support, help with all non-lab-related issues, accepting stressed grumpyness, the world's best Marmorkuchen, taking care of my plants during needed vacation periods and regular checks if I drive with Winterreifen or Sommerreifen to Garching in the correct season.

It was a great time, even if not everything worked from the start or didn't work at all. I want to thank every one who helped me, to make the decision to start a PhD. And even more: to finish it.

It's still magic even if you know how it's done.

Terry Pratchett, A Hat Full of Sky